



The
University
Of
Sheffield.

Synthesis of amphiphilic acrylic copolymers and investigation of their
self-assembly using X-ray scattering techniques

Thomas Joseph Neal

A thesis submitted in partial fulfilment of the requirements for the degree of
Doctor of Philosophy

The University of Sheffield
Faculty of Science
Department of Chemistry

September 2019

Declaration

The work described in this thesis was undertaken at the University of Sheffield under the supervision of Dr Oleksandr Mykhaylyk and Dr Sebastian Spain between October 2015 and September 2019 and has not been submitted, either wholly or in part, for this or any other degree. All the work is original work of the author, except where acknowledged.

Signature: _____

Thomas Joseph Neal

September 2019

Dedicated to my folks

Acknowledgements

I am incredibly grateful to the many people who have helped me through the blur that is undergrad chemistry and then through the trials and tribulations of postgraduate research. Firstly, I would like to thank my two supervisors Sash (Dr Oleksandr Mykhaylyk) and Seb-Spanol (Dr Sebastian Spain) for their many ideas, unending knowledge, and hours of support. Our Friday meetings seemed to last for hours, and sometimes they did, but I am extremely appreciative of the time and energy that you have put into this project. Additionally, thank you for all the amazing opportunities that I have been allowed to experience throughout this PhD, from conferences in America to skiing in the Alps!

A huge thank you to my industrial supervisors Martin Murray, Neal Williams, Simon Emmett at AkzoNobel. Thank you for providing me with an invaluable insight into the world of industrial research and allowing me to spend three months gaining vital experience in an industrial lab. I have thoroughly enjoyed our regular update meetings and your individual input into this project has been instrumental to its success. I would also like to thank everybody I had the pleasure of working with at my time at Akzo, especially to Sylvie, Krystina, Dee, Sahar, Agnieszka, John, Neil, Amy, and finally Rob... my rock! It was wonderful to meet you all and you helped make my time in Slough a very enjoyable experience ... despite being in Slough and breaking my arm. Additionally, I would like offer massive thanks to my Nan for letting me crash at your digs for the three months I spent in the south, I can truly say I haven't eaten so well since I started uni – it was a dream.

Thank you to Steve Armes and Tony Ryan for your input during our update meetings with AkzoNobel and for your constant support over the last four years. A huge thank you to Cockers (Dr Amy Cockram) for lab help, meeting prep, and for always being up for a chat in the office. A huge thank you to Debs for the quality work you did at the beginning of this project, the ground work you put in made it very easy to get to grips with the project. A huge thank you to every member of the Spain, Armes, and Ryan-Mykhaylyk groups, past and present, who I have had the privilege to work with. Thank you to the past members of the Spain group Dom, Kat, Layla and Laura for welcoming me into the group and for the massive amount of help you offered at the beginning of my PhD. Thank you to Spain group members, Emma, Jasmine, Rheanna, Marrisona, Anna, Josh, Ellen, and Sam for making the Spain group a pleasure to be a part of. Thank you to all the members of the Armes and Ryan-Mykhaylyk group that have helped me over the past few years, especially to Emma and Byard for all the TEMs I asked you both to run. A special thank you to Dr Matt Derry for all your guidance and SAXS help over the past four years.

Finally, a massive thankyou to all my friends and family who have supported me unconditionally! Thank you to the Wednesday footy crew and the badminton big dogs. Thank you to Liam, Spud, Mike and Sharkey for your amazing friendship and for always being there for me. Thank you to Alex, Alexandra, Charlotte, Diane, Eliot, Georgie, Iain, Isaac, Jess, Natasha, Loz, G-force, Cat, Lou, and Byard for making my time at Uni some of the best years of my life. A special thanks to Emma, for your love and support over the last year and a half, for proof reading my work (that was riddled with grammatical mistakes), and for being the best boozing buddy anyone could ask for. Finally, an enormous thank you to my Mum, Dad and my

bros, Ant, Will, and Ed! Thank you for always believing in me and for everything you have done for me over the years. Without you I would not be the person I am today.

Peace.

Publications and conferences

Publications directly related to this thesis

T. J. Neal, D. L. Beattie, S. J. Byard, G. N. Smith, M. W. Murray, N. S. J. Williams, S. N. Emmett, S. P. Armes, S. G. Spain, O. O. Mykhaylyk, Self-Assembly of Amphiphilic Statistical Copolymers and Their Rheological Properties, *Macromolecules*, 2018, **51**, 1474

T. J. Neal, A. J. Parnell, S. M. King, M. W. Murray, N. S. J. Williams, S. N. Emmett, S. P. Armes, S. G. Spain, O. O. Mykhaylyk, Controlled self-assembly of statistical ionic amphiphilic methacrylate copolymers by tuning their composition and hydrophobicity, manuscript in preparation.

T. J. Neal, J. Llewelyn, E. E. Brotherton, M. W. Murray, N. S. J. Williams, S. N. Emmett, S. G. Spain, O. O. Mykhaylyk, The effect of molecular Structure on the self-Assembly of amphiphilic BMA-MAA copolymers, manuscript in preparation.

T. J. Neal, R. Bradley, M. W. Murray, N. S. J. Williams, S. N. Emmett, S. G. Spain, O. O. Mykhaylyk, Solution and film behaviour of amphiphilic triblock acrylate copolymers, manuscript in preparation.

Collaborative publications

A. A. Cockram, T. J. Neal, M. J. Derry, O. O. Mykhaylyk, N. S. J. Williams, M. W. Murray, S. N. Emmett, S. P. Armes, Effect of Monomer Solubility on the Evolution of Copolymer Morphology during Polymerization-Induced Self-Assembly in Aqueous Solution, *Macromolecules*, 2017, **50**, 796

S. L. Canning, T. J. Neal, S. P. Armes, pH-Responsive Schizophrenic Diblock Copolymers Prepared by Polymerization-Induced Self-assembly, *Macromolecules*, 2017, **50**, 6108

P. Yang, Y. Ning, T. J. Neal, E. R. Jones, B. R. Parker, S. P. Armes, Block copolymer microparticles comprising inverse bicontinuous phases prepared *via* polymerization-induced self-assembly, *Chem. Sci.*, 2019, **10**, 4200

G. N. Smith, M. J. Derry, J. E. Hawlett, J. R. Lovett, O. O. Mykhaylyk, T. J. Neal, S. Prevost, S. P. Armes, Refractive index matched, nearly hard polymer colloids, *Proc. R. Soc. A.*, 2019, DOI:10.1098/rspa.2018.0763

A. Rawlings, L Somner, M. Fitzpatrick-Milton, T. Roebuck, C. Gwyn, P. Liravi, V. Seville, T. Neal, O. Mykhaylyk, S. Baldwin, S. Staniland, Artificial coiled coil biomineralisation protein for the synthesis of magnetic nanoparticles, *Nature Communications*, 2019, DOI:NCOMMS-18-26970D

Presentation at conferences

Oral - ACS National Meeting, Fall 2019, San Diego, USA

Oral - 255th ACS National Meeting, Spring 2018, New Orleans, USA

Oral - CDT Annual Summer School, August 2018, Sheffield, UK

Oral - CDT Industrial Showcase Day, September 2018, Sheffield, UK

Poster - Macro Group Young Researchers Meeting (YRM), June 2017, Edinburgh, UK

Poster - 12th international conference on Advanced Polymers via Macromolecular Engineering (APME), May 2017, Ghent, Belgium

Abstract

In this thesis, the effect of copolymer composition, molecular weight, and monomer hydrophobicity on the self-assembly of anionic amphiphilic statistical copolymers in aqueous solutions was investigated using structural characterisation techniques such as small angle X-ray scattering (SAXS) and transmission electron microscopy (TEM). It was found that they preferably form spherical particles. The size of the particles formed by the aggregation of amphiphilic statistical copolymers is heavily dependent on the copolymer composition but is largely independent of molecular weight, where particles with larger ratios of the hydrophilic monomer produced smaller particles. Particle size was only found to be dependent of molecular weight when unimolecular micelles (single chain nanoparticles) were formed. Additionally, the hydrophobicity ($\log P$) of the hydrophobic comonomer has a great influence on particle size, where increasing the hydrophobicity increases the copolymer particle size. The relationship between copolymer composition and particle size was rationalised in terms of particle surface charge density, where the copolymers aggregate together to induce a critical surface charge density that allows colloidal stability to be achieved. The critical surface charge density was quantified as the fraction of the particle surface covered by the charged monomer ($SA_{\text{frac.MAA}}$), leading to the development of the particle surface charge density (PSC) model. It was found that the PSC model fit well to the experimental data collected for all the copolymer series and a $SA_{\text{frac.MAA}}$ was calculated for each series where the hydrophobic monomer was varied. Furthermore, a linear relationship between the $\log P$ of the hydrophobic component and the $SA_{\text{frac.MAA}}$ required to induce stabilisation of the particle dispersion was observed.

Additionally, the effect of hydrophile-hydrophobe distribution along polymer backbones has been examined. It was found that there was a clear correlation between the monomer distribution and the particle size, where blockier structures, in comparison with evenly distributed monomers, produce larger copolymer particles. This result was rationalised as a reduction in the efficiency by which the charged hydrophile, when in a blocky arrangement, can stabilise the hydrophobic component leading to an increase in particle size. Finally, a range of amphiphilic triblock copolymers were synthesised, where the DPs of the individual hard and soft blocks were varied. The amphiphilic triblocks were found to assemble into spherical particles in water but remained dissolved in methyl ethyl ketone (MEK). Films were cast of the triblock copolymers from both solvent environments, and the structural phase separation in the films was studied using a combination of SAXS and AFM. It was found that the copolymer films cast from MEK were able to phase separate into well-defined structures, where the size and morphology of the phase separation was dependent on the block length and hard-to-soft block ratio, respectively. These morphologies were consistent with the predicted self-assembly of diblock copolymers in the bulk. Conversely, the water-cast films partially retained the particulate structure present in solution, produced kinetically trapped phase separated structures. However, by annealing the water-cast film at 150 °C the lower energy phase-separated structure observed in the MEK films can be achieved.

List of abbreviations

2θ	Scattering angle
λ	Wavelength
ε	Particle aspect ratio
ζ	Scattering length density
ρ	Density
σ	Standard deviation
AA	Acrylic acid
ACVA	4,4-Azobis(4-cyanovaleric acid)
AD	1-Adamantyl methacrylamide
AFM	Atomic force microscopy
AIBN	2,2'-Azobisbutyronitrile
AM	Acrylamide copolymers
AMPS	Sodium 2-(acrylamido)-2-methylpropanesulfonate
APC	Advanced polymer chromatography
ATRP	Atom transfer radical polymerisation
BA	Butyl acrylate
BHT	Butylhydroxytoluene
BMA	Butyl methacrylate
BzBr	Benzyl bromide
CD	Cyclodecyl methacrylamide
CS_{MAA}	Cross-sectional area of one MAA unit
CTA	Chain transfer agent
d_{AFM}	Length scale of phase separation measured by AFM
d_{SAXS}	Real space distance corresponding to q^*

d_{011}	Distance between the crystallographic planes in a BCC structure
d_{010}	Distance between the crystallographic planes in a hexagonal structure
D	Molar-mass dispersity
DAMAB	Dimethyldodecyl (2-acrylamidoethyl)ammonium bromide
DBzTTC	Dibenzyltrithiocarbonate
DLS	Dynamic light scattering
DNA	Dioxyribonucleic acid
D ₂ O	Deuterium oxide
DP	Number-average degree of polymerisation
DSC	Differential scanning calorimetry
E_0	Energy of incident radiation
E_i	Energy of scattered radiation
EMA	Ethyl methacrylate
EM	P(ethyl methacrylate-stat-methacrylic acid) copolymer series
EHMA	2-Ethyl hexyl methacrylate
EHM	P(2-ethyl hexyl methacrylate-stat-methacrylic acid) copolymer series
f	Volume fraction
f_{HP}	Effective volume fraction for the charged particle structure factor
f_{PY}	Effective volume fraction for the hard sphere structure factor
FRP	Free radical polymerisation
FT-IR	Fourier-transform infra-red
GPC	Gel permeation chromatography
GISAXS	Grazing incident small angle X-ray scattering
HCl	Hydrochloric acid
HDPE	High density polyethylene
HMA	Hexyl methacrylate
HM	P(hexyl methacrylate-stat-methacrylic acid) copolymer series
H ₂ O	Water
HPLC	High-performance liquid chromatography

I	Initiator
i	Total number of species
IPA	Isopropanol
IUPAC	International Union of Pure and Applied Chemistry
K	Reciprocal efficiency coefficient
k_a	Rate constant of activation
k_B	Boltzmann constant
k_d	Rate constant of deactivation
k_p	Rate constant for propagation
k_t	Rate constant for termination
LA	Lauryl methacrylamide
LDPE	Low density polyethylene
M	Molar mass
M	Ionic strength
M	Monomer
M_1	Single monomer unit
MAA	Methacrylic acid
macro-CTA	Macromolecular chain transfer agent
MEK	Methyl ethyl ketone
MMA	Methyl methacrylate
M_n	Number-average molecular weight
$M_{n/m}$	Propagation of a monomer chain
$Mol.frac.MAA$	Mole fraction of MAA in a copolymer chain
M_w	Weight-average molecular weight
M_w/M_n	Dispersity
N	Number of repeat units
N_A	Avagadro's number
N_{agg}	Aggregation number
$N_{MAA,p}$	Number of MAA unit within a particle

$N_{\text{BMA,p}}$	Number of BMA units within a particle
$N_{\text{AMA,p}}$	Number of AMA units within a particle
NMP	Nitroxide-mediated polymerisation
NMR	Nuclear magnetic resonance
2-NP	2-naphthyl methacrylamide
P	Point scatterer
p	Packing parameter
PDI	Polydispersity index
PE	Polyethylene
PETTC	4-cyano-4-(2-phenylethanesulfanylthiocarbonyl)sufanylpentanoic acid
PISA	Polymerisation-induced self-assembly
P_m	Propagating polymer radical
PMMA	Polymethyl methacrylate
P_n	Propagating polymer radical
P_{n+m}	Dead polymer chain
PP	Polypropylene
PSC	Particle surface charge density model
PSt	Polystyrene
PTFE	Polytetrafluoroethylene (Teflon)
PVC	Poly(vinyl chloride)
Py	Pyrenyl methacrylamide
Q	Effective particle charge
q	Scattering vector
$R\cdot$	Radical species
RAFT	Reversible addition-fragmentation chain transfer
R_{dry}	Radius of dried particles on carbon coated grid
R_g	Radius of gyration
R_h	Hydrodynamic radius

R_{HP}	Effective interparticle correlation radius for the charged particle structure factor
R_{PY}	Effective interparticle correlation radius for the hard structure factor
R_s	Sphere radius
SA_{frac}	Particle surface area fraction covered by MAA
SANS	Small angle neutron scattering
SAXS	Small angle X-ray scattering
SEC	Size exclusion chromatography
SLD	Scattering length density
SLS	Static light scattering
T	Temperature
TEA	Triethanolamine
TEM	Transmission electron microscopy
TEMPO	2,2,6,6-tetramethyl-1-piperidynyl-N-oxyl
T_g	Glass transition temperature
THF	Tetrahydrofuran
USAXS	Ultra-small angle X-ray scattering
UV	Ultra-violet
V_{cop}	Volume of a single copolymer chain
V_{AMA}	Volume of one AMA unit
V_{BMA}	Volume of one BMA unit
V_{MAA}	Volume of one MAA unit
v_{IPA}	Volume fraction of IPA in IPA-water solution
v_{Water}	Volume fraction of water in IPA-water solutions
w	Weight fraction
WAXS	Wide angle X-ray scattering
X	Mole fraction
x_{sol}	Volume fraction of solvent within the nano-object

Contents

Chapter 1. General Introduction	1
1.1 What is a polymer?	2
1.2 Polymer Architectures	3
1.3 Methods of polymer synthesis	4
1.3.1 Step polymerisation.....	5
1.3.2 Chain polymerisation	6
1.4 Copolymers	14
1.5 Polymer characterisation.....	15
1.5.1 Gel permeation chromatography (GPC)	15
1.5.2 Scattering techniques	18
1.6 Self-assembly of surfactants and copolymers.....	24
1.6.1 Surfactants.....	24
1.6.2 Electrostatic stabilisation	25
1.6.3 Steric stabilisation.....	28
1.6.4 Self-assembly of block copolymers in bulk.....	28
1.6.5 Self-assembly of block copolymers in solution	31
1.6.6 Self-assembly of statistical copolymers	35
1.7 Thesis outline	41
1.8 References.....	43
Chapter 2. Materials, general methods and SAXS models.....	51
2.1. Materials	52
2.1.1 List of chemicals and suppliers.....	52
2.2. Characterisation methods.....	54
2.2.1 Methylation and Alkylation	54

2.2.2 ^1H Nuclear Magnetic Resonance (NMR) Spectroscopy	54
2.2.3 Gel Permeation Chromatography (GPC)	55
2.2.4 Advanced Polymer Chromatography (APC)	55
2.2.5 Small-Angle X-ray Scattering (SAXS) measurements	55
2.2.6 Grazing Incident Small-Angle X-ray Scattering (GISAXS) measurements	56
2.2.7 Small-Angle Neutron Scattering (SANS) measurements	57
2.2.8 Dynamic Light Scattering (DLS)	57
2.2.9 Aqueous Electrophoresis	58
2.2.10 Transmission Electron Microscopy (TEM)	58
2.2.11 Atomic Force Microscopy (AFM)	58
2.2.12 Differential scanning calorimetry (DSC)	59
2.2.13 Rheology	59
2.2.14 Mechanical testing	60
2.3. SAXS Structural Models	60
2.3.1 Intensity equation	60
2.3.2 Intensity equation with linear background	61
2.3.3 Intensity equation with linear background and unified parametrisation	61
2.3.4 Distribution function of the structural model parameters.	62
2.4. Structure factor	62
2.4.1 Percus-Yevick approximation	62
2.4.2 Hayter-Penfold approximation	63
2.5 Form factors	63
2.5.1 Gaussian chain model	63
2.5.2 Sphere model (Figure 2.1a)	63
2.5.3 Spheroid model (Figure 2.1b)	64
2.5.4 Blob model (Figure 2.1c)	65
2.5.5 Core-Shell sphere model (Figure 2.1d)	66
2.5.6 Spherical micelle model (Figure 2.1e)	68
2.5.7 Adapted spherical micelle model	69

2.5.8 Two-population model (Figure 2.1e)	70
2.6 References	71
Chapter 3. Self-assembly of amphiphilic statistical copolymers and their aqueous rheological properties	74
3.1 Introduction	75
3.2 Results and discussion	77
3.2.1 Synthesis of BMA-MAA amphiphilic statistical copolymers	77
3.2.2 Copolymer self-assembly in water	80
3.2.3 Effect of varying the IPA/water solvent composition at a fixed copolymer concentration	88
3.2.4 Effect of varying both the copolymer concentration and the solvent composition	91
3.2.5 Rheology of copolymer dispersions	95
3.2.6 The relationship between particle size and the copolymer composition	99
3.3 Conclusions	103
3.4 References	105
Chapter 4. Self-assembly of amphiphilic statistical copolymers in aqueous solution by tuning copolymer composition and hydrophobicity	109
4.1 Introduction	110
4.2 Results and discussion	112
4.2.1 Synthesis of amphiphilic statistical copolymers by RAFT solution polymerisation	112
4.2.2 Aggregation behaviour of amphiphilic P(AMA- <i>stat</i> -MAA) statistical copolymers	116
4.2.3 Determination of internal particle structure using contrast variation SANS	122
4.2.4 Relationship between nanoparticle size and copolymer composition	125
4.3 Conclusions	131
4.4 References	132
Chapter 5. The effect of molecular structure on the self-assembly of amphiphilic BMA-MAA copolymers	138
5.1 Introduction	139
5.2 Copolymer synthesis	142
5.2.1 Polymerisation of MAA for kinetic analysis.	142

5.2.2 Statistical copolymerisation to form P(BMA- <i>st</i> -MAA).....	143
5.2.3 Pseudo-gradient copolymerisation to form P(BMA- <i>gr</i> -MAA).....	143
5.2.4 Block copolymerisation to form P(BMA- <i>b</i> -MAA).....	144
5.2.5 Formation of aqueous copolymer dispersions.....	145
5.3 Results and discussion	146
5.3.1 Synthesis and characterisation of copolymers.	146
5.3.2 Self-assembly of copolymers to form spherical particles	150
5.3.3 Utilisation of MAA within the copolymer particle	157
5.3.4 Comparison against the behaviour of statistical copolymers	161
5.4 Conclusions.....	163
5.5 References.....	165
Chapter 6. Solution and film behaviour of amphiphilic triblock acrylate copolymers.....	169
6.1 Introduction.....	170
6.2 Triblock copolymer synthesis	173
6.2.1 Synthesis of P(AA- <i>st</i> -St) macro-CTA <i>via</i> RAFT solution polymerisation.....	173
6.2.2 High-throughput syntheses of triblock copolymers <i>via</i> RAFT solution polymerisation ...	173
6.3 Results and discussion	174
6.3.1 Synthesis and characterisation of copolymers	174
6.3.2 Solution behaviour of the macro-CTAs and triblock copolymers in an organic solvent ...	180
6.3.3 Solution behaviour of the macro-CTAs and triblock copolymers in an aqueous solution....	182
6.3.4 Structural characterisation of triblock copolymer films cast from an organic solvent	189
6.3.5 Structural characterisation of triblock copolymer films cast from aqueous dispersion	201
6.3.6 Structural characterisation of annealed triblock copolymer films cast from aqueous dispersion	210
6.3.7 Mechanical characterisation of the triblock copolymer films	213
6.4 Conclusions.....	217
6.5 References.....	219
Chapter 7. Conclusions and future work.....	223
7.1 References.....	230

Chapter 8. Appendices231

Chapter 1. General Introduction

Chapter 1.

General Introduction

Polymers have a wide range of properties that can be tuned for particular applications.¹⁻⁵ Natural polymers such as DNA, cellulose, and proteins are fundamental to life and others such as natural rubber have been enhanced using synthetic techniques (*e.g.*, vulcanised rubber) to modify their properties for specific applications.⁶⁻⁸ Examples of synthetic polymers include polyamide (Nylon), low and high density polyethylene (LDPE and HDPE), polytetrafluoroethylene (PTFE, or Teflon), and poly(vinyl chloride) (PVC). Each of these polymers exhibit unique properties such as specific strength, elasticity, surface tension, and hardness, that have been found to be useful in applications such as in fabrics, beverage bottles, non-stick frying pans, drain pipes, contact lenses, and artificial hip joints.⁵ This thesis will focus on a specific class of polymer known as amphiphilic polymers, which are composed of both hydrophilic and hydrophobic components. This unique property makes amphiphilic polymers interesting and useful in various applications such as transporting hydrophobic drugs *in vitro* for targeted drug delivery, and as the binder in water-borne paints, and coatings.⁹⁻¹²

1.1 What is a polymer?

A polymer is a long chain molecule that is composed of multiple smaller molecules known as monomers or repeat units. The length of a polymer chain is often defined by the degree of polymerisation (DP) which describes the average number of repeat units per polymer chain. Since, a single polymer sample can have a number of different chain lengths, they do not have

a single unique molecular weight, but rather have a molecular weight distribution represented by the dispersity (\mathcal{D} or M_w/M_n): The dispersity is defined as

$$\mathcal{D} = \frac{M_w}{M_n} \quad (1.1)$$

where M_w and M_n are terms that are commonly used to describe the weight average molecular weight and the number average molecular weight of a polymer, respectively.¹³ M_n is defined as the sum of the products of the molar mass, M_i , multiplied by the mole fraction, X_i :

$$M_n = \sum X_i M_i \quad (1.2)$$

Whereas, M_w is defined as the sum of the products of the molar mass multiplied by the weight fraction, w_i :

$$M_w = \sum w_i M_i \quad (1.3)$$

If all of the polymer chains in a polymer ensemble are equal in mass then M_w/M_n is equal to 1 and the polymer is considered to be monodisperse. However, any value for M_w/M_n that is lower than 1.5 is considered to have a narrow molecular weight distribution.¹⁴

1.2 Polymer Architectures

A key property of polymers is that they can come in a variety of different architectures (Figure 1.1). The architecture of a polymer describes the way in which the monomer units are linked together. The simplest polymer architecture is linear (Figure 1.1a), this is where the monomer units are covalently bonded together in a continuous linear chain. More complex architectures include comb (Figure 1.1b), brush (Figure 1.1c) and star (Figure 1.1d). The different architectures will affect the overall physical and chemical properties of the polymer.¹⁵

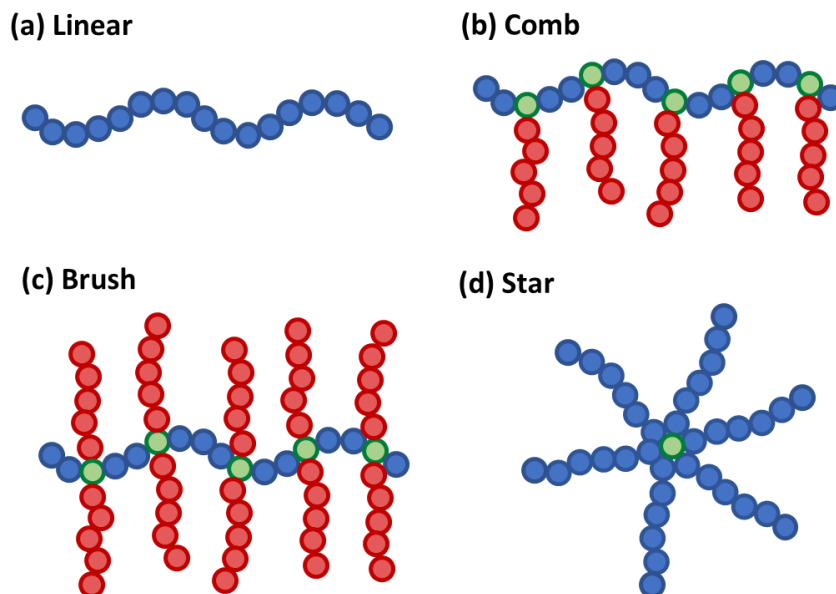


Figure 1.1. A cartoon describing four examples of polymer architectures, where the red and blue circles represent two different monomers, and the green circles indicate branching points on the copolymer backbone.

1.3 Methods of polymer synthesis

Over the years many different methods have been developed and utilised to synthesise a variety of polymers. However, all of these methods were later categorised by Carothers based upon the comparison between the molecular formula of the monomer and the polymer formed; these two categories were known as condensation and addition polymerisations.⁵ A condensation polymerisation yields a polymer with a repeat unit of a lower molecular weight than the monomers reacted together, normally through the loss of a small molecule, for example, H₂O or HCl. Whereas an addition polymerisation produces a polymer where the molecular weight of the repeat unit is the same as the monomers used. Carothers later found this initial classification to be unsatisfactory since certain condensation reactions were observed to have typical features of addition polymerisations, and *vice versa*. With this realisation he altered his

classifications to reflect the polymerisation mechanism and the two categories became step polymerisations and chain polymerisation.⁵

1.3.1 Step polymerisation

A step polymerisation is where multifunctional monomers combine through mutually-reactive functional groups to form a long chain polymer (Figure 1.2).¹⁶ This method of synthesis is used to produce a wide range of industrially relevant polymers such as polyurethanes and polyesters. Step polymerisations can be further sub-categorised into polycondensation reactions and polyaddition reactions. The former involves the elimination of small molecules such as H₂O during the polymerisation, whereas a polyaddition takes place without the loss of any molecules (Figure 1.2).

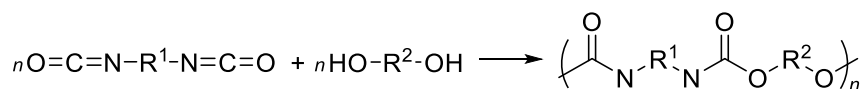


Figure 1.2. The reaction between diisocyanates and diols to form a polyurethane as an example of a polyaddition step polymerisation.⁵

The reaction mechanism involved in step polymerisation means that there is rapid loss of monomer in the early stages; however, the average molecular weight only increases slowly at the beginning of the reaction. A rapid increase in molecular weight is only observed as a high extent of reaction is achieved. Therefore, it is important to achieve a high extent of reaction in step polymerisations to achieve high molecular weight polymers. Furthermore, since there is no termination of chains throughout the polymerisation, the functional groups remain present at the termini of the polymer and can be further reacted in post-polymerisation processes.

1.3.2 Chain polymerisation

Unlike step polymerisation, chain growth within a chain polymerisation occurs through reactions between the monomers and an active-sites (radical or ion) on the polymer chain. Once the reaction between monomer and active-site has occurred, the active component is regenerated so that the process can reoccur and the polymer chain can grow. Many useful copolymers are synthesised using chain polymerisation methods such as poly(vinyl chloride) (PVC), poly(methyl methacrylate) (PMMA), polyethylene (PE), and polypropylene (PP), which are used for water pipes, transparent sheets and mouldings, tubing and packaging.⁵ The two main types of chain polymerisation are categorised as radical and ionic polymerisations.

1.3.2.1 Ionic polymerisation

Ionic polymerisation is an example of a chain polymerisation. Here monomer addition occurs through reaction with ionic active sites on the polymer chain, where the ionic active site can either be positive (cationic) or negative (anionic). Since this method requires stabilisation of an ion to provide the active centre for reaction to proceed, this technique is not applicable to a wide range of monomers and reaction conditions.

In a cationic polymerisation a cationic initiator, such as a protic acid, reacts with the monomer and transfers the positive charge to form a carbocation. The charged monomer will then undergo propagation through addition of monomer molecules to the active centre. The chains can be terminated either by unimolecular rearrangement of the ion pair or by chain transfer to the monomer, solvent, or any impurities such as H₂O. If the chains are not terminated, they will grow until all the monomer has been consumed.^{5,13} Cationic polymerisation is often used in the production of polyisobutylene, which is used to make innertubes.¹⁷

An anionic polymerisation is very similar to a cationic polymerisation except the ions are negatively charged in this case. For example, an anionic initiator is used to transfer a negative charge onto the monomer. Here, the monomer is required to stabilise an anionic charge and therefore monomers have to be carefully selected. It is rare that a monomer is applicable for both cationic and anionic polymerisations since charge stabilisation within the monomer is an important requirement. The key property of an anionic polymerisation is that it doesn't undergo termination during the polymerisation.^{18,19} Ion pair rearrangement is unable to occur since the formation of a hydride ion is highly unfavourable.⁵ Furthermore, chain transfer is improbable since the counter ions used in anionic polymerisations (alkali metals) are unlikely to react with the anionic active centres to form an unreactive covalent bond.⁵ Since no termination can occur, the active centre of the polymer is permanently retained and the polymer chain can grow until all the monomer is consumed, this phenomenon is given the term living polymerisation.^{18,19} Anionic polymerisation is often used for the polymerisation of monomers such as styrene²⁰⁻²² and butadiene.^{23,24}

1.3.2.2 Free radical polymerisation

Free radical polymerisation is defined by IUPAC as a chain polymerisation where the kinetic chain carriers are radicals.²⁵ This synthetic technique has been of scientific interest for eighty years and is used for producing high molecular weight polymers such as polystyrene (PSt) and poly(methyl methacrylate) (PMMA). Since free radical polymerisation was first utilised, it has been the topic of a large amount of research with the ultimate aim of improving its reproducibility, control of molecular weight, and composition.²⁶ In the past fifty years a considerable amount of work has been devoted to developing techniques to confer control over radical polymerisations.²⁷

Free radical polymerisation offers many advantages compared to ionic polymerisation, including: (a) applicability to a wide range of monomers; (b) high tolerance to many functional groups and reaction conditions; (c) simplicity in comparison to other polymerisation chemistries. However, traditional free radical polymerisation also has many limitations. These include deficiencies in control over the molecular weight distribution, composition and architecture. The mechanism of free radical polymerisation involves a chain reaction where chains are initiated by radicals adding to monomer molecules (Figure 1.3). Unlike ionic polymerisations, where two propagating centres cannot recombine, termination of chains in radical polymerisation can occur either by combination or disproportionation.²⁶ Combination is where two radical chain ends couple together to form one polymer chain, and disproportionation is where a hydrogen atom is abstracted from one end to produce an unsaturated terminus on one of the two dead polymer chains.²⁶

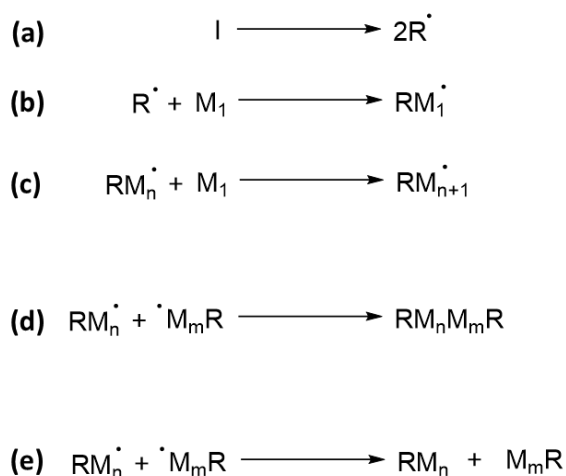


Figure 1.3. Mechanism for free radical polymerisation where I is an initiator that undergoes homolytic fission (a) to form radicals (R^{\cdot}) when subjected to heat, electromagnetic radiation, or chemical reaction, (b) shows the initiation of a single monomer molecule (M_1), (c) shows the propagation of a monomer chain ($\text{M}_{n/m}$), and (d) and (e) show termination by combination and disproportionation, respectively.

In standard free radical polymerisation, slow initiation and a fast propagation leads to high molecular weight chains forming in the early stages of the reaction which leads to a broad dispersity of molecular weights. However, in an ideal living radical polymerisation all the chains are initiated at the start and grow at the same rate. Furthermore, in an ideal situation all of the chains continue to exist throughout the polymerisation and hence there is no termination. Therefore, in order to achieve this living nature, the irreversible termination of polymer chains must be suppressed, such as in anionic polymerisation.²⁸

There are three main controlled radical polymerisation techniques that are coined “pseudo-living” polymerisations: nitroxide-mediated polymerisation (NMP),^{29,30} atom transfer radical polymerisation (ATRP),³¹ and reversible addition-fragmentation chain transfer (RAFT).³² A mediating radical species ($R\cdot$) enables reversible termination to be achieved for a living free radical polymerisation (Figure 1.4). A rapid equilibrium is established between the active and dormant polymer radicals, which means that each chain has an equal probability of growth.³³

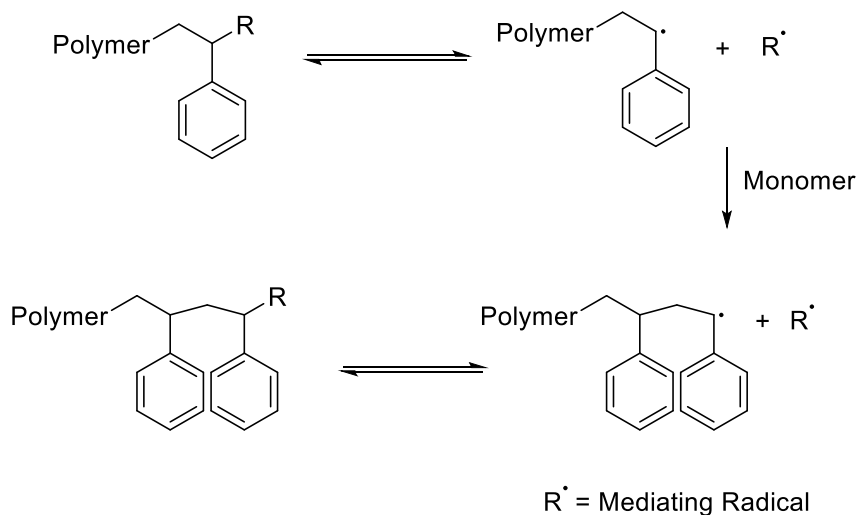


Figure 1.4. Mechanism for the living free radical polymerisation of styrene demonstrating a rapid equilibrium between active and dormant polymer radicals.

1.3.2.3 Nitroxide-mediated polymerisation (NMP)

NMP is an example of a controlled radical polymerisation that has attracted a lot of interest.^{33–35} It is a robust technique where narrow dispersities can be achieved for various polymer architectures (M_w/M_n lower than 1.20). The origin of NMP comes from studies of initiation mechanisms.³³ Through the course of these investigations, various nitroxides were used as radical traps. It was found that under certain conditions, capping of propagating radical species by certain nitroxides was reversible.³³

NMP is a typical living free radical polymerisation in which termination is suppressed relative to propagation due to the rapid reaction between a stable radical and a carbon-centred radical. In the case of NMP, the stable radical species are established by thermolysis of the C-ON bond in an alkoxyamine to form a nitroxide radical and a carbon-centred radical (Figure 1.5).²⁹ The carbon-centered radical can react *via* two steps that facilitate a controlled polymerisation: (1) regeneration of the dormant alkoxyamine end-group by recombination with the nitroxide radical; (2) chain extension by addition to the alkene group of the monomer. The latter reaction produces a new polymer radical that can continue *via* either one of these two pathways.²⁹

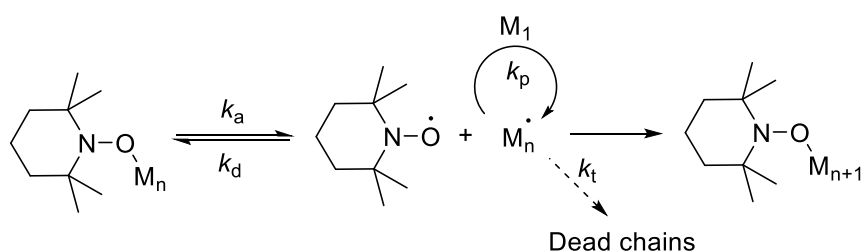


Figure 1.5. General mechanism for NMP using TEMPO as the nitroxide radical where M_n is the propagating polymer chain, M_1 is an unreacted monomer unit, and k_a , k_d , k_p , and k_t , are the rates of activation, deactivation, polymerisation, and termination, respectively.

The transition metal complex undergoes a one-electron oxidation with concurrent abstraction of a halogen atom from a latent compound R-X; this catalysed reversible redox process generates the radicals or active species.³¹ Like all other controlled radical polymerisations, ATRP involves a dynamic equilibrium between active and dormant chain ends, which allows narrow polydispersities to be achieved due to reduced radical concentrations, and therefore reduced termination rates, and each chain having an equal chance to grow.

In ATRP, the main role of the ligand is to solubilise the transition metal salt in organic media and to also modify the redox potential of the metal for suitable reactivity in terms of atom transfer. One drawback to ATRP is its incompatibility with acidic monomers such as methacrylic acid or acrylic acid. This is because the nitrogen-based ligands tend to be susceptible to protonation and thus cannot coordinate with the transition metal.³¹ However, ATRP is used commonly to polymerise styrene, acrylamides such as N-isopropylacrylamide (NIPAM), along with non-acidic acrylates and methacrylates.

1.3.2.5 Reversible addition-fragmentation chain transfer (RAFT)

RAFT was introduced by Rizzardo, Moad, and Thang in 1998.³² Although it is one of the more recent additions to the field of living free radical polymerisations, it has become very popular through its convenience and versatility.^{39,40} Their seminal 1998 paper described living free radical polymerisation using thiocarbonylthio RAFT agents.³² Figure 1.7 depicts the thiocarbonylthio compound used as a chain transfer agent in RAFT polymerisation. Z can be aryl, alkyl, SR', OR' or NR₂', while R must be a good homolytic leaving group with respect to the polymer. In addition, R must be able to form a radical (R·) which is capable of initiating further polymerisation.¹⁶

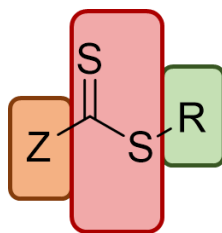


Figure 1.7. General thiocarbonylthio chain transfer agent used in RAFT polymerisation.

RAFT polymerisation is compatible with a wide range of reaction conditions and monomers, including acidic monomers such as methacrylic acid⁴¹ and acrylic acid⁴², while still achieving narrow polydispersities. This makes RAFT more popular than other methods of living free radical polymerisation. RAFT polymerisation can be subdivided into four steps (Figure 1.8).

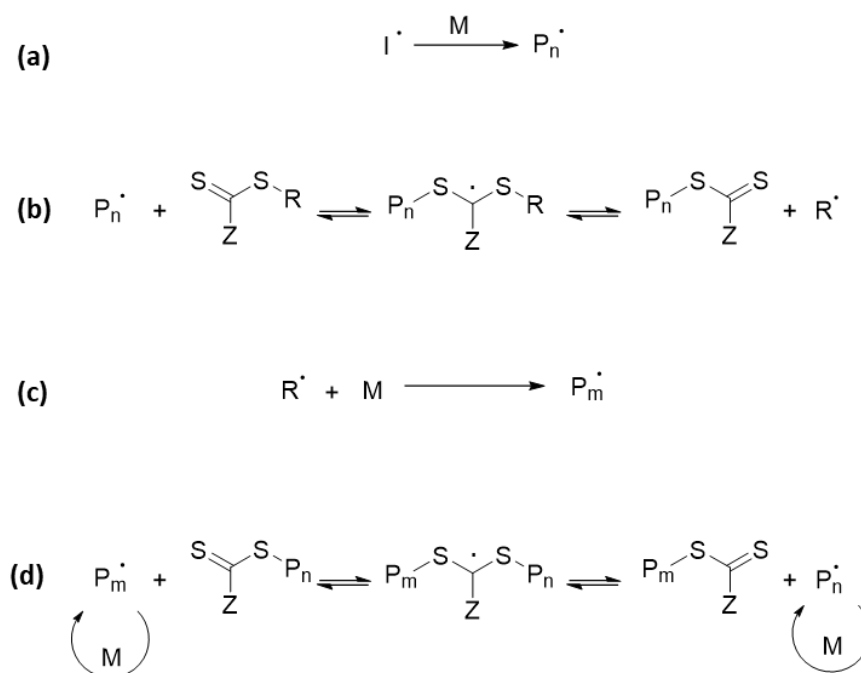


Figure 1.8. The four main steps of RAFT polymerisation: (a) initiation, (b) addition-fragmentation, (c) reinitiation, (d) chain equilibrium, M is the monomer, I^{\cdot} is the initiator radical and P_n^{\cdot} and P_m^{\cdot} are the growing polymer chains of mean degrees of polymerisation n and m, respectively.

The key to success in RAFT polymerisation is the rapid reversible chain transfer between the propagating polymer chains by the thiocarbonylthio chain transfer agents.⁴³ This reduces the probability of bimolecular termination significantly compared to a conventional free radical polymerisation. The thiocarbonylthio species enables the polymer chains to grow with minimal termination, and hence produces polymers with narrow polydispersities ($M_w/M_n < 1.2$).

1.4 Copolymers

Polymers are defined as long chain molecules that are composed of multiple smaller molecules. If the polymer is formed from numerous repeats of the same small molecule (monomer), then this is known as a homopolymer. However, polymers can be composed of a number of different monomers assembled in a certain sequence and these polymers are known as copolymers. When multiple monomers with different properties are introduced, the distribution of the monomer along the copolymer chain becomes very important and has a large effect on the resultant copolymer properties. Therefore, copolymers can be further subdivided into several categories based on the repeat unit arrangement (Figure 1.9) in addition to polymer architecture (Figure 1.1).⁵ Two important categories of copolymer that will be described in this introduction are statistical (Figure 1.9a) and block (Figure 1.9b) copolymers; however there are several other categories such as gradient (Figure 1.9c) and alternating (Figure 1.9d). A statistical copolymer is one where the distribution of repeat units is determined by the reactivity ratios of the monomers.^{16,44} One of the advantages offered by this type of copolymer is that it tends to have intermediate properties in relation to the corresponding homopolymers, which enables tuning of polymer properties, such as the glass transition temperature, T_g . However, a block copolymer is one where two or more chemically distinct homopolymers are covalently linked together.⁴⁵ Since the chemically different repeat units are segregated, block copolymers can incorporate distinct properties of the two monomer blocks.

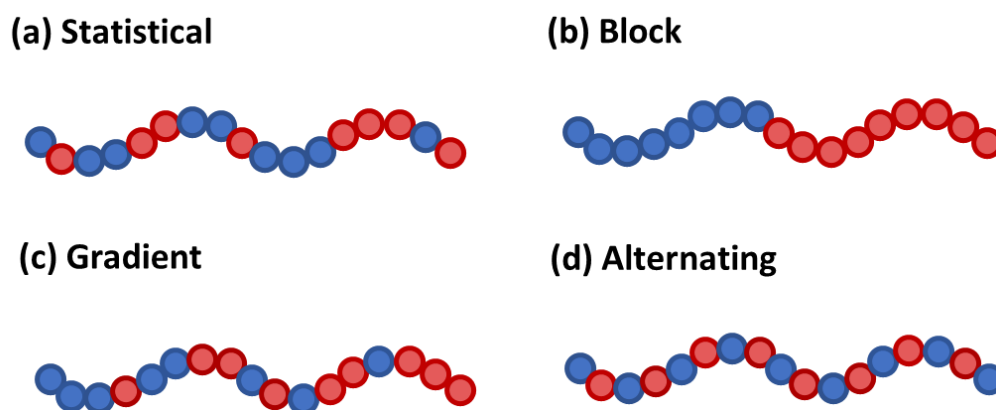


Figure 1.9. A cartoon describing the monomer distribution within a linear (a) statistical, (b) block, (c) gradient, and (d) alternating copolymer.

1.5 Polymer characterisation

Once a polymer has been synthesised, it is important to characterise what has been made. This is done by using a number of standard techniques that are commonly used in small molecule characterisation, such as nuclear magnetic resonance (NMR) spectroscopy, Fourier-transform infra-red (FT-IR) spectroscopy, and mass spectrometry. However, in addition to these techniques, there are analytical methods that are designed for the characterisation of large molecules such as polymers, these include gel permeation chromatography (GPC), dynamic light scattering (DLS), static light scattering (SLS), and small angle X-ray and neutron scattering (SAXS and SANS).

1.5.1 Gel permeation chromatography (GPC)

A key technique for analysing polymers is gel permeation chromatography (GPC),⁴⁶ which is also known as size exclusion chromatography (SEC). GPC is a technique that allows the molecular weight of a polymer to be measured by interpolation against polymer samples of

known molecular weight.⁴⁶ Like all chromatography techniques, GPC works by separating a sample into fractions based upon a certain fundamental property; in the case of GPC this property is the hydrodynamic volume of a polymer chain. GPC can be separated into two phases - the mobile phase and the stationary phase. The mobile phase consists of a solvent known as the eluent and the dissolved polymer or analyte, whereas the stationary phase is a column filled with a porous gel. The mobile phase is pumped through the porous column where the dissolved polymer will enter a different number of pores based upon its hydrodynamic volume. Smaller polymers will enter a greater number of pores than larger polymers since some pores will be too small for large polymers to enter. This means that smaller polymers will take a longer time to be eluted from the column since they have a longer pathway (Figure 1.10). The time in which it takes for the polymer to leave the column is known as the retention time. The eluted polymer can be detected using a number of methods, such as differential refractive index (RI), UV-visible spectroscopy, and evaporative light-scattering. The detected signal is compared against a calibration curve created using polymer standards of known molar mass and the M_n and M_w (eqs 1.2 and 1.3) of the sample can be obtained (Figure 1.11).

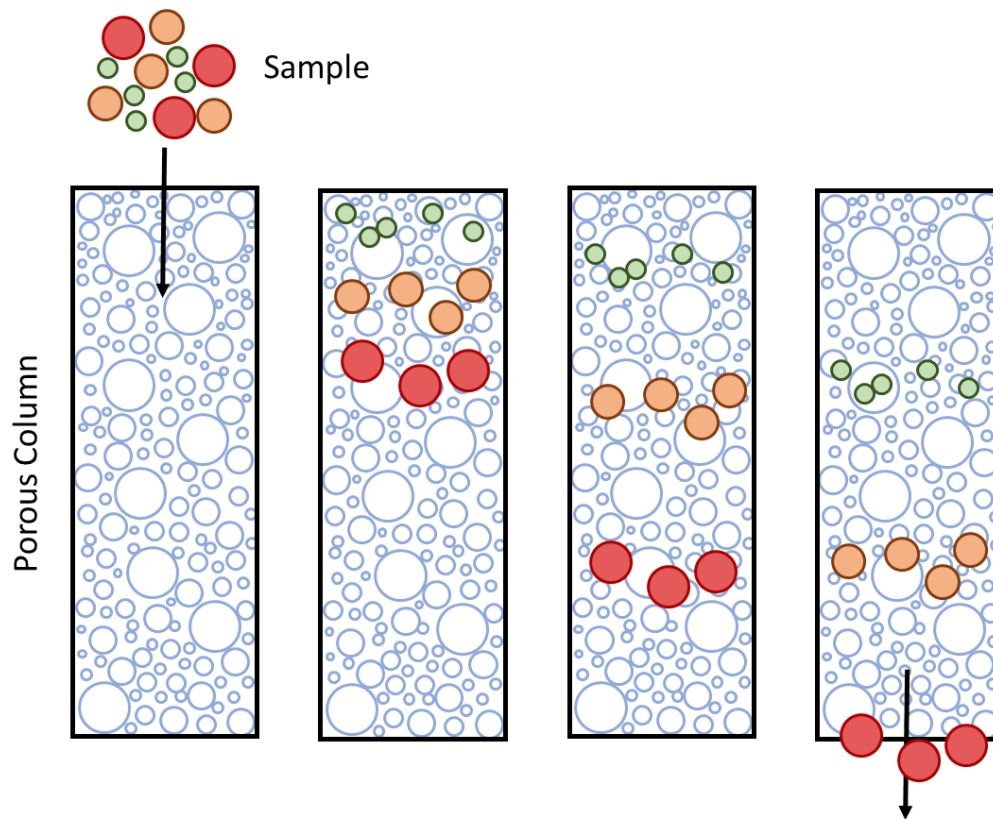


Figure 1.10. A schematic demonstrating the separation of polymers with different molar masses using GPC.

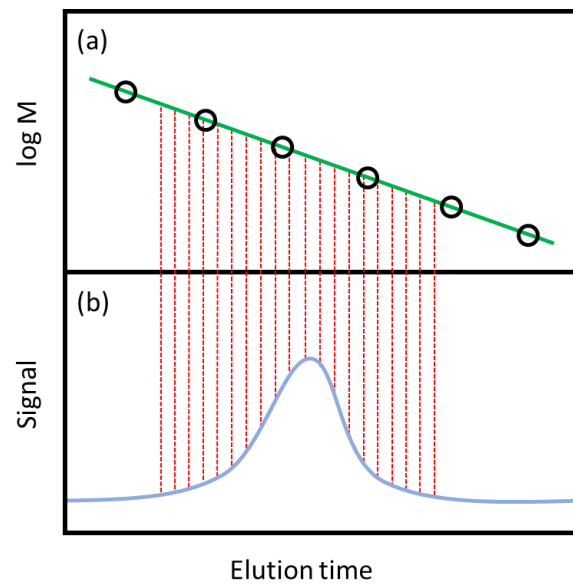


Figure 1.11. A schematic of the process by which molar mass distribution is calculated by interpolation against a calibration curve created using standards of known molecular weights, where (a) is a calibration curve, and (b) is an example GPC trace for a polymer with an unknown molar mass.

Since GPC calculates molar masses based upon interpolation against known standards, the resulting molecular weight is only relative to the standards used and cannot be considered to be absolute. This means that discrepancies are observed when the analyte has a significantly different chemistry or polymer architecture than the calibrants, *e.g.*, a branched polymer will appear to have a lower molecular weight than reality when interpolated from a set of linear polymer standards. Furthermore, different modes of detecting the eluting polymer chains will offer different advantages and disadvantages and may give varying results depending on the polymer being analysed. Throughout this thesis, GPC signals are monitored using an RI detector as it is a relatively cheap method that can be used for most polymer systems (*i.e.*, no chromophores are required). Whereas UV detection requires the analyte to contain a chromophore and evaporative light-scattering detection tend to be expensive and require an inert gas supply.

1.5.2 Scattering techniques

Scattering techniques are important for polymer chemistry. They are used for structural characterisation and can provide information about the shape and size of polymer chains and their self-assemblies. In these techniques most of the incident radiation passes straight through the polymer sample, but some waves will be scattered by polymers. The scattering mechanism depends on the type of radiation. X-rays are scattered by electrons; neutrons are scattered by nuclei; and light scattering requires a difference in refractive index between the polymer and the solvent. The angular-dependence of the scattered intensity of these waves provides important structural information, such as size and shape.

1.5.2.1 Static light scattering (SLS)

The choice of radiation depends on the properties of the sample itself and the purpose of the measurements. Light scattering is an important technique for determining the M_w of a polymer and the size of a polymer aggregate. In 1871 Lord Rayleigh developed the theory of light scattering during his study of gases.⁴⁶ He determined that the ratio of the intensity of the scattered unpolarised light I_θ at a certain scattering angle θ and the intensity of the unpolarised incident beam I_0 of wavelength λ is related to the polarizability of the molecule α , and the distance between the sample and the detector r by the equation:¹⁶

$$\frac{I_\theta}{I_0} = \frac{8\pi^4 \alpha^2 (1 + \cos^2 \theta)}{\lambda^4 r^2} \quad (1.4)$$

This is the case for small molecules but for larger particles, such as polymers, the situation is different. If a polymer has dimensions greater than $\lambda'/20$, where λ' is the wavelength of the light in the medium, then intraparticle interference causes scattered light to be considerably out of phase. The angular attenuation of scattering for large molecules is measured by the particle scattering factor $P(\theta)$. This can be defined as the ratio of the scattering intensity to the intensity where there is no interference at the same angle θ . Guinier showed how the light scattered by a large molecule can be related to the radius of gyration R_g . The radius of gyration is defined as the root-mean-square distance of the segments of the molecule from its centre of mass. $P(\theta)$ can be related to the R_g using the Debye equation shown below.¹⁶

$$P(\theta) = \left(\frac{2}{u^2} \right) [e^{-u} - (1-u)] \quad (1.5)$$

where u is defined as:

$$u = \left\{ \left(\frac{4\pi}{\lambda} \right) \sin \left(\frac{\theta}{2} \right) \right\}^2 R_g^2 \quad (1.6)$$

where R_g is the radius of gyration.

1.5.2.2 Small angle X-ray and neutron scattering (SAXS and SANS)

Small-angle scattering of X-rays and neutrons, known as SAXS and SANS respectively, are extensively used analytical methods for studying the nano scale structure of soft matter (Figure 1.12). These methods are based on to the classical work of Guiner published in 1938.⁴⁷ Guinier's seminal work was followed by studies from Porod,⁴⁸ Kratky,⁴⁹ Luzzati,^{50,51} and Beeman,⁵² which has led to the development of both theoretical and experimental understanding.⁵³

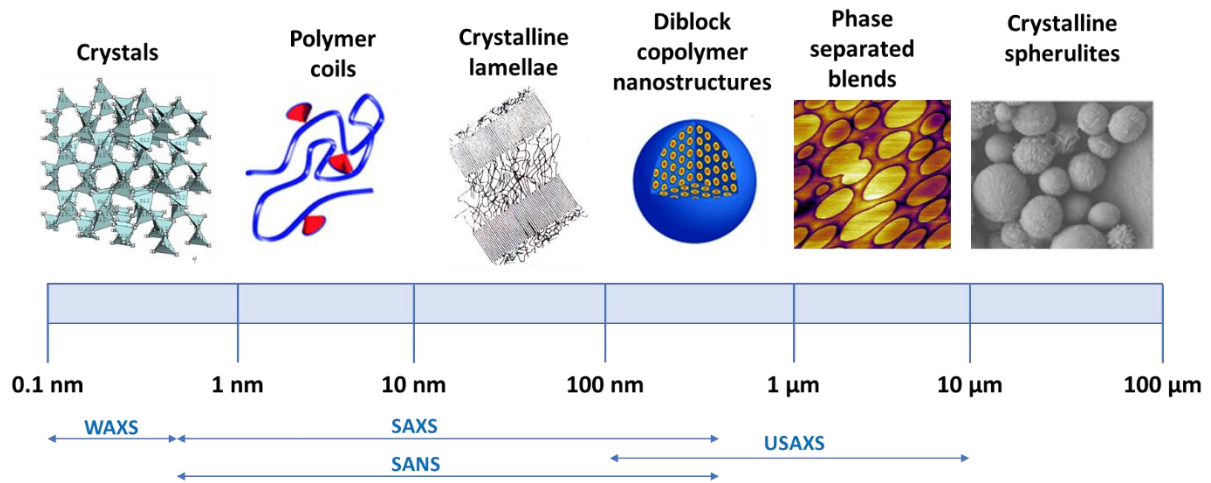


Figure 1.12. Demonstrating the accessible length scales in which scattering techniques, such as SAXS and SANS can be used as a means for structural characterisation. Where WAXS, SAXS, and USAXS is wide-, small- and ultra small- angle X-ray scattering, respectively, and SANS is small-angle neutron scattering.

Scattering can either be inelastic (with loss of energy) such as Compton scattering⁵⁴ and fluorescence radiation, or elastic (without loss of energy) such as Rayleigh or Thompson scattering (Figure 1.13).⁵⁵ In Compton scattering, the photon transfers some of its energy to the scattering electron, which then results in scattered radiation at a different wavelength to the

incident radiation. This radiation is incoherent and therefore cannot interfere with the incident beam. This means that it does not provide any structural information about the particle. Furthermore, fluorescence occurs when an X-ray photon expels an electron from an atom, causing the excited atom to emit fluorescence radiation as the remaining electrons rearrange to fill the resulting hole. On the other hand, with Rayleigh and Thompson scattering there is no energy transfer from the photon to the electrons in the atoms. However, interaction with electrons can cause them to oscillate at the same frequency acting as an oscillating electric dipole producing a spherical wave of electromagnetic radiation, at this same frequency. This radiation is coherent, which means that interference can occur between waves irradiated by different oscillators belonging to the same scattering object and information regarding the object structure can be extracted.

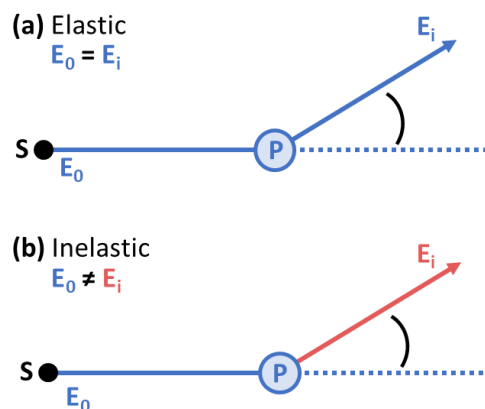


Figure 1.13. A schematic depicting how an X-ray photon behaves during (a) elastic scattering, and (b) inelastic scattering, where S is the X-ray source, P is the point scatterer, and E_0 and E_i are the energies of the incident and scattered radiation, respectively.

X-rays that have been scattered by a material are observed using a detector, which allows the scattering angle, 2θ , to be measured. This can be converted into the commonly used scattering vector, q , which takes into account the wavelength, λ , of the X-ray:

$$q = \frac{4\pi}{\lambda} \sin \theta \quad (1.7)$$

The efficiency at which radiation is scattered depends on the amount of point scatterers per irradiated material volume and is known as the scattering length density. In the case of X-ray scattering, the scattering length density is related to the electron density of a material. In order to observe scattering from a material in a solution (*i.e.*, a polymer nanoparticle dispersion) there must be a difference in scattering length density (ξ) defined as:

$$\xi = \frac{b_e \rho_m N_A}{M} \sum_i n_i z_i \quad (1.8)$$

where b_e is the scattering length density of an electron, ρ_m is the molecule (material) density, N_A is Avogadro's number, M is the molecular weight, z_i is the number of electrons in each element, n_i is the number of each element and the subscript i indicates the total number of elements in a compound.

In 1940 Ewald suggested that the electron density in a sample can be represented by the concept of a form factor.⁵⁵ Subsequently, the form factor has become an important function in determining information about a scatterer's shape and size.^{56,57} The form factor can be defined as the interference pattern of a particle, where the oscillations are characteristic of the particle shape. In order to gather information regarding the latter parameter, the system must be sufficiently dilute ($\approx 1\%$ vol) to ensure that the particles are well-separated from each other. Thus, it can be assumed that the waves scattered by different particles lack phase coherence. The overall intensity is then simply the sum of the independent X-ray intensities scattered from individual particles. Information about the size, shape and surface can be extracted by investigating different regions of the scattering pattern, these are known as the Guinier, Fourier, and Porod regions (Figure 1.14). A plateau in the Guinier/Fourier region suggests spherical

particles whereas slopes of -1 and -2 suggests cylindrical and disc-like (or flat) particles, respectively. Information about the particle surface can be extracted from the scattering in the Porod region. A slope of -4 in this region suggests that the particle has a sharp interface between components comprising the system, such as aqueous dispersion of silica particles (Figure 1.14). However, often polymer nanoparticles have a stabilising polymer chain on the nanoparticle surface which behaves as a gaussian coil and creates a slope of -2 in this region.^{58,59}

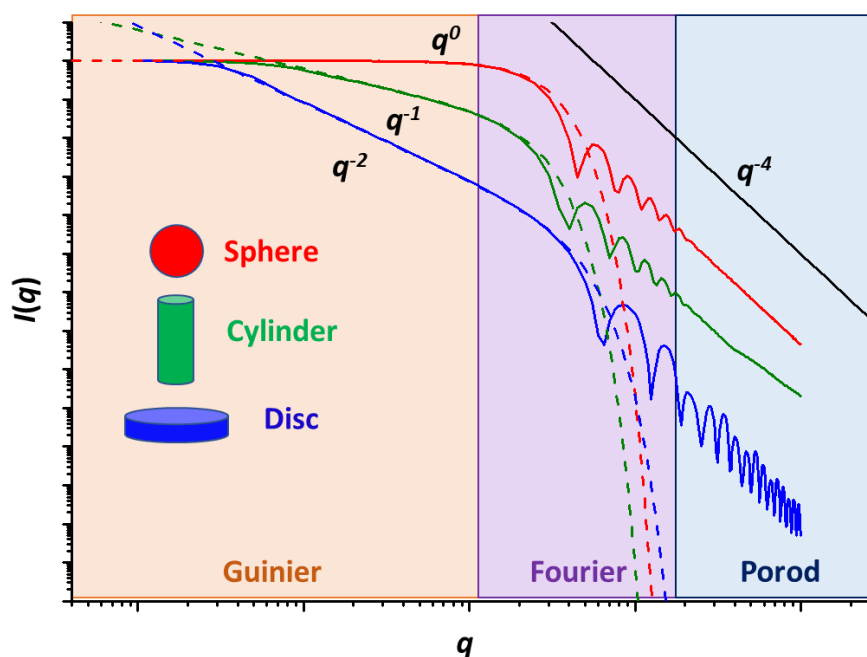


Figure 1.14. Log-log scattering patterns describing the how particles of various shape with different aspect ratio scatter X-rays in the different regions of the scattering pattern, where the red, green and blue traces represent the scattering patterns of a sphere, cylinder and disc, respectively. The three regions of the scattering pattern are the Guinier, Fourier, and Porod region.

1.5.2.3 Dynamic light scattering (DLS)

Dynamic light scattering is another important scattering technique that has been used extensively in polymer science.^{60–64} It is used primarily for assessing the hydrodynamic

diameter, D_h , of a polymer chain or particle in solution. However, the principles of DLS differ slightly from the scattering techniques described in sections 1.5.2.1-2.

Dynamic light scattering uses scattered light to monitor the random motion of chains/particles in solution, this phenomenon is known Brownian motion.^{65,66} The scattered light has time-dependent fluctuations in intensity which are directly related to the rate of diffusion of the chains/particles, where rapid fluctuations indicate quick diffusion and *vice versa*. The rate of diffusion can be used to calculate the hydrodynamic radius of the material *via* the Stokes-Einstein equation (which assumes a spherical morphology).⁶⁷

$$D = \frac{RT}{N_A} \frac{1}{6\pi\eta R_h} \quad (1.9)$$

Where D is the diffusion coefficient, R is the gas constant, N_A is Avogadro's number, T is the absolute temperature, η is the viscosity of the diffusion medium, and R_h is the hydrodynamic radius of the diffusing particle. Since the Stokes Einstein equation assumes a spherical morphology, DLS is not a good technique for investigating particle size where the morphology differs from spherical.

1.6 Self-assembly of surfactants and copolymers

1.6.1 Surfactants

An amphiphile is defined as a compound that possesses both hydrophilic (solvophilic) and hydrophobic (solvophobic) components, such as a surfactant. Surfactants are generally composed of a charged or polar head-group, which is hydrophilic, and a long carbon chain tail, which is hydrophobic.⁶⁸ Due to their amphiphilic nature, surfactants are known to readily assemble into micelles in an aqueous environment (Figure 1.15).⁶⁹ The aggregation of

surfactants is caused by unfavourable interactions between water and the hydrophobic tail. Additionally, the stability of surfactant micelles can be understood by looking at either the electrostatic or steric forces between the micelles.

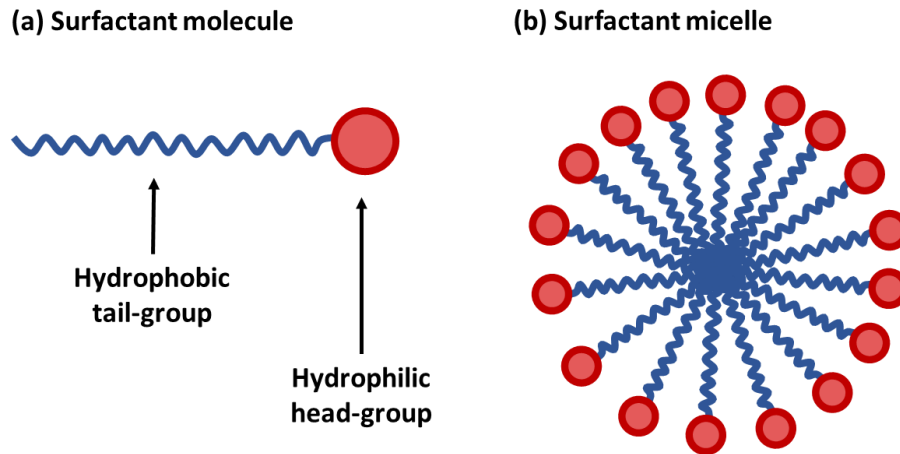


Figure 1.15. A cartoon describing (a) a surfactant molecule and (b) a surfactant micelle.

1.6.2 Electrostatic stabilisation

Electrostatic stabilisation is where the attractive van der Waals forces between the micelles are countered by the repulsive columbic forces caused by charges on the micellar surface. This phenomenon was described by Deryagin, Landau, Vewey and Overbeek in the 1940s and is known as DLVO theory.^{70,71} It states that the colloidal stability of a particle dispersion is determined by the pair interaction potential energy, $U(h)$, of particles at a distance h , which is a sum of the attractive and repulsive forces, $U_A(h)$ and $U_R(h)$, respectively.

$$U(h) = U_A(h) + U_R(h) \quad (1.10)$$

The attractive van der Waals forces between the particles are caused by constantly fluctuating dipoles of atoms in molecules and these attractive forces can cause the colloidal particles to

aggregate together. An example of this interaction is the attraction between two spheres in solution, $U_A(h)$, of radius R_1 and R_2 :

$$U_A(h) = -\frac{A}{6h} \frac{R_1 R_2}{R_1 + R_2} \quad (1.11)$$

where A is the Hamaker constant and is a function of the polarizability and density of a material.⁷² The attractive van der Waals forces are most prominent at small distances.

The repulsive forces are caused by similarly charged points (molecule parts) on the colloidal surface. If the surface is in solution then the columbic charges interact with the surrounding ions and alter the distribution of ions close to the colloidal surface. This phenomenon is known as the electric double layer (EDL) and can be described most simply as two distinct layers (Figure 1.16). The first layer is an immobile layer of ions, with opposite charge to the surface. These ions are bound to the surface, and form what is known as the Stern layer. After the Stern layer, there is a diffuse layer of ions where the ion concentration decreases as the distance from the surface increases, this is known as the Gouy-Chapman or more commonly the diffuse layer. Due to the differences between the two layers, the electric potential across the layers behaves very differently. The electric potential decreases linearly across the Stern layer; however, it decreases exponentially across the diffuse layer (Figure 1.16). The electric potential at the particle surface and at the edge of the Stern layer can be denoted as ψ_0 and ψ_s , respectively (Figure 1.16). However, one additional potential is often quoted when investigating the electrostatic stability of a colloid, this is the zeta potential (ζ). In a colloidal dispersion there is a layer of liquid that will adhere and move with the particle known as the slip or shear plane, the potential at this point is named as the ζ -potential (Figure 1.16).

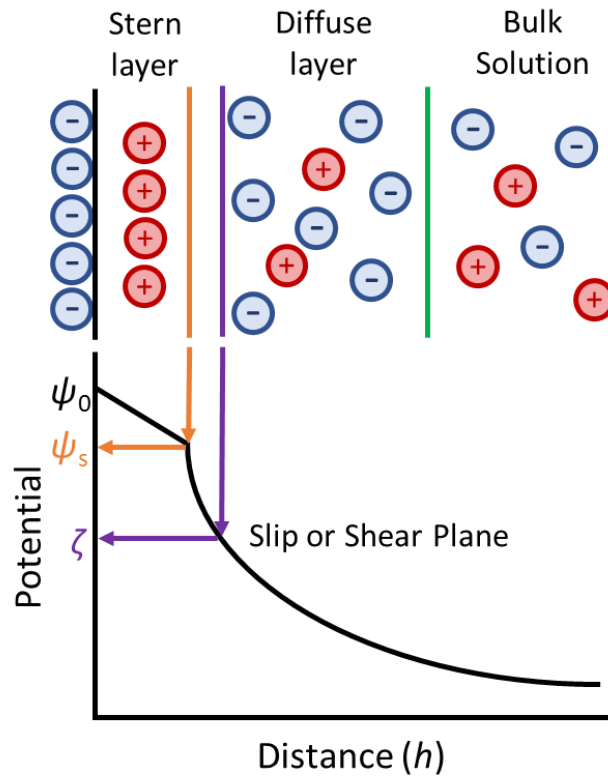


Figure 1.16. A schematic describing the electric double layer of a negatively charged surface in terms of the ion distribution and electric potential.

The screened $U_R(h)$ between two spheres can be calculated by:

$$U_R(h) = \frac{Z^2 e^2}{4\pi \epsilon_r \epsilon_0 (1 + \kappa r)^2} \frac{e^{-\kappa h}}{2r + h} \quad (1.12)$$

where Z is the number of charges on the surface, e is the elementary charge, r is the particle radius, and ϵ_0 and ϵ_r are the vacuum and relative state permittivity, respectively. Additionally, κ^{-1} is the Debye length of a charged surface describing how rapidly the Coulomb potential decreases with inter particle separation.

1.6.3 Steric stabilisation

Colloidal dispersions can also be stabilised *via* steric repulsion and is often used to stabilise colloids in high salt solutions or in nonpolar solvents.^{73,74} In this case polymer chains are often adsorbed to the particle surface to provide steric stabilisation. As the particles move towards each other to a distance that is less than twice the length of the polymer layer, the polymer chains will either compress or interpenetrate. This behaviour results in an osmotic pressure that causes the particles to repel each other.

1.6.4 Self-assembly of block copolymers in bulk

Block copolymers are known to phase separated into self-assembled structures in both a bulk state and in solution.⁷⁵ Phase separation is driven by unfavourable mixing enthalpy of the copolymer blocks. Similar phase separation would occur if two unfavourable homopolymers were mixed together in bulk however this phase separation would be macroscopic since the two homopolymers are separate molecules. Whereas, macroscopic phase separation is prevented in block copolymer systems since the blocks of the copolymer are covalently bonded together, limiting the phase separation to microscopic length scales. The phase separation can lead to multiple different self-assembled morphologies in the bulk state, such as spheres, cylinders, gyroids, and lamellae. This self-assembly is influenced by the individual volume fractions of the copolymer blocks (f_A and f_B), the number of repeat units ($N = N_A + N_B$), and the Flory-Huggins interaction parameter (χ).⁷⁶ The Flory-Huggins interaction parameter describes the degree of incompatibility between the copolymer blocks, which consequently drives the phase separation. This incompatibility is temperature dependent and the relationship is given by:

$$\chi_{AB} = \left(\frac{z}{k_B T} \right) \left[\epsilon_{AB} - \frac{1}{2} (\epsilon_{AA} + \epsilon_{BB}) \right] \quad (1.13)$$

where z is the coordination number of the repeat units in the polymer, k_B is the Boltzmann constant, T is the temperature, and ϵ_{AB} , ϵ_{AA} , and ϵ_{BB} are the interaction energies per repeat unit of AB, AA and BB, respectively. The free energy of mixing (ΔG_{mix}) for two incompatible polymers can be calculated using the Flory-Huggins lattice model.^{77,78}

$$\frac{\Delta G_{\text{mix}}}{k_B T} = \left(\frac{f_A \ln f_A}{N_A} \right) + \left(\frac{f_B \ln f_B}{N_B} \right) + f_A f_B \chi \quad (1.14)$$

Equation 1.14 demonstrates that a negative value of χ is required for two polymers (or two distinct blocks within a diblock copolymer) to spontaneously mix. Whereas a positive χ results in de-mixing. The degree of phase separation is determined by the segregation product, χN . Since χN is inversely related to T , the incompatibility between blocks A and B decreases as the temperature increases and *vice versa*. Therefore, higher temperatures are often required to induce mixing and undergo an order-to-disorder transition (ODT) and become disordered or homogeneous. The temperature at which this phenomenon occurs is known as the T_{ODT} .

A theoretical phase diagram has been established for the morphological transitions of block copolymers within the bulk using the self-consistent mean-field (SCMF) theory (Figure 1.19).^{79,80} In this theory two different regimes are introduced to describe the stretching of individual polymer chains within the microdomain of period, d , the weak segregation limit (WSL) ($\chi N < 10$) and the strong segregation limit (SSL) ($\chi N \gg 10$). The SCMF theory shows that by increasing f_A at a fixed χN (above the ODT), the order-to-order transition (OOT) goes from closely packed spheres (CPS), to body-centered cubic spheres (Q^{229}), to hexagonally packed cylinders (H), to a gyroidal structure (Q^{230}), and finally to lamellae. If f_A continues to increase the morphological transitions are reversed and the phases are inverted (Figure 1.17).

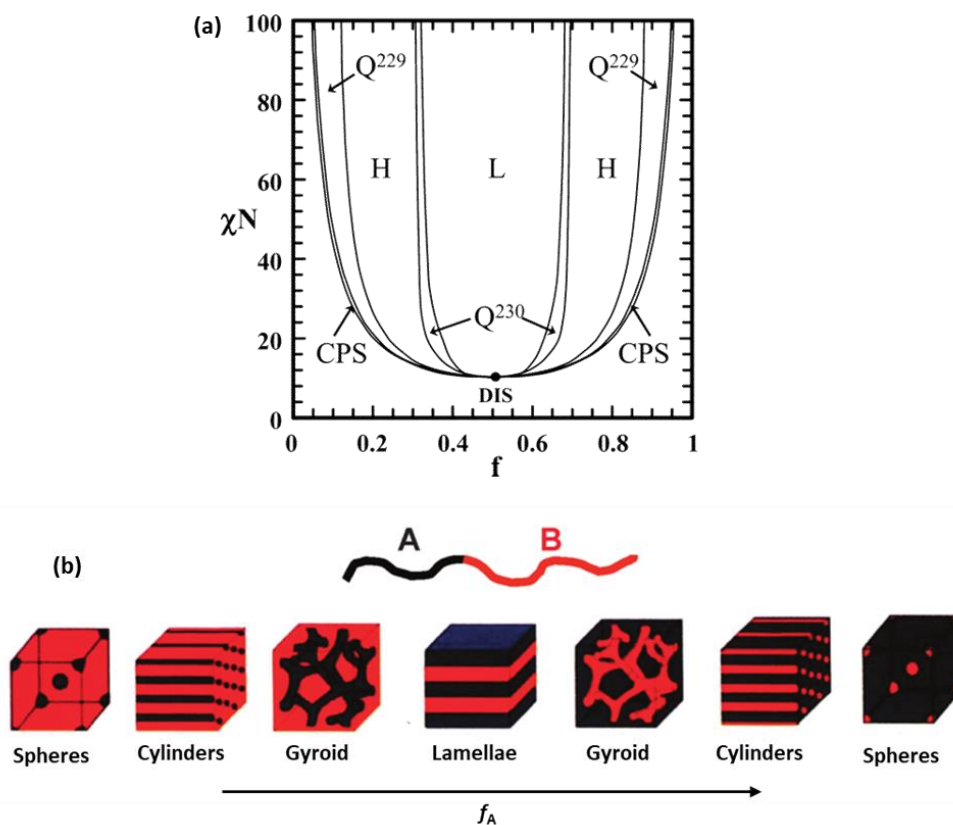


Figure 1.17. (a) Phase diagram of diblock copolymer morphologies where f is the volume fraction of one block, χ is the Flory-Huggins interaction parameter, N is the degree of polymerisation, L represents a lamellae structure, H represents hexagonally packed cylinders, Q²³⁰ represents a gyroid structure, Q²²⁹ represents body centered spheres, CPS represents close-packed spheres, and DIS represents the region where the two blocks are mixed. Reproduced with permission from E. Cochran, C. Garcia-Cervera, and G. Fredrickson, *Macromolecules*, 2006, **39**, 2449–2451. Copyright (2016) American Chemical Society.⁸¹ (b) Cartoon images of diblock copolymer morphologies in the bulk state – demonstrating how the morphology varies with the volume fraction of component A, f_A . Reproduced with permission of The Royal Society of Chemistry.⁸²

Block copolymers can be synthesised where the number of blocks is greater than two, these are known as multiblock copolymers. Increasing the number of blocks increases the number of covalently linked phase separated domains along the copolymer chain, which can lead to interesting and useful copolymer properties. One specific type of multiblock copolymer is

where there are three distinct monomer blocks, these are known as triblock copolymers. Additionally, these copolymers can either be symmetric (ABA) or asymmetric (ABC), where A, B, and C are different monomer units. The additional blocks create physical crosslinks across the phase-separated structure in the bulk state.⁸³ This increases the dimensional stability of the triblock structure compared to a diblock system, and can improve physical properties such as the toughness and extensibility.⁸⁴

1.6.5 Self-assembly of block copolymers in solution

A copolymer that comprises both solvophobic and solvophilic repeat units is known as an amphiphilic copolymer and much like surfactants they self-assemble through unfavourable interactions between the hydrophobic component and water.⁸⁵ Amphiphilic copolymers are of great interest in scientific research and are used as functional materials in paints, coatings, cosmetics, and drug delivery.⁸⁶ The way monomer units are distributed along a copolymer chain has a large effect on the copolymer behaviour; this is especially the case for amphiphilic copolymers since the monomer units have such distinctive properties. This work focuses on how both block and statistical amphiphilic copolymers assemble and what developments have been made in these respective areas of research.

In an amphiphilic diblock copolymer both the hydrophilic component and the hydrophobic component are segregated into two sections along the copolymer chains. This segmented structure can be easily compared to the structure of a surfactant that has a well-defined hydrophilic head-group and a hydrophobic tail. The self-assembly of diblock copolymers has been widely reported since 1962.⁷² However, in 1983, Noolandi and Hong constructed a simple model for AB diblock copolymer micelles in solution.⁸⁷ The model assumed spherical micelles with a completely homogeneous core formed by the insoluble B block, with a uniform shell

composed of the soluble A blocks (Figure 1.18). The shell thickness (ΔR) and the core radius (R_1) are governed by the minimisation of total free energy.

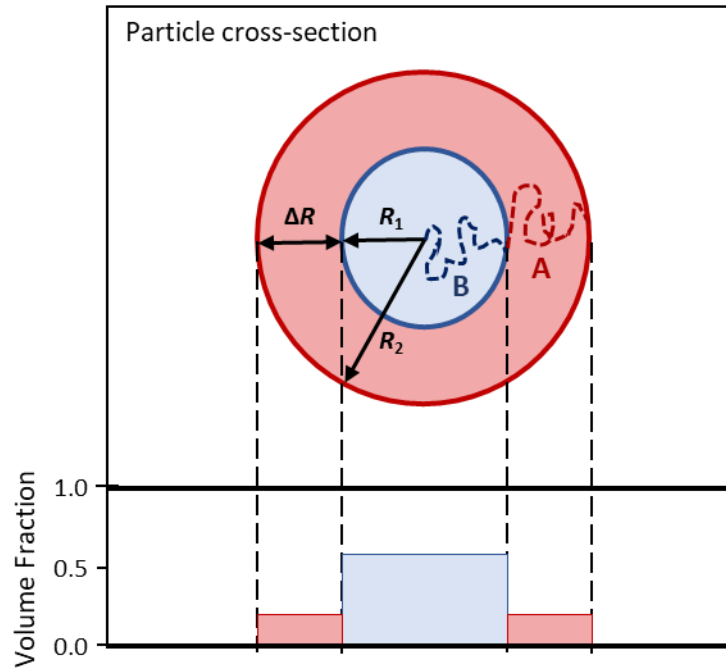


Figure 1.18. Cross-section of the core-shell micelle model proposed by Noolandi and Hong where the insoluble B block forms a uniform core with the soluble A block making up a uniform shell where R_1 is the radius of the core, R_2 is the distance from the centre of the core and the edge of the shell, ΔR is the shell thickness which is equal to difference between R_1 and R_2 .

This model has since been modified and more physically realistic models have been reported. For example, the segment density of the micelle should vary monotonically at the corona-core interface, which is in contrast with the sharp change proposed by Noolandi and Hong.

In the early 1990's much experimental and analytical research was conducted on the aggregation of amphiphilic block copolymers in aqueous media,⁸⁸⁻⁹¹ and this topic is still of considerable interest.^{9,12} In 1996 Zhang and Eisenberg investigated a series of polystyrene-*block*-poly(acrylic acid), PS-*b*-PAA, copolymers where the weight fraction of the PS component was varied from 80 to 98%.⁹² The copolymers aggregated to form various copolymer morphologies when introduced into an aqueous environment and these structures were studied by TEM. It was found that different aggregate morphologies were achieved by varying the copolymer composition. When the proportion of the hydrophilic PAA block was reduced the morphology altered gradually from spheres to worms, to both vesicles and lamellae bilayers and ultimately to compound or inverted micelles (Figure 1.19).

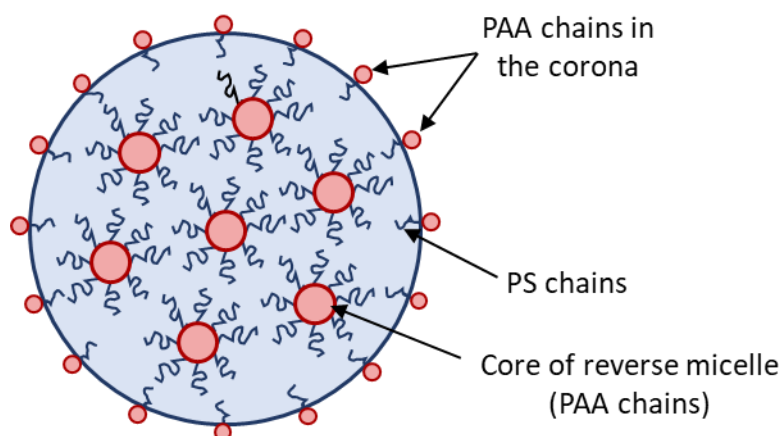


Figure 1.19. Internal structure of the large compound micelles published by Zhang and Eisenberg in 1996.

Due to the substantial number of studies of amphiphilic block copolymers and the various morphologies that they can form, it is now known that the copolymer morphology is principally caused by the inherent molecular curvature and thus the resulting geometric packing of the copolymer chains which can be described using a dimensionless packing parameter p often used to describe surfactant assemblies.⁹³

$$p = \frac{v}{a_0 \cdot l_c} \quad (1.15)$$

Here v is the volume of the hydrophobic chains, a_0 is the optimal area of soluble group, and l_c is the length of the hydrophobic tail. Generally, spherical micelles are favoured when $p \leq 1/3$, cylindrical or wormlike micelles when $1/3 < p \leq 1/2$, vesicles when $1/2 < p \leq 1$, and lamellae when $p \approx 1$ (Figure 1.20).

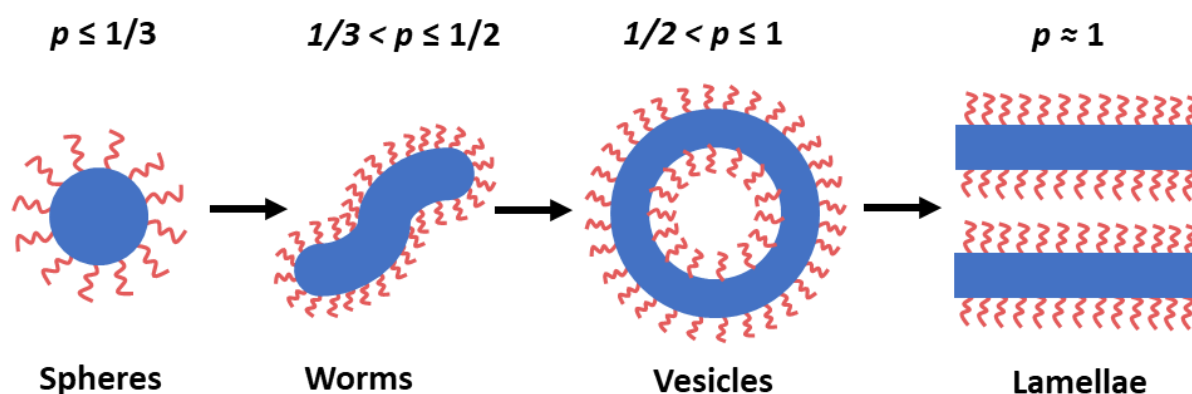


Figure 1.20. A cartoon representation of the common morphologies (spherical micelles, wormlike micelles, vesicles, and lamellae) formed by block copolymers and the respective packing parameter regime where the morphology is favoured. spherical micelles, wormlike micelles, vesicles, and lamellae.

1.6.6 Self-assembly of statistical copolymers

Although it is known that amphiphilic statistical copolymers can form micelles in aqueous media, the amount of scientific research performed on statistical copolymer self-assemblies is significantly less than the work that has been done investigating diblock copolymers. However, in 1993 McCormick's group reported a hydrophobic cationic monomer, dimethyldodecyl (2-acrylamidoethyl)ammonium bromide also known as DAMAB⁹⁴, and the effect of DAMAB

distribution on the solution behaviour of the associated acrylamide (AM) copolymers was assessed. DAMAB and AM were statistically copolymerised in water in the presence or absence of an external cationic surfactant (cetyltrimethyl ammonium bromide). The presence of the surfactant diluted the number of DAMAB molecules in each micelle to limit the length of any hydrophobic “blocks” and so increase the randomness of the comonomer distribution. Six copolymers were synthesised with varying DAMAB content from 0% to 10.5% with differing levels of “blockiness”, where the DAMAB content was assessed using elemental analysis for bromine content. The association behaviour of the copolymers was assessed using fluorescence studies and it was found that stronger intermolecular hydrophobic associations were obtained as the length and number of hydrophobic blocks in the chain were increased, whereas a statistical distribution of the monomers promoted intramolecular interactions between the hydrophobes.⁹⁴ Therefore, McCormick and co-workers concluded that the distribution of hydrophobic units was an important factor in how the copolymer chains associated in aqueous conditions and hydrophobic self-assembly could be either intramolecular or intermolecular.⁹⁴

In 1995, Kamachi and co-workers studied how various bulky hydrophobic substituents affected copolymer intramolecular *vs.* intermolecular self-association.⁹⁵ The copolymers in question were random copolymers of sodium 2-(acrylamido)-2-methylpropanesulfonate (AMPS) and containing bulky hydrophobes, such as lauryl (LA), cyclodecyl (CD), and 1-adamantyl (AD) methacrylamides. These copolymers were labelled with a small amount of either pyrenyl (Py) or 2-naphthyl (2-Np) methacrylamide in order to carry out fluorescence studies (Figure 1.21). These studies involved a mixture of 2-Np and Py labelled polymers with the same substituent in aqueous solution. Due to the electrostatic repulsion caused by the ionic substituents, each type of copolymer should exist separately as unimers. However, if intermolecular association occurs then some fraction of the two labels will be in sufficiently close proximity to induce

fluorescence from the Py label caused by energy transfer from the excited 2-Np. The LA-based polymers exhibited greater fluorescence intensity at higher copolymer concentration from around 0.2 wt %.⁹⁵ On the other hand, the other two copolymers didn't show the same increase in fluorescence until the copolymer concentration reached around 7 wt %. The effect of copolymer composition was not closely examined in this paper. However, reducing the hydrophobic group content significantly decreases both the aggregation number and the micelle core radius. The fluorescence studies in this paper showed that the copolymers with CD and AD substituents more strongly favoured intramolecular association than the LA-based polymer.⁹⁵

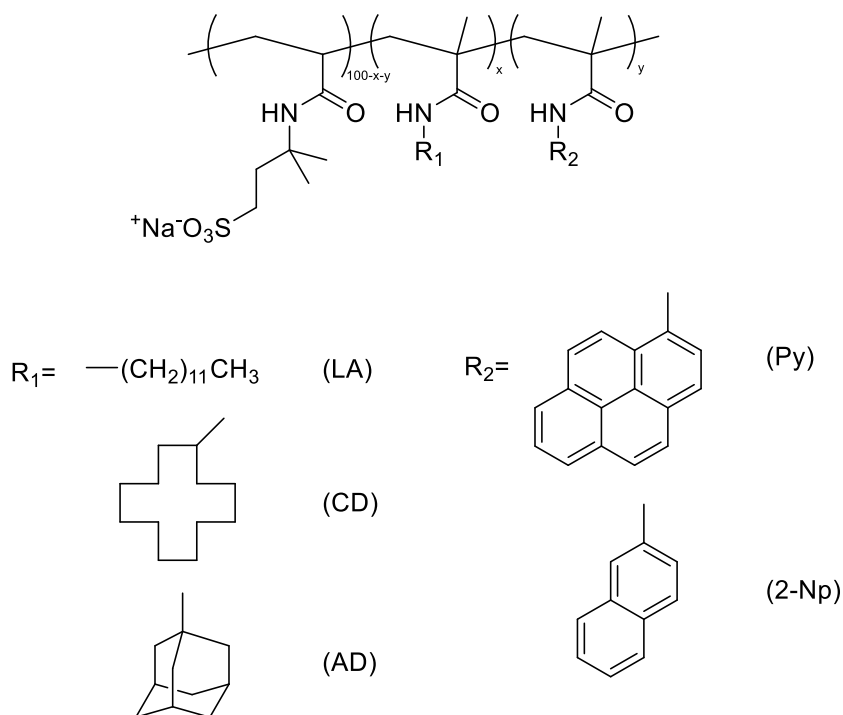


Figure 1.21. Chemical structures of the various AMPS-based polymers investigated by Kamachi *et al.* and the bulky side groups used to examine their effect on the micellisation.⁸⁶

In 2006, Sato's group investigated how the composition of the amphiphilic statistical copolymers affected their aqueous micellisation.⁹⁶ In addition to compositional effects, how

the degree of polymerisation influenced the aggregation was also studied. The group synthesised amphiphilic copolymers comprising sodium 2-(acrylamido)-2-methylpropanesulfonate (AMPS) and *n*-hexyl methacrylate were synthesised with different degree of polymerisation and composition. Self-aggregating copolymer solutions in 0.1 M aqueous NaCl were studied using static and dynamic light scattering, fluorescence spectroscopy, viscometry, and gel permeation chromatography. Light scattering techniques were used to determine the hydrodynamic radius and the micelle aggregation number, whereas the number of hydrophobic microdomains in each of the aggregates was determined by time-resolved fluorescence measurements. The results from these techniques indicated a high dependence of the aggregation number on the degree of polymerisation and the composition. Higher degrees of polymerisation lead to lower micelle aggregation numbers and smaller micelles but the number of hydrophobic microdomains increased.

In 2015, Riemer *et al* synthesised a range of amphiphilic acrylate statistical copolymers, where the hydrophilic component was acrylic acid (AA), and investigated the effect varying the degree of amphiphilicity has on the copolymer aggregation.⁹⁷ The degree of amphiphilicity was altered by changing the copolymer composition and length of alkyl chain from the butyl to dodecyl. SLS, DLS and SANS studies demonstrated that the particle size and aggregation number increased as the alkyl chain increases in length. Additionally, the aggregation behaviour was studied in respect to the ionisation of the AA. It was found that at a low pH, when the AA is not ionised, the copolymers will aggregate to form larger particles than at a higher pH. Furthermore, increasing the ionisation further suppresses the formation of well-defined particles and the copolymers form loosely connected aggregates.⁹⁷

More recently, work by Terashima and Sawamoto has re-energised this area of research, and over the last 5 years a number of papers on the self-assembly of statistical copolymers has been published by his group.^{98–105} In 2014, Terishima *et al.* demonstrated how poly(ethylene glycol)

(PEG) based amphiphilic statistical copolymers could undergo reversible single-chain self-folding in water to form a single-chain nano particle (SCNP).⁹⁸ Structural analysis revealed that the self-folded structure is stable at high concentrations (up to 6% w/w) and unfolding can be induced by the addition of methanol or raising the solution temperature. SCNPs are of great scientific interest as they are thought of as biomolecule mimics and have potential applications in drug delivery and catalysis.^{106–109} Moreover, in 2016 the same group built upon this initial research by investigating the self-sorting behaviour, and discrete compartmentalisation of PEG-based amphiphilic statistical copolymers (Figure 1.22).¹⁰⁴ It was found that mixtures of copolymers with different compositions and molecular weights would self-sort into well-defined and distinct aggregates where the size was determined by the copolymer composition. Furthermore, it was found that copolymers synthesised *via* both metal-catalysed living and conventional free radical polymerisation underwent self-assembly and self-recognition to produce uniform and self-sorted nanoparticles.¹⁰⁴

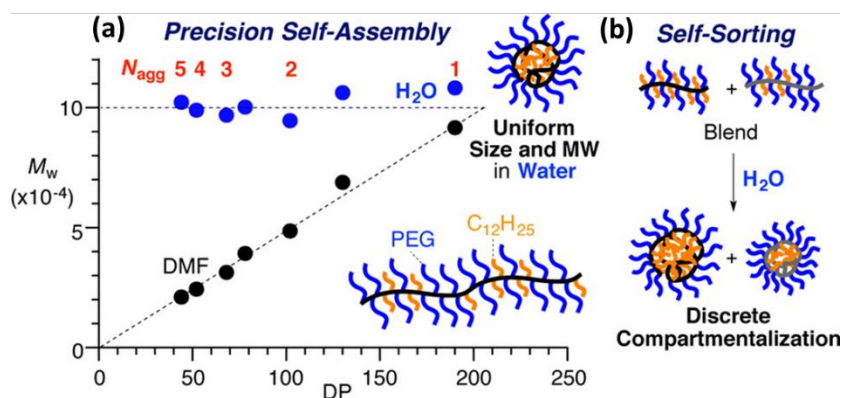


Figure 1.22. (a) A graph depicting how copolymers of different DPs self-assemble in water to form nanoparticles with a uniform size, and (b) a cartoon describing the self-sorting and discrete compartmentalisation behaviour of amphiphilic statistical copolymers. Reproduced with permission from Y. Hirai, T. Terashima, M. Takenaka and M. Sawamoto, *Macromolecules*, 2016, **49**, 5084–5091. Copyright (2016) American Chemical Society.

Finally, in 2019 Terashima and Sawamoto combined the self-assembly behaviour of both statistical and block copolymers by synthesising a range of amphiphilic/fluorous random block copolymers (Figure 1.23).¹⁰⁵ By utilising properties from both varieties of copolymer, he was able to create complex and multicompartment structures. A range A/C-B/C random block copolymers were synthesised by ATRP where A was a hydrophobic dodecyl methacrylate, B was 1*H*,1*H*,2*H*,2*H*-perfluorooctyl methacrylate, and C was a hydrophilic PEG methacrylate. It was found that the copolymers underwent site selective folding in fluoroalcohol resulting in a tadpole unimer micelle whereas in water the copolymer form a double-compartment micelle. Furthermore, heavily asymmetric and highly hydrophobic copolymers would self-fold to produce a multicompartment micelle.¹⁰⁵

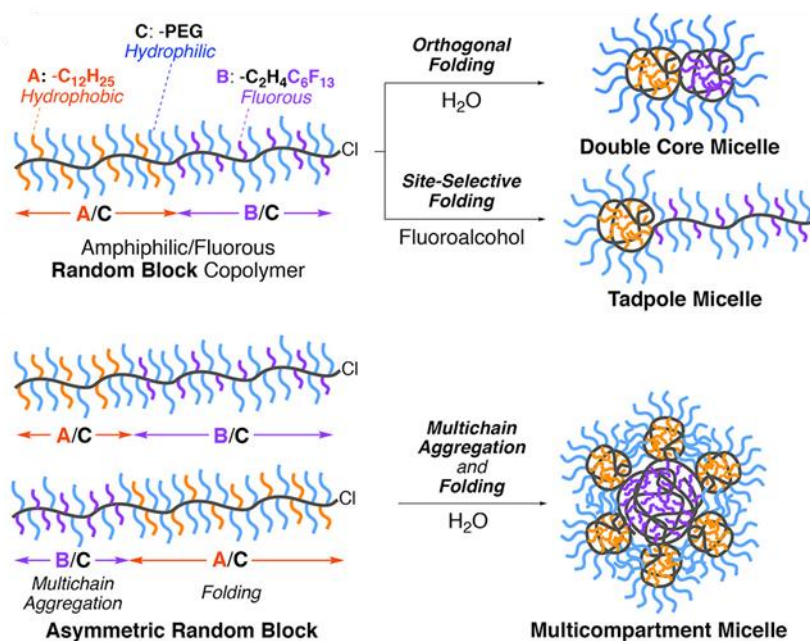


Figure 1.23. (a) A cartoon depicting the complete and site-selective folding of amphiphilic/fluorous random block copolymers to form double core micelles, tadpole micelles and multicompartment micelles. Reproduced with permission from M. Matsumoto, M. Sawamoto and T. Terashima, *ACS Macro Lett.*, 2019, **8**, 320–325. Copyright (2019) American Chemical Society.

The work presented in this section demonstrates that amphiphilic statistical copolymers can assemble into nano-particles in an aqueous environment depending on the balance of attractive forces between the hydrophobes and the electrostatic or steric repulsion of the hydrophiles. Furthermore, the properties of the particles formed depend upon the copolymer composition, the DP of the copolymer, and the nature of the comonomers. Although, research in this area over the last decade has led to some significant insights, there is still a substantial amount of research still to be done in order to fully understand these systems. Further research in this area will lead to a greater understanding of the self-assembly mechanisms that statistical copolymers follow and the associated limits and constraints. This greater understanding will allow well-defined bespoke statistical copolymer polymer particles to be synthesised easily, offering a cheaper and more industrially-viable alternative to diblock copolymer particles in applications such as drug-delivery, cosmetics, and paints.

1.7 Thesis outline

The research presented in this thesis aims to better understand the self-assembly behaviour of amphiphilic statistical copolymers in aqueous media, how this behaviour compares to the well-known self-assembly of diblock copolymers, and finally how this understanding can be incorporated into a copolymer system targeted for an industrial application. Chapter 2 describes the materials, methods, and the SAXS models used throughout the thesis. Chapter 3 presents an in-depth investigation into the self-assembly behaviour of poly(butyl methacrylate – *stat* – methacrylic acid) P(BMA-*st*-MAA) copolymers and the effect on the rheological properties, exploring the effects of copolymer composition, molecular weight, and molecular weight distribution. In this chapter a series of P(BMA-*st*-MAA) copolymers were synthesised *via* RAFT solution polymerisation at different molecular weights and compositions alongside a small series of P(BMA-*st*-MAA) synthesised using standard free-radical polymerisation. The

self-assembly behaviour of the copolymers was assessed using SAXS, TEM and rheology. This led to the development of a model describing the relationship between particle size and copolymer composition and the structural transitions that occur in within alcohol-water mixtures. Chapter 4 expands upon the work performed in chapter 3, in particular the model that was developed. However, this chapter explores relationship between the hydrophobicity of the statistical copolymers and the size of the particle formed. This work involved the synthesis of a variety of different amphiphilic copolymers using RAFT solution polymerisation where the hydrophilic component remained MAA, however the hydrophobic component was varied. Additionally, this chapter explores the internal structure of the statistical copolymer particles using a complex contrast matching SANS experiment, focussing of the relative positions of the hydrophile and hydrophobe within the particle. Chapter 5 firstly compares the self-assembly behaviour of P(BMA-MAA) statistical copolymers and diblock copolymers, and secondly expands upon this comparison by examining the effect of hydrophile-hydrophobe distribution along the copolymer backbone. This involved synthesising a range of copolymers with different intermediate monomer distributions, to compare with statistical and block copolymers, these copolymers were coined “pseudo-gradient” copolymers. Chapter 6 is the final results chapter and studies the self-assembly behaviour of amphiphilic triblock copolymers in the solution and bulk states. This work aims to apply the knowledge gained throughout this thesis about copolymer self-assembly and structural characterisation techniques to an industrial application. This chapter incorporates the self-assembly of both statistical and block copolymers by synthesising ABA triblock copolymers where the A block is a statistical distribution of acrylic acid and styrene, whereas the B block is butyl acrylate. These copolymers were designed with the intention of forming water-resistant phase-separated films where the mechanical properties are tuned by the copolymer properties. The structure of the copolymers in solution and bulk state were investigate using SAXS and AFM and the

mechanical properties of the copolymer films were evaluated using elongational rheology. Finally, chapter 7 contains concluding remarks and suggestions for future work.

1.8 References

- 1 M. A. C. Stuart, W. T. S. Huck, J. Genzer, M. Müller, C. Ober, M. Stamm, G. B. Sukhorukov, I. Szleifer, V. V. Tsukruk, M. Urban, F. Winnik, S. Zauscher, I. Luzinov and S. Minko, *Nat. Mater.*, 2010, **9**, 101–113.
- 2 Z. M. Huang, Y. Z. Zhang, M. Kotaki and S. Ramakrishna, *Compos. Sci. Technol.*, 2003, **63**, 2223–2253.
- 3 T. Hayashi, *Prog. Polym. Sci.*, 1994, **19**, 663–702.
- 4 F. Haaf, A. Sanner and F. Straub, *Polym. J.*, 1985, **17**, 143–152.
- 5 P. A. Lovell and R. J. Young, *Introduction to Polymers*, CRC Press, Boca Raton, 2011.
- 6 D. Chen, S. Yi, W. Wu, Y. Zhong, J. Liao, C. Huang and W. Shi, *Polymer (Guildf.)*, 2010, **51**, 3867–3878.
- 7 D. Chen, S. Yi, P. Fang, Y. Zhong, C. Huang and X. Wu, *React. Funct. Polym.*, 2011, **71**, 502–511.
- 8 M. A. López-Manchado, B. Herrero and M. Arroyo, *Polym. Int.*, 2004, **53**, 1766–1772.
- 9 P. Schattling, F. D. Jochum and P. Theato, *Polym. Chem.*, 2014, **5**, 25–36.
- 10 R. Albigès, P. Klein, S. Roi, F. Stoffelbach, C. Creton, L. Bouteiller and J. Rieger, *Polym. Chem.*, 2017, **8**, 4992–4995.

- 11 P. Alexandridis, *Curr. Opin. Colloid Interface Sci.*, 1996, **1**, 490–501.
- 12 M. Huo, J. Yuan, L. Tao and Y. Wei, *Polym. Chem.*, 2014, **5**, 1519–1528.
- 13 P. C. Hiemenz, *Polymer Chemistry the basic concepts*, Marcel Dekker, New York, 1984.
- 14 P. C. Hiemenz and T. P. Lodge, *Polymer Chemistry*, CRC Press, New York, 2007.
- 15 A. Gregory and M. H. Stenzel, *Prog. Polym. Sci.*, 2012, **37**, 38–105.
- 16 J. M. G. Cowie and V. Arrighi, *Polymers: Chemistry and physics of modern materials*, CRC Press, Boca Raton, 2008.
- 17 M. Bochmann and D. M. Dawson, *Angew. Chemie - Int. Ed.*, 1996, **35**, 2226–2228.
- 18 M. Szwarc, *Nature*, 1956, **178**, 1168–1169.
- 19 M. Morton, *Anionic Polymerization: Principles and Practice*, Academic Press, New York, 2012.
- 20 U. Akbulut, S. Eren and L. K. Toppare, *Polymer (Guildf.)*, 1984, **25**, 1028–1030.
- 21 T. Higashimura, Y. Ishihama and M. Sawamoto, *Macromolecules*, 1993, **26**, 744–751.
- 22 Y. Ishihama, M. Sawamoto and T. Higashimura, *Polym. Bull.*, 1990, **24**, 201–206.
- 23 C. S. Marvel, R. Gilkey, C. R. Morgan, J. F. Noth, R. D. Rands and C. H. Young, *J. Polym. Sci.*, 1951, **6**, 483–502.
- 24 Y. Tabata, H. Sobue and E. Oda, *J. Phys. Chem.*, 1961, **65**, 1645–1647.
- 25 A. D. McNaught and A. Wilkinson, *IUPAC. Compendium of Chemical Terminology*, Blackwell Scientific Publications, Oxford, 2nd edn., 1997.

- 26 K. Matyjaszewski and T. P. Davis, *Handbook of Radical Polymerisation*, John Wiley & Sons, New York, 1st edn., 2002.
- 27 G. Moad and D. H. Solomon, *The Chemistry of Free Radical Polymerization*, Elsevier Ltd, Oxford, 1st edn., 2006.
- 28 C. J. Hawker, *Acc. Chem. Res.*, 1997, **30**, 373–382.
- 29 R. B. Grubbs, *Polym. Rev.*, 2011, **51**, 104–137.
- 30 B. Lessard, C. Tervo and M. Marić, *Macromol. React. Eng.*, 2009, **3**, 245–256.
- 31 K. Matyjaszewski and J. Xia, *Chem. Rev.*, 2001, **101**, 2921–2990.
- 32 J. Chiefari, Y. K. Chong, F. Ercole, J. Krstina, J. Jeffery, T. P. T. Le, R. T. A. Mayadunne, G. F. Meijs, C. L. Moad, G. Moad, E. Rizzardo and S. H. Thang, *Macromolecules*, 1998, **31**, 5559–5562.
- 33 C. J. Hawker, A. W. Bosman and E. Harth, *Chem. Rev.*, 2001, **101**, 3661–3688.
- 34 Y. Guilleaen, D. Gigmes, S. R. A. Marque, P. Astolfi, L. Greci, P. Tordo and D. Bertin, *Macromolecules*, 2007, **40**, 3108–3114.
- 35 J. Nicolas, Y. Guilleaen, D. Bertin, D. Gigmes and B. Charleux, *Polym. Sci. A Compr. Ref. 10 Vol. Set*, 2012, **3**, 277–350.
- 36 C. Chevigny, D. Gigmes, D. Bertin, R. Schweins, J. Jestin and F. Boué, *Polym. Chem.*, 2011, **2**, 567–571.
- 37 J. S. Wang and K. Matyjaszewski, *J. Am. Chem. Soc.*, 1995, **117**, 5614–5615.
- 38 M. Kato, M. Kamigaito, M. Sawamoto and T. Higashimura, *Macromolecules*, 1995, **28**, 1721–1723.

- 39 S. Perrier, *Macromolecules*, 2017, **50**, 7433–7447.
- 40 G. Moad, Y. K. Chong, A. Postma, E. Rizzardo and S. H. Thang, *Polymer (Guildf)*., 2005, **46**, 8458–8468.
- 41 I. Chaduc, M. Lansalot, F. D’Agosto and B. Charleux, *Macromolecules*, 2012, **45**, 1241–1247.
- 42 I. Chaduc, A. Crepet, O. Boyron, B. Charleux, F. D’Agosto and M. Lansalot, *Macromolecules*, 2013, **46**, 6013–6023.
- 43 B. Y. K. Chong, J. Krstina, T. P. T. Le, G. Moad, A. Postma, E. Rizzardo and S. H. Thang, *Macromolecules*, 2003, **36**, 2256–2272.
- 44 A. Rudin and P. Choi, *The Elements of Polymer Science and Engineering*, Academic Press, Waltham, 3rd edn., 2013.
- 45 M. Lazzari, G. Liu and S. Lecommandoux, *Block Copolymers in Nanoscience*, John Wiley & Sons, Weinheim, 2007.
- 46 J. C. Moore, *J. Polym. Sci. Part A Polym. Chem.*, 1996, **34**, 1833–1841.
- 47 A. Guinier, *C. R. Hebd. Seances Acad. Sci.*, 1983, **206**, 1374–1376.
- 48 O. Kratky and G. Porod, *J. Colloid Sci.*, 1949, **4**, 35.
- 49 O. Kratky, I. Pilz and P. J. Schmitz, *J. Colloid Interface Sci.*, 1966, **21**, 24–34.
- 50 F. Reiss-Husson and V. Luzzati, *J. Phys. Chem.*, 1964, **68**, 3504–3511.
- 51 F. Reiss-Husson and V. Luzzati, 1966, **21**, 534–546.
- 52 J. W. Anderegg, W. W. Beeman, S. Shulman and P. Kaesberg, *J. Am. Chem. Soc.*, 1955, **77**, 2927–2937.

- 53 A. Guinier and G. Fournet, *Small-Angle Scattering of X-rays*, John Wiley & Sons, New York, 1955.
- 54 D. T. Cromer, *J. Chem. Phys.*, 1969, **50**, 4857–4859.
- 55 K. Clays and A. Persoons, *Phys. Rev. Lett.*, 1991, **66**, 2980.
- 56 J. S. Pedersen and M. C. Gerstenberg, *Macromolecules*, 2002, **29**, 1363–1365.
- 57 J. S. Pedersen, *J. Appl. Crystallogr.*, 2000, **33**, 637–640.
- 58 J. S. Pedersen and M. C. Gerstenberg, *Macromolecules*, 1996, **29**, 1363–1365.
- 59 J. S. Pedersen and M. C. Gerstenberg, *Colloids Surfaces A Physicochem. Eng. Asp.*, 2003, **213**, 175–187.
- 60 K. Hu, H. Zhou, Y. Liu, Z. Liu, J. Liu, J. Tang, J. Li, J. Zhang, W. Sheng, Y. Zhao, Y. Wu and C. Chen, *Nanoscale*, 2015, **7**, 8607–8618.
- 61 Q. Zhang, C. Weber, U. S. Schubert and R. Hoogenboom, *Mater. Horizons*, 2017, **4**, 109–116.
- 62 R. Xu, *Particuology*, 2015, **18**, 11–21.
- 63 K. Kratz, T. Hellweg and W. Eimer, *Polymer (Guildf.)*, 2001, **42**, 6631–6639.
- 64 C. Charbonneau, M. M. De Souza Lima, C. Chassenieux, O. Colombani and T. Nicolai, *Phys. Chem. Chem. Phys.*, 2013, **15**, 3955–3964.
- 65 A. Einstein, *Ann. Phys.*, 1905, **17**, 549.
- 66 A. Einstein, *Investigations on the Theory of Brownian Movement*, Dover, New York, 1956.

- 67 G. Stokes, *Trans. Camb*, 1856, **9**, 5.
- 68 D. Myers, *Surfactant Science and Technology*, Wiley, Chichester, 3rd edn., 206AD.
- 69 J. Eastoe, in *Colloid Science: Principles, methods, and applications*, Wiley, Chichester, 2nd edn., 2010, pp. 61–89.
- 70 B. Derjaguin and L. D. Landau, *Acta Physicochim. URSS*, 1941, **14**, 633–662.
- 71 E. J. W. Verwey and J. T. G. Overbeek, *Theory of the stability of lyophobic colloids: The interaction of sol particles having an electric double layer*, Elsevier, New York, 1948.
- 72 G. E. Molau, in *Block Copolymers*, Plenum Press, New York, 1970, pp. 79–106.
- 73 M. J. Santander-Ortega, A. B. Jódar-Reyes, N. Csaba, D. Bastos-González and J. L. Ortega-Vinuesa, *J. Colloid Interface Sci.*, 2006, **302**, 522–529.
- 74 X. Zhang, M. R. Servos and J. Liu, *J. Am. Chem. Soc.*, 2012, **134**, 9910–9913.
- 75 Y. Mai and A. Eisenberg, *Chem. Soc. Rev.*, 2012, **41**, 5969.
- 76 F. S. Bates, *Science (80-.)*, 1991, **251**, 898–905.
- 77 P. J. Flory, *J. Chem. Phys.*, 1942, **10**, 51–61.
- 78 M. L. Huggins, *J. Am. Chem. Soc.*, 1942, **64**, 1712–1719.
- 79 M. W. Matsen and F. S. Bates, *Macromolecules*, 1996, **29**, 1091–1098.
- 80 M. W. Matsen and M. Schick, *Phys. Rev. Lett.*, 1994, **72**, 2660–2663.
- 81 E. W. Cochran, C. J. Garcia-Cervera and G. H. Fredrickson, *Macromolecules*, 2006, **39**, 2449–2451.

- 82 Y. Mai and A. Eisenberg, *Chem. Soc. Rev.*, 2012, **41**, 5969–5985.
- 83 M. T. Shaw, *Introduction to Polymer Rheology*, John Wiley & Sons, New Jersey.
- 84 C. M. Koo, M. A. Hillmyer and F. S. Bates, *Macromolecules*, 2006, **39**, 667–677.
- 85 S. K. Tripathy, J. Kumar and H. S. Nalwa, *Handbook of Polyelectrolytes and their Applications*, American Scientific Publishers, Nalwa.
- 86 Y. Morishima, S. Nomura, T. Ikeda, M. Seki and M. Kamachi, *Macromolecules*, 1995, **28**, 2874–2881.
- 87 J. Noolandi and K. M. Hong, *Macromolecules*, 1983, **16**, 1443–1448.
- 88 R. Xu, M. A. Winnik, F. R. Hallett, G. Riess and M. D. Croucher, *Macromolecules*, 1991, **24**, 87–93.
- 89 M. Wilhelm, C. Le Zhao, Y. Wang, R. Xu, M. A. Winnik, J. L. Mura, G. Riess and M. D. Croucher, *Macromolecules*, 1991, **24**, 1033–1040.
- 90 K. Prochazka, D. Kiserow, C. Ramireddy, P. Munk, S. E. Webber and Z. Tuzar, *Macromolecules*, 1992, **25**, 454–460.
- 91 I. Astafieva, X. F. Zhong and A. Eisenberg, *Macromolecules*, 1993, **26**, 7339–7352.
- 92 L. Zhang and A. Eisenberg, *J. Am. Chem. Soc.*, 1996, **118**, 3168–3181.
- 93 A. Blanz, S. P. Armes and A. J. Ryan, *Macromol. Rapid Commun.*, 2009, **30**, 267–277.
- 94 Y. Chang and C. L. McCormick, *Macromolecules*, 1993, **26**, 6121–6126.
- 95 Y. Morishima, S. Nomura, T. Ikeda, M. Seki and M. Kamachi, *Macromolecules*, 1995, **28**, 2874–2881.

- 96 A. Hashidzume, A. Kawaguchi, A. Tagawa, K. Hyoda and T. Sato, *Macromolecules*, 2006, **39**, 1135–1143.
- 97 S. Riemer, S. Prévost, M. Dzionara, M.-S. Appavou, R. Schweins and M. Gradzielski, *Polymer (Guildf.)*, 2015, **70**, 194–206.
- 98 T. Terashima, T. Sugita, K. Fukae and M. Sawamoto, *Macromolecules*, 2014, **47**, 589–600.
- 99 S. Imai, Y. Hirai, C. Nagao, M. Sawamoto and T. Terashima, *Macromolecules*, 2018, **51**, 398–409.
- 100 G. Hattori, M. Takenaka, M. Sawamoto and T. Terashima, *J. Am. Chem. Soc.*, 2018, **140**, 8376–8379.
- 101 K. Matsumoto, T. Terashima, T. Sugita, M. Takenaka and M. Sawamoto, *Macromolecules*, 2016, **49**, 7917–7927.
- 102 M. Matsumoto, T. Terashima, K. Matsumoto, M. Takenaka and M. Sawamoto, *J. Am. Chem. Soc.*, 2017, **139**, 7164–7167.
- 103 M. Shibata, M. Matsumoto, Y. Hirai, M. Takenaka, M. Sawamoto and T. Terashima, *Macromolecules*, 2018, **51**, 3738–3745.
- 104 Y. Hirai, T. Terashima, M. Takenaka and M. Sawamoto, *Macromolecules*, 2016, **49**, 5084–5091.
- 105 M. Matsumoto, M. Sawamoto and T. Terashima, *ACS Macro Lett.*, 2019, **8**, 320–325.
- 106 M. Ouchi, N. Badi, J.-F. Lutz and M. Sawamoto, *Nat. Chem.*, 2011, **3**, 917–924.
- 107 O. Altintas and C. Barner-Kowollik, *Macromol. Rapid Commun.*, 2016, **37**, 29–46.

- 108 A. M. Hanlon, C. K. Lyon and E. B. Berda, *Macromolecules*, 2016, **49**, 2–14.
- 109 C. K. Lyon, A. Prasher, A. M. Hanlon, B. T. Tuten, C. A. Tooley, P. G. Frank and E. B. Berda, *Polym. Chem.*, 2015, **6**, 181–197.

Chapter 2. Materials, general methods and SAXS models

Chapter 2.

Materials general methods and SAXS models

This chapter will discuss the materials used in each chapter and the analytical methods of characterisation of used throughout this scientific thesis.

2.1. Materials

2.1.1 List of chemicals and suppliers

All materials were used as received unless stated otherwise in the text.

Monomers

Monomers were passed through basic alumina to remove inhibitors prior to use.

- Butyl methacrylate (BMA, 99%, Sigma-Aldrich)
- Methacrylic acid (MAA, 99.5%, Sigma-Aldrich)
- Hexyl methacrylate (HMA, 98%, Sigma-Aldrich)
- Ethyl methacrylate (EMA, 99%, Sigma-Aldrich)
- Methyl methacrylate (MMA, 99%, Sigma-Aldrich)
- 2-Ethylhexyl methacrylate (EHMA, 98%, Alfa Aesar)
- Butyl acrylate (BA, 99%, Sigma-Aldrich)

- Acrylic acid (AA, 99%, Sigma-Aldrich)
- Styrene (St, 99%, Sigma-Aldrich)

Solvents

- Isopropanol (IPA, 99.9%, Sigma-Aldrich)
- Tetrahydrofuran (THF, High-performance liquid chromatography grade, VWR)
- 1,4-Dioxane (99.5%, Sigma-Aldrich)
- Methyl ethyl ketone (MEK, 99.9%, Sigma-Aldrich)
- Deuterated chloroform (CDCl₃, VWR)
- Deuterated acetone (d₆-acetone, Sigma-Aldrich)
- Deuterated dimethyl sulfoxide (d₆-DMSO, VWR)
- Deuterated methanol (d₄-methanol, Acros Organic)
- Deuterium oxide (D₂O, Sigma-Aldrich)

Chemicals

- Triethanolamine (TEA, 99%, Sigma-Aldrich)
- Glacial acetic acid (99.85%, Sigma-Aldrich)
- 4,4'-Azobis(4-cyanovaleric acid) (ACVA, 98%, Sigma-Aldrich)
- 2,2'-Azobis(2-methylpropionitrile) (AIBN, 98%, Sigma-Aldrich)
- Trimethylsilyl diazomethane solution (2.0M in diethyl ether, Sigma-Aldrich)

- 4-cyano-4-(2-phenyl-ethanesulfanylthiocarbonyl) sulfanylpentanoic acid (PETTC, prepared in-house as reported previously¹)
- Benzyl bromide (BzBr, 98%, Sigma-Aldrich)
- Ammonia (NH₃, 25% aqueous solution, Sigma-Aldrich)
- *S,S*-Dibenzyl trithiocarbonate (DBTTC, Boron Molecular)

2.2. Characterisation methods

2.2.1 Methylation and Alkylation

The compositions of copolymers containing MAA were calculated using alkylated versions of the copolymers. MAA units were alkylated prior to ¹H NMR spectroscopy analysis using either trimethylsilyldiazomethane, therefore forming methyl methacrylate units,² or by using benzyl bromide (BzBr) to form benzyl methacrylate units. The latter reaction was performed at 5 wt% polymer in DMF with CsCO₃ added to deprotonate the methacrylic acid and then excess BzBr was added. The reaction was left for 24 h., excess solvent was removed under vacuum and the product was purified by washing with water.

2.2.2 ¹H Nuclear Magnetic Resonance (NMR) Spectroscopy

¹H NMR spectroscopy was used throughout this study in order to monitor polymerisation kinetics and to calculate the copolymer composition. Spectra were recorded on either a Bruker AV1-400 or AV3HD-400 MHz spectrometer in either d₆-DMSO, d₆-acetone, d₄-methanol or CDCl₃. These spectra were analysed using Bruker Topspin software (version 3.5p17) and chemical shifts are reported relative to a residual solvent peak.

2.2.3 Gel Permeation Chromatography (GPC)

Molecular weight distributions of the statistical, pseudo-gradient, and diblock copolymers in chapters 3, 4, and 5 were determined by GPC using THF containing 4% v/v acetic acid and 0.054 w/v% butyl hydroxytoluene (BHT) as the eluent. Measurements were performed on a PL-GPC50 integrated GPC system (Agilent, UK) equipped with a refractive index detector. Separations were carried out using a pair of PLgel Mixed-C columns (7.8×300 mm, 5 μ m bead size), fitted with a PLgel guard column (7.8×50 mm, 5 μ m bead size), at a flow rate of 1.0 mL min⁻¹. All the samples were measured relative to a set of ten low-dispersity poly(methyl methacrylate) (PMMA) standards (Agilent, UK) with peak molecular weight values ranging from 550 Da to 1,568,000 Da.

2.2.4 Advanced Polymer Chromatography (APC)

Molecular weight distributions of the triblock copolymers in chapter 6 were determined by APC using THF with 1% v/v acetic acid as the eluent. Measurements were performed on a Waters ACQUITY APC system equipped with a refractive index detector. Separations were carried out using a set of 150 mm XT columns (45, 125, and 450), at a flow rate of 1.0 mL min⁻¹. All the samples were filtered with 0.2 μ m PTFE membrane filters prior to analysis and measured relative to a low-dispersity polystyrene (PSt) standards with peak molecular weight values ranging from 580 to 8,000,000 Da.

2.2.5 Small-Angle X-ray Scattering (SAXS) measurements

Throughout this work SAXS patterns were collected using laboratory SAXS instruments [either a Bruker AXS Nanostar equipped with a two-dimensional (2D) Hi-STAR multi-wire gas detector and modified with Xenocs GeniX 3D X-ray source (CuK α radiation, X-ray

wavelength $\lambda = 1.54 \text{ \AA}$) and motorised collimating scatterless slits or Xenocs Xeuss 2.0 laboratory beamline equipped with a 2D Dectris Pilatus 1M detector and an Excillum liquid gallium MetalJet X-ray source ($\lambda = 1.34 \text{ \AA}$]. Samples were run in either an open-top capillary with a diameter of 2 mm and placed vertically in a capillary holder or in a sealed flow-through cell, with a thickness of 2 mm, to allow experiments to be run under vacuum. The patterns were collected over a scattering vector length range of $0.008 \text{ \AA}^{-1} < q < 0.16 \text{ \AA}^{-1}$, where $q = \frac{4\pi}{\lambda} \sin \theta$ and θ is a half of the scattering angle. One-dimensional (1D) scattering curves were obtained by an azimuthal binning and averaging of corresponding two-dimensional scattering patterns using software packages supplied with the SAXS instruments. Normalization, background subtraction, and further analysis of the 1D data was performed using Irena SAS macros for Igor Pro.³

2.2.6 Grazing Incident Small-Angle X-ray Scattering (GISAXS) measurements

In chapter 6 additional grazing incident SAXS (GISAXS) measurements were performed using the Xenocs Xeuss 2.0 laboratory beamline equipped with a 2D Dectris Pilatus 1M detector and an Excillum liquid gallium MetalJet X-ray source ($\lambda = 1.34 \text{ \AA}$). Time-resolved GISAXS was performed on block copolymer films during annealing at elevated temperatures (150 °C). To perform the measurements the films were cast on to a mica disc and were mounted on a homemade GISAXS heating stage. Prior to acquisition, the incident angle was established by measuring the maximum intensity of the scattered X-rays as a function of the mounted angle, Ω ; the maximum intensity was achieved at an angle of 0.8° . This incident angle was fixed throughout the length of the experiment. One-dimensional (1D) scattering curves were obtained by an azimuthal binning, taking into account the incident angle, and averaging of corresponding two-dimensional scattering patterns using software packages supplied with the SAXS instruments.

2.2.7 Small-Angle Neutron Scattering (SANS) measurements

In chapter 4 the SANS measurements were performed at a spallation neutron source (ISIS, beamline LOQ, Didcot, UK)⁴ using a contrast variation technique. The sample-to-detector distance was 4.1 m and the beam diameter was 10 mm. The solutions were pipetted into either 1 mm and 2 mm pathlength PTFE-stoppered quartz cuvettes (Hellma UK) depending on the solvent used (H₂O or D₂O, respectively). The cuvettes were mounted on a computer-controlled sample changer maintained at a fixed temperature of 25 °C and the scattering recorded. Each raw scattering dataset was corrected for the incident neutron wavelength distribution, the detector efficiency and spatial linearity, the measured transmission and cuvette pathlength, before being azimuthally binned, averaged and converted to coherent elastic differential scattering cross-section per unit sample volume data ($\partial\Sigma/\partial\Omega$) as a function of q using the Mantid software framework.⁵ A convention of referring to ($\partial\Sigma/\partial\Omega$) as the intensity, I , is followed further in the thesis. A partially deuterated polymer blend standard of known molecular weight was used to normalize the reduced 1D SANS data to an absolute intensity scale in accordance with well established procedures.⁶ Background subtraction and further analysis of the data was performed using Irena SAS macros for Igor Pro.³ Simultaneous fitting of the contrast series scattering patterns was performed using SASfit.⁷

2.2.8 Dynamic Light Scattering (DLS)

Aqueous dispersions (0.1% w/w) were placed into disposable plastic cuvettes and analysed using a Malvern Zetasizer NanoZS instrument. The scattered light was detected at 173° and the Stokes-Einstein equation (eq 1.9) was used to calculate the intensity-averaged hydrodynamic diameter.

2.2.9 Aqueous Electrophoresis

The electrophoretic mobility of aqueous copolymer dispersions, with an electrolyte background of 0.75 mM KCl, was measured using phase-analysis light scattering (PALS) on a Malvern Zetasizer NanoZS instrument.

2.2.10 Transmission Electron Microscopy (TEM)

TEM studies were conducted using either a Philips CM 100 instrument operating at 100 kV and equipped with a Gatan 1k CCD camera or a FEI Tecnai Spirit 2 microscope fitted with an Orius SC1000B camera. Copper/palladium TEM grids (Agar Scientific, UK) were coated with a thin layer of carbon and then glow discharged for 30 seconds. Samples were prepared by placing a droplet (10 μL) of diluted copolymer dispersions (0.1 % w/w) to the carbon-coated copper grids for 1 minute. Once the excess dispersion was removed by dabbing the grids with filter paper uranyl formate (9.0 μL of a 0.75% w/w solution) was placed on the grids for 20 seconds and then dabbed again with a filter paper. Each sample was additionally dried using a vacuum hose.

2.2.11 Atomic Force Microscopy (AFM)

In chapter 6 the triblock copolymers investigated were either dried on to small metal AFM plates or attached using double-sided tape. AFM height images were collected using ScanAsyst® PeakForce® tapping mode on a Bruker MultiMode atomic force microscope. A 2 nm silicon ScanAsyst-Air cantilever was used to perform the measurements. The WsXM 4.0 software was used for the image analysis including measurements of the copolymer phase separation lengthscale.

2.2.12 Differential scanning calorimetry (DSC)

40% w/w triblock solutions in MEK were decanted into pre-weighed aluminium pans and the solvent was left to evaporate overnight. The pans were weighed again once the copolymer was dry so that an accurate sample mass could be calculated. The pans were sealed with a lid and calorimetry measurements were performed under nitrogen using a TA Instrument DSC Q2000 differential scanning calorimeter. The Thermograms were collected at a rate of 10 °C/min from -80 °C to 150 °C. Only one thermal cycle was performed on each sample as the acrylic acid within the triblock copolymer begins to dehydrate into an anhydride above temperature of 100 °C.^{8,9} Therefore, the calorimetry measurements would vary during each thermal cycle as the acid begins to dehydrate.

2.2.13 Rheology

An MCR 502 rheometer (Anton Paar, Graz, Austria) equipped with a TruGap system for automatic gap control and configured for cone-and-plate geometry (50 mm diameter, cone angle 2°) with a solvent trap was used to perform rheological measurements of the copolymer dispersions at various concentrations and solvent compositions. In order to reduce any shear-induced change in copolymer morphology, an oscillatory mode was chosen for the measurements. Preliminary strain sweep experiments, between 0.1% and 20% strain at constant angular frequencies were performed for all copolymer samples to identify the linear viscoelastic region. Once a suitable strain had been identified, an angular frequency sweep, downwards from 200 rad s⁻¹ to 0.1 rad s⁻¹, was conducted at a constant strain (typically 1%) and temperature (21 °C) to measure the dynamic viscosity. The dynamic viscosity determined for each copolymer dispersion displayed almost no frequency dependence (shear thinning) at frequencies below 10 rad s⁻¹. Thus, this region of the rheological data was used to obtain zero

shear viscosity defined by an extrapolation of the experimental results to zero angular frequency. Such obtained values of zero shear viscosity were used for the characterization of copolymer dispersions.

2.2.14 Mechanical testing

Triblock copolymer films were cast from solutions into plastic moulds and left to dry in ambient conditions for 1 week. The films were then removed from the moulds and cut into strips with a width of 7 mm and a length greater than 13 mm (the set gap). The individual thicknesses were measured using a micrometer and both the extension-to-break and the Young's modulus was measured on an Instron 5500R instrument at ambient conditions.

2.3. SAXS Structural Models.

2.3.1 Intensity equation

The intensity of the X-rays scattered by a particle dispersion, $I(q)$, is defined as:

$$I(q) = N \cdot S(q) \cdot \int_0^{\infty} \dots \int_0^{\infty} F(q, r_1, \dots, r_k) \cdot \Psi(r_1, \dots, r_k) dr_1 \dots dr_k \quad (2.1)$$

where $F(q, r_1, \dots, r_k)$ is the particle form factor defined by a k number of structural model parameters, $\Psi(r_1, \dots, r_k)$ is a function describing distribution of these parameters, $S(q)$ is the structure factor describing particle interactions in the dispersion and N is the number density per unit sample volume defined as:

$$N = \frac{\phi}{\int_0^{\infty} \dots \int_0^{\infty} V(r_1, \dots, r_k) \cdot \Psi(r_1, \dots, r_k) dr_1 \dots dr_k} \quad (2.2)$$

where ϕ is the total particle volume fraction and $V(r_1, \dots, r_k)$ is the particle volume.

2.3.2 Intensity equation with linear background

A plateau in intensity at high q was observed in the majority of the scattering patterns after subtraction of background scattering originating from the solvent and the sample holder (*i.e.*, glass capillary). This scattering signal is likely to be associated with fluctuations in scattering length density across the particles caused by random distribution of monomer units in the self-assembled copolymers. In order to account for these fluctuations a linear fitting parameter (C_1) that is independent of the scattering vector q was added to the equation describing the intensity of scattered X-rays (eq. 2.1):

$$I(q) = N \cdot S(q) \cdot \int_0^{\infty} \dots \int_0^{\infty} F(q, r_1, \dots, r_k) \cdot \Psi(r_1, \dots, r_k) dr_1 \dots dr_k + C_1 \quad (2.3)$$

2.3.3 Intensity equation with linear background and unified parametrisation

An upturn in intensity at low q was observed in the scattering patterns of some dispersions. This deviation from the model was caused by the formation of large aggregates often related to mass fractals. Scattering signal of these objects is commonly described using a combination of Guinier and power law functions expressed *via* unified parametrisation.¹⁰⁻¹² Since the Guinier region is located at very low q -values that are not generally measured in these SAXS experiments, only a power law function was incorporated into the intensity equation (equations 2.1 and 2.3) in order to account for the presence of large aggregates:

$$I(q) = N \cdot S(q) \cdot \int_0^{\infty} \dots \int_0^{\infty} F(q, r_1, \dots, r_k) \cdot \Psi(r_1, \dots, r_k) dr_1 \dots dr_k + C_1 + B \cdot q^{-P} \quad (2.4)$$

where B is a prefactor that is related to the type of power-law scattering and the regime in which the power-law exponent, P , falls.

2.3.4 Distribution function of the structural model parameters.

The polydispersity of particle radius, r , expressed as a Gaussian distribution, is considered for the structural models using eq. 2.1 (or equations 2.3 and 2.4):

$$\Psi(r) = \frac{1}{\sqrt{2\pi\sigma_R^2}} e^{-\frac{(r-R)^2}{2\sigma_R^2}} \quad (2.5)$$

where R is the mean particle radius and σ_R is its standard deviation. All other fitting parameters describing the structural models were considered to be monodisperse (their distribution functions correspond to Dirac's delta function).

2.4. Structure factor

2.4.1 Percus-Yevick approximation

A hard sphere structure factor solved using the Percus-Yevick closure relation:¹³

$$S(q) = S_{PY}(q, R_{PY}, f_{PY}) \quad (2.6)$$

where R_{PY} is an effective interparticle correlation radius and f_{PY} is an effective volume fraction, has been incorporated into eq. 2.1 to account for long range interactions between the charged particles.¹⁴

2.4.2 Hayter-Penfold approximation

A charged particle Coulomb interaction is described by the Hayter-Penfold approximation:¹⁵

$$S(q) = S_{\text{HP}}(q, R_{\text{HP}}, f_{\text{HP}}, M, T, \varepsilon, Q) \quad (2.7)$$

where R_{HP} is an interparticle correlation radius, f_{HP} is an effective volume fraction, M is the ionic strength of the solvent, T is the absolute temperature, ε is the solvent dielectric constant and Q is the particle charge expressed in electrons.

2.5 Form factors

2.5.1 Gaussian chain model

In a theta solvent, a copolymer will behave as a Gaussian chain with a radius of gyration, R_g . This behaviour can be described as a Debye function for a Gaussian polymer chain:

$$F_{\text{chain}}(x) = \frac{2(e^{-x} - 1 + x)}{x^2} \quad (2.8)$$

where $x = (qR_g)^2$.

2.5.2 Sphere model (Figure 2.1a)

The self-assembled statistical copolymers studied in this work to a first approximation can be described as a dispersion of homogenous spherical particles. Thus, the form factor for eq. 2.1 (or equations 2.3 and 2.4) can be defined as:^{16,17}

$$F_s(q, r) = N_{\text{agg}}(r) \beta_s^2 \cdot A_s^2(q \cdot r) \quad (2.9)$$

where r is the spherical particle radius, β_s is the scattering length density contrast of a nano object of volume $V(r)$ defined as $\beta_s = V(r)(\xi_{\text{cop}} - \xi_{\text{sol}})$ where ξ_{cop} and ξ_{sol} represent the scattering length densities (SLDs) of the copolymer and background solvent, respectively. ξ_{cop} in this case represents the averaged SLD of the copolymer calculated as:

$$\xi_{\text{cop}} = \xi_x \cdot v_x + \xi_y \cdot v_y \quad (2.10)$$

where ξ_x and ξ_y are the SLDs of different monomer units (x and y) along the copolymer chain and where v_x and v_y are the volume fractions of x and y units, respectively. $A_s(qr)$ corresponds to a function describing the normalized sphere form factor amplitude:

$$A_s(x) = \frac{3[\sin(x) - x \cdot \cos(x)]}{x^3} \quad (2.11)$$

When using this model volume of the particle for eq. 2.2 is expressed as $V(r) = \frac{4\pi r^3}{3}$.

Additionally, the molecule aggregation number can be calculated from the model parameters:

$$N_{\text{agg}} = (1 - x_{\text{sol}}) \frac{V(r)}{V_{\text{cop}}} \quad (2.12)$$

where V_{cop} , is the volume of a single copolymer molecule and is calculated by $V_{\text{cop}} = \frac{M_n}{N_A \rho_{Px}}$

where ρ_{Px} is the density of a homopolymer of monomer x and x_{sol} is the volume fraction of solvent within the sphere.

2.5.3 Spheroid model (Figure 2.1b)

For a more general case when the particles are distorted from a spherical shape a spheroid model with one extra parameter describing aspect ratio of the particle dimensions is used.¹⁷

Considering uniaxial distortion (elongation or flattening) of a spherical particle, the particle form factor for eq. 2.1 (or equations 2.3 and 2.4) can be expressed as:^{16,17}

$$F_{\text{sph}}(q, r, \varepsilon) = \Delta \xi^2 \cdot \int_0^{\pi/2} A_s^2(q \cdot r \cdot \sqrt{\sin^2 b + \varepsilon \cos^2 b}) \cdot \sin b db \quad (2.13)$$

where r is radius of the spheroid rotational (major) axis, ε is the aspect ratio (the ratio between radius of the major axis and the minor axis of spheroid) and the integration is performed over the angle of particle orientation, b . When using this model, volume of the particle for eq. 2.2 is

expressed as $V(r) = \frac{4\pi\varepsilon r^3}{3}$. Additionally, the particle volume can be used to calculate the

molecule aggregation number from eq. 2.12.

2.5.4 Blob model (Figure 2.1c)

This model accounts for scattering length density fluctuations that occur within a copolymer micelle. These fluctuations are described as independent “blobs” and account for an increased intensity at high q . Therefore, this model can be as an alternative to adding a constant linear intensity as described in equation 2.3. Originally, this approach was developed to interpret neutron scattering from the solvated cores of spherical micelles¹⁸ but it can be also adapted for the structural model describing the form factor of spherical particles formed by statistical copolymers:

$$F_{\text{sb}}(q, r) = \frac{N_{\text{agg}}^2(r) \beta_s^2 [n_{\text{blob}}(n_{\text{blob}} - 1) \psi^2(qR_g^{\text{blob}}) A_s^2(q, r) + n_{\text{blob}} F_{\text{chain}}(qR_g^{\text{blob}})]}{n_{\text{blob}}^2} \quad (2.14)$$

where $\psi(y) = \frac{(1 - e^{-y})}{y}$, $y = (qR_g^{\text{blob}})^2$ is the form factor amplitude of a “blob”, R_g^{blob} is the

“blob” radius or gyration and $F_{\text{chain}}(qR_g^{\text{blob}})$ is the self-correlation term of the Gaussian polymer

chain (“blob”) represented by the Debye function (eq. 2.8). $n_{\text{blob}} = \frac{A_1 V_s}{V_{\text{blob}}}$ is the approximate number of “blobs”, where A_1 is a fitting parameter, $V_s = \frac{4\pi r^3}{3}$ and $V_{\text{blob}} = \frac{4\pi(R_g^{\text{blob}})^3}{3}$. The scattering length contrast of the spherical particle is given by $\beta_s = V_s(\xi_{\text{cop}} - \xi_{\text{sol}})$. ξ_{cop} in this case represents the averaged scattering length density of the copolymer, which is calculated as by eq 2.10.

2.5.5 Core-Shell sphere model (Figure 2.1d)

This model is used when the statistical copolymer particles are considered to be inhomogeneous due to a partial redistribution of the statistical segments between core and surface of the particles. In this case it is assumed that SLD of the particle core and the surface shell is different. Thus, the form factor for eq. 2.1 is defined as:

$$F_{\text{cs}}(q, r, \Delta r, \xi_{\text{core}}, \xi_{\text{shell}}) = A_{\text{cs}}^2(q, r, \Delta r, \xi_{\text{core}}, \xi_{\text{shell}}) \quad (2.15)$$

where the form factor amplitude is defined as:^{16,17}

$$A_{\text{cs}}(q, r, \Delta r, \xi_{\text{core}}, \xi_{\text{shell}}) = (\xi_{\text{core}} - \xi_{\text{sol}})V_{\text{part}}A_s(q \cdot r) + (\xi_{\text{core}} - \xi_{\text{shell}})V_{\text{core}}A_s[q \cdot (r - \Delta r)] \quad (2.16)$$

where ξ_{shell} and ξ_{core} are the SLDs of the shell and core, respectively. r and $V_{\text{part}}(r) = \frac{4\pi r^3}{3}$ are the radius and volume of the entire particle, and Δr is the shell thickness. In chapter 4, ξ_{sol} was varied during the contrast variation SANS experiment by using H₂O–D₂O mixtures. The ξ_{sol} for each mixture can be calculated from a linear relationship based on the scattering length density and volume fraction of each component:

$$\xi_{\text{sol}} = \xi_{\text{H}_2\text{O}}v_{\text{H}_2\text{O}} + \xi_{\text{D}_2\text{O}}v_{\text{D}_2\text{O}} \quad (2.17)$$

In order to link ξ_{core} and ξ_{shell} to give physically realistic values based upon the copolymer composition, certain parameters must be known or calculated. The first parameter required is the relative volume fractions of the monomers, x and y , in the particle, $v_{\text{part}(x)}$ and $v_{\text{part}(y)}$, respectively. Since the relative mole fractions are known (e.g., 0.8:0.2, $x:y$), these can easily be converted to volume fractions to give $v_{\text{part}(x)} = 0.89$ and $v_{\text{part}(y)} = 0.11$. Secondly, the volume of the particle (V_{part}), core (V_{core}), and shell (V_{shell}), are calculated respectively. V_{part} and V_{core} can be calculated using the equation $V_{\text{core}}(r) = \frac{4}{3}\pi r^3$ and $V_{\text{shell}} = V_{\text{part}} - V_{\text{core}}$. From this the volume of x in the particle, $V_{\text{part}(x)}$, can be calculated:

$$V_{\text{part}(x)} = v_{\text{part}(x)} \cdot V_{\text{part}} \quad (2.18)$$

Additionally, the volume fraction of x in the core, $v_{\text{core}(x)}$, can be calculated:

$$v_{\text{core}(x)} = \frac{|\xi_{\text{core}} - \xi_y|}{|\xi_x - \xi_y|} \quad (2.19)$$

From this the volume of x in the shell, $V_{\text{shell}(x)}$, can be calculated:

$$V_{\text{shell}(y)} = V_{\text{part}(y)} - (v_{\text{core}(x)} \cdot V_{\text{core}}) \quad (2.20)$$

Since the $V_{\text{shell}(x)}$ is known, the volume fractions of x and y in the shell, $v_{\text{shell}(x)}$ and $v_{\text{shell}(y)}$, can now be calculated:

$$v_{\text{shell}(x)} = \frac{V_{\text{shell}(x)}}{V_{\text{shell}}} \quad (2.21)$$

$$v_{\text{shell}(y)} = 1 - v_{\text{shell}(x)} \quad (2.22)$$

Finally, the scattering length density of the shell (ξ_{shell}) can be calculated:

$$\xi_{\text{shell}} = (v_{\text{shell}(x)} \cdot \xi_x) + (v_{\text{shell}(y)} \cdot \xi_y) \quad (2.23)$$

2.5.6 Spherical micelle model (Figure 2.1e)

This model is commonly used for describing AB block copolymer spherical nanoparticles in solution. The insoluble A block forms a spherical core which is stabilised by the soluble B block that forms the micelle corona. Since the second block is dissolved in the solvent it behaves like a Gaussian chain and scatters X-rays in the high q region resulting in a slope close to -2. The form factor for the spherical micelle model is:¹⁹

$$F_{\text{smic}} = N_s^2 \beta_s^2 f_s^2(q, r_s) + N_s \beta_s^2 F_{\text{chain}}(q, R_g) + N_s (N_s - 1) \beta_c^2 A_c(q) + 2N_s^2 \beta_s \beta_c f_s(q, r_s) A_c(q) \quad (2.24)$$

where r_s is the radius of the spherical micelle core, R_g is the radius of gyration of the soluble block that forms the micelle corona. The scattering length contrast of the core and corona is given by $\beta_s = V_s(\xi_s - \xi_{\text{sol}})$ and $\beta_c = V_c(\xi_c - \xi_{\text{sol}})$, respectively, where ξ_s and ξ_c represent the scattering length densities of the core block and corona block, respectively. V_s and V_c are the volumes of the core block and corona block, respectively. F_{chain} is the self-correlation term for the corona block and is given by the Debye function (eq 2.7). f_s describes the core form factor amplitude and the sigmoidal interface between the two copolymer blocks:

$$f_s(q, r_s) = A_s(q r_s) \exp\left(-\frac{q^2 \sigma^2}{2}\right) \quad (2.25)$$

where A_s is the sphere form factor amplitude described in eq 2.10 and σ is the layer thickness that accounts for the decaying SLD at the membrane interface.

The form factor amplitude of the spherical micelle corona, A_c , is described as:

$$A_c(q) = \frac{\int_{R_s}^{R_s+2s} \mu_c(r) \frac{\sin(qr)}{qr} r^2 dr}{\int_{R_s}^{R_s+2s} \mu_c(r) r^2 dr} \exp\left(-\frac{q^2 \sigma^2}{2}\right) \quad (2.26)$$

where μ_c is a radial profile described as a linear combination of two cubic splines, with two fitting parameters s and a corresponding to the width of the profile and the weight coefficient, respectively. Additionally, an effective structure factor (S_{eff}) used to describe the interactions between spherical micelles has been used in equations 2.1, 2.3, or 2.4.²⁰

$$S_{\text{eff}}(q) = 1 + \frac{A_{\text{mic}}^{\text{av}}(q)^2 [S_{\text{PY}}(q, R_{\text{PY}}, f_{\text{PY}}) - 1]}{F_{\text{mic}}(q)} \quad (2.27)$$

where $A_{\text{mic}}^{\text{av}}$ is the scattering amplitude of the average radial scattering length density distribution of the micelles and is defined as $A_{\text{mic}}^{\text{av}}(q) = N_s [\beta_s A_s(q, R_s) + \beta_c A_c(q)]$ and S_{PY} is the hard-sphere structure factor solved using the Percus-Yevick closure relation (eq 2.6).

2.5.7 Adapted spherical micelle model

The spherical micelle model has been adapted for the purpose of fitting spherical micelles formed by gradient copolymer where the volume of the copolymer in the core and corona depends on the distribution of hydrophile and hydrophobe along the copolymer backbone. In this case the form factor for the spherical micelle described in eq. 2.23 is used, however, V_c becomes a fitted parameter in the model and $V_s = V_{\text{cop}} - V_c$, where V_{cop} is the total volume of the copolymer chain.

2.5.8 Two-population model (Figure 2.1e)

In chapter 6 a two-population structural model that has been used to model core-particulate shell colloidal particles²¹ was used to describe the triblock copolymer dispersions where the stabiliser block forms a surface structure that is assumed to be spherical.

Generally, the intensity of the X-rays scattered by a particle dispersion, $I(q)$, is defined as eq 2.1. However, in this case eq. 2.1 is altered to account for the additional surface structure.

$$I(q) = S_1(q) \cdot N_1 \cdot \int_0^{\infty} F_1(q, r_1) \cdot \Psi(r_1) dr_1 + S_2(q) \cdot N_2 \cdot \int_0^{\infty} F_2(q, r_2) \cdot \Psi(r_2) dr_2 \quad (2.28)$$

where the subscript 1 and 2 denotes the two populations of spherical particles, where population 1 is used to describe the triblock copolymer particle core, and population 2 describes the particulate structure of the particle surface.

In this case population 1 is described as a core-shell particle and therefore F_1 can be described using equations 2.15 and 2.16. Whereas population 2 is described as a simple sphere and therefore F_2 can be described using equations 2.9, 2.10, and 2.11.

Additionally, the structure factors S_1 and S_2 are described using the hard-sphere structure factor solved using the Percus-Yevick closure relation described by eq. 2.6.

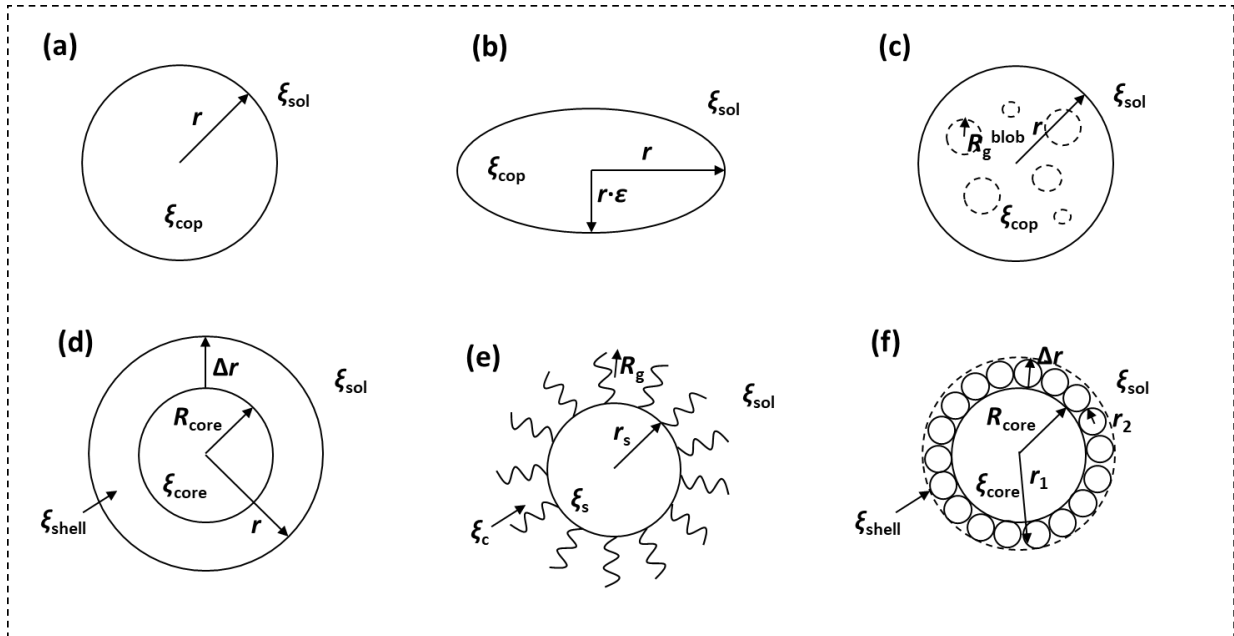


Figure 2.1. Schematic diagram illustrating the copolymer morphologies for the three structural models (eqs 2.7-13, 2.15-23): (a) the solid sphere model where r is the radius of the particle, ζ_{cop} is the scattering length density of the particle, and ζ_{sol} is the scattering length density of the solvent (eqs 2.9-12); (b) the spheroid model with an aspect ratio ε that is less than unity (eq 2.13); (c) the blob model where R_g^{blob} is the radius of gyration of the blob (eq 2.14); (d) the core-shell model, where r is the overall particle radius, Δr is the shell thickness, $R_{\text{core}} = r - \Delta r$ is the core radius, and ζ_{core} and ζ_{shell} are the scattering length densities of the core and the shell, respectively (eqs 2.15-23); (e) the spherical micelle model where r_s is the radius of the spherical core, R_g is the radius of gyration of the corona block, , and ζ_s and ζ_c are the scattering length densities of the spherical core and the corona, respectively (eqs 2.25-27); (f) the two population model where r_1 is the overall particle radius (core + shell) and r_2 is the radius of the sphere on the particle surface (eq 2.28).

2.6 References

- 1 M. Semsarilar, V. Ladmiral, A. Blanzas and S. P. Armes, *Polym. Chem.*, 2014, **5**, 3466–3475.
- 2 A. A. Cockram, T. J. Neal, M. J. Derry, O. O. Mykhaylyk, N. S. J. Williams, M. W.

- Murray, S. N. Emmett and S. P. Armes, *Macromolecules*, 2017, **50**, 796–802.
- 3 J. Ilavsky and P. R. Jemian, *J. Appl. Crystallogr.*, 2009, **42**, 347–353.
- 4 R. K. Heenan, J. Penfold and S. M. King, *J. Appl. Crystallogr.*, 1997, **30**, 1140–1147.
- 5 O. Arnold, J. C. Bilheux, J. M. Borreguero, A. Buts, S. I. Campbell, L. Chapon, M. Doucet, N. Draper, R. Ferraz Leal, M. A. Gigg, V. E. Lynch, A. Markvardsen, D. J. Mikkelson, R. L. Mikkelson, R. Miller, K. Palmén, P. Parker, G. Passos, T. G. Perring, P. F. Peterson, S. Ren, M. A. Reuter, A. T. Savici, J. W. Taylor, R. J. Taylor, R. Tolchenov, W. Zhou and J. Zikovsky, *Nucl. Instruments Methods Phys. Res. Sect. A Accel. Spectrometers, Detect. Assoc. Equip.*, 2014, **764**, 156–166.
- 6 G. D. Wignall and F. S. Bates, *J. Appl. Crystallogr.*, 1987, **20**, 28–40.
- 7 I. Breßler, J. Kohlbrecher and A. F. Thünemann, *J. Appl. Crystallogr.*, 2015, **48**, 1587–1598.
- 8 M. C. McGaugh and S. Kottle, *Polym. Lett.*, 1967, **5**, 817–820.
- 9 A. Eisenberg, T. Yokoyama and E. Sambalido, *J. Polym. Sci. Part A-1 Polym. Chem.*, 1969, **7**, 1717–1728.
- 10 G. Beaucage, *J. Appl. Crystallogr.*, 1996, **29**, 134–146.
- 11 G. Beaucage and D. W. Schaefer, *J. Non. Cryst. Solids*, 1994, **172–174**, 797–805.
- 12 L. Borges, R. Passini, P. M. Meyer, A. V Pires and P. H. M. Rodrigues, *Rev. Bras. Zootec. J. Anim. Sci.*, 2008, **37**, 681–688.
- 13 J. K. Percus and G. J. Yevick, *Phys. Rev.*, 1958, **110**, 1–13.
- 14 T. J. Neal, D. L. Beattie, S. J. Byard, G. N. Smith, M. W. Murray, N. S. J. Williams, S.

- N. Emmett, S. P. Armes, S. G. Spain and O. O. Mykhaylyk, *Macromolecules*, 2018, **51**, 1474–1487.
- 15 J. B. Hayter and J. Penfold, *Mol. Phys.*, 1981, **42**, 109–118.
- 16 J. S. Pedersen, *Adv. Colloid Interface Sci.*, 1997, **70**, 171–210.
- 17 J. S. Pedersen, *J. Appl. Crystallogr.*, 2000, **33**, 637–640.
- 18 J. S. Pedersen and M. C. Gerstenberg, *Macromolecules*, 1996, **29**, 1363–1365.
- 19 J. S. Pedersen, *J. Appl. Crystallogr.*, 2000, **33**, 637–640.
- 20 J. S. Pedersen, *J. Chem. Phys.*, 2001, **114**, 2839–2846.
- 21 J. A. Balmer, O. O. Mykhaylyk, A. Schmid, S. P. Armes, J. P. A. Fairclough and A. J. Ryan, *Langmuir*, 2011, **27**, 8075–8089.

*Chapter 3. Self-assembly of amphiphilic statistical
copolymers and their aqueous rheological
properties*

Reproduced in part with permission from T. J. Neal, D. L. Beattie, S. J. Byard, G. N. Smith, M. W. Murray, N. S. J. Williams, S. N. Emmett, S. P. Armes, S. G. Spain and O. O. Mykhaylyk, *Macromolecules*, 2018, **51**, 1474–1487. Copyright [2016] The American Chemical Society.

Chapter 3.

Self-assembly of amphiphilic statistical copolymers and their aqueous rheological properties

3.1 Introduction

Amphiphilic copolymers are used in various applications including drug delivery, cosmetics, paints, and coatings.^{1,2} They comprise both hydrophilic and hydrophobic monomers and are known to self-assemble in aqueous solution to form a wide range of nanoscale morphologies.³ The self-assembly of diblock copolymers has been extensively studied as they can produce well-defined morphologies, such as spheres,⁴⁻¹² worms¹³ or vesicles,^{14,15} which can often be predicted by their molecular parameters such as the chemical nature of each comonomer and the mean degree of polymerisation (DP) of each block.¹⁶ In comparison, the nanostructures formed by amphiphilic statistical copolymers are relatively under-studied. Nevertheless, both spherical nano-objects and other morphologies have been reported depending on the hydrophilic/hydrophobic balance.¹⁷⁻²¹

Chang and McCormick demonstrated how the distribution of a hydrophobe along the backbone of a statistical copolymer affected its self-assembly.²² Statistical copolymers prepared *via* conventional free radical polymerisation (FRP), had a tendency to undergo intramolecular hydrophobic interactions. In contrast, copolymers containing micro-domains (short blocks) of

the hydrophobe displayed intermolecular association that was enhanced by the size of these micro-domains. This association behaviour was further investigated by studying the effects of incorporating various bulky hydrophobic substituents, such as lauryl (LA), cyclodecyl (CD), and 1-adamantyl (AD) methacrylamides into the copolymer chain.²³ Copolymers containing bulkier CD and AD substituents more strongly favoured intramolecular association compared with the LA-based copolymer. Moreover, reducing the number of hydrophobic groups significantly reduced both the aggregation number and the particle radius.²³ More recently, Sato *et al.* investigated how the composition and the degree of polymerisation affected the aqueous micellisation behaviour of a series of amphiphilic statistical copolymers synthesised *via* reversible addition-fragmentation chain transfer (RAFT) polymerisation.²³ The results from this study indicated a strong influence of the mean DP and copolymer composition on the aggregation number, with higher DPs leading to lower aggregation numbers. Sato and co-workers, further analysed the self-assembly of statistical copolymers by investigating the effect of varying both the hydrophobic and ionic (hydrophilic) comonomer units on the micellar structure.²⁴ They found that higher hydrophobic monomer contents led to larger particle sizes. Furthermore, varying the type of ionic monomer had little effect on the micellar structure.²⁴

As well as spherical nano-objects, other relatively unusual copolymer assemblies, such as giant vesicles, honeycomb films and bowl-shaped aggregates, have been achieved through the aggregation of amphiphilic statistical copolymers.²⁵⁻³⁰ An example of one of these higher-order architectures was reported by Lui and Zhu in 2011, who demonstrated that vesicles could be formed by the self-assembly of L-glutamic acid-based amphiphilic random copolymers in an ethanol/water mixture.²⁵ Structures such as honeycomb films and spheres were also achieved using evaporative self-assembly from various solvents, including dichloromethane and methanol.

Although the self-assembly of amphiphilic statistical copolymers has been investigated to some extent, there is only a rather limited understanding of how this behaviour can affect the physical properties of such dispersions. Although this question has been overlooked, it is essential when evaluating these systems for commercial applications. Furthermore, there have been only limited studies of such systems using scattering techniques combined with detailed structural analysis and modelling.³¹ In this chapter an extensive study is conducted to assess the effect of composition, molecular weight, molecular weight distribution, concentration and solvent composition on the self-assembly of a series of anionic amphiphilic statistical copolymers in *iso*-propanol/water solution and the resulting physical properties of such colloidal dispersions. More specifically, a series of methacrylic statistical copolymers were synthesised *via* RAFT copolymerisation in order to achieve a wide range of comonomer compositions and narrow molecular weight distributions. Additionally, a series of similar copolymers were synthesised *via* conventional free radical copolymerisation to examine the effect of dispersity (M_w/M_n) on copolymer self-assembly. The micellar structures formed by these amphiphilic copolymers were characterised by small-angle X-ray scattering (SAXS) in dilute solution in order to evaluate their morphology. A series of structural models have been developed to analyse the resulting SAXS patterns. Finally, SAXS studies were also conducted at higher copolymer concentrations to account for the anomalous rheological behaviour of such dispersions, which leads to an increase in solution viscosity on dilution with water.

3.2 Results and discussion

3.2.1 Synthesis of BMA-MAA amphiphilic statistical copolymers

A series of twelve poly(*n*-butyl methacrylate-*stat*-methacrylic acid) [P(BMA-*stat*-MAA)] copolymers was synthesised with varying comonomer compositions and molecular weights *via*

RAFT solution copolymerisation (Figure 3.1). PETTC and ACVA were used as the chain transfer agent (CTA) and initiator, respectively, and the CTA/initiator molar ratio was maintained at 5.0. RAFT chemistry was used to ensure narrow molecular weight distributions and good control over the target copolymer molecular weight. The twelve copolymers were purified by precipitation from solution into a 1:1 ratio of water/methanol mixture to remove any residual comonomers. The purified copolymers were isolated as white/yellow powders. The lower molecular weight copolymers were more yellow owing to their higher proportion of RAFT chain-ends. GPC analysis showed that the copolymer molecular weight ranged from 6.1 kDa to 22.3 kDa with M_w/M_n values always below 1.25 (Table 3.1).

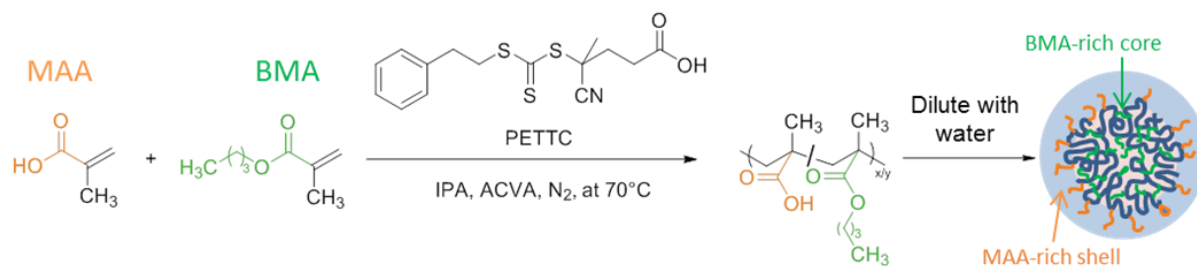


Figure 3.1 Synthesis of amphiphilic P(BMA-*stat*-MAA) statistical copolymers by RAFT solution copolymerisation using a PETTC RAFT agent and an ACVA initiator followed by micellar self-assembly on addition of water.

BMA and MAA comonomers were added into the reaction solution at molar feed ratios of 70:30, 80:20, and 90:10, respectively (Appendix 1). Determination of the copolymer compositions using ^1H NMR spectroscopy (Section 2.2.1-2) indicated that there were fewer MAA units present in the copolymer than expected from the initial feed ratio (Table 3.1). Instantaneous comonomer conversions were determined throughout the polymerisation by ^1H NMR spectroscopy (Appendix 2) and comparable initial rates of polymerisation were obtained for each comonomer ($k_{\text{obs}} \approx 0.0028 \text{ s}^{-1}$), which should lead to statistical incorporation. However, after 430 minutes the reaction rate of MAA decreases significantly ($k_{\text{obs}} \approx 0.0001 \text{ s}^{-1}$), resulting in a substantially lower MAA conversion compared to that of BMA (65 mol % vs. 93 mol %,

respectively). It is not known why the observed MAA conversion is limited but such kinetic data does clarify why the MAA content of the final copolymers is always less than that targeted. Taking the lower ultimate MAA conversion into account, the theoretical BMA/MAA copolymer compositions can be recalculated as 77:23, 85:15, and 93:7, which is in good agreement with compositions determined from ^1H NMR analysis of the methylated copolymers. However, because the BMA comonomer continues to polymerise after MAA polymerisation has essentially stopped, this produces a short BMA-rich ‘blocky’ sequence at the end of each copolymer chain.

Table 3.1 Compositional data obtained from ^1H NMR analysis of methylated copolymers [P(BMA-*stat*-MMA)], and weight-average molecular weight (M_w) and dispersity (M_w/M_n) obtained by GPC analysis of P(BMA-*stat*-MAA) copolymers using a THF eluent containing 1.0 wt% acetic acid (AcOH).

	Label	NMR		THF + 1 wt% AcOH GPC	
		BMA content	MMA content	M_w (kDa)	M_w/M_n
RAFT	BM _{77:23(22k)}	0.79	0.21	21.9	1.25
	BM _{77:23(15k)}	0.76	0.24	13.1	1.20
	BM _{77:23(10k)}	0.80	0.2	11.2	1.19
	BM _{77:23(5k)}	0.78	0.22	6.1	1.20
	BM _{85:15(22k)}	0.87	0.13	22.3	1.24
	BM _{85:15(15k)}	0.85	0.15	11.4	1.19
	BM _{85:15(10k)}	0.88	0.12	8.6	1.19
	BM _{85:15(5k)}	0.84	0.16	6.6	1.19
	BM _{93:7(22k)}	0.94	0.06	22.3	1.23
	BM _{93:7(15k)}	0.93	0.07	12.5	1.16
	BM _{93:7(10k)}	0.93	0.07	10.6	1.16
	BM _{93:7(5k)}	0.92	0.08	7.0	1.16
FRP	FRP _{70:30(24k)}	0.69	0.31	23.9	1.81
	FRP _{80:20(31k)}	0.78	0.22	31.2	1.89
	FRP _{90:10(21k)}	0.88	0.12	21.2	1.85

An additional series of P(BMA-*stat*-MAA) copolymers was synthesised by monomer-starved conventional free radical solution copolymerisation in IPA. This protocol should produce copolymer molecules with evenly distributed BMA and MAA units along the chain, which enables a comparison to be made to the potentially less even monomer distribution in the copolymers prepared by RAFT copolymerisation. Again, copolymer compositions of 70:30, 80:20 and 90:10 were targeted by varying the BMA/MAA comonomer feed ratios. These target compositions were fully consistent with ^1H NMR analysis of the methylated copolymers (Table 3.1). These copolymers have significantly higher dispersities ($M_w/M_n \approx 1.85$) than those synthesised *via* RAFT copolymerisation ($M_w/M_n \approx 1.20$). Thus, the latter technique provides better control over the molecular weight distribution (Table 3.1).³²

3.2.2 Copolymer self-assembly in water.

The self-assembly behaviour of these amphiphilic copolymers in water was investigated using SAXS. To avoid formation of large copolymer aggregates, dispersions were prepared using IPA as a co-solvent. Furthermore, TEA (1.1 mol. equivalents to the MAA residues) was added to the copolymer dispersions to deprotonate the MAA units and hence increase their water solubility. Thus, copolymers were first dissolved at 50% w/w in IPA and deprotonated with TEA before dilution to 1.0% w/w with water. This protocol yielded colloiddally stable dispersions/solutions for most formulations. However, attempts to prepare copolymer dispersions at high copolymer concentrations with low IPA contents (indicated in Appendix 3) were unsuccessful, owing to aggregation and precipitation.

SAXS patterns recorded for 1.0% w/w copolymer dispersions in water showed features consistent with the formation of particles with a clearly defined Guinier region at $q < 0.04 \text{ \AA}^{-1}$ and the first minimum of the form factor at $q \sim 0.08 \text{ \AA}^{-1}$ (Figures 3.2 and 3.3). Analysis of these

scattering patterns was undertaken by attempting to fit the data using appropriate structural models (Section 2.3.5). The copolymers under investigation comprise either a fully statistical or a predominantly statistical distribution of BMA and MAA units. Thus, according to the literature, such copolymers should form approximately spherical nano-objects (or, for the sake of simplicity, particles).^{17,18} However, since there is no diblock copolymer architecture, it can be assumed that phase separation between the hydrophobic and hydrophilic units is negligible. Therefore, no well-defined core and corona domains are expected for these self-assembled morphologies. This means that a spherical form factor should be appropriate to describe these particles (Section 2.5.2)

It is commonly accepted that the Percus-Yevick approximation of the hard-sphere structure factor is suitable for describing structural peaks originating from particle interactions at high concentrations (at or above 5% v/v).³³ However, a pronounced peak of intensity at $q \sim 0.02 \text{ \AA}^{-1}$ was observed consistently in the scattering patterns even at copolymer concentrations as low as 1.0 wt% owing to long-range repulsive interactions between the anionic particles (Figures 3.2 and 3.3). Indeed, addition of a small amount of NaCl results in the loss of this feature (Appendix 4). Thus, two structure factors were evaluated within the SAXS model (eq. 2.1) to account for this additional feature. The first is based on the Percus-Yevick approximation,^{33,34} $S(q) = S_{PY}(q, R_{PY}, f_{PY})$, where R_{PY} is an interparticle correlation radius and f_{PY} is an effective volume fraction, and second is based on the Hayter-Penfold approximation for charged particle Coulomb interactions,³⁵ $S(q) = S_{HP}(q, R_{HP}, f_{HP}, M, T, \varepsilon, Q)$, where R_{HP} is an interparticle correlation radius, f_{HP} is an effective volume fraction, M is the ionic strength of the solvent, T is the absolute temperature, ε is the solvent dielectric constant and Q is the particle charge expressed in electrons.

The particle charge required for the Hayter-Penfold approximation could be calculated from the electrophoretic mobility (μ_e) of the P(BMA-*stat*-MAA) particles as determined by aqueous electrophoresis. Mobility can be converted into a ζ -potentials using the Henry equation:³⁶

$$\mu_e = \frac{2}{3} \frac{\varepsilon_{rs} \varepsilon_0}{\eta_w} \zeta f(\kappa R_s) \quad (3.1)$$

where ε_{rs} is the dielectric constant of water, ε_0 is the permittivity of vacuum, η_w is the dynamic viscosity of water, κ is the inverse Debye length and $f(\kappa R_s)$ can be obtained from the Oshima expression.³⁶ The apparent charge (Q) can be related to the effective ζ -potential by solving the linearized Poisson-Boltzmann equation:³⁷

$$Q = \frac{R_s(1 + \kappa R_s)}{\lambda_B} \frac{e\zeta}{k_B T} \quad (3.2)$$

where λ_B is the Bjerrum length,³⁷ and k_B is the Boltzmann constant. The aggregation observed for MAA-rich copolymer nano-objects means that their electrophoretic mobility value is less reliable than for well-dispersed nano-objects. Nonetheless, there is a clear correlation between the particle radius and the particle surface charge (Appendix 5). From these measurements, an average charge was calculated for the copolymer compositions and used in the Hayter-Penfold approximation (Table 3.2).

The proposed model (Section 2.5.2) should demonstrate a strong power law dependence at high q [$I(q) \sim q^{-4}$]. However, the experimental SAXS data (Figures 3.2 and 3.3) indicate a relatively flat curve in this q range ($q > 0.1 \text{ \AA}^{-1}$), especially for the pattern corresponding to BM_{93:7(22k)} (Figure 3.3b). This type of behaviour is commonly observed for diblock copolymer micelles owing to scattering from the corona blocks.³⁸ For random copolymers, this is an unexpected result. Nevertheless, randomly-packed MAA and BMA residues within the particles may well produce regions with differing scattering length densities. Such fluctuations in scattering length

density within the nano-objects should cause scattering at high q . Similar structural formation has been analysed using a ‘blob’ model.³⁷ This approach was developed to interpret neutron scattering from the solvated cores of spherical micelles, where the Debye function for a Gaussian polymer chain (Section 2.5.4) was used in the analytical form factor calculations.³⁹

The approach produced a reasonably good fit to the experimental SAXS data (Figure 3.2, black line). However, a reliable set of ‘blob’ parameters could not be obtained from data fits owing to relatively noisy data at high q . Thus, although some fittings returned physically reasonable values (for example, $R_g^{\text{blob}} \approx 4 \text{ \AA}$, and $n_{\text{blob}} \approx 0.07$) suggesting that the average ‘blob’ size might correspond to approximately two repeat units, this ‘blob’ model was replaced with a simplified approach. Since it is associated with a minor component of the copolymer chains, the characteristic ‘blob’ size should be relatively small. Hence any function describing the ‘blob’ scattering (*e.g.*, a Debye function) should be more or less constant within the studied q range. Therefore, a constant C_1 was simply incorporated into the structural model to account for the flat background produced by the SLD fluctuations across the nano-object.

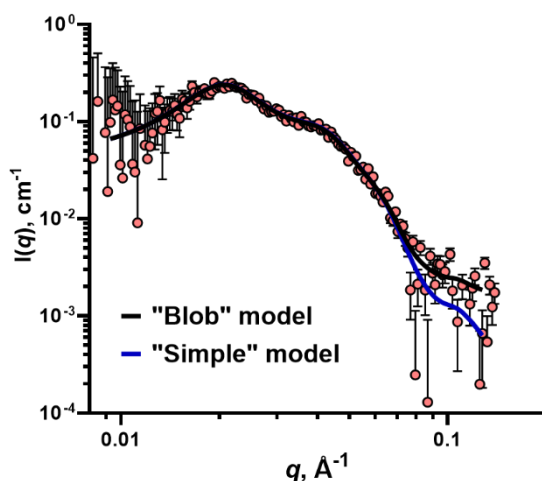


Figure 3.2. SAXS pattern recorded for a 1.0 wt% aqueous dispersion of BM_{85:15(22k)} (symbols) fitted with both the ‘blob’ model (Section 2.5.4; black line) and the simple sphere model (Section 2.5.2; blue line). A Bruker AXS Nanostar instrument was used for these measurements.

The proposed model produced reasonably good fits to the scattering patterns obtained for 1.0% w/w P(BMA-*stat*-MAA) copolymer aqueous dispersions (Figure 3.3), yielding the nano-object radii for each system (Table 3.2). However, SAXS patterns for the BM_{77:23} samples displayed some upturn at low q (Figure 3.3b), suggesting the presence of large aggregates. A combination of Guinier and power law functions is commonly employed to describe the scattering from large randomly-shaped structures.^{40–42} However, the Guinier region located at very low q is often inaccessible in SAXS experiments and only the power law region is recorded in scattering patterns. Thus, in order to fit the upturn in intensity observed in the scattering patterns, an additional term describing the power law dependence at low q was incorporated into the model (Section 2.3.4, eq. 2.4). The refined model was used for SAXS analysis and a least-squares algorithm was employed for data fits. However, a genetic optimization algorithm was applied when the global minimum of the figure of merit for the fitting (“chi-squared” parameter) had to be identified, in some cases, particularly for the model utilizing the Hayter-Penfold approximation.

When fitting experimental SAXS patterns using eq 2.4, the two structure factor approximations produced different values for the structural parameters describing particle packing in these copolymer dispersions (Table 3.2). More specifically, the interparticle distances and effective volume fractions obtained using the Percus-Yevick approximation were systematically larger than those values calculated when employing the Hayter-Penfold approximation. Nevertheless, the form factor parameters (FF column in Table 3.2) were not influenced by the chosen structure factor functions and employing either Percus-Yevick or Hayter-Penfold approximation produced very similar results for the particle radius, which was the most important parameter for this study. In view of this finding, the less parameterised Percus-Yevick approximation was used for SAXS analysis of the work in this chapter and also the entire thesis.

Considering 2.4 in combination with eqs 2.2, 2.9 and 2.12 suggests that the total volume fraction of copolymer molecules in the sample, ϕ , and the volume fraction of solvent within the nano-object, x_{sol} , are positively covariant. Thus, when the above model was used for data fitting, the volume fraction was fixed at the known concentration of the copolymer dispersion in order to evaluate x_{sol} . This approach yielded x_{sol} values close to zero, suggesting minimal ingress of the water molecules within the P(BMA-*stat*-MAA) nano-objects.

Table 3.2. Summary of SAXS analyses of a series 1.0 wt% P(BMA-*stat*-MAA) copolymer particles in aqueous media: mean particle radius (R), standard deviation of the mean particle radius (σ_R) and mean aggregation number (N_{agg}) calculated from the form factor function (FF), and the interparticle correlation distance (R_{HP} or R_{PY}), the effective volume fraction (f_{HP} or f_{PY}) and particle charge (Q) obtained using the Hayter-Penfold (HP) and Percus-Yevick (PY) approximations of structure factors, respectively.

Sample	FF			HP*		PY		
	R (Å)	σ_R (Å)	N_{agg}	R_{HP} (Å)	Q (electrons)	f_{HP}	R_{PY} (Å)	f_{PY}
BM _{77:23} (22k)	37	7	6	70	20	0.05	113	0.13
BM _{77:23} (15k)	33	6	7	61	20	0.05	100	0.12
BM _{77:23} (10k)	34	7	9	54	20	0.03	96	0.12
BM _{77:23} (5k)	37	5	22	65	20	0.05	85	0.10
BM _{85:15} (22k)	51	9	16	114	30	0.14	144	0.23
BM _{85:15} (15k)	49	7	28	91	30	0.08	139	0.20
BM _{85:15} (10k)	53	8	47	116	30	0.11	156	0.19
BM _{85:15} (5k)	54	7	64	92	30	0.05	156	0.18
BM _{93:07} (22k)	85	11	74	-	67	-	230	0.19
BM _{93:07} (15k)	81	19	114	-	67	-	284	0.15
BM _{93:07} (10k)	66	12	73	-	67	-	220	0.20
BM _{93:07} (5k)	68	17	120	-	67	-	233	0.17
FRP _{70:30} (24k)	35	13	5	47	20	0.05	77	0.15
FRP _{80:20} (31k)	66	16	25	97	30	0.04	176	0.16
†FRP _{90:10} (21k)	137	33	281	-	-	-	-	-

*No reliable results could be obtained for the BM_{93:07} copolymers using the HP approximation

†No structural peak was observed in the FRP_{90:10}(21k) scattering pattern

SAXS analysis indicates a correlation between the copolymer composition and the mean particle radius, with MAA-rich copolymers producing smaller nano-objects (Table 3.2). In contrast, the copolymer molecular weight has rather little effect on the particle size, particularly for the 77:23 and the 85:15 compositions. The anionic MAA groups stabilise the particles and higher MAA contents lead to lower mean aggregation numbers. Analysis of the 93:7 copolymer series indicates that the particle radius increases for the two higher molecular weight copolymers (Table 3.2). This suggests that the RAFT chain-ends help to solubilise the lower molecular weight copolymers: using PETTC as the CTA produces copolymer chains with an ionizable carboxylic acid end-group, which behaves like an additional MAA group. For relatively low MAA contents and copolymer molecular weights, such as $\text{BM}_{93:7(10\text{k})}$ or $\text{BM}_{93:7(5\text{k})}$, these end-groups effectively increase the carboxylic acid content of these MAA-based and, as a result, smaller particle radii are formed. Thus, higher molecular weight copolymers (15 kDa or 22 kDa) are more representative of the 93:7 composition.

Since there is no consistent correlation between copolymer molecular weight and particle size, the dispersity should have relatively little effect. Indeed, similar analysis undertaken on the FRP-synthesised copolymer series demonstrates a comparable trend, whereby the MAA composition is inversely related to the particle dimensions (Table 3.2). Although the compositional dependence is similar for the two synthesis methods, some discrepancies can be identified when a direct comparison between RAFT- and FRP- synthesised copolymers is made. Generally, the particles formed by the FRP series tend to be larger than those formed by the RAFT series as the MAA content is lowered. This size difference could be the result of statistical variations in the distribution of MAA units along the copolymer chains, as indicated by the BMA/MAA copolymerization rate (Appendix 2), as well as the incorporation of an additional carboxylic acid group per chain for the RAFT-synthesised copolymers.

TEM images obtained after drying 0.1% w/w copolymer dispersions confirm the formation of spherical particles (Figure 3.4) and are consistent with the SAXS data. Moreover, TEM analysis also suggests that MAA-rich copolymers form smaller particles. However, SAXS is considered far more statistically robust than TEM, with the latter technique also prone to staining artefacts and the possibility of nano-object flattening occurring during drying.

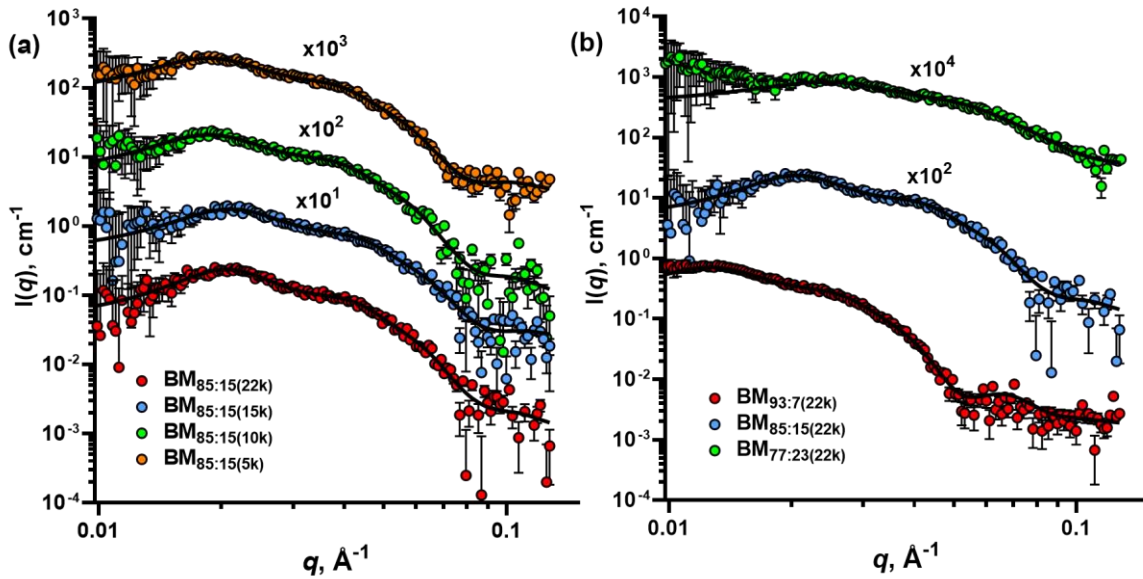


Figure 3.3. SAXS patterns recorder for 1.0% w/w aqueous dispersions of P(BMA-*stat*-MAA) copolymer particles (symbols) fitted using a refined spherical particle model (eq 2.3, solid lines) and (eq 2.4, dashed line); where (a) compares the scattering from a series of copolymers of the same composition (BM_{85:15}) but differing molecular weights and (b) compares the scattering for copolymers of the same molecular weight (22 kDa) but differing copolymer compositions. A Bruker AXS Nanostar instrument was used for these measurements. Some patterns are shifted upward by arbitrary factors (as indicated on the plots) to avoid overlap.

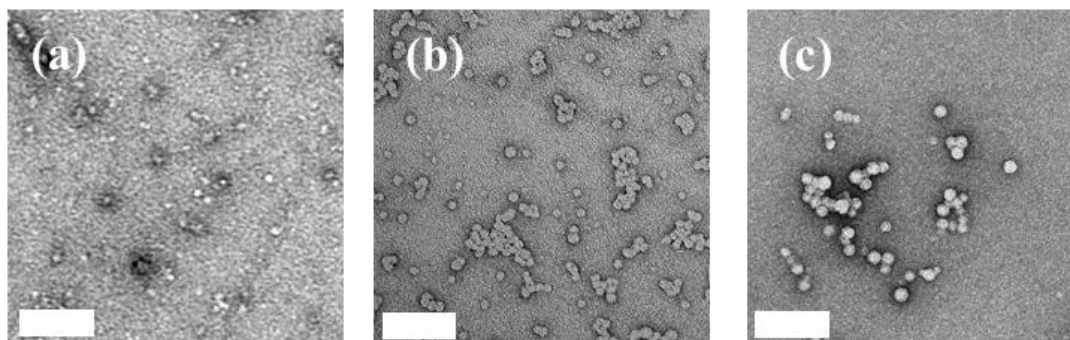


Figure 3.4. TEM images recorded for P(BMA-*stat*-MAA) spherical particles formed after dilution to 0.1% w/w with water from an initial 50% w/w copolymer solution in IPA for: (a) BM_{77:23}(22k); (b) BM_{85:15}(22k); and (c) BM_{93:7}(22k). The white scale bar in each TEM image corresponds to 100 nm.

3.2.3 Effect of varying the IPA/water solvent composition at a fixed copolymer concentration

The colloidal stability of the spherical nano-objects was examined by increasing the IPA content of the solvent mixture. More specifically, a series of SAXS measurements were conducted on 1.0% w/w copolymer dispersions with differing IPA/water contents (Figure 3.5a). Firstly, the structure factor observed in 1.0% w/w aqueous copolymer dispersions disappears on addition of IPA, indicating that the long-range order arising from the mutually repulsive anionic nano-objects is lost. This is a result of a reduction in the dielectric constant for the IPA/water mixture, and thus an increase in pK_a ,⁴³ reducing the effective anionic charge density on the surface of the nano-objects. Furthermore, larger, more solvated (*i.e.*, higher x_{sol}) nano-objects are formed as the IPA content is increased (Figure 3.5a). The scattering pattern recorded when the IPA volume fraction is 0.43 shows an upturn in scattering intensity at $q < 0.02 \text{ \AA}^{-1}$, suggesting the formation of significantly larger nano-objects. In pure IPA, there is no self-assembly because IPA is a sufficiently good solvent to fully solubilise the copolymer

chains. A similar experiment was conducted using a 25% w/w copolymer dispersion (Figure 3.5b). In this case, well separated spherical nano-objects are formed when the binary solvent is water-rich, as indicated by the pronounced structure factor peak observed under these conditions. However, as the solvent environment becomes IPA-rich, this feature becomes less prominent suggesting a reduction in particle size and an increase in the mean interparticle distance. A slight upturn at low q is evident at an IPA volume fraction of 0.31, which suggests the formation of larger nano-objects. At IPA volume fractions above 0.43, the structure factor peak is no longer observed (Figure 3.5b), which indicates molecular dissolution of individual copolymer chains under these conditions.

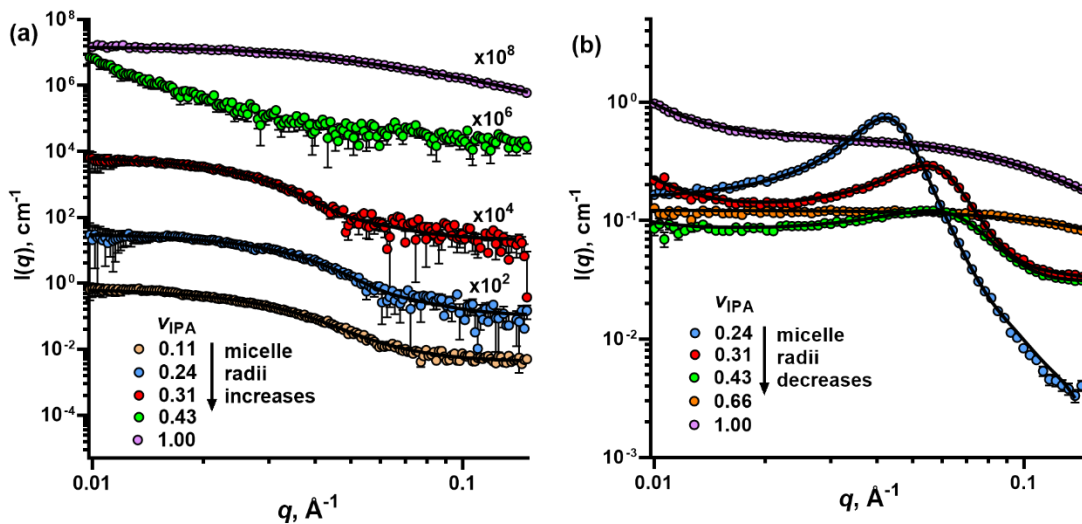


Figure 3.5. (a) SAXS patterns recorded for 1.0% w/w $\text{BM}_{85:15(22k)}$ copolymer dispersions (symbols) where the solvent composition is varied from water-rich to IPA-rich (a Bruker AXS Nanostar instrument was used for these measurements), with some patterns shifted upward by an arbitrary factor (indicated on the plots) to avoid overlap; (b) SAXS patterns recorded for 25 wt% $\text{BM}_{85:15(22k)}$ copolymer dispersions where the solvent composition is varied from water-rich to IPA-rich (a Xenocs Xeuss instrument was used for these measurements). The IPA/water solvent composition is indicated by the IPA volume fraction, v_{IPA} . SAXS data are fitted to a simple sphere model (eq 2. 9-12 solid lines).

These SAXS studies confirm that these P(BMA-*stat*-MAA) copolymers are mainly present as molecularly-dissolved Gaussian chains in IPA-rich media, whereas micellar self-assembly occurs at high water volume fractions owing to the hydrophobic nature of the BMA residues. This is true for both high (25% w/w) and low (1.0% w/w) copolymer concentrations. Under the latter conditions, the spherical nano-objects become swollen in IPA and hence grow in size when the solvent composition is gradually changed from water-rich to IPA-rich. In contrast, the particles appear to *decrease* in size when performing the same solvent switch at 25% w/w copolymer. This observation is accompanied by a scattering intensity upturn at low q -values suggesting the formation of larger objects.

Clearly, the extent of self-assembly is affected by both the solvent composition and the copolymer concentration. However, it is also important to compare the above two data sets to understand why different trends are observed. At 1.0% w/w, the nano-objects are well-separated, which enables them to swell unhindered on IPA addition, as confirmed by SAXS (Figure 3.5a). However, at 25% w/w copolymer, the particles are much closer together and the IPA-swollen particles interpenetrate to form a copolymer network interconnected by relatively small nano-object cores. This structural arrangement produces large scattering objects, resulting in a discernible upturn in scattered intensity at low q (Figure 3.5b). Thus, SAXS patterns of the dilute copolymer dispersion correspond to a system comprising large, non-interacting particles composed of solvated coronas and non-solvated cores. In contrast, the scattering patterns obtained for the corresponding concentrated dispersion of interpenetrating particles are consistent with smaller non-solvated particle cores embedded within a homogeneous matrix comprising highly solvated copolymer chains and solvent. Hence the apparent size reduction observed at higher IPA concentrations for concentrated dispersions is associated with an effective reduction in volume of the particle cores.

3.2.4 Effect of varying both the copolymer concentration and the solvent composition

To further investigate the effect of copolymer concentration on particle self-assembly, SAXS studies were conducted on 10, 20, 25, and 30% w/w copolymer dispersions in IPA-rich solvent compositions (Figure 3.6). Simultaneous variation of the copolymer concentration and solvent compositions enables a wide range of sample compositions to be examined by performing relatively few experiments. A structure factor peak was observed in the scattering patterns these studies were conducted at high copolymer concentrations, for which of IPA solvation of the BMA segments is less significant (Figure 3.6). This feature shifts to higher q at higher copolymer concentrations, indicating a shorter interparticle distance and hence more densely-packed nano-objects (Figure 3.6). Moreover, it becomes less pronounced at higher copolymer and IPA concentrations. This trend is particularly evident for BM_{77:23(22k)} – its structure factor is barely discernible at 30% w/w copolymer. In contrast, the more moderate change in the structure factor peak associated with BM_{93:7(22k)} series of samples indicates a correlation between particle stability and copolymer composition: BMA-rich copolymer particles are less likely to undergo dissociation under these conditions.

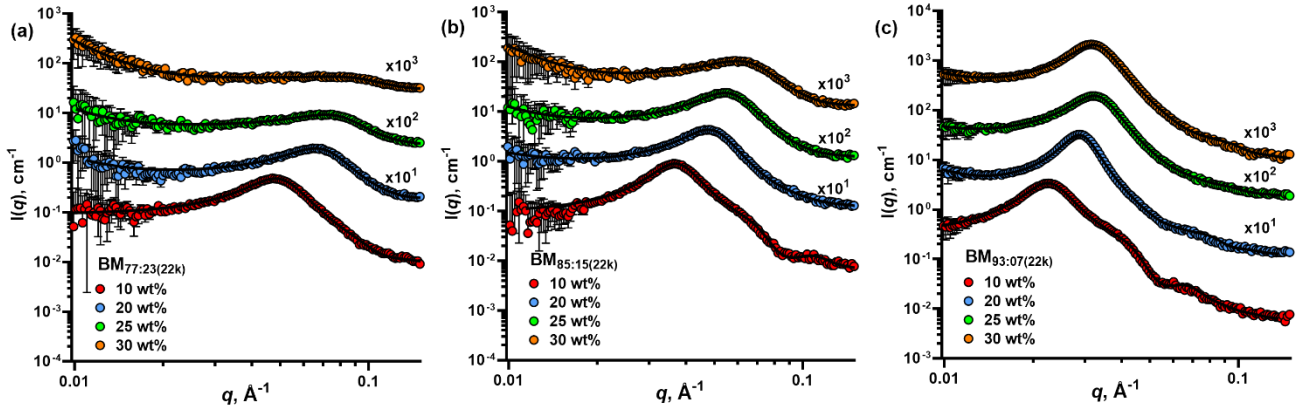


Figure 3.6. SAXS patterns recorded at 10, 20, 25 and 30% w/w copolymer dispersions (see symbols) for (a) $\text{BM}_{77:23}(22\text{k})$, (b) $\text{BM}_{85:15}(22\text{k})$ and (c) $\text{BM}_{93:7}(22\text{k})$ in various IPA/water solvent mixtures (the IPA volume fraction, v_{IPA} , is 0.11, 0.24, 0.31 and 0.43, respectively). A Bruker AXS Nanostar instrument was used for these measurements. Some patterns are shifted upward by an arbitrary factor indicated on the plots to avoid overlap. The SAXS data are fitted using an adapted spherical nano-object model (eq 2.3, solid lines).

The spherical particles formed at 10% w/w copolymer concentration are of a similar size to that determined at 1.0% w/w but the relative interparticle distance is significantly reduced, as expected at this higher copolymer concentration (compare Tables 3.2 and 3.3). The observed reduction in particle dimensions when increasing the copolymer concentration (Table 3.3) is attributed to the higher IPA content in the binary solvent mixture. This is consistent with the observed increase in the solvent volume fraction within the particle (x_{sol}) obtained from SAXS analysis (eqs 2.9-12). Thus, the particle size and mean aggregation number are reduced in IPA-rich media. The shift and attenuation in the structure factor peak observed in these scattering patterns, despite the higher copolymer concentration, suggests a morphological transformation from spherical particles at low copolymer concentration in water-rich media towards molecularly-dissolved copolymer chains in IPA-rich media. As expected, this trend is most noticeable for MAA-rich copolymers (Figure 3.6a). At 30% w/w copolymer, the particles possess their smallest dimensions and are highly swollen. Indeed, x_{sol} is close to unity, which

seems to be physically unrealistic. The model assumes the sole presence of spherical particles and that all the copolymer chains are located within the particles. Since the copolymer volume fraction is fixed during data fitting, such high x_{sol} values suggest that the fitting algorithm artificially lowers the particle scattering contribution by reducing the $(1 - x_{\text{sol}})$ term in eq 2.12. A reasonable explanation is that not all copolymer chains are located within the particles. Given that IPA is a reasonably good solvent for the BMA residues and that the structural morphology is less defined at high copolymer concentrations and IPA volume fractions, the single population of spherical particles assumed in this scattering model is an over-simplified approximation. Indeed, given the broad distribution of copolymer compositions, BMA-rich chains are more likely to form particles, whereas MAA-rich chains are more likely to be molecularly dissolved. Thus, these two populations may well coexist, particularly at higher IPA volume fractions. In this case the SAXS pattern can be represented by a superposition of scattering contributions from both particles (eq 2.9-12) and random coils (eq 2.8) where the total copolymer concentration, redistributed between these two populations, is fixed. However, this refined two-population model does not provide a satisfactory fit to the experimental data at high q . An alternative model involves a single population of particles whereby some of the copolymer chains form bridges between neighbouring particles to produce an extended network (Figure 3.7). In this case the copolymer volume fraction located within the particles and, therefore, the total particle volume will be reduced. At the same time, the interconnected particles form a larger network of objects that scatter coherently. Indeed, the relevant SAXS patterns exhibit a gradual upturn in scattering at low q values (Figure 3.6) with the scattering intensity following a power law dependence (with an exponent of ~ -3 at the highest IPA content, see Figures 3.6a and 3.6b) that suggests the formation of large fractals. However, the Guinier region for these structures could not be resolved at low q ($\sim 0.002 \text{ \AA}^{-1}$), which suggests that their dimensions exceed 3000 \AA . In general, these SAXS observations support the

formation of a particle network interconnected by partially released copolymer chains (Figure 3.7). Satisfactory qualitative fits to scattering patterns can be obtained using a relatively simple structural model (eq 2.3) incorporating a spherical micelle form factor (eqs 2.9-12) (Figure 3.6). However, quantitative SAXS analysis of this inter-connected particle network is beyond the scope of this work. In addition, redistribution of solvent molecules is likely for IPA-rich dispersions, since this co-solvent can readily penetrate the nano-objects. Such variation of the solvent composition inside and outside the particles and concomitant reduction in the scattering length density contrast between IPA-swollen nano-objects and the binary solvent mixture may account for the artificially high x_{sol} suggested by the data fits.

SAXS analysis suggests that the self-assembled morphology transforms from well-defined particles to interconnected particles to molecularly-dissolved copolymers (Figure 3.7). At low copolymer concentrations in a water-rich environment, the copolymer chains self-assemble to form stable particles. However, increasing the copolymer concentration along with the IPA volume fraction causes a reduction in particle size and formation of an interconnected nano-object network. At the highest IPA volume fractions, the copolymer chains become fully solvated and undergo molecular dissolution.

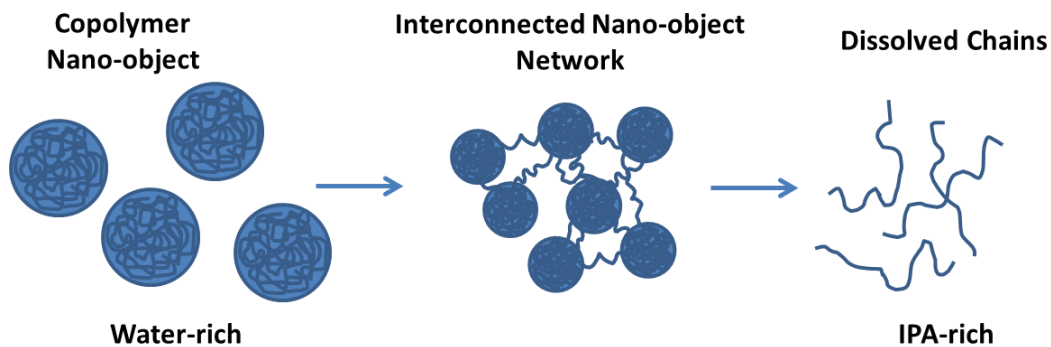


Figure 3.7. A schematic describing the transformation from self-assembled copolymer nano-objects (at low copolymer concentrations in a water-rich environment) to dissolved chains (at high copolymer concentrations in an IPA-rich environment) *via* an interconnected nano-object network.

Table 3.3. Summary of the structural parameters obtained from SAXS studies of a three series of amphiphilic P(BMA-*stat*-MAA) statistical copolymers [BM_{77:22(22k)}, BM_{85:15(22k)}, and BM_{93:7(22k)}] dissolved at various concentrations in IPA-water solutions using a refined model (eq 2.3) comprising a spherical form factor (FF) and Percus-Yevick structure factor (PY): mean particle radius (R), solvent fraction in the particles (x_{sol}), the interparticle correlation radius (R_{PY}) and effective volume fraction (f_{PY}).

Polymer	% w/w	Solvent content		FF		PY	
		v_{IPA}	v_{Water}	R (Å)	x_{sol}	R_{PY} (Å)	f_{PY}
BM _{77:23(22k)}	10	0.11	0.89	41	0.39	62	0.30
	20	0.24	0.76	32	0.84	44	0.28
	25	0.31	0.69	25	0.93	37	0.23
	30	0.43	0.57	17	0.97	30	0.21
BM _{85:15(22k)}	10	0.11	0.89	52	0.45	85	0.34
	20	0.24	0.76	45	0.85	63	0.32
	25	0.31	0.69	39	0.92	54	0.30
	30	0.43	0.57	33	0.97	45	0.24
BM _{93:7(22k)}	10	0.11	0.89	84	0.46	139	0.35
	20	0.24	0.76	80	0.82	112	0.40
	25	0.31	0.69	69	0.88	95	0.35
	30	0.43	0.57	68	0.92	96	0.35

3.2.5 Rheology of copolymer dispersions

Rheological studies were performed on the same copolymer dispersions of various concentrations and solvent composition to determine their dynamic viscosity and to monitor any physical consequences of the structural phenomena detected by SAXS (Figures 3.5, 3.6, and 3.7). Initial experiments were conducted on 25% w/w copolymer dispersions with the binary solvent composition being varied from IPA-rich to water-rich (Figure 3.8) to assess how this parameter affects their rheological behaviour. When the solvent environment is IPA-rich (*i.e.*, when the volume fraction of IPA, v_{IPA} , is at least 0.66) a relatively low viscosity is observed (Figure 3.8), which is attributed to the molecularly-dissolved copolymer chains (Figure 3.5b and Figure 3.7). However, when the water content is increased ($0.43 \geq v_{IPA} \geq$

0.31), the copolymer chains self-assemble to form interconnected particles (Figure 3.5b and Figure 3.7). This particle network leads to a sharp increase in the dispersion viscosity (Figure 3.8), indicating a significant reduction in chain mobility. When the solvent environment is water-rich ($v_{IPA} \leq 0.24$) the copolymers form well-defined spherical particles (Figure 3.5b and Figure 3.7) leading to a significant reduction in the dispersion viscosity (Figure 3.8), as expected for isolated particles in a Newtonian liquid. An extended series of viscosity measurements on BM_{85:15(22k)} performed over a wider range of copolymer concentrations and solvent compositions indicates the local maximum in zero shear viscosity (Appendix 3). These data confirms that both a high copolymer concentration and a higher proportion of IPA co-solvent are required for the formation of a particle network.⁴⁴

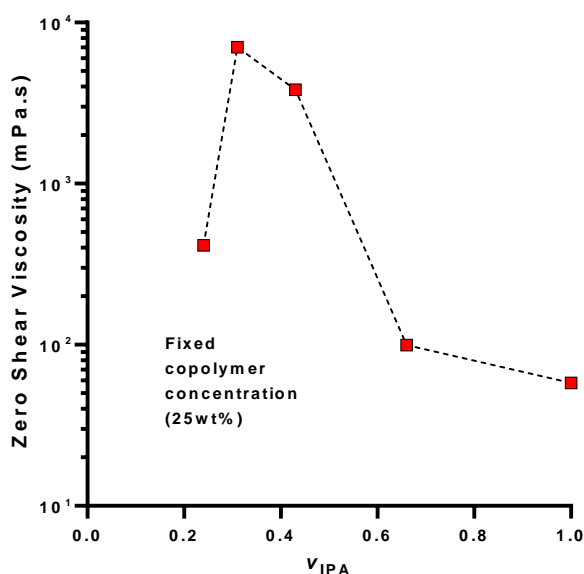


Figure 3.8. Zero shear viscosity observed for 25% w/w BM_{85:15(22k)} copolymer dispersions containing various volume fractions of IPA co-solvent (v_{IPA}).

In order to compare various P(BMA-*stat*-MAA) copolymers, rheological measurements were conducted for copolymer concentrations ranging from 1.0 to 40% w/w (Figure 3.9). Formulations were selected with appropriate copolymer concentration and v_{IPA} to correspond approximately with the diagonal line crossing the local maximum of zero shear viscosity

(Appendix 3). These studies were combined with the SAXS data (Figure 3.6 and Table 3.3) in order to evaluate the effect of self-assembly on the copolymer dispersion viscosity.

Dilute copolymer dispersions (1.0% w/w) and water-rich solvent compositions exhibited zero shear viscosities (Figure 3.9) comparable with that of water (~ 1 mPa.s). These observations are consistent with the corresponding SAXS data (Figure 3.3), which indicate the formation of spherical particles under these conditions. Such repulsive anionic copolymer particles (as indicated by combined electrophoresis and SAXS studies) do not significantly affect the rheological properties of the dispersion. Indeed, rheology measurements performed at copolymer concentrations up to 20% w/w indicate relatively low dispersion viscosities of 20-100 mPa.s (Figure 3.9b). The viscosity trend at 20% w/w copolymer concentration appears to be inversely correlated to the particle size, where the dispersions with larger sphere radii displaying lower viscosities.

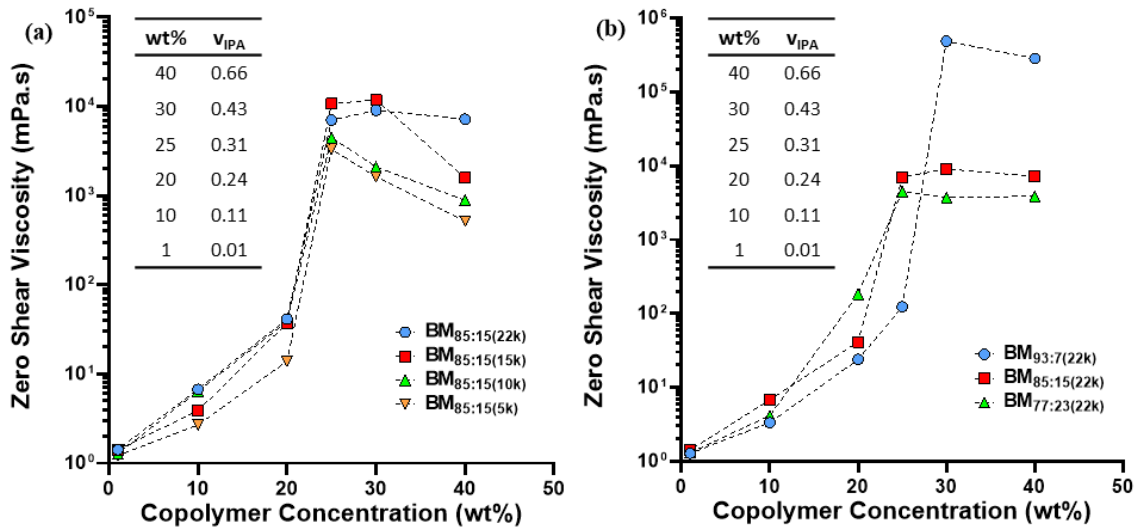


Figure 3.9. Zero shear viscosity *versus* copolymer concentration for P(BMA-*stat*-MAA) dispersions diluted from a 50 wt% copolymer stock solution in IPA with water: (a) copolymer dispersions of the same copolymer composition but differing molecular weights (BM_{85:15}(22k), BM_{85:15}(15k), BM_{85:15}(10k), and BM_{85:15}(5k)); (b) copolymer dispersions of the same molecular weight but differing copolymer composition [BM_{77:23}(22k), BM_{85:15}(22k), and BM_{93:7}(22k)]. The table in each plot shows the composition of the studied samples (copolymer concentrations and respective IPA volume fraction in the solvent).

Each copolymer displays a local maximum in viscosity at concentrations ranging from 25% w/w to 30% w/w. For example, the copolymer series containing the highest MAA content (Figure 3.9b) displays a sharp increase in viscosity at the lowest copolymer concentration (25% w/w) and v_{IPA} (0.31). This correlates well with the SAXS data (Figure 3.6a), which suggests that BM_{77:23}(22k) copolymers no longer form well-defined spherical particles at this concentration but instead form an interconnected particle network, as indicated by the scattering intensity upturn at low q . Furthermore, rheology measurements show that BMA-rich copolymers (Figure 3.9b) display a viscosity maximum at the highest concentration of 30% w/w where the v_{IPA} is 0.43. Again, this observation is consistent with the SAXS data (Figure 3.6c), which shows that BM_{93:7}(22k) copolymers at this concentration form a nano-object network at this concentration.

Further inspecting the rheology data indicates a strong relationship between the maximum viscosity and the copolymer composition. The former parameter increases with lower MAA contents, consequently there is a correlation between the maximum viscosity and the particle radius. At 40% w/w copolymer, the IPA content in the copolymer dispersions becomes significant, which promotes molecular dissolution. Moreover, the viscosity depends on the copolymer molecular weight such that the longest chains produce the most viscous solutions (Figure 3.9a). This is consistent with the SAXS data and suggests that the copolymer chains are molecularly dissolved at this concentration. Furthermore, the viscosity of 40% w/w copolymer solution not only depends on the molecular weight but also on the copolymer composition, with the highest viscosity being achieved for the lowest MAA fraction (Figure 3.9b). An extended set of viscosity measurements using a wider range of copolymer concentrations and solvent compositions to further map out the peak in viscosity (Appendix 3).

Overall, there is a good correlation between the copolymer morphologies determined by SAXS and viscoelastic properties of the copolymer dispersions: well-defined spherical particles behave as a Newtonian liquid,⁴⁴ interconnected particle networks are characterized by an increase in dispersion viscosity by more than two orders of viscosity compared to well separated particles, while molecularly-dissolved copolymer chains exhibit the rheological behaviour expected for a polymer solution.

3.2.6 The relationship between particle size and the copolymer composition

According to the SAXS data the particle size is strongly dependent on the copolymer composition. In principle, this trend can be mathematically modelled and used as a predictive tool. However, a suitable physical model is required to account for the structure of the copolymer particles. SAXS studies indicate structural order for the particles at low copolymer

concentration (Figure 3.3), while the electrophoretic data (Appendix 5) confirms that the particles have anionic character. Thus, following Derjaguin, Landau, Verwey and Overbeek (DLVO) theory⁴⁵ the observed colloidal stability of these particles is consistent with a charge stabilization mechanism. In this context, it is noteworthy that the surface charge increases with the radius (Appendix 5). Considering that both parameters responsible for the colloidal stability⁴⁶ are related to each other, it is possible to hypothesise that the particles become colloidally stable by acquiring a critical surface charge density. Since the MAA repeat units confer the surface charge, copolymer self-assembly most likely involves localization of this component at the particle surface. If this is correct, then reducing the MAA fraction in the copolymer chains leads to the formation of larger particles in order to maintain a constant surface charge density. As an idealized approximation of the proposed scenario it could be assumed that *all* MAA units congregate at the particle surface. To test this assumption, the fraction of the particle surface covered by MAA residues was calculated for each particle from the known properties of the copolymer chains and the particles they form.

Using a relatively simple geometric model and structural information obtained from SAXS, the location of the MAA units within the particle can be identified and used to relate the particle radius to the copolymer composition. First, various reasonable assumptions are made for this model: (1) the particles are assumed to be perfect spheres; (2) all of the MAA segments are located on the particle surface; (3) the total surface area covered by *all* the MAA residues is calculated using the volume occupied by one MAA unit, where each unit is represented by a cube and one face makes up a fraction of the particle surface.

The mole fraction of MAA residues in an individual copolymer chain is directly related to the mole fraction of MAA within a particle, which can be defined by the equation:

$$Mol.frac_{,MAA} = \frac{N_{MAA,p}}{N_{MAA,p} + N_{BMA,p}} \quad (3.3)$$

where $N_{MAA,p}$ and $N_{BMA,p}$ are the mean number of MAA and BMA units per nano-object, respectively. These parameters can be obtained either from experiment using the copolymer composition or from the proposed model using the following equations:

$$N_{MAA,p} = \frac{4\pi R \times SA_{frac}}{CS_{MAA}} \quad (3.4)$$

$$N_{BMA,p} = \frac{\frac{4}{3}\pi R^3 - \left(\frac{4\pi R^2 \times SA_{frac} \times V_{MAA}}{CS_{MAA}} \right)}{V_{BMA}} \quad (3.5)$$

where $V_{MAA} = 121 \text{ \AA}^3$ and $V_{BMA} = 224 \text{ \AA}^3$, calculated by the equation $V_{BMA \text{ or } MAA} = M_w / (N_A \rho_{BMA \text{ or } MAA})$ where the solid-state densities of the homopolymers, $\rho_{PBMA \text{ or } PMAA}$, were determined by helium pycnometry [$\rho_{PBMA} = 1.05 \text{ g cm}^{-3}$ and $\rho_{PMAA} = 1.18 \text{ g cm}^{-3}$]. CS_{MAA} is the approximate cross-sectional area of one MAA unit calculated from V_{MAA} ($= V_{MAA}^{2/3} \approx 24.5 \text{ \AA}^2$). SA_{frac} is the fraction of the particle surface covered by MAA residues. Equations 3.3-5 can be used to theoretically predict how the particle radius, R , is related to the mole fraction of MAA residues in the copolymer composition assuming that all these repeat units are located within the particle surface and given that SA_{frac} , which is proportional to the surface charge density and assumed to be constant.

From the experimental data, larger particles are formed as the MAA volume fraction of the copolymer is reduced (Figure 3.10). A similar dependence is also predicted by the structural model if it is assumed that all MAA residues are located at the particle surface and its surface fraction, SA_{frac} , is constant and independent of the particle size (Figure 3.10). The striking similarity between the experimental data and the theoretical prediction by this model suggests

that most of the MAA units are indeed localised at the particles surface. All the experimental data lie within a narrow interval of SA_{frac} values and approximately follow a curve corresponding to $SA_{\text{frac}} = 0.30$ (Figure 3.10). The discrepancies observed between the idealised model and the experimental results is likely to be related to the slight blockiness of the copolymers that was observed during the RAFT synthesis. Additionally, the average length of the mean sequence of BMA repeat unit is probably shorter than the particle diameter. As a result, some MAA units are surrounded by neighbouring BMA units and hence may become ‘trapped’ within the particle cores. Thus, a more physically realistic structural model should have a core-shell morphology (or perhaps a gradient distribution of MAA repeat units) with a relatively high concentration of MAA units in the particle shell (surface) and a relatively low concentration of MAA units within the particle core. A similar model has been invoked in a recent work on self-assembly of a poly(methyl methacrylate-*co*-2-dimethyl aminoethyl methacrylate) random copolymer.¹⁹ Nevertheless, the proposed idealised model suggests that the colloidal stability involves achieving a critical surface charge density that is mainly governed by the MAA content of the copolymer chains. This crude structural model can be used to estimate the dimensions of particles formed by the self-assembly of a series of amphiphilic statistical copolymers of variable MAA content. In principle, incorporating an additional parameter that accounts for the spatial distribution of MAA repeat units throughout an individual particle would improve the predictions of this model, but has not been investigated within this chapter of work.

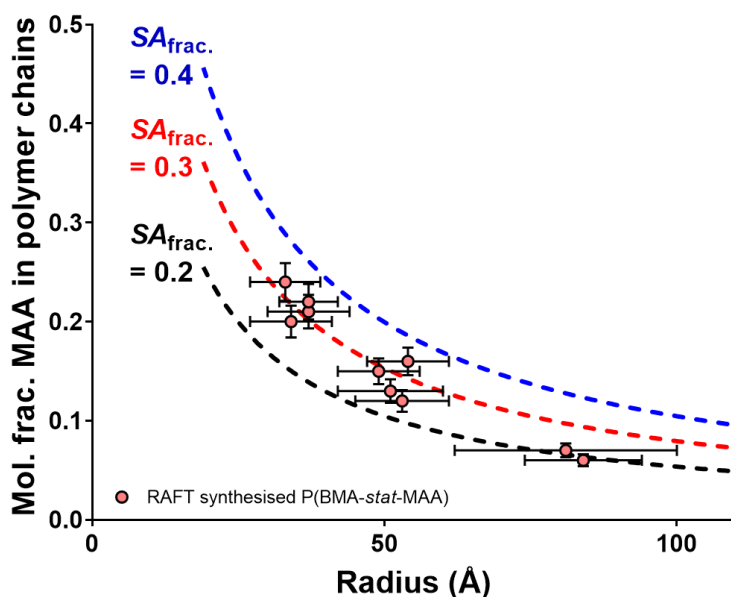


Figure 3.10. Relationship between the mole fraction of MAA in the copolymer chains and the corresponding nano-object radius formed in aqueous solution for the RAFT synthesised P(BMA-*stat*-MAA) copolymers that have a blocky BMA terminus: experimental data (circles) and estimated values (dashed lines) using the model (eqs 3.3-3.5) when $SA_{\text{frac.}} = 0.40$ (blue), 0.30 (red), and 0.20 (black).

3.3 Conclusions

A series of P(BMA-*stat*-MAA) statistical copolymers have been synthesized with various BMA/MAA compositions (77:23 – 93:7) and copolymer molecular weights (6 – 22 kDa) *via* RAFT solution copolymerisation and compared to similar statistical copolymers prepared *via* monomer-starved conventional FRP. RAFT copolymerisation produced low-dispersity copolymers ($M_w/M_n \approx 1.20$), whereas FRP produced copolymers with somewhat higher dispersities ($M_w/M_n \approx 1.85$). Kinetic analysis of the RAFT copolymerisation found that both comonomers react at similar rates initially. However, the MAA conversion was lower than BMA towards the end of the copolymerisation, leading to a short ‘blocky’ BMA-rich sequence towards the end of each copolymer chain. Conversely, FRP produced copolymers with an essentially random distribution of comonomer units.

SAXS studies of the effect of varying the IPA/water binary solvent composition on the morphology of the self-assembled structures in the presence of base (*ca.* pH 8) indicated that the copolymers are largely present as molecularly-dissolved Gaussian chains when the solvent is IPA-rich but self-assemble to form well-defined spherical particles when the solvent composition becomes water-rich. Particle radii are inversely proportional to the MAA content of such copolymers but remain independent of molecular weight. At high copolymer concentrations and intermediate IPA/water solvent compositions, SAXS indicated the formation of relatively large objects. This is interpreted in terms of an inter-connected particle network created by the overlap of swollen particles confined in space. These morphological insights correlate well with rheological measurements. At low copolymer concentrations, non-interacting spherical particles are formed and the dispersions exhibit viscosities comparable to that of water. At high copolymer and IPA concentrations, when the dispersions become molecularly-dissolved copolymer chains, the solution viscosities are molecular weight-dependent, as expected. At intermediate copolymer and IPA concentrations, a pronounced maximum in solution viscosity is observed, which is consistent with the formation of the inter-connected particle network structures indicated by the SAXS data.

A relatively simple structural model involving just a form factor for spherical particles proved to be a good first approximation for the SAXS analysis of particles formed by self-assembly of amphiphilic P(BMA-*stat*-MAA) statistical copolymers. This model has been refined by incorporating additional terms to account for fluctuating scattering length density associated with randomly-packed MAA and BMA repeat units, and scattering arising from a large inter-connected particle network. An appropriate structure factor has also been incorporated into this model to analyse the particle packing. This more sophisticated model provided good fits to all experimental SAXS patterns obtained for these copolymer dispersions, allowing determination

of particle size, particle size distribution, the solvent concentration inside the particle cores and the mean molecule aggregation number.

Combined SAXS and electrophoretic measurements indicate that the particle size is directly related to the surface charge density and, therefore, the fraction of the particle surface covered by MAA. A new structural model assuming that the hydrophilic (MAA) units are localised at the particle surface and the hydrophobic (BMA) units mainly form the particle core has been proposed that is consistent with the experimental data and can be used as a first approximation to predict particle dimensions for aqueous dispersions of amphiphilic statistical copolymers.

3.4 References

- 1 A. Rösler, G. W. M. Vandermeulen and H. A. Klok, *Adv. Drug Deliv. Rev.*, 2012, **64**, 270–279.
- 2 Y. Morishima, S. Nomura, T. Ikeda, M. Seki and M. Kamachi, *Macromolecules*, 1995, **28**, 2874–2881.
- 3 L. Li, K. Raghupathi, C. Song, P. Prasad and S. Thayumanavan, *Chem. Commun.*, 2014, **50**, 13417–13432.
- 4 R. Xu, M. A. Winnik, F. R. Hallett, G. Riess and M. D. Croucher, *Macromolecules*, 1991, **24**, 87–93.
- 5 M. Wilhelm, C. Le Zhao, Y. Wang, R. Xu, M. A. Winnik, J. L. Mura, G. Riess and M. D. Croucher, *Macromolecules*, 1991, **24**, 1033–1040.
- 6 K. Prochazka, D. Kiserow, C. Ramireddy, Z. Tuzar, P. Munk and S. E. Webber, *Macromolecules*, 1992, **25**, 454–460.

- 7 I. Astafieva, X. F. Zhong and A. Eisenberg, *Macromolecules*, 1993, **26**, 7339.
- 8 A. Qin, M. Tian, C. Ramireddy, S. E. Webber, P. Munk and Z. Tuzar, *Macromolecules*, 1994, **27**, 120–126.
- 9 M. Guo, L. M. Pitet, H. M. Wyss, M. Vos, P. Y. W. Dankers and E. W. Meijer, *J. Am. Chem. Soc.*, 2014, **136**, 6969–6977.
- 10 M. Huo, J. Yuan, L. Tao and Y. Wei, *Polym. Chem.*, 2014, **5**, 1519–1528.
- 11 P. Schattling, F. D. Jochum and P. Theato, *Polym. Chem.*, 2014, **5**, 25–36.
- 12 Y. Sun, Z. Wang, Y. Li, Z. Zhang, W. Zhang, X. Pan, N. Zhou and X. Zhu, *Macromol. Rapid Commun.*, 2015, 1341–1347.
- 13 A. Blanazs, J. Madsen, G. Battaglia, A. J. Ryan and S. P. Armes, *J. Am. Chem. Soc.*, 2011, **133**, 16581–16587.
- 14 A. Blanazs, A. J. Ryan and S. P. Armes, *Macromolecules*, 2012, **45**, 5099–5107.
- 15 C. J. Mable, R. R. Gibson, S. Prevost, B. E. McKenzie, O. O. Mykhaylyk and S. P. Armes, *J. Am. Chem. Soc.*, 2015, **137**, 16098–16108.
- 16 A. Blanazs, S. P. Armes and A. J. Ryan, *Macromol. Rapid Commun.*, 2009, **30**, 267–277.
- 17 U. Scheler, *Handbook of Polyelectrolytes and Their Application*, Vol. 2, American Scientific Publishers, California, 2002.
- 18 Y. Hu, R. S. Armentrout and C. L. McCormick, *Macromolecules*, 1997, **30**, 3538–3546.
- 19 J. C. Pegg, A. Czajka, C. Hill, C. James, J. Peach, S. E. Rogers and J. Eastoe,

- Langmuir*, 2017, **33**, 2628–2638.
- 20 K. Hales and D. J. Pochan, *Curr. Opin. Colloid Interface Sci.*, 2006, **11**, 330–336.
- 21 Y. Hirai, T. Terashima, M. Takenaka and M. Sawamoto, *Macromolecules*, 2016, **49**, 5084–5091.
- 22 Y. Chang and C. L. McCormick, *Macromolecules*, 1993, **26**, 6121.
- 23 A. Hashidzume, A. Kawaguchi, A. Tagawa, K. Hyoda and T. Sato, *Macromolecules*, 2006, **39**, 1135–1143.
- 24 T. Kawata, A. Hashidzume and T. Sato, *Macromolecules*, 2007, **40**, 1174–1180.
- 25 X. Zhu and M. Liu, *Langmuir*, 2011, **27**, 12844–12850.
- 26 P. Guo, W. Guan, L. Liang and P. Yao, *J. Colloid Interface Sci.*, 2008, **323**, 229–234.
- 27 X. Liu, J.-S. Kim, J. Wu and A. Eisenberg, *Macromolecules*, 2005, **38**, 6749–6751.
- 28 F. Tian, Y. Yu, C. Wang and S. Yang, *Macromolecules*, 2008, **41**, 3585–3588.
- 29 X. Wu, Y. Qiao, H. Yang and J. Wang, *J. Colloid Interface Sci.*, 2010, **349**, 560–564.
- 30 F. Ilhan, T. H. Galow, M. Gray, G. Clavier and V. M. Rotello, *J. Am. Chem. Soc.*, 2000, **122**, 5895–5896.
- 31 S. Riemer, S. Prévost, M. Dzionara, M.-S. Appavou, R. Schweins and M. Gradzielski, *Polymer (Guildf.)*, 2015, **70**, 194–206.
- 32 J. Chiefari, Y. K. Chong, F. Ercole, J. Krstina, J. Jeffery, T. P. T. Le, R. T. A. Mayadunne, G. F. Meijs, C. L. Moad, G. Moad, E. Rizzardo and S. H. Thang, *Macromolecules*, 1998, **31**, 5559–5562.

- 33 J. S. Pedersen and M. C. Gerstenberg, *Macromolecules*, 1996, **29**, 1363–1365.
- 34 J. K. Percus and G. J. Yevick, *Phys. Rev.*, 1958, **110**, 1–13.
- 35 J. B. Hayter and J. Penfold, *Mol. Phys.*, 1981, **42**, 109–118.
- 36 A. V. Delgado, F. González-Caballero, R. J. Hunter, L. K. Koopal and J. Lyklema, *Pure Appl. Chem.*, 2005, **77**, 1753–1805.
- 37 M. F. Hsu, E. R. Dufresne and D. A. Weitz, *Langmuir*, 2005, **21**, 4881–4887.
- 38 J. S. Pedersen, *J. Appl. Crystallogr.*, 2000, **33**, 637–640.
- 39 M. Doi and S. F. Edwards, *The Theory of Polymer Dynamics*, Clarendon Press, Oxford, 1986.
- 40 G. Beaucage and D. W. Schaefer, *J. Non. Cryst. Solids*, 1994, **172–174**, 797–805.
- 41 G. Beaucage, *J. Appl. Crystallogr.*, 1995, **28**, 717–728.
- 42 G. Beaucage, *J. Appl. Crystallogr.*, 1996, **29**, 134–146.
- 43 C. Lee, E. Jeoung and I. Lee, *J. Heterocycl. Chem.*, 2000, **37**, 159–166.
- 44 N. Willenbacher and K. Georgieva, in *Product Design and Engineering: Formulation of Gels and Pastes*, eds. U. Brockel, W. Meier and G. Wgner, Wiley-VCH Verlag GmbH & Co. KGaA., Weinheim, 1st edn., 2013, pp. 7–49.
- 45 R. J. Hunter, *Foundations of colloid science*, Oxford University Press, New York, 2nd edn., 2000.
- 46 R. Hidalgo-Álvarez, A. Martín, A. Fernández, D. Bastos, F. Martínez and F. J. De Las Nieves, *Adv. Colloid Interface Sci.*, 1996, **67**, 1–118.

*Chapter 4. Self-assembly of amphiphilic statistical
copolymers in aqueous solution by tuning copolymer
composition and hydrophobicity*

Chapter 4.

Self-assembly of amphiphilic statistical copolymers in aqueous solution by tuning copolymer composition and hydrophobicity

4.1 Introduction

Self-assembled copolymers have many diverse applications in a wide range of fields, including healthcare,¹⁻³ energy,^{4,5} and coatings.⁶⁻⁸ The assembly of diblock copolymers has been studied extensively and is known to occur to minimize the energetically unfavourable interactions between the solvent and the solvophobic block. The morphology of diblock copolymer nano-objects depends on the relative volume fractions of solvophilic and solvophobic blocks and can be rationalised in terms of the fractional packing parameter.⁹⁻¹¹ For a fixed diblock composition, the nano-object dimensions depend on the overall copolymer molecular weight.¹²

Amphiphilic statistical copolymers comprise hydrophilic and hydrophobic monomers that are distributed throughout each copolymer chain rather than spatially segregated. In principle, such copolymers are readily synthesised without recourse to the controlled/living polymerisation techniques that are required for diblock copolymers. Indeed, they are routinely prepared on an industrial scale (i.e. millions of tonnes per annum) using conventional free radical copolymerisation. Amphiphilic statistical copolymers are known to self-assemble to form a range of copolymer morphologies, including spheres,¹³⁻¹⁵ rods/worms¹⁶⁻¹⁸ and vesicles^{15,19}.

Furthermore, Liu *et al.* reported that statistical copolymers comprising styrene and acrylic acid could form a more complex bowl-like morphology in aqueous solution.²⁰ Zhu and Liu demonstrated that statistical copolymers of *N*-acryloyl-L-glutamic acid and *N*-dodecyl acrylamide could self-assemble to form either spheres or vesicles depending on the choice of solvent.²¹ Distribution of the solvophobic groups along the copolymer backbone also allows microphase separation on shorter length scales (< 10 nm) than that typically achieved for block copolymers. Moreover, both composition and solvophobe type can affect the domain size, thus providing an opportunity to expand functionality of the formed particles.^{22–24} Recently, Imai *et al.* demonstrated that amphiphilic statistical copolymers composed of poly(ethylene glycol) methacrylate with either *n*-butyl methacrylate or *n*-dodecyl methacrylate undergo self-sorting into defined copolymer assemblies in aqueous solution, where copolymers were sorted on the basis of both copolymer composition and choice of hydrophobic comonomer.²⁵ Matsumoto *et al.* found that block copolymers consisting of two different statistical blocks with a shared hydrophilic monomer (poly(ethylene glycol) methacrylate) self-sort to yield nano-objects with distinct compartments.²⁴

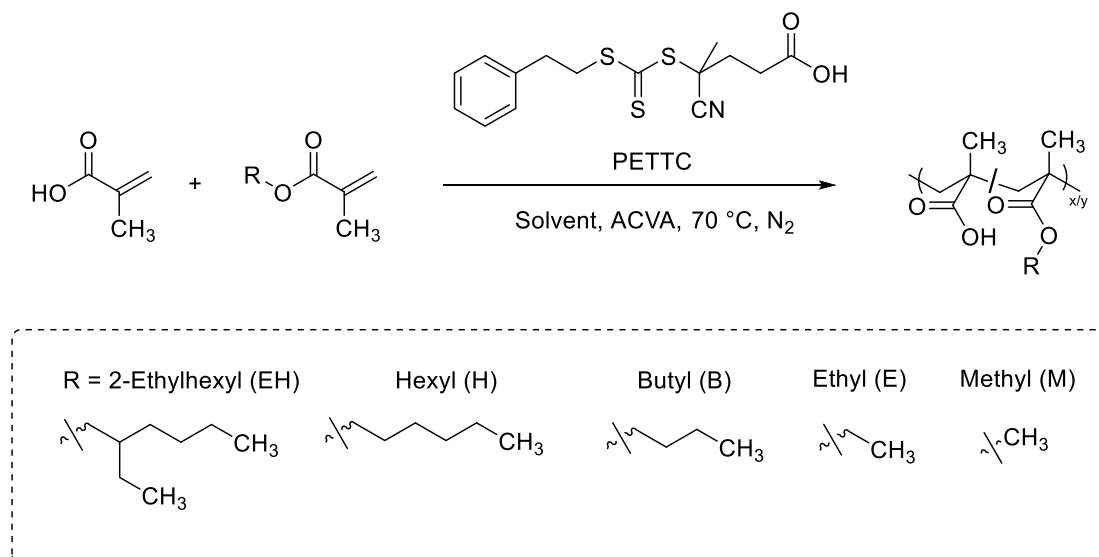
Despite these advances, the rationalisation and understanding of nano-object size and morphology has been limited. In chapter 3 it was reported that the size of self-assembled nanoparticles formed by amphiphilic poly(methacrylic acid-*stat*-butyl methacrylate) P(MAA-*stat*-BMA) depended on the copolymer composition but was independent of the copolymer molecular weight.²⁶ A structural model was developed to rationalise the observed particle size based on the anionic surface charge density arising from the ionised MAA repeat units. Herein, this model is verified for a series of statistical MAA copolymers comprising various other hydrophobic alkyl methacrylate comonomers. Importantly, we demonstrate that (i) the particle size can be correlated with the partition coefficient ($\log P$) of the hydrophobic monomer and (ii) this model can be used to predict the particle size for a given comonomer and composition.

4.2 Results and discussion

4.2.1 Synthesis of amphiphilic statistical copolymers by RAFT solution polymerisation

A series of amphiphilic methacrylate-based statistical copolymers was synthesised where both the hydrophobic component and the overall copolymer composition were systematically varied. The hydrophobic component was adjusted using a range of alkyl methacrylate comonomers (AMA), where A corresponds to 2-ethylhexyl (EH), *n*-hexyl (H), *n*-butyl (B), ethyl (E), or methyl (M).

P(AMA_x-*stat*-MAA_y) copolymers, where x and y are the mol% of AMA and MAA units in the comonomer feed, respectively, were synthesised *via* RAFT solution copolymerisation (Scheme 4.1) targeting a consistent molecular weight (*ca.* 30 kDa) but differing copolymer compositions. IPA was used as the solvent for EHMA, HMA, EMA, and MMA copolymer syntheses because kinetic studies of such batch copolymerisations conducted at 50% w/w suggested that the instantaneous rate of consumption of each comonomer was comparable to that of MAA throughout the course of the reaction (Appendix 6). Thus, an approximately statistical distribution of the hydrophobic and hydrophilic comonomers within each copolymer chain can be assumed and the final copolymer composition is close to that targeted. Recently, we reported that copolymerisation of BMA and MAA in IPA 20% w/w produces somewhat ‘blocky’ copolymer chains with an undesirable BMA-rich terminus caused by a significant reduction in the rate of the acidic comonomer towards the end of the reaction.²⁶ To avoid this problem, IPA was replaced with 1,4-dioxane and the copolymerization was performed at 50% w/w; this strategy resulted in both comonomers being consumed at comparable rates throughout the copolymerization (Appendix 6).



Scheme 4.1. RAFT solution polymerization of MAA with either EHMA, HMA, BMA, EMA, or MMA to form P(EHMA_y-stat-MAA_x), P(HMA_y-stat-MAA_x), P(BMA_y-stat-MAA_x), P(EMA_y-stat-MAA_x) and P(MMA_y-stat-MAA_x), respectively. The copolymerization of MAA with either EHMA, HMA, EMA or MMA was performed in IPA at 50 wt%, whereas the copolymerization of BMA with MAA was performed in 1,4-dioxane at 50 wt%.

Three AMA:MAA copolymers (containing 20, 30 or 40 mol % MAA, respectively) were initially targeted for each comonomer pair to facilitate direct comparison. However, initial results indicated that each series formed stable colloidal dispersions at different acid contents according to the hydrophobic character of the alkyl methacrylate comonomer. Consequently, further copolymer compositions were targeted with the aim of forming stable colloidal dispersions. For example, initial results suggested that P(EHMA-*stat*-MAA) copolymers required higher acid contents to form stable colloidal dispersions compared to P(MMA-*stat*-MAA) because the EHMA comonomer is significantly more hydrophobic than MMA (Table 4.1).

Table 4.1. Analytical data for poly(alkyl methacrylate-*stat*-methacrylic acid) [P(AMA-*stat*-MAA)] copolymers.

AMA	Copolymer name	Composition (AMA:MAA) ^a		GPC ^b		
		Targeted	Actual	M_n / kDa	M_w / kDa	M_w/M_n
MMA	MM ₆₀₄₀	60:40	62:38	21.5	30.4	1.42
	MM ₇₀₃₀	70:30	71:29	28.0	39.8	1.42
	MM ₈₀₂₀	80:20	81:19	25.6	31.0	1.21
	MM ₈₈₁₂	88:12	88:12	27.3	32.8	1.19
	MM ₉₀₁₀	90:10	90:10	23.6	29.6	1.25
	MM ₉₅₀₅	95:05	95:05	23.1	28.7	1.24
	MM ₉₈₀₂	98:02	97:03	21.7	26.8	1.24
EMA	EM ₆₀₄₀	60:40	60:40	33.5	44.4	1.33
	EM ₇₀₃₀	70:30	70:30	33.0	42.8	1.30
	EM ₈₀₂₀	80:20	80:20	27.3	33.2	1.22
	EM ₈₁₁₉	81:19	81:19	30.7	38.3	1.25
	EM ₈₄₁₆	84:16	84:16	22.6	28.8	1.27
	EM ₈₆₁₄	86:14	86:14	24.1	30.1	1.25
	EM ₉₀₁₀	90:10	90:10	26.2	32.5	1.24
BMA	BM ₆₀₄₀	60:40	61:39	37.9	44.6	1.18
	BM ₇₀₃₀	70:30	71:29	36.4	45.4	1.25
	BM ₇₅₂₅	75:25	76:24	35.2	44.9	1.28
	BM ₈₀₂₀	80:20	80:20	39.0	48.8	1.25
	BM ₈₅₁₅	85:15	86:14	33.6	40.6	1.21
	BM ₉₀₁₀ ^c	90:10	90:10	27.1	30.1	1.11
HMA	HM ₅₀₅₀	50:50	49:51	28.6	34.4	1.20
	HM ₆₀₄₀	60:40	61:39	28.3	33.6	1.19
	HM ₇₀₃₀	70:30	68:32	31.1	37.2	1.19
	HM ₈₀₂₀	80:20	76:24	33.5	40.1	1.20
EHMA	EHM ₃₀₇₀	30:70	31:69	34.7	57.9	1.66
	EHM ₄₀₆₀	40:60	41:59	37.0	48.8	1.31
	EHM ₅₀₅₀	50:50	49:51	37.5	47.3	1.26
	EHM ₆₀₄₀	60:40	61:39	40.8	54.7	1.34
	EHM ₇₀₃₀	70:30	71:29	25.5	32.6	1.28
	EHM ₈₀₂₀ ^c	80:20	80:20	29.8	33.0	1.11

^a Copolymer composition data obtained from ¹H NMR analysis of either methylated copolymers [P(AMA-*stat*-MMA)] or benzylated copolymers [P(AMA-*stat*-BzMA)]. ^b Copolymers analysed in THF containing 4.0% v/v acetic acid against a series of PMMA standards. ^c Did not form stable colloidal dispersions at pH 9.

Final copolymer compositions were determined by ^1H NMR spectroscopy after alkylation of the MAA residues. The resulting copolymers were dissolved in a suitable NMR solvent and their compositions were calculated by comparing the integrated methoxy or benzylic signals of the MMA or BzMA residues to a resonance from the AMA component. Both alkylation protocols were performed on a selected copolymer (BM₈₅₁₅, see Table 4.1 for the sample notation) and afforded essentially identical copolymer compositions within experimental error (Appendix 7). As suggested by the kinetic analysis, final copolymer compositions were always in good agreement with the initial comonomer feed ratios (Table 4.1).

A consistent molecular weight was targeted for each copolymer to minimise the number of variables for a given copolymer type and composition. Copolymers within each monomer series exhibited similar M_w values by GPC; however, some discrepancies between series were observed (Table 4.1). As such molecular weight data are expressed relative to PMMA calibration standards, discrepancies between the series are expected since each copolymer chain should occupy its own effective volume in the GPC eluent. Previous research indicates little or no correspondence between particle and copolymer molecular weight when the aggregation number is large, so minor inconsistencies between molecular weights are unlikely to adversely affect the particle size measurements within this regime.^{26,27} However, for relatively low aggregation numbers, when copolymer interactions are mainly intramolecular in nature, it is likely that the copolymer molecular weight will affect the particle size. In particular, this aspect should be taken into consideration when considering the formation of single-chain nanoparticles for which the aggregation number is unity.

4.2.2 Aggregation behaviour of amphiphilic P(AMA-*stat*-MAA) statistical copolymers

Aqueous copolymer dispersions were obtained using the same solvent-switch method outlined in chapter 2, where the copolymer was dissolved at 50% w/w in a good solvent (IPA) and then diluted slowly to a lower concentration using water in the presence of TEA (1.1 molar equivalents relative to the MAA residues). This organic base was added to the solution to deprotonate the MAA units, which confers anionic character. The addition of water drives *in situ* self-assembly of the strongly amphiphilic copolymer chains. The hydrophobic alkyl methacrylate repeat units aggregate to form nanoparticles that are stabilised by the anionic MAA groups, as confirmed by aqueous electrophoresis measurements (Appendix 8). Copolymer dispersions were diluted to 1.0% w/w to (i) minimize the volume fraction of the remaining water-miscible good solvent (IPA) and (ii) reduce the inter-particle interactions that are present at high copolymer concentrations.

SAXS was utilised to investigate the copolymer morphology of such colloidal dispersions. SAXS patterns recorded for 1.0% w/w dispersions indicate the formation of spherical particles (Figure 4.1 and Appendix 9), which is consistent with our transmission electron microscopy and SAXS studies of closely-related copolymer systems examined in chapter 3.²⁶ Initially, the scattering patterns (Figure 4.1 and Appendix 9) were fit with an intensity equation (eqs 2.1-2.5) that utilised the spherical form factor (eqs 2.9-2.12) and hence determine the mean nanoparticle radius, along with additional structural information (Table 4.2).

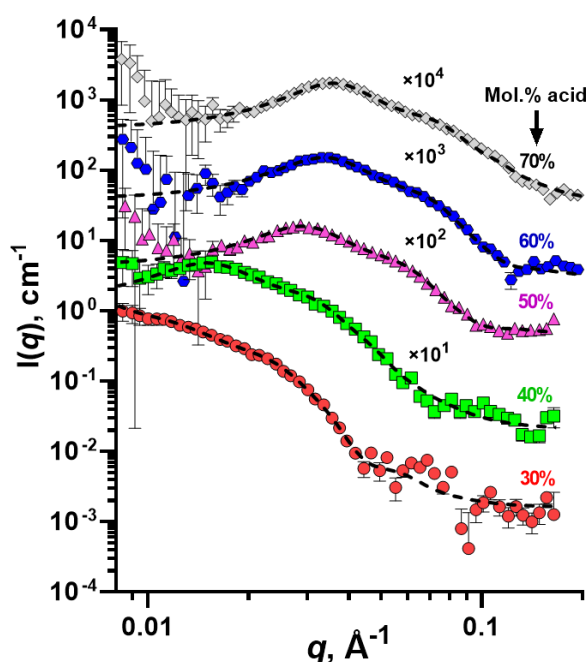


Figure 4.1. SAXS patterns recorded for 1.0% w/w aqueous dispersions of P(EHMA-*stat*-MAA) copolymer particles (symbols) fitted using a refined model for spherical particles (eqs 2.3 and 2.9-2.12) (dotted lines). The mean size of the particles formed by copolymers with differing MAA mole fractions (30%, 40%, 50%, 60% or 70%). A Bruker AXS Nanostar instrument was used for these measurements. Some patterns are shifted upwards by arbitrary numerical factors to aid clarity.

Despite the relatively low copolymer concentration used for these measurements, each SAXS scattering pattern exhibits a structure peak at low q , indicating long-range interactions between neighbouring particles (Figures 4.1 and Appendix 9). This phenomenon was observed in the investigation performed in chapter 3 and is well-known for charged copolymer nanoparticles in aqueous media, where the interaction distance is controlled by the copolymer concentration and the nanoparticle surface charge.^{26,28,29} Thus, an appropriate structure factor was incorporated into the intensity function (eqs 2.1, 2.3 or 2.4) in order to account for these long-range interparticle interactions. In chapter 3, Percus-Yevick^{30,31} and Hayter-Penfold³² approximations of the structure factor were evaluated when modelling the scattering patterns

obtained for such systems. These approaches gave different values for the parameters associated with interparticle interactions but had no discernible effect on form factor parameters such as the nanoparticle radius,²⁶ which is the key parameter for the current study. Thus, for the sake of simplicity, the Percus-Yevick approximation for the hard sphere structure factor (eq 2.6) was incorporated into the SAXS intensity equation (eqs 2.1, 2.3 or 2.4). This analysis indicates that larger nanoparticles are always formed as the acid content is reduced (Table 4.2) for all five series of copolymer compositions, regardless of the type of hydrophobic comonomer. This finding is consistent with the data obtained for similar systems in chapter 3.²⁶

A stabilisation limit is observed within the BMA and EHMA series whereby the BM₉₀₁₀ and the EHM₈₀₂₀ copolymers form macroscopic precipitates rather than colloidally stable nanoparticles (Table 4.2 and Appendix 10). Presumably, the acid content of these copolymers is insufficient to confer colloidal stabilisation. This demonstrates that nanoparticle formation is confined to a finite range of copolymer compositions.

Table 4.2. Structural characteristics of 1.0% w/w dispersions of P(AMA-*stat*-MAA) amphiphilic statistical copolymers (where AMA is either EHMA, HMA, BMA, EMA, or MMA) obtained from SAXS analysis: the mean particle radius (R) and its corresponding standard deviation (σ_R), the mean aggregation number (N_{agg}) as calculated using eq. 2.12, the particle aspect ratio (ε), the mean interparticle distance (R_{PY}) and the effective volume fraction (f_{PY}) corresponding to the structure factor based on the Percus-Yevick (PY) approximation.

Copolymer	R (Å)	Form factor			Structure factor	
		σ_R (Å)	N_{agg}	ε	R_{PY} (Å)	f_{PY}
MM ₆₀₄₀	19	12	<1 ^a	0.27	56	0.17
MM ₇₀₃₀	20	12	<1 ^a	0.30	62	0.16
MM ₈₀₂₀	17	10	1 ^b	-	78	0.17
MM ₈₈₁₂	22	15	1 ^b	-	99	0.13
MM ₉₀₁₀	30	20	3	-	126	0.13
MM ₉₅₀₅	45	19	10	-	152	0.13
MM ₉₈₀₂	89	19	75	-	271	0.08
EM ₆₀₄₀	23	11	<1 ^a	0.48	63	0.17
EM ₇₀₃₀	19	10	1 ^b	-	69	0.19
EM ₈₀₂₀	31	7	3	-	85	0.17
EM ₈₁₁₉	34	12	4	-	113	0.14
EM ₈₄₁₆	38	11	5	-	109	0.13
EM ₈₆₁₄	43	12	8	-	124	0.14
EM ₉₀₁₀	74	21	38	-	209	0.14
BM ₆₀₄₀	32	6	3	-	84	0.20
BM ₇₀₃₀	41	8	6	-	106	0.11
BM ₇₅₂₅	59	12	19	-	142	0.15
BM ₈₀₂₀	63	12	23	-	163	0.16
BM ₈₅₁₅	87	14	59	-	238	0.11
BM ₉₀₁₀ ^c	-	-	-	-	-	-
HM ₅₀₅₀	34	5	4	-	70	0.21
HM ₆₀₄₀	44	5	8	-	86	0.22
HM ₇₀₃₀	60	10	19	-	125	0.20
HM ₈₀₂₀	89	16	61	-	187	0.15
EHM ₃₀₇₀	27	12	2	-	81	0.21
EHM ₄₀₆₀	36	6	4	-	85	0.2
EHM ₅₀₅₀	43	7	7	-	99	0.2
EHM ₆₀₄₀	69	19	28	-	190	0.18
EHM ₇₀₃₀	98	16	79	-	253	0.13
EHM ₈₀₂₀ ^c	-	-	-	-	-	-

^a Fitted using a spheroid model for anisotropic particles with an aspect ratio different from unity, ^b Single-chain nanoparticles, ^c copolymer compositions did not form stable colloidal dispersions when diluted with water.

In the MMA and EMA copolymer series (the sample name abbreviation is MM and EM, respectively), SAXS analysis indicates that the mean aggregation number (N_{agg}) becomes unity under certain conditions (Table 4.2). This means that the copolymer chains no longer self-

assemble *via* intermolecular hydrophobic interactions but instead form single-chain nanoparticles (SCNP) or self-folded chains.^{33–37} The critical acid content at which SCNPs are formed depends on the type of alkyl methacrylate comonomer. For example, this corresponds to 20 mol% MAA for the MMA series, whereas the EMA series requires an acid content of 40 mol%. On the other hand, the BMA, HMA, and the EHMA series do not form SCNPs within the investigated compositional range (Table 4.2). One important assumption for the structural models (Figure 4.2 and eqs 2.9-13, 2.15-23) used in this study is that no solvent is present within the particle cores. The same assumption was made in chapter 3.²⁶ Thus, N_{agg} can be calculated by dividing the mean volume of a spherical particle by the volume occupied by a single copolymer chain (eq 2.12). Consequently, for an aggregation number of unity, the particle volume is simply equal to that of an individual copolymer chain.

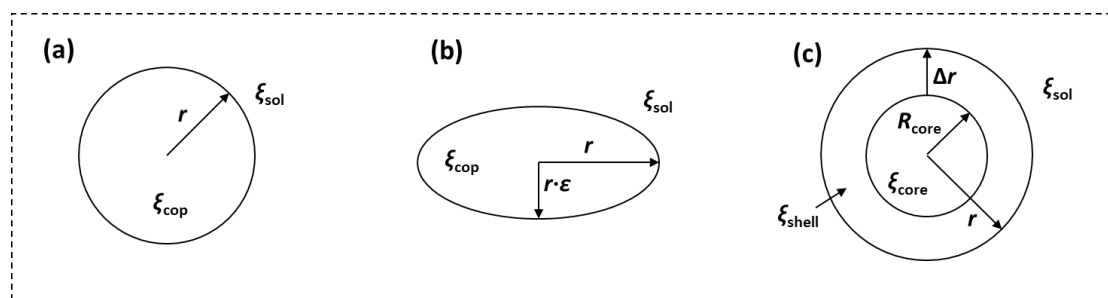


Figure 4.2. Schematic diagram illustrating the copolymer morphologies for the three structural models (eqs 2.9-13, 2.15-23): (a) the solid sphere model where r is the radius of the particle, ξ_{cop} is the scattering length density of the particle, and ξ_{sol} is the scattering length density of the solvent (eqs 2.9-12); (b) the spheroid model with an aspect ratio ϵ that is less than unity (eq 2.13); (c) the core-shell model, where r is the overall particle radius, Δr is the shell thickness, $R_{\text{core}} = r - \Delta r$ is the core radius, and ξ_{core} and ξ_{shell} are the scattering length densities of the core and the shell, respectively (eqs 2.15-2.23).

Above the critical acid content, SAXS analysis indicates that the sphericity of the SCNPs becomes less well-defined. In this case, satisfactory data fits to scattering patterns can only be obtained by using a spheroidal model (Figure 4.2b, eq. 2.13) that incorporates an aspect ratio

parameter for elongated particles (Appendix 11). In addition, an upturn in the X-ray scattering intensity at low q suggests the formation of large aggregates under such conditions. This is not unexpected: higher acid contents lead to increasingly hydrophilic copolymer chains that eventually become molecularly dissolved in aqueous media. This leads to a scattering pattern that is characteristic for Gaussian chains. Moreover, it is well-known that poly(methacrylic acid) forms either an extended structure in its highly ionised form or a relatively compact, globular structure in its neutral form.³⁸⁻⁴¹ This suggests that the more hydrophilic copolymers are likely to adopt a spheroidal structure. Furthermore, these MAA-rich copolymers are dispersed at around pH 9, hence their elongated structures indicated by SAXS are consistent with the behaviour expected for highly ionised poly(methacrylic acid).³⁸⁻⁴¹

These results have demonstrated that most of the amphiphilic copolymers self-assembled to form spherical particles when using the solvent switch method. The resulting aqueous copolymer dispersions were assessed using SAXS and the scattering patterns were modelled using a sphere model. This analysis indicated that the particle size is strongly dependent on both the copolymer composition and also the nature of the alkyl methacrylate comonomer. Copolymers with lower MAA contents only formed macroscopic precipitates, rather than colloidal dispersions. Furthermore, MAA-rich copolymers formed elongated structures similar to that expected for highly ionised poly(methacrylic acid); in such cases, a spheroid model containing an appropriate aspect ratio was utilised.

4.2.3 Determination of internal particle structure using contrast variation SANS

Since the hydrophobic and hydrophilic comonomers are statistically distributed along the copolymer chain, well-defined hydrophilic and hydrophobic domains within the particles were considered unlikely. Hence relatively good fits to the scattering patterns recorded for these amphiphilic copolymer particles can be obtained using either a spherical or a spheroid form factor (Figures 4.1 and Appendix 9). However, the anionic MAA residues should be preferentially located at the particle surface for colloidal stability. This hypothesis underpins the derivation of an analytical equation in chapter 3 describing the relationship between copolymer composition and particle size observed for aqueous dispersions of P(BMA-*stat*-MAA) particles.²⁶ Although the well-defined core-shell structure often associated with diblock copolymer nanoparticles is unlikely, there is nevertheless a thin MAA-rich “shell-like” region and a “core-like” region that mainly contains the hydrophobic alkyl methacrylate comonomer. However, appropriate structural studies are required to validate this assumption. Accordingly, contrast variation SANS was used to investigate the internal structure of the copolymer particles. Since H₂O and D₂O have differing neutron scattering length densities (SLDs) ($-0.56 \times 10^{10} \text{ cm}^{-2}$ and $6.33 \times 10^{10} \text{ cm}^{-2}$, respectively),^{42–49} H₂O/D₂O mixtures can be used to adjust the SLD of the aqueous milieu (ζ_{sol}) to highlight any hydrophilic and hydrophobic domains that may be present. Initially, a pair of 2% w/w dispersions of BM₈₀₂₀ were prepared in H₂O and D₂O, respectively. Two further copolymer dispersions were prepared in H₂O/D₂O mixtures with 83.5:16.5 and 40:60 volume compositions. These binary solvent mixtures have ζ_{sol} values of $0.58 \times 10^{10} \text{ cm}^{-2}$ and $3.58 \times 10^{10} \text{ cm}^{-2}$, respectively (eq 2.17). SANS patterns were recorded for all four dispersions (Figure 4.3). Following the same principles adopted for the SAXS data (Figure 4.1), each SANS pattern was analysed using the sphere model and reasonably good data fits were obtained in each case. However, if the MAA comonomer is preferentially located near the particle surface to produce a pseudo core-shell structure, then a spherical core-shell

model (Figure 4.2c, equations 2.15-23) should be more appropriate than a homogeneous sphere model (Figure 4.2a, eq. 2.9-12) for analysing such SANS patterns (Figure 4.3). Therefore, all patterns were fitted using the core-shell model (eq. 2.15-23). In order to account for the long-range interactions between these highly anionic particles, the Percus-Yevick approximation for the hard sphere structure factor (eq. 2.6) was included in the intensity equation (eq. 2.3). Since the copolymer composition was known (80:20 BMA:MAA) and the particle composition is identical to that of the copolymer, the SLDs for the core and shell were linked (eq. 2.23) so that a physically realistic distribution of the monomer units could be modelled. In other words, if the particle shell is MAA (or BMA)-rich, then the particle core must be MAA (or BMA)-depleted to the same extent and *vice versa*. Furthermore, the shell thickness was fixed at 4.95 Å, which corresponds to the approximate dimensions of a single MAA repeat unit. The shell thickness was constrained so that this parameter remained physically realistic, which ensured that the fitting remained stable. The average values for ζ_{core} and ζ_{shell} for all the individually-fitted patterns were $0.610 \times 10^{10} \text{ cm}^{-2}$ and $0.715 \times 10^{10} \text{ cm}^{-2}$, respectively. Since the core SLD is lower than that of the shell, this suggests that the MAA residues (which have a higher neutron SLD compared to the BMA residues) are preferentially located at (or near) the surface. Unfortunately, the parameters obtained from individual fits were spread over a relatively broad range and hence were not suitable for evaluating the core and shell composition.

Nevertheless, since each copolymer dispersion differs only in terms of its scattering contrast with respect to the aqueous continuous phase, their SANS patterns can be fitted simultaneously using certain global parameters for the contrast series such as particle size (and its associated standard deviation), shell thickness, and mean SLD for the particle core and shell components. In principle, this simultaneous SANS fitting approach should provide a much more statistically robust outcome compared to individually fitting each pattern (Appendix 12). Indeed, satisfactory fits were obtained for all four SANS scattering patterns (Figure 4.3). This allowed

the mean core radius and the SLDs for the particle core and particle shell (Figure 4.2c) to be determined ($R_{\text{core}} = 35\text{\AA}$, $\zeta_{\text{core}} = 0.625 \times 10^{10} \text{ cm}^{-2}$ and $\zeta_{\text{shell}} = 0.685 \times 10^{10} \text{ cm}^{-2}$, respectively).

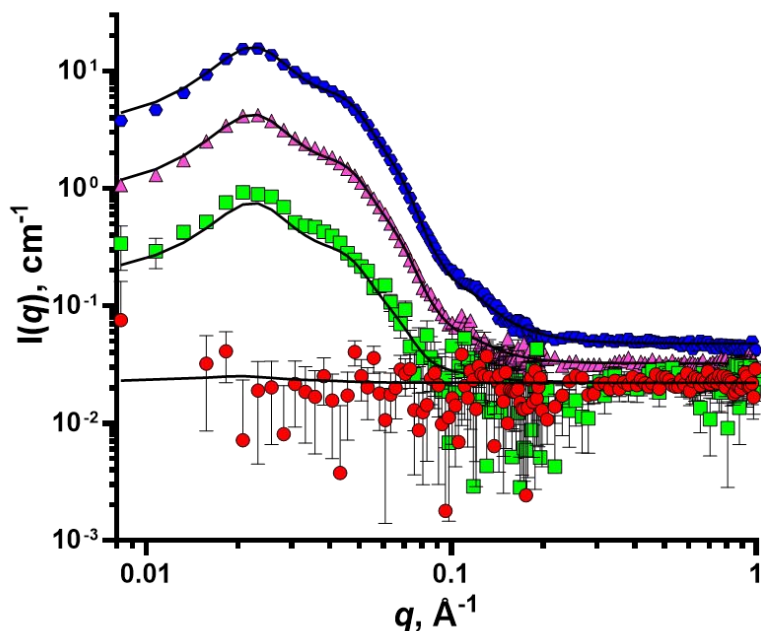


Figure 4.3. SANS patterns recorded for 2.0% w/w aqueous dispersions of BM₈₀₂₀ in four different H₂O/D₂O binary mixtures (symbols). For this contrast variation experiment, the solvent SLD corresponds to $-0.56 \times 10^{10} \text{ cm}^{-2}$ (H₂O; squares), $0.58 \times 10^{10} \text{ cm}^{-2}$ (83.5:16.5 H₂O/D₂O; circles), $3.58 \times 10^{10} \text{ cm}^{-2}$ (40:60 H₂O/D₂O; triangles) and $6.33 \times 10^{10} \text{ cm}^{-2}$ (D₂O; hexagons). All four data sets were fitted simultaneously to a spherical core-shell particle model using five fixed global parameters (eqs 2.15-23) (solid lines).

According to this data analysis, the particle core has a significantly lower neutron SLD than the shell ($\zeta_{\text{core}} = 0.625 \times 10^{10} \text{ cm}^{-2} < \zeta_{\text{shell}} = 0.685 \times 10^{10} \text{ cm}^{-2}$). Moreover, by comparing these values with the ζ_{BMA} and ζ_{MAA} ($0.55 \times 10^{10} \text{ cm}^{-2}$ and $1.38 \times 10^{10} \text{ cm}^{-2}$, respectively), calculated using respective mass densities of BMA and MAA ($\rho_{\text{BMA}} = 1.05 \text{ g cm}^{-3}$ and $\rho_{\text{MAA}} = 1.25 \text{ g cm}^{-3}$) it can be concluded that approximately half of the MAA residues lie within the particle core while the remainder are located within the shell. Thus, when simultaneously fitted using the spherical core-shell model, the contrast variation SANS data confirms that the particle surface is enriched with anionic MAA residues, thus creating core and shell components with differing SLDs. However, the copolymer chains are somewhat constrained in terms of their mobility

owing to the statistical distribution of MAA and BMA residues. Thus, up to 50% of the MAA residues remain trapped within the particle cores.

4.2.4 Relationship between nanoparticle size and copolymer composition

SAXS analysis has indicated that the particle size is strongly dependent on the MAA content of these amphiphilic statistical copolymers (Table 4.2). This finding is consistent with our earlier observations. Given that the copolymer molecular weight has minimal influence on the particle size, a model describing the relationship between the particle radius and the MAA mole fraction within the copolymer was developed (chapter 3) in order to estimate (or predict) the surface coverage by the anionic MAA units (PSC model).²⁶ It was assumed that a certain minimum number of ionised surface MAA groups is required for colloidal stability. This critical surface charge density can be expressed in terms of a fractional surface coverage ($SA_{\text{frac.MAA}}$). This PSC model assumes (i) perfectly spherical particles, (ii) a constant surface charge density across a copolymer series regardless of the copolymer composition, and (iii) that all of the MAA groups are located at the particle surface. However, the latter assumption is not consistent with the contrast variation SANS experiments reported herein (Figure 4.3), which suggest that only approximately 50% of the MAA groups are located at the particle surface, with the remainder lying within the BMA-rich cores.

Since the particle radius is known, the particle surface area can be calculated. Moreover, if $SA_{\text{frac.MAA}}$ is independent of the particle size, then the mean number of MAA groups present in a single particle can be estimated using:

$$N_{\text{MAA,p}} = \frac{1}{k} \times \frac{4\pi R_s^2 \times SA_{\text{frac.MAA}}}{CS_{\text{MAA}}} \quad (4.1)$$

where CS_{MAA} is the cross-sectional area of a single MAA repeat unit calculated from the approximate volume of a single MAA unit ($CS_{MAA} = V_{MAA}^{2/3} \approx 24.5 \text{ \AA}^2$, where $V_{MAA} = 121 \text{ \AA}^3$) and k is the fraction of the MAA groups located at the particle surface (with contrast variation SANS experiments suggesting that $k \sim 0.50$).

The mean number of hydrophobic alkyl methacrylate repeat units can be obtained from the volume of the hydrophobic domain within a particle, which is equal to the difference between the overall particle volume and the volume occupied by the MAA repeat units in the same particle, divided by the approximate volume of a single hydrophobic (AMA) unit (V_{AMA}):

$$N_{AMA,p} = \frac{\frac{4}{3}\pi R_s^3 - \left(\frac{1}{k} \times \frac{4\pi R_s^2 \times SA_{frac,MAA} \times V_{MAA}}{CS_{MAA}}\right)}{V_{AMA}} \quad (4.2)$$

Using both $N_{MAA,p}$ and $N_{AMA,p}$ the mole fraction of MAA groups in a particle can be calculated:

$$Mol.frac_{MAA} = \frac{N_{MAA,p}}{N_{MAA,p} + N_{AMA,p}} \quad (4.3)$$

This parameter is equivalent to the MAA mole fraction in the copolymer. If their MAA content is sufficiently high, the amphiphilic copolymer chains undergo intramolecular interactions to form SCNPs or self-folded chains. At this point, the particle size is simply equal to the volume of a single copolymer chain. Hence the corresponding copolymer compositions do not fit the structural model (equations 4.1-3) because it is assumed that the particle size is independent of chain length. It follows that the data points corresponding to SCNPs should be excluded from further analysis using this model.

Bearing in mind this important caveat, the proposed PSC model was used to fit the experimental particle size data for each copolymer series (Table 4.2) and the mean surface area occupied per MAA group was predicted (Figure 4.4). The model provides a satisfactory fit to

all the experimental data, with larger particles being formed by copolymers with lower acid contents. Given the contrast variation SANS results (Figure 4.3), such good agreement between the experimental data and the model fit for the five copolymer series (Figure 4.4) validates our assumption that the ionised MAA groups located preferentially at the particle surface in order to confer a sufficiently high surface charge density and ensure good long-term colloidal stability in aqueous media.

For the copolymer series with differing hydrophobic AMA units (Figure 4.4), incorporating a more hydrophobic comonomer produces larger particles even for comparable MAA contents. This is a direct result of the difference in critical surface charge density required for colloidal stability. For example, the PSC model fits indicate that the EHM copolymer series requires 42% surface coverage for the MAA units, whereas only 9% surface coverage is required for the MM copolymers (Figure 4.4). These observations are consistent with the more hydrophobic character of EHMA compared to MMA. In order to achieve a higher surface charge density for the same mole fraction of MAA units, more copolymer chains must undergo self-assembly to reduce the particle surface-to-volume ratio and hence increase the number of surface-confined MAA units. This leads to a larger overall copolymer volume and hence a corresponding increase in the mean particle radius (Figure 4.4, compare particle radii observed for copolymers with the same MAA content).

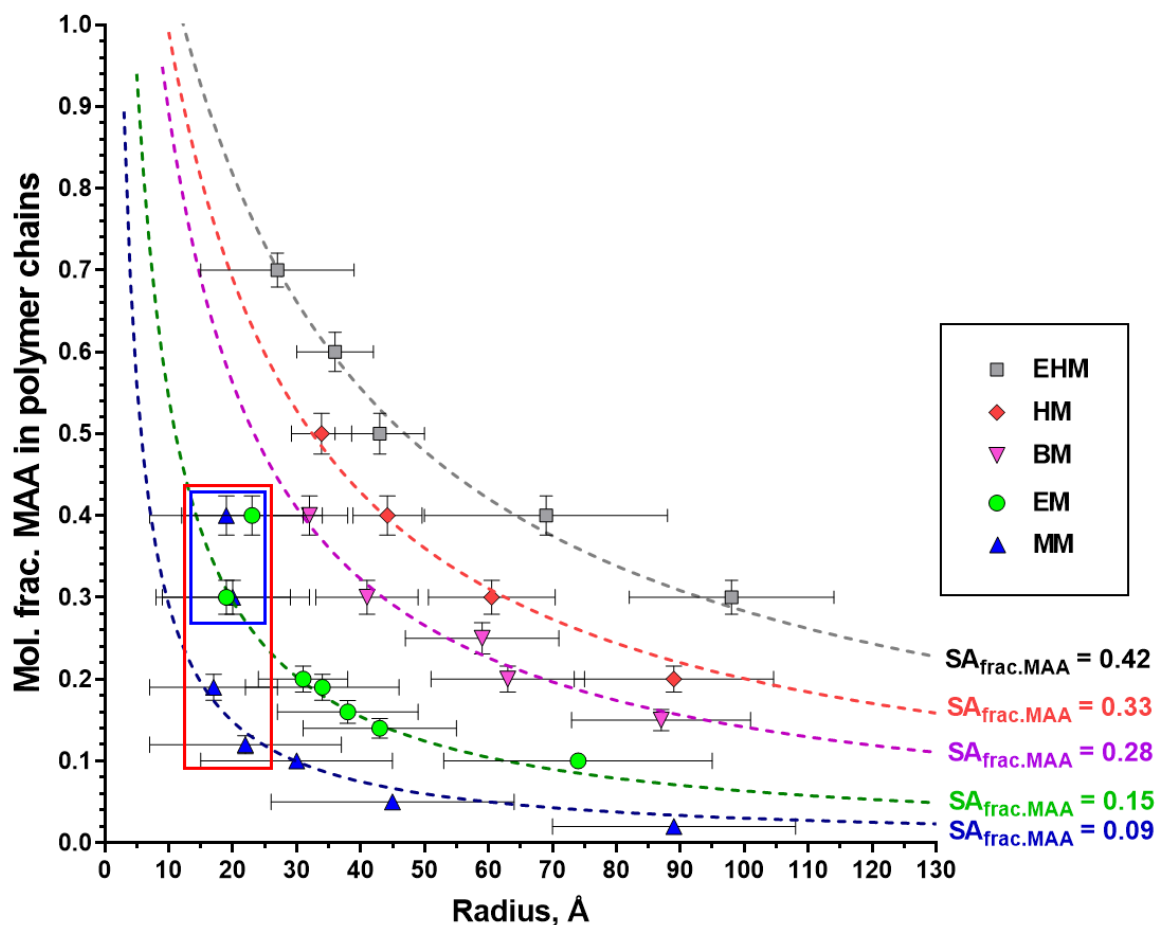


Figure 4.4. Relationship between the mole fraction of MAA units in the amphiphilic statistical copolymer chains and the corresponding mean particle radius formed by copolymer self-assembly in aqueous solution: comparison of the experimental data (symbols) with the theoretical curves (dashed lines) calculated using the PSC model (equations 4.1-3). Data points located within the red box are excluded from the latter model because such particles have an N_{agg} of unity and hence correspond to single-chain nanoparticles. Moreover, data points within the blue box correspond to ill-defined, elongated particles (for which the particle aspect ratio, ε , is less than unity). The horizontal bars indicate standard deviations for the mean particle radius, rather than experimental error. The MAA fractional surface coverage ($SA_{\text{frac.MAA}}$) calculated using the PSC model is given for each curve.

Although the PSC model provides good fits to the experimental data, it would be more practical to relate the model parameters to the hydrophobic character of the alkyl methacrylate comonomer. The partition coefficient ($\log P$) is commonly used to assess hydrophobicity and

is defined as the concentration distribution of a compound between two immiscible solvents, typically water and *n*-octanol.⁵⁰⁻⁵³ Previously, $\log P$ values have been used to quantify the hydrophobicity of methacrylic ester units within the copolymer particles.⁵⁰⁻⁵³ Recently, this parameter has also been used to predict suitable monomers for polymerisation-induced self-assembly (PISA) in aqueous media.⁵³ The $\log P$ of the hydrophobic monomer and the $SA_{\text{frac.MAA}}$ (assuming that 50% of MAA units are located at the particle surface, *i.e.*, $k = 0.50$), as determined from the PSC model fitting (Figure 4.4), are plotted in Figure 4.5. This linear relationship ($SA_{\text{frac.MAA}} = 0.1035(\log P) - 0.0454$; $R^2 = 0.99$) can be used to predict the self-assembly behaviour of other statistical methacrylic copolymers by predicting the $SA_{\text{frac.MAA}}$ based on the $\log P$ of the hydrophobic component and then determining the particle size using the PSC model (equations 4.1-3).

Although all the copolymer data are presented together for convenience, the P(HMA-*stat*-MAA) series (assigned as HM) were actually synthesised at a later stage in order to test the predictive power of the PSC model using linear regression for the $SA_{\text{frac.MAA}}$ vs. $\log P$ plot (Appendix 13). The new experimental data set is in good agreement with the expected particle size trend, providing further justification for the relationship between copolymer composition, hydrophobicity and particle size elucidated herein for the self-assembly of amphiphilic statistical copolymer chains in aqueous media.

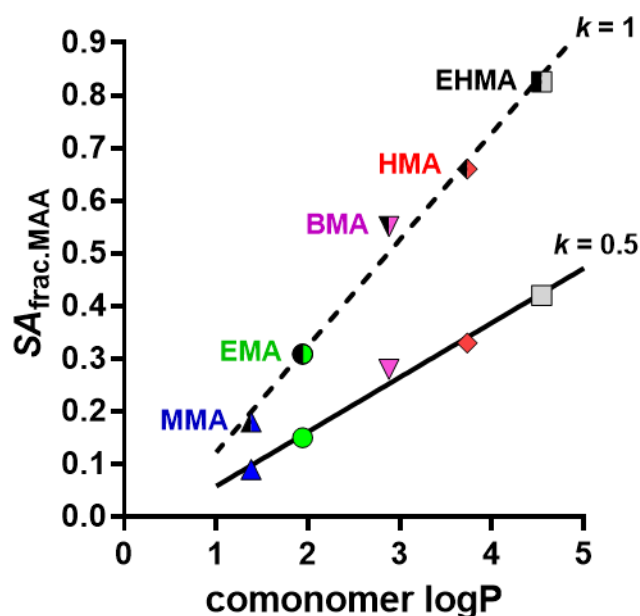


Figure 4.5. Linear relationship between the $\log P$ values obtained for five hydrophobic alkyl methacrylate and the $SA_{\text{frac.MAA}}$ evaluated by PSC model fitting (Figure 4.4). The half-closed symbols correspond to the previously assumed scenario²⁶ in which the MAA units are exclusively located at the particle surface ($k = 1.00$) while the open symbols correspond to the more physically realistic situation indicated by the contrast variation SANS experiments ($k = 0.5$). These two data sets have been fitted using $SA_{\text{frac.MAA}} = 0.2021(\log P) - 0.0781$ (dashed line) and $SA_{\text{frac.MAA}} = 0.1035(\log P) - 0.0454$ (solid line) linear regressions, respectively.

The previously assumed scenario in which all of the MAA groups are located at the particle surface ($k = 1.00$) is also plotted against the $\log P$ values for the five hydrophobic comonomers (Figure 4.5). These data are fitted by linear regression to afford the equation $SA_{\text{frac.MAA}} = 0.2021(\log P) - 0.0781$ which can be used as a predictive tool. The difference between the two data sets is that the $SA_{\text{frac.MAA}}$ values are arbitrary when $k = 1.00$, but these values become absolute when $k = 0.50$.

4.3 Conclusions

A series of five alkyl methacrylate comonomers (MMA, EMA, BMA, HMA and EHMA) were copolymerised in turn with MAA *via* RAFT solution copolymerisation to generate a library of amphiphilic statistical copolymers with varying levels of acid content and tunable hydrophobic character. Kinetic analysis confirmed that the EHMA, HMA, EMA, and MMA react at a similar rate to MAA when copolymerisations are performed at 50% w/w concentration in IPA. This suggests that an approximately statistical distribution of each comonomer within the copolymer chains can be achieved using a one-shot batch synthesis. However, the statistical copolymerisation of BMA with MAA was performed at 50% w/w in dioxane. This is because prior observations²⁶ indicated differing rates of copolymerisation for these two comonomers in IPA, which leads to their non-uniform distribution within the copolymer chains. A solvent-switch technique was used to form aqueous dispersions of self-assembled copolymer nanoparticles, whereby each copolymer was first molecularly dissolved in IPA and then slowly diluted using an alkaline aqueous solution. The resulting dispersions were analysed by SAXS and the particle size was strongly dependent on both the copolymer composition and the acid content. Furthermore, if the copolymer chains have a sufficiently high acid content, self-folding occurs to form a single-chain nanoparticle *via* intramolecular hydrophobic interactions. Contrast variation SANS was used to investigate the internal structure of selected particles to determine the location of the hydrophobic and hydrophilic comonomers. It was found that BMA-rich particles studied are more likely to possess a core-shell morphology. As expected, the anionic MAA residues are preferentially located at the particle surface. However, owing to their statistical distribution along the copolymer chains, approximately 50% of the MAA repeat units remain trapped within the particle cores. SANS analysis enables a previously proposed structural model (PSC model), which uses surface charge density to correlate copolymer

composition with particle size, to be extended and placed on an absolute scale. This model is remarkably consistent with the experimental SAXS data obtained for all five series of copolymers and enables the reliable prediction of particle size for a given copolymer composition. Furthermore, by fitting the SAXS data to the structural model, the surface area per MAA unit can be calculated. Using this approach, it was determined that the EHMA-MAA copolymer particles required an $SA_{\text{frac.MAA}}$ of 0.42 to stabilise the assembly, whereas the MMA-MAA copolymer particles only required an $SA_{\text{frac.MAA}}$ of 0.09. This analysis indicates a strong correlation between the chemical structure of the hydrophobic comonomer and the surface charge density required to stabilise the copolymer particles. More specifically, there is a linear relationship between the $SA_{\text{frac.MAA}}$ calculated using the structural model and the $\log P$ value for the hydrophobic copolymer unit $SA_{\text{frac.MAA}} = 0.1035(\log P) - 0.0454$. Therefore, the particle size of similar methacrylate copolymer aggregates can be predicted using the same approach. Moreover, the PSC model is relatively insensitive to differences in copolymer structure and hence significantly extends our understanding of the self-assembly behaviour of statistical copolymers in aqueous solution. Importantly, particle size can be predicted using the relationship between $\log P$ and $SA_{\text{frac.MAA}}$, thus making such amphiphilic statistical copolymers an attractive alternative to diblock copolymer nanoparticles for a range of industrial applications.

4.4 References

- 1 H. Duan, M. Donovan, A. Foucher, X. Schultze and S. Lecommandoux, *Sci. Rep.*, 2018, **8**, 1–9.
- 2 D. Kai, Y. K. Chua, L. Jiang, C. Owh, S. Y. Chan and X. J. Loh, *RSC Adv.*, 2016, **6**, 86420–86427.

- 3 S. Hartmann, L. Nuhn, B. Palitzsch, M. Glaffig, N. Stergiou, B. Gerlitzki, E. Schmitt, H. Kunz and R. Zentel, *Adv. Healthc. Mater.*, 2015, **4**, 522–527.
- 4 L. Peng, Z. Fang, J. Li, L. Wang, A. M. Bruck, Y. Zhu, Y. Zhang, K. J. Takeuchi, A. C. Marschilok, E. A. Stach, E. S. Takeuchi and G. Yu, *ACS Nano*, 2018, **12**, 820–828.
- 5 Z. Lin, H. Tian, F. Xu, X. Yang, Y. Mai and X. Feng, *Polym. Chem.*, 2016, **7**, 2092–2098.
- 6 J. R. C. Costa, C. Correia, J. R. Góis, S. M. C. Silva, F. E. Antunes, J. Moniz, A. C. Serra and J. F. J. Coelho, *Prog. Org. Coatings*, 2017, **104**, 34–42.
- 7 I. Martín-Fabiani, A. Fortini, J. Lesage De La Haye, M. L. Koh, S. E. Taylor, E. Bourgeat-Lami, M. Lansalot, F. D’Agosto, R. P. Sear and J. L. Keddie, *ACS Appl. Mater. Interfaces*, 2016, **8**, 34755–34761.
- 8 J. E. Mates, R. Ibrahim, A. Vera, S. Guggenheim, J. Qin, D. Calewatts, D. E. Waldroup and C. M. Megaridis, *Green Chem.*, 2016, **18**, 2185–2192.
- 9 A. Blanz, S. P. Armes and A. J. Ryan, *Macromol. Rapid Commun.*, 2009, **30**, 267–277.
- 10 A. H. Gröschel and A. Walther, *Angew. Chemie Int. Ed.*, 2017, **56**, 10992–10994.
- 11 Y. Zhang, Z. Wang, K. Matyjaszewski and J. Pietrasik, *Macromol. Rapid Commun.*, 2019, **40**, 1–6.
- 12 J. Rieger, *Macromol. Rapid Commun.*, 2015, **36**, 1458–1471.
- 13 X. Wu, Y. Qiao, H. Yang and J. Wang, *J. Colloid Interface Sci.*, 2010, **349**, 560–564.
- 14 T. Kawata, A. Hashidzume and T. Sato, *Macromolecules*, 2007, **40**, 1174–1180.

- 15 X. Zhu and M. Liu, *Langmuir*, 2011, **27**, 12844–12850.
- 16 F. Tian, Y. Yu, C. Wang and S. Yang, *Macromolecules*.
- 17 G. Sun, M. Zhang and P. Ni, 2009, **47**, 4670–4684.
- 18 T. Stephan, S. Muth and M. Schmidt, *Macromolecules*, 2002, **35**, 9857–9860.
- 19 F. Ilhan, T. H. Galow, M. Gray, G. Clavier and V. M. Rotello, *J. Am. Chem. Soc.*, 2000, **122**, 5895–5896.
- 20 X. Liu, J.-S. Kim, J. Wu and A. Eisenberg, *Macromolecules*, 2005, **38**, 6749–6751.
- 21 J. Wang and J. Zhu, *Eur. Polym. J.*, 2013, **49**, 3420–3433.
- 22 G. Hattori, M. Takenaka, M. Sawamoto and T. Terashima, *J. Am. Chem. Soc.*, 2018, **140**, 8376–8379.
- 23 M. Matsumoto, M. Sawamoto and T. Terashima, *ACS Macro Lett.*, 2019, **8**, 320–325.
- 24 M. Matsumoto, T. Terashima, K. Matsumoto, M. Takenaka and M. Sawamoto, *J. Am. Chem. Soc.*, 2017, **139**, 7164–7167.
- 25 S. Imai, Y. Hirai, C. Nagao, M. Sawamoto and T. Terashima, *Macromolecules*, 2018, **51**, 398–409.
- 26 T. J. Neal, D. L. Beattie, S. J. Byard, G. N. Smith, M. W. Murray, N. S. J. Williams, S. N. Emmett, S. P. Armes, S. G. Spain and O. O. Mykhaylyk, *Macromolecules*, 2018, **51**, 1474–1487.
- 27 A. Hashidzume, A. Kawaguchi, A. Tagawa, K. Hyoda and T. Sato, *Macromolecules*, 2006, **39**, 1135–1143.
- 28 M. Rawiso, J.-G. Zilliox, B. Demé, F. Boué, J. Combet and M. Heinrich, *Polymers*

- (Basel)., 2016, **8**, 228.
- 29 J. C. Pegg, A. Czajka, C. Hill, C. James, J. Peach, S. E. Rogers and J. Eastoe, *Langmuir*, 2017, **33**, 2628–2638.
- 30 J. S. Pedersen and M. C. Gerstenberg, *Macromolecules*, 1996, **29**, 1363–1365.
- 31 J. K. Percus and G. J. Yevick, *Phys. Rev.*, 1958, **110**, 1–13.
- 32 J. B. Hayter and J. Penfold, *Mol. Phys.*, 1981, **42**, 109–118.
- 33 M. Ouchi, N. Badi, J.-F. Lutz and M. Sawamoto, *Nat. Chem.*, 2011, **3**, 917–924.
- 34 O. Altintas and C. Barner-Kowollik, *Macromol. Rapid Commun.*, 2016, **37**, 29–46.
- 35 A. M. Hanlon, C. K. Lyon and E. B. Berda, *Macromolecules*, 2016, **49**, 2–14.
- 36 C. K. Lyon, A. Prasher, A. M. Hanlon, B. T. Tuten, C. A. Tooley, P. G. Frank and E. B. Berda, *Polym. Chem.*, 2015, **6**, 181–197.
- 37 M. Artar, E. Huerta, E. W. Meijer and A. R. A. Palmans, 2014, pp. 313–325.
- 38 L. Ruiz-Pérez, A. Pryke, M. Sommer, G. Battaglia, I. Soutar, L. Swanson and M. Geoghegan, *Macromolecules*, 2008, **41**, 2203–2211.
- 39 Y. Muroga, T. Yoshida and S. Kawaguchi, *Biophys. Chem.*, 1999, **81**, 45–57.
- 40 C. Heitz, M. Rawiso and J. François, *Polymer (Guildf.)*, 1999, **40**, 1637–1650.
- 41 J. Pleštil, Y. M. Ostanevich, V. Y. Bezzabotnov and D. Hlavatá, *Polymer (Guildf.)*, 1986, **27**, 1241–1246.
- 42 S. K. Filippov, B. Verbraeken, P. V. Konarev, D. I. Svergun, B. Angelov, N. S. Vishnevetskaya, C. M. Papadakis, S. Rogers, A. Radulescu, T. Courtin, J. C. Martins,

- L. Starovoytova, M. Hruby, P. Stepanek, V. S. Kravchenko, I. I. Potemkin and R. Hoogenboom, *J. Phys. Chem. Lett.*, 2017, **8**, 3800–3804.
- 43 J. Kříž, P. Kadlec, Z. Tuzar, V. I. Gordeliy, H. Pospíšil and J. Pleštil, *Polymer (Guildf)*., 2002, **42**, 2941–2946.
- 44 J. H. E. Hone, T. Cosgrove, M. Saphiannikova, T. M. Obey, J. C. Marshall and T. L. Crowley, *Langmuir*, 2002, **18**, 855–864.
- 45 I. Estrela-Lopis, S. Leporatti, S. Moya, A. Brandt, E. Donath and H. Möhwald, *Langmuir*, 2002, **18**, 7861–7866.
- 46 J. Eastoe, P. Brown, G. N. Smith, D. A. J. Gillespie, C. James, S. E. Rogers, R. Kemp, S. Alexander, R. K. Heenan and I. Grillo, *Langmuir*, 2014, **30**, 3422–3431.
- 47 E. W. Kaler, N. J. Wagner, F. Nettesheim, M. W. Liberatore, M. Vethamuthu and T. K. Hodgdon, *Langmuir*, 2008, **24**, 7718–7726.
- 48 K. Haraguchi, S. Okabe, T. Takehisa, S. Miyazaki, T. Karino and M. Shibayama, *Macromolecules*, 2005, **38**, 10772–10781.
- 49 K. Nusser, S. Neueder, G. J. Schneider, M. Meyer, W. Pyckhout-Hintzen, L. Willner, A. Radulescu and D. Richter, *Macromolecules*, 2010, **43**, 9837–9847.
- 50 K. Klein, J. Simon, T. Wolf, V. Mailänder, F. R. Wurm and K. Landfester, *Angew. Chemie Int. Ed.*, 2018, **57**, 5548–5553.
- 51 E. Yildirim, D. Dakshinamoorthy, M. J. Peretic, M. A. Pasquinelli and R. T. Mathers, *Macromolecules*, 2016, **49**, 7868–7876.
- 52 J. A. Richards, D. A. Savin, A. J. D. Magenau, R. T. Mathers and M. A. Pasquinelli, *Macromolecules*, 2015, **48**, 7230–7236.

- 53 J. C. Foster, S. Varlas, B. Couturaud, J. R. Jones, R. Keogh, R. T. Mathers and R. K. O'Reilly, *Angew. Chemie - Int. Ed.*, 2018, **57**, 15733–15737.

*Chapter 5. The effect of molecular structure on
the self-assembly of amphiphilic BMA-MAA
copolymers*

Chapter 5.

The effect of molecular structure on the self-assembly of amphiphilic BMA-MAA copolymers

5.1 Introduction

An amphiphile is a chemical compound that possesses both hydrophobic and hydrophilic functionality, therefore an amphiphilic copolymer is a copolymer which is made-up of both hydrophilic and hydrophobic monomer units arranged along the polymer backbone. This functionality makes these copolymers very useful in a variety of applications (industrial and scientific) such as in drug delivery,¹⁻³ cosmetics,⁴ and coatings.⁵⁻⁷ The unique properties and usefulness of amphiphilic copolymers make them an interesting and quickly developing area of research.

Amphiphilic copolymers self-assemble in aqueous media through the minimisation of energetically unfavourable interactions between the hydrophobic component and water – the attractive forces within the hydrophobic moieties leads to aggregation of the copolymers and the repulsive forces between the hydrophilic components prevents unlimited growth of the aggregate. Various factors can influence how amphiphilic copolymers self-assemble, such as hydrophobicity, molecular weight, electrostatics, and sterics. However, in this chapter the

effect of copolymer architecture will be investigated and how the distribution of the hydrophilic monomer units within a polymer chain affects the structure of the particles it forms.

It is important to investigate how a diverse range of properties and nano-morphologies can be obtained by polymerising the same reagents in a variety of ways since the polymer industry is largely restricted to inexpensive and industrially-viable monomers. Monomer distribution can be simplified to three different copolymer architectures; these are statistical, where the monomer units are distributed sequentially obeying statistical laws; gradient, where the copolymer backbone exhibits a gradual change from one monomer to the other; and finally block copolymers, where the monomers are grouped together in blocks.

Statistical copolymers have been known to form nano-particles for a number of years,⁸⁻¹² however, recent work by Sawamoto and co-workers¹³⁻¹⁷ and Neal *et al.*¹⁸ has rejuvenated this scientific area. Hattori *et al.* demonstrated how amphiphilic statistical copolymers of poly(ethylene glycol) acrylate and octadecyl acrylate could self-assemble in water to form thermoresponsive spherical micelles and vesicles.¹⁴ The nano-morphology formed was directly related to the ratio of hydrophobe to hydrophile along the backbone, where larger fractions of the hydrophobic component would produce a higher order morphology. More recently Matsumoto *et al.* have shown how complex compartmentalised assemblies can be formed by multi-block statistical copolymers.¹⁵ These compartmentalised systems are seen as a mimic for biomolecules such as proteins and enzymes and therefore are an accessible route to create synthetic catalytic molecules.¹⁷ In chapter 3 it was demonstrated how the self-assembly of statistical copolymers is independent of molecular weight but is heavily dependent on the copolymer composition and more specifically the mole fraction of hydrophile present.¹⁷ Furthermore, a model (the PSC model) was developed that describes the relationship between the size of the copolymer assembly and the molecular composition of the copolymer based

around a constant charge density on the particle surface. This PSC model can be used as a prediction tool to create bespoke nano-particles from copolymers with known compositions.

Research into the self-assembly of block copolymers is extensive and they are known to form morphologies such as spheres,^{19–23} worms^{19,24,25} and vesicles.^{19,26,27} These types of nano-structures are useful in a range of applications from bio-applications and drug delivery to thickening agents in oil.²⁸ Albigès *et al.* recently demonstrated how amphiphilic worm-like micelles synthesised *via* reversible addition-fragmentation chain transfer (RAFT) polymerisation can be used in paint formulations as binders to create enhanced film properties.⁶ In this case, the block copolymer worm-like micelles were formulated *via* polymerisation-induced self-assembly (PISA) and were composed of a high T_g styrene core and a hydrophilic stabiliser block comprising a statistical copolymer of methacrylic acid and methoxy(polyethylene oxide) methacrylate. They also demonstrated that adding these high T_g worm-like micelles into a soft acrylic latex increased the stiffness of the dried copolymer film, whilst preserving high extensional properties.

Rabyk *et al.* recently used nitroxide-mediated polymerisation (NMP) to synthesise a range of novel block-gradient copolymers composed of an initial block of poly(2-dimethylaminoethylacrylate) and an amphiphilic gradient block of poly(styrene-grad-2-dimethylaminoethyl acrylate).²⁹ It was demonstrated that these two monomers spontaneously form a gradient copolymer when reacted together as the reactivity ratios of 2-dimethylaminoethylacrylate and styrene are $r_{\text{DMAEA}} = 0.25$ and $r_{\text{St}} = 1.15$, respectively. Dynamic light scattering and small-angle neutron scattering techniques were used to show how the copolymer dispersions have pH and temperature sensitivity, whereby the copolymer assemblies will disassemble into individual copolymer chains at high pH and will swell when the temperature is increased.

The effects of hydrophile and hydrophobe distribution have also been investigated in biomolecules such as peptides.^{30–34} In 2013, Lee *et al* demonstrated the importance of amino acid sequence on the self-assembly behaviour of an Ac-(FKFE)₂-NH₂ peptide chain.³³ These peptides are known to assemble into β -sheets in water (between pH 3 and 4) when they have an alternating sequence of amino acids. However, TEM images showed that varying the sequence of the peptide led to variations in the self-assembled structure and affected the concentration at which β -sheets would form. They concluded that varying the amino acid sequence has a large influence on the resultant peptide morphology and that this effect can be exploited in order to create novel peptide self-assemblies.³³

This small selection of current research demonstrates the exciting possibilities (*e.g.*, reinforcing agents in paint binders, biomolecule mimics, etc.) for amphiphilic copolymers with different molecular architectures. However, more research still needs to be performed in order to fully understand how monomer distribution can affect the copolymer assemblies in terms of particle structure and properties. This chapter aims to systematically demonstrate the effect of hydrophile-hydrophobe distribution by formulating aqueous dispersions of statistical, gradient, and block copolymers of butyl methacrylate (BMA) and methacrylic acid (MAA) and studying the structures formed in aqueous solution using small-angle X-ray scattering.

5.2 Copolymer synthesis

5.2.1 Polymerisation of MAA for kinetic analysis.

MAA (1.24 g, 14.4 mmol), ACVA (0.0112 g 0.04 mmol), and PETTC (0.0678 g, 0.197 mmol) were mixed in ethanol (3.70 mL), and placed in an ice-bath to cool. The mixture was degassed with N₂ for 30 minutes and then heated to 75 °C to initiate polymerisation. Kinetic samples

(0.1 mL) were collected at regular intervals until the reaction was complete (*c.a.* 330 min). Once complete the reaction was quenched in the presence of oxygen.

5.2.2 Statistical copolymerisation to form P(BMA-*st*-MAA).

BMA (9.53 g, 67.1 mmol), MAA (2.47 g, 28.8 mmol), ACVA (0.0373 g, 0.133 mmol), and PETTC (0.136 g 0.399 mmol) were mixed in dioxane (12.2 mL) creating a 50% w/w monomer solution, and placed in an ice-bath to cool (Figure 5.1a). The mixture was degassed with N₂ for 30 minutes and then heated to 70 °C to initiate copolymerisation. The reaction was left for 24 hours before being cooled to ambient temperature and quenched by exposure to air. The product was purified by multiple precipitations into petroleum ether and then dried in a 30 °C vacuum oven overnight to give a pale-yellow powder.

5.2.3 Pseudo-gradient copolymerisation to form P(BMA-*gr*-MAA).

Initially, MAA (0.62 g, 7.19 mmol), ACVA (0.0056 g, 0.0200 mmol), and PETTC (0.0339 g, 0.0984 mmol) were mixed in ethanol (1.85 mL), and placed in an ice-bath to cool (Figure 5.1b). The mixture was degassed with N₂ for 30 minutes and then heated to 70 °C to initiate copolymerisation. A degassed solution of BMA (2.38 g, 16.8 mmol) and ethanol (3.99 mL) was added to the copolymerisation at various reaction times to create gradient copolymers, where the initial MAA block was varied in length. The reaction was left at 75 °C for 24 hours before being cooled to ambient temperature and quenched by exposure to air. The product was purified by multiple precipitations into petroleum ether and then dried in a 30 °C vacuum oven overnight to give a pale-yellow powder.

5.2.4 Block copolymerisation to form P(BMA-*b*-MAA).

MAA (10.00 g, 116 mmol), ACVA (0.0945 g, 0.337 mmol), and PETTC (0.572 g, 1.69 mmol) were mixed in ethanol (20.3 mL), and placed in an ice-bath to cool (Figure 5.1c). The mixture was degassed with N₂ for 30 minutes and then heated to 75 °C to initiate polymerisation. This polymerisation was quenched in air once a 70% monomer conversion had been reached in order to preserve the RAFT chain ends and allow for good blocking efficiency. The initial PMAA macro-CTA was purified by multiple precipitations into diethyl ether. Following purification, the polymer was dissolved in water and the solid polymer was isolated by lyophilisation.

The purified PMAA macro-CTA (1.37 g, 0.219 mmol) was then dissolved in ethanol (18.9 mL) at 50 °C. Once the all the PMAA was fully dissolved, the solution was cooled to ambient temperature and BMA (5.00 g, 35.2 mmol), and ACVA (0.0123 g, 0.0437 mmol) were added. The reaction mixture was placed in an ice-bath to cool and degassed with N₂ for 30 minutes. Following this, the mixture was heated to 75 °C to initiate polymerisation and left to react for 24 hours. The reaction was then cooled to ambient temperature and quenched with oxygen. The resulting block copolymer was purified by multiple precipitations into petroleum ether and then dried in a 30 °C vacuum oven overnight to give a pale-yellow powder.

5.2.5 Formation of aqueous copolymer dispersions.

Purified copolymer (1.00 g) was dissolved in IPA to create a 50 % w/w solution. Triethanolamine (0.357 g, 2.40 mmol) in water was added to reduce the concentration of the copolymer solution to 40% w/w. Following this, the solution was slowly diluted to 1% w/w by sequential additions of water.

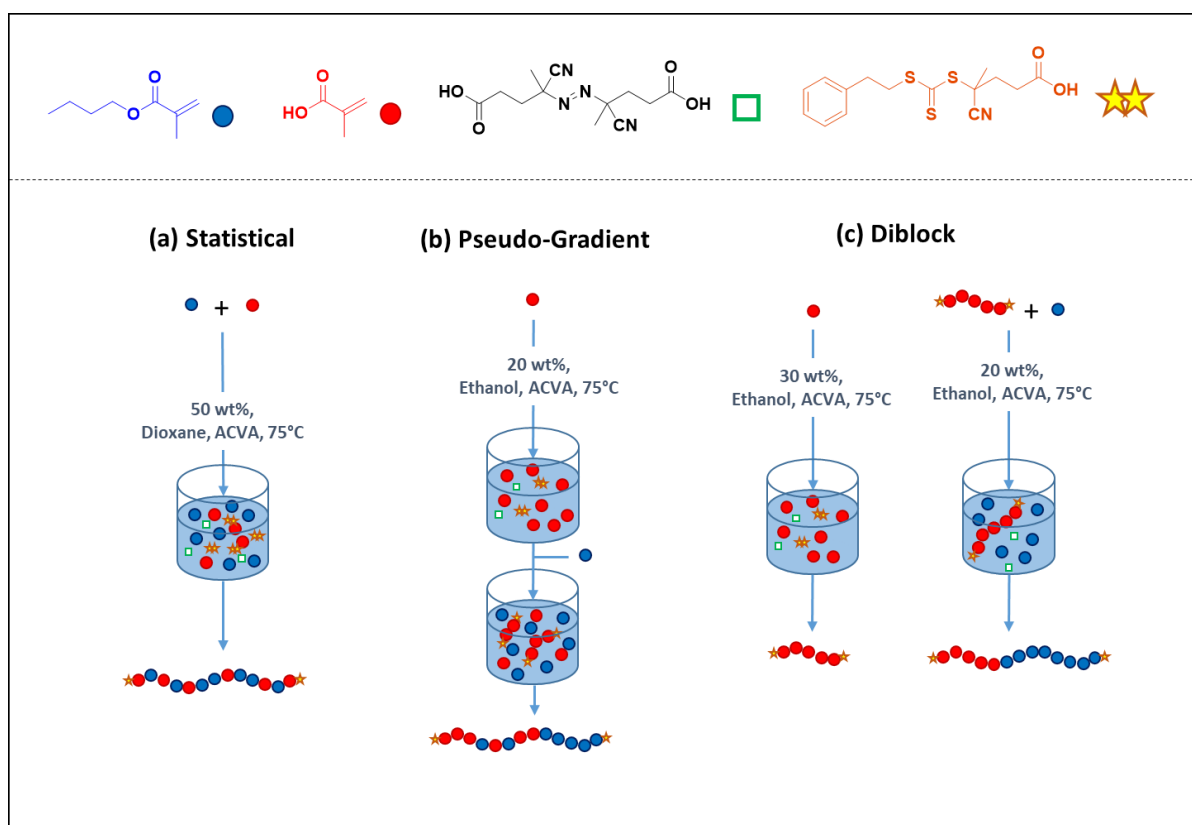


Figure 5.1. The synthetic procedures used to produce the three different molecular architectures of BMA-MAA copolymers, where (a) forms a statistical copolymer, (b) forms a pseudo-gradient copolymer, and (c) forms a block copolymer.

5.3 Results and discussion

5.3.1 Synthesis and characterisation of copolymers.

In order to analyse the effect of hydrophile-hydrophobe distribution on copolymer self-assembly, a series of BMA-MAA copolymers was synthesised with a variety of molecular architectures. All copolymers were synthesised with a constant copolymer composition of 70% mol. of BMA and 30% mol. of MAA to allow an effect of the molecule architecture on copolymer self-assembly to be studied. Three different architectures were investigated, specifically statistical, pseudo-gradient, and block. The term “pseudo-gradient” is used here since the copolymers synthesised were not “true” gradient copolymers, which often form spontaneously due to the reactivity ratios of the two monomers involved.³⁵ Kinetic analysis of the conversion rates of BMA and MAA in both a statistical copolymerisation (Figure 5.2a) and a “pseudo”-gradient copolymerisation (Figure 5.2b) demonstrate that both monomers react at a similar rate. Therefore, following the synthetic procedure described above will not produce “true” gradient copolymers but, rather, will produce copolymers with an initial pure MAA block followed by a statistical block of BMA and MAA (Figure 5.3). However, these copolymers still offer a third molecular architecture with a unique distribution of monomer units along the polymer backbone. Furthermore, by varying the addition-time of BMA to the polymerisation allows a wide range of pseudo-gradient copolymers to be produced where the length of the initial MAA block is systematically varied.

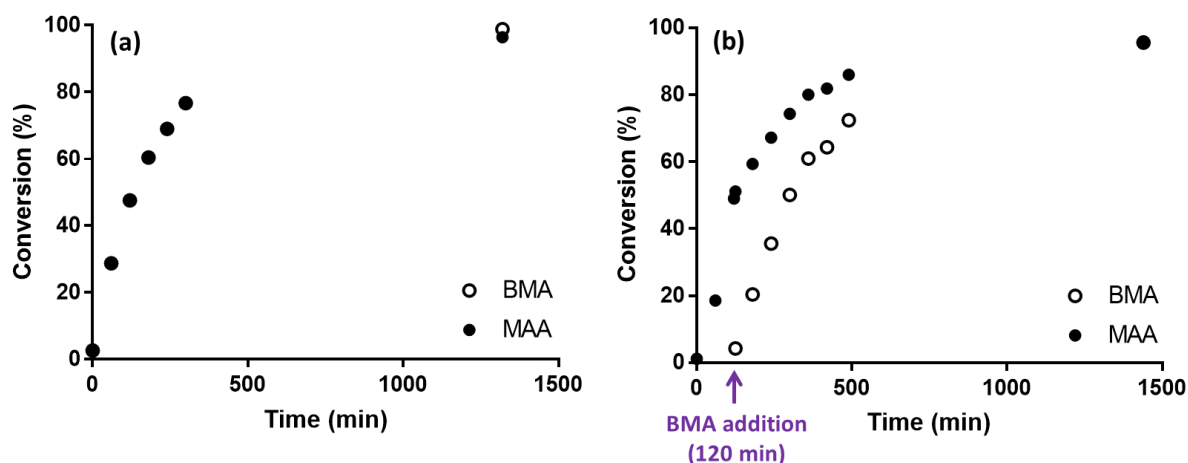


Figure 5.2. Kinetic data where (a) is the conversion rate of a statistical RAFT copolymerisation of MAA and BMA in dioxane, and (b) is the conversion rate of a "pseudo"-gradient RAFT copolymerisation in ethanol.

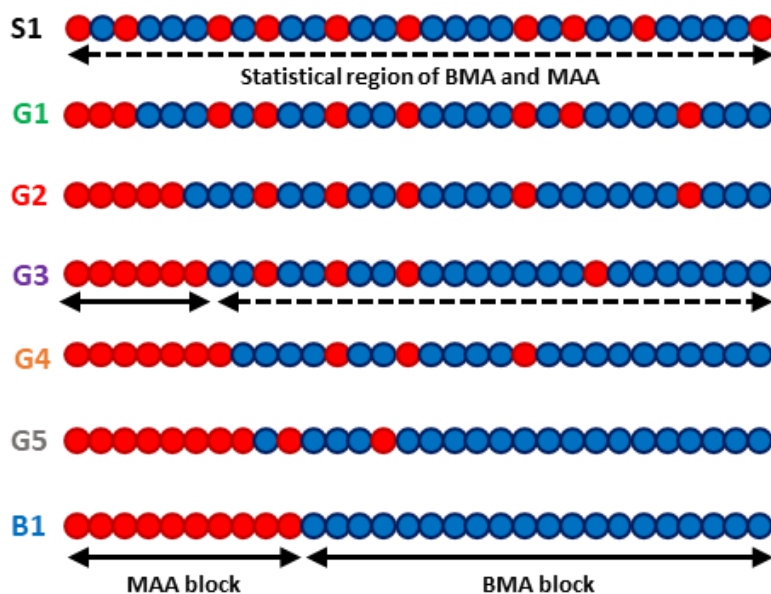


Figure 5.3. A schematic representation of copolymers with different sequences of components along the chain produced by the synthetic procedures where the letters S, G, and B refer to statistical, pseudo-gradient, and block, respectively.

Since the reactivity ratios of BMA and MAA are close to 1,³⁵ they should form a statistical copolymer (S1), which has an approximately random distribution of monomer along the copolymer backbone (Figure 5.3). These systems can be synthesised relatively simply using

standard free-radical copolymerisation making them a popular choice for industrial applications. However, in this case RAFT copolymerisation was used to enable the molecular weight of the copolymer to be controlled and to allow direct comparison to the pseudo-gradient and block copolymers. The structures of statistical copolymer particles have been found to be largely independent of molecular weight (Chapter 3). However, here it is important to keep the targeted molecular weight relatively constant so that comparisons between the dispersions can be made across all three copolymer designs. In order to produce two distinct homopolymer blocks of BMA and MAA when synthesising the block copolymer (B1) architecture (Figure 5.3), the initial PMAA block was synthesised as a macro-CTA and purified by multiple precipitations into diethyl ether to remove any residual monomer (Figure 3.1c). The PMAA macro-CTA was then extended with BMA to produce a well-defined block copolymer (Figure 3.1c). Statistical copolymers and block copolymers are the two extreme cases of monomer distribution. Therefore, by investigating these two extremes, whilst maintaining a constant copolymer composition and molecular weight, the limits of structural variations can be assessed.

Whilst statistical and block copolymers allow the extreme effects of monomer distribution to be investigated, the intermediate effects also need to be mapped. Therefore, pseudo-gradient copolymers were synthesised to investigate the effect of an intermediate monomer distribution. The time-point at which BMA is added to the gradient copolymer reaction will produce copolymers with different monomer distributions, specifically the length of the initial MAA block and, as a consequence, the mole ratio of MAA in the BMA/MAA statistical region (Figure 5.1b). Five different pseudo-gradient copolymers (G1, G2, G3, G4, and G5) were synthesised (Figure 5.3) where the BMA solution was added to each polymerisation at 30, 60, 120, 180, and 240 minutes corresponding to 13, 29, 62, 83 and 94% MAA conversion, respectively (Figure 5.4a). As the time at which BMA was added increases, the MAA in the

reaction reaches a higher conversion. Therefore, the length of the MAA block will increase with respect to the time at which the BMA was added. The length of the MAA block for each pseudo-gradient copolymer can be calculated based upon the monomer conversion reached at the point of BMA addition (Figure 5.4b).

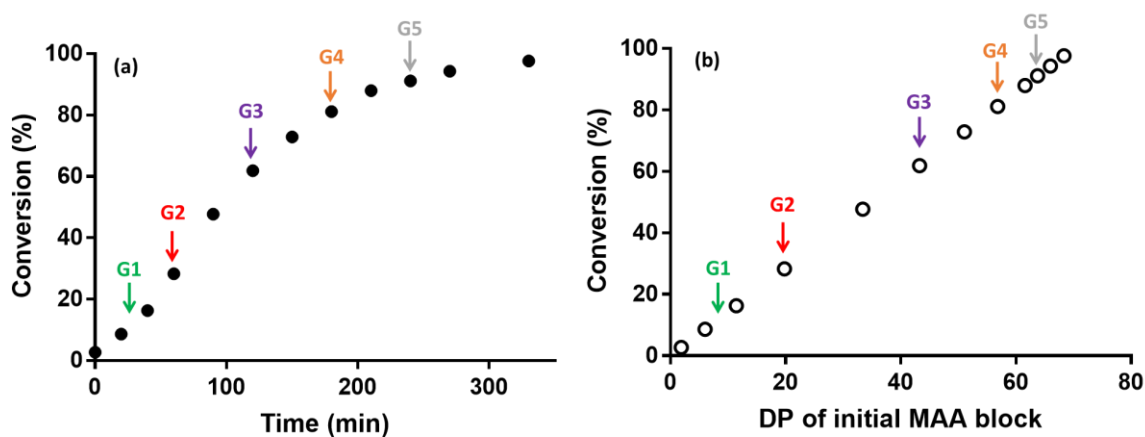


Figure 5.4. Monomer conversion (a) for the RAFT polymerisation of MAA in ethanol and (b) the theoretical DP of the initial MAA block during the polymerisation. The arrows indicate when the BMA was added during the synthesis of each respective pseudo-gradient copolymer.

The purified copolymers were methylated with trimethylsilyldiazomethane to convert MAA units to methyl methacrylate (MMA). ^1H NMR spectra were collected of the methylated products in order to determine the final copolymer composition (Table 5.1) and the copolymers were found to have compositions similar to their respective monomer feed ratios (Table 5.1). Additionally, molecular weight measurements were collected using GPC and the M_w was found to be fairly consistent across the entire series. Furthermore, the copolymers all have an $M_w/M_n < 1.3$ indicating a well-controlled copolymerisation (Table 5.1).

Table 5.1. Composition and molecular weight data collected for the P(BMA-MAA) copolymers.

Copolymer	DP of initial MAA block ^a	Composition (BMA:MAA) ^c	GPC ^d		
			M_n (kDa)	M_w (kDa)	M_w/M_n
S1	-	70:30	36.4	45.4	1.25
G1	9	72:28	29.6	34.7	1.17
G2	20	70:30	29.6	36.3	1.23
G3	43	72:28	24.8	30.1	1.21
G4	57	70:30	24.8	29.0	1.17
G5	64	69:31	23.9	28.1	1.17
B1	69 ^b	70:30	23.1	26.7	1.16

^a DP of initial PMAA block calculated for the pseudo-gradient copolymers using the PMAA kinetic data and the monomer conversion. ^b DP calculated from ¹H NMR spectrum of the PMAA macro-CTA. ^c Composition data obtained from ¹H NMR analysis of methylated copolymers [P(BMA-MMA)]. ^d Polymers analysed in THF containing 4.0% v/v acetic acid against of PMMA standards.

5.3.2 Self-assembly of copolymers to form spherical particles

The copolymers were formulated into aqueous dispersions of 1% w/w and 0.1% w/w using a solvent switch method as described in chapter 3; these dispersions were consequently analysed by SAXS, DLS and TEM. All the copolymer dispersions were stable at low concentrations and in general TEM images collected of the dispersions show that the copolymers self-assemble into spherical nanoparticles (Figure 5.5). The morphologies of S1 and G1 are hard to determine purely using TEM as the particles size is small making them difficult to resolve. Furthermore, the particles are clustered together on the grid, which could be a consequence of the drying process. SAXS has been used in combination with TEM to confidently determine the particle morphology. By analysing the TEM images it is clear that the monomer distribution has a large

effect on the particle size, where a more statistical distribution of MAA along the copolymer chain results in a smaller particle size, and *vice versa* (Table 5.2). DLS measurements were taken of 0.1% w/w dispersions and a value for hydrodynamic radius, R_h , was determined (Table 5.2). The data collected from DLS deviates substantially from the particle size observed in both TEM and SAXS, where the measured R_h is considerably larger. In this case, the unrealistically large R_h is caused by the electrostatic interactions of the particles because of the anionic surface charge. These interactions affect the diffusion of the particles through the solvent and result in an inconsistent measurement. The deviation between the techniques demonstrates why SAXS is an essential characterisation method to investigate these charged systems.

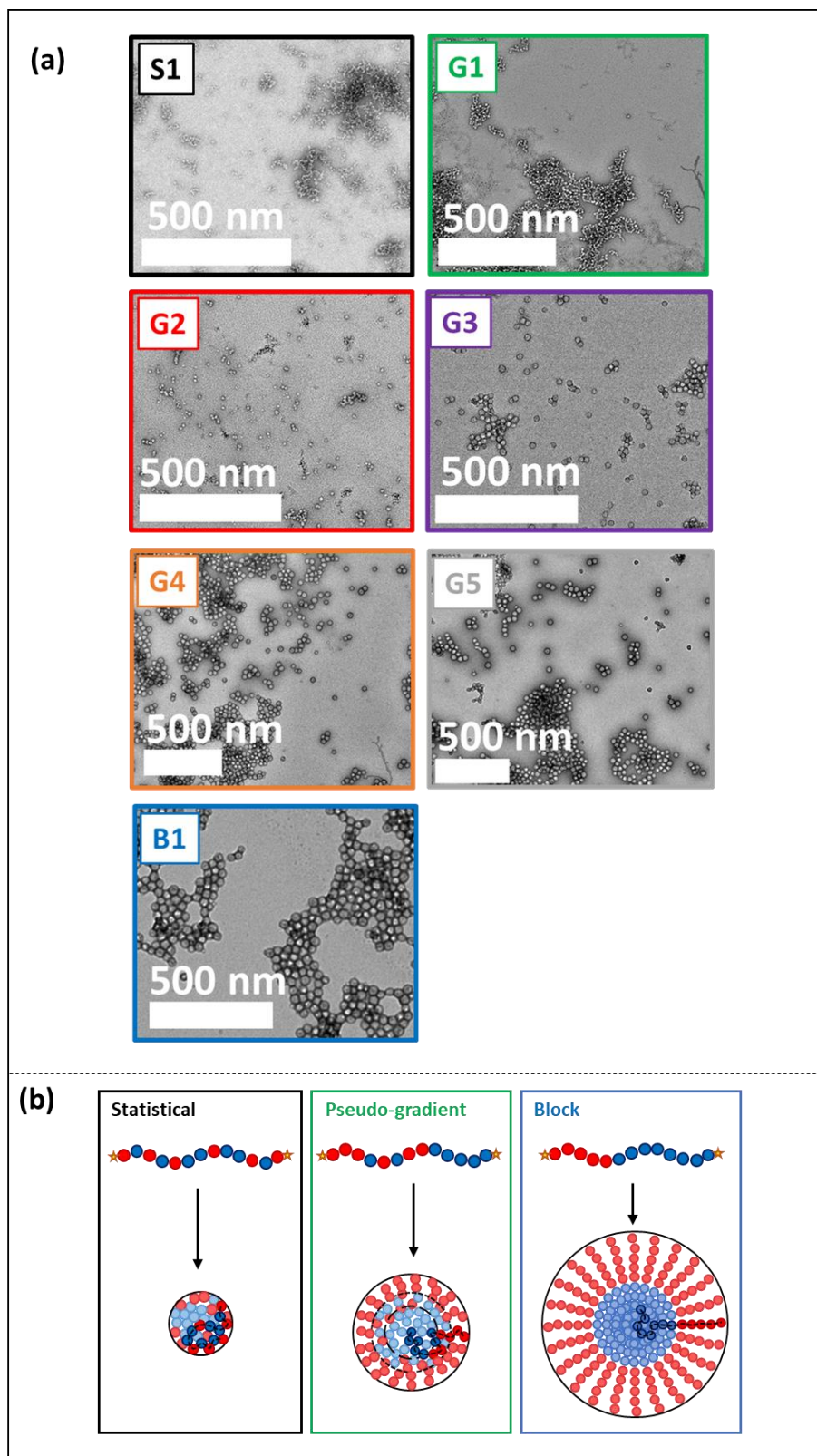


Figure 5.5. (a) TEM images recorded for BMA-MAA copolymer 0.1% w/w aqueous dispersions showing the assembly of spherical nanoparticles. (b) Cartoon interpretation of the particle structure formed by the three different monomer distributions.

The SAXS pattern of the S1 dispersion displays a well-defined region of the first intensity minima at $q \approx 0.1 \text{ \AA}^{-1}$ resulting from the particle form factor (Figure 5.5b). Chapters 3 and 4 of this thesis suggest that the statistical copolymers assemble into spherical particles with minimal phase separation and no well-defined core and shell. Therefore, the patterns were initially fitted with a simple sphere model (eqs 2.9-12). At low concentrations (*i.e.* 1% w/w) the particles should be far enough away from each other that they do not interact. However, a structure factor peak is observed at low q -values resulting from long-range particle interactions caused by anionic charges present on the particle surface (Figure 5.6). A hard sphere structure factor (eq 2.6) accounting for this structural organisation was incorporated into the model as was previously done for similar charged systems (Chapters 3 and 4). The mean particle size was determined by SAXS and the mean particle radius was found to be 41 \AA (Table 5.2). This value for the radius is comparable with the radius of the dry particle ($R_{\text{dry}} = 37 \text{ \AA}$) measured by TEM.

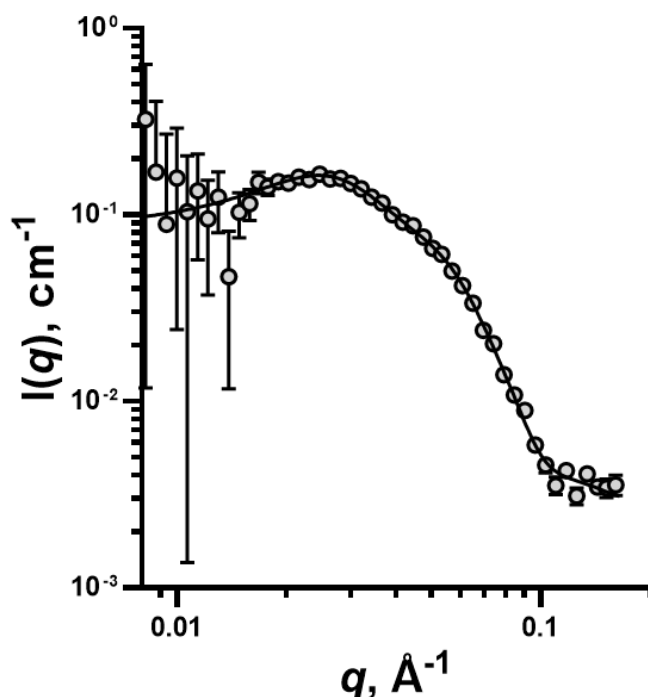


Figure 5.6. SAXS pattern of a 1% w/w aqueous dispersion of S1 (symbols) fit using a simple sphere model with an incorporated hard sphere structure factor (solid line).

Unlike statistical copolymer particles, block copolymers are expected to phase separate within the particle to form a well-defined core surrounded by hydrophilic blocks forming a corona.^{22,36} This means that a simple spherical model cannot be used to analyse the SAXS pattern for the B1 dispersion (Figure 5.7). Instead, a more complex model needs to be selected. In this case, a polymer micelle model was used as this model allows for a distinct core and corona with respective scattering length densities (eqs 2.25-27). SAXS determined the particles in the B1 dispersion to have a total radius ($R_{\text{tot}} = R_s + 2R_g$) of 271 Å (Table 5.2). Furthermore, the R_{core} measured using SAXS (175 Å) is comparable with R_{dry} measured using TEM (157 Å) (Table 5.2).

Table 5.2. Structural analysis results for P(BMA-MAA) copolymer dispersions, where R_s is the mean particle core radius, σ_s is the standard deviation of the mean particle core radius, R_g is the radius of gyration of the hydrophilic corona block, R_{tot} is the total particle radius, V_s is the volume of copolymer chain in the core, V_c is the volume of copolymer chain in the corona, R_h is the hydrodynamic radius and R_{dry} is the radius of dried particles on a carbon coated grid.

Copolymer	R_s^\dagger (Å)	σ_s^\dagger (Å)	R_g^\dagger (Å)	R_{tot}^\dagger (Å)	V_s (Å ³)	V_c (Å ³)	R_h^\ddagger (Å)	R_{dry}^* (Å)
S1	41	8	-	41	45774	-		37
G1	57	13	1	59	45774	0	80	46
G2	53	22	9	71	42677	3097	165	48
G3	107	22	17	141	37631	8143	200	85
G4	150	23	32	215	37597	8177	293	141
G5	157	21	36	229	37561	8213	542	141
B1	175	20	38	271	37561	8213		157

[†] Determined by SAXS, [‡] determined by DLS, ^{*} determined by TEM.

By comparison of the SAXS results between the spherical dispersions formed by both S1 and B1, it is clear that monomer distribution has a large effect on both particle size and particle

structure. A blockier structure induces the formation of a distinct corona and this results in a larger particle size. Since these two copolymer systems have relatively similar molecular weights, the “blockier” monomer distribution induces intermolecular aggregation and an increase in the aggregation number.

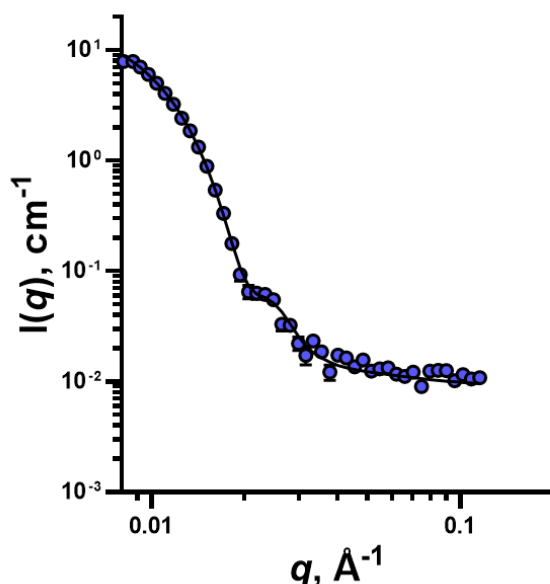


Figure 5.7. SAXS pattern of a 1% w/w aqueous dispersion of B1 (symbols), where the solid line is the polymer micelle model.

Statistical and block copolymers are extreme cases of the copolymer component sequence studied and the particles that they form have to be analysed with vastly different structural models. However, the pseudo-gradient copolymers that were synthesised cover the varying monomer distributions between these two extremes. Therefore, the particle structure will also vary between the two extremes and consequently requires a model with the ability to adapt to the individual copolymer architecture and more importantly the presence and size of a corona block.

In order to create a model that fits the structural criteria of the entire range of monomer distributions, the polymer micelle model was adapted with a parameter that would model the relative volumes of the copolymer found in the core and shell. This model (Section 2.5.7) had

a good fit to the SAXS patterns of all gradient copolymer dispersions demonstrating its versatility (Figure 5.8).

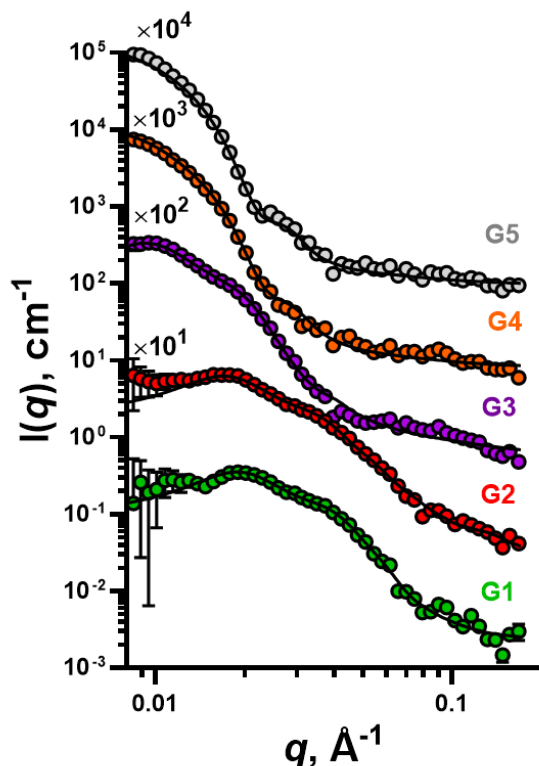


Figure 5.8. SAXS patterns of 1% w/w aqueous dispersions of pseudo-gradient copolymers (G1-G5) (symbols) fitted using an adapted polymer micelle model (Section 2.5.7) with an incorporated hardsphere structure factor (solid line).

The structural model was used to analyse the scattering patterns of the gradient copolymer dispersions and it was found that the size of the particle increases with respect to the size of the initial PMAA block *i.e.*, copolymers with larger PMAA blocks, and therefore less MAA in the statistical block, self-assembled into larger particles (Table 5.2 and Figure 5.9). This observation is consistent with the data for the S1 and B1 dispersions as it was found that copolymers without any defined “blockiness” (S1) aggregated to form much smaller particles than copolymers with well-defined, segregated blocks (B1). As the gradient copolymers become “blockier” (G3, G4 and G5), the copolymers induce larger scale phase separation in the particle resulting in more of the copolymer being found outside of the core to form a distinct corona.

Larger particles have a lower surface area to volume ratio and therefore require less stabilisation. This phenomenon is seen in emulsion polymerisation, where a higher concentration of surfactant will produce a smaller latex than one with less surfactant. This suggests that by inducing segregation of hydrophilic and hydrophobic components means that the hydrophilic groups are less able to stabilise the hydrophobic segments. This causes an increase in aggregation number, and therefore larger particles, to reduce the surface area to volume ratio. Therefore, despite the added steric stability provided by the corona block, the electrostatic stabilisation of the particle reduces as the copolymers become “blockier”.

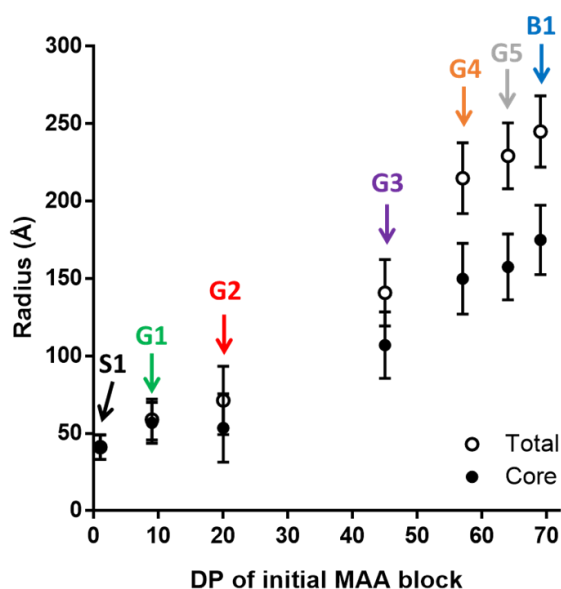


Figure 5.9. The radius of the copolymer particles in aqueous dispersion, calculated by modelling the SAXS patterns with an adapted polymer micelle model, against the DP of the initial PMAA block.

5.3.3 Utilisation of MAA within the copolymer particle

From SAXS analysis of particle size and structure, it is clear that the hydrophile-hydrophobe distribution has a significant influence on the particle size. This particle size dependence is a result of the reduction in electrostatic stability provided by the anionic MAA units. Since all of the copolymers reported in this investigation are targeted to have the same composition

(70:30, BMA:MAA) all of the copolymer particles should have near identical monomer compositions and the measured compositions support this (Table 5.1). As all the particles have the same ratio of BMA to MAA, it may be expected that the electrostatic stability would remain constant and all the particles should be the same size. However, since this is not the case, it can be concluded that the location of the hydrophile both within the particle and along the copolymer chain has a significant effect on whether it can be utilised for electrostatic stabilisation.

The electrostatic stabilisation of particles in a dispersion is a consequence of the repulsion of similar charges present on the particle surface. Therefore, if MAA is unable to locate near the surface of the particle then it will be unable to contribute to the stability of the particle. In order to assess the proportion of MAA being utilised the ratio, K (also known here as the reciprocal efficiency coefficient), between the total area that MAA in the particle could potentially cover ($tSA_{MAA,p}$) and the total surface area of the particle (SA_p) was determined:

$$tSA_{MAA,p} = N_{MAA} \cdot N_{agg} \cdot CS_{MAA} \quad (5.1)$$

$$SA_p = 4\pi R_s^2 \quad (5.2)$$

$$K = \frac{tSA_{MAA,p}}{SA_p} \quad (5.3)$$

where N_{MAA} is the number of MAA units in each copolymer chain. N_{MAA} is assumed to be 69 which is the theoretical DP based on the monomer feed ratios and the quantity of RAFT agent. N_{agg} is the aggregation number of copolymer chains in a particle, CS_{MAA} is the approximate cross-sectional area of one MAA unit ($CS_{MAA} \approx 24.5 \text{ \AA}^2$), R_s is the core particle radius, and K defines the maximum surface coverage of MAA on any given particle.

Table 5.3. Calculation of the MAA fraction that is utilised for electrostatic stabilisation, where R_s is the particle core radius, $tSA_{MAA,p}$ is the total surface area which could be potentially covered by MAA, SA_p is the total particle surface area, K is the ratio between $tSA_{MAA,p}$ and SA_p .

Copolymer	R_s	N_{agg}	$tSA_{MAA,p}$	SA_p	K
S1	41	6	10,662	21,124	0.50
G1	57	17	28,649	40,828	0.70
G2	53	15	24,702	35,299	0.70
G3	107	136	230,520	143,872	1.60
G4	150	376	635,659	282,743	2.25
G5	157	432	729,568	309,748	2.36
B1	175	598	1,010,371	384,845	2.63

The calculated values of K (Table 5.3) indicate that changing the molecular architecture of the copolymer, and the distribution of the hydrophile along the backbone, affects how much of the MAA can be utilised for stabilisation (Figure 5.10). Firstly, S1 forms the smallest particle and has the lowest value of K at 0.5. This demonstrates that if all the MAA is assumed to locate on the particle surface, only 50% of the surface is covered with MAA, and this creates a large enough surface charge density to induce stabilisation. This observation indicates that 0.50 can be considered as a threshold for the maximum value of K . Thus, a K value that is greater than 0.50 suggests that not all the MAA is being utilised for stabilisation. Furthermore, a K value of 0.50 is in agreement with conclusions made in Chapter 4 of this thesis as it was found that fully statistical copolymers of BMA and MAA required a fractional MAA surface coverage of 0.55 to achieve stabilisation if all MAA is assumed to locate on the surface (0.27 if 50% remains trapped in the bulk of the particle).

There is a slight increase in K for the G1 and G2 dispersions suggesting that there is some reduction in the utilisation of MAA as the monomer distribution in the copolymers become less statistical. However, this change is very small and so most of the MAA is still contributing to stabilisation. On-the-other-hand, as the DP of the initial PMAA block surpasses 20 the relative fraction of MAA being utilised reduces significantly, as indicated by a K much larger than 0.50 (Table 5.3), - this results in an increase in particle size (Figure 5.10). When the length of the PMAA block is increased, the particles become more phase separated and form distinct cores and corona structures, where the PMAA blocks locate within the corona. Although the corona is positioned on the surface of the particle, allowing the majority of MAA to penetrate out of the BMA core, it has an inherent thickness ($2R_g$). This means that MAA that is located deep within the corona are unable to contribute to the charge stabilisation of the particle, since they are shielded by other (surface) MAA units. According to the calculation results (eqs 5.1 – 5.3 and Table 5.3), this charge shielding effect only occurs when the DP of the PMAA block reaches a certain length (>20) (Figure 5.10). Once the DP is greater than 20, the contribution of the MAA decreases as the block length increases (Figure 5.10); this corresponds with an increase in corona thickness (Table 5.2). Since the majority of the MAA units are unable to contribute to the electrostatic stability of the particle once the DP of the PMAA block is greater than 20, more chains are required to aggregate together to achieve a certain surface charge density. This aggregation results in an increase in particle size (Figure 5.10).

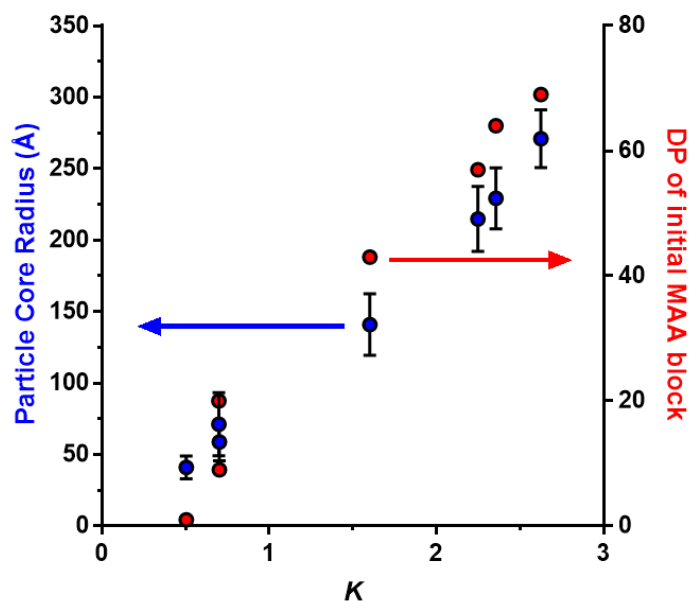


Figure 5.10. The normalised fraction of MAA per copolymer chain that contributes to the electrostatic stabilisation of the copolymer particle against the particle core radius (blue symbols), and the DP of the initial PMAA block (red symbols).

5.3.4 Comparison against the behaviour of statistical copolymers

Since this is a study of the effect of monomer distribution on particle size, it is important to compare the behaviour observed to that of copolymer systems with a known behaviour, *e.g.*, the charge density dependence of statistical copolymers described in Chapters 3 and 4. Therefore, the composition of the statistical section of the copolymers (Figure 5.3) was calculated and plotted against the core radius of the particles formed (Figure 5.11). The charge density dependence of the statistical copolymers was also plotted to see how copolymers with different monomer distributions deviate from the statistical behaviour.

The obtained results show (Figure 5.11) that up until G4 all the copolymer particles formed are comparable to statistical copolymers that do not possess any “blocky” structure. G4, G5, and B1 all clearly deviate from the statistical model suggesting that the “blocky” nature of these

copolymers means that the particle size is not completely determined by the surface charge density but other factors need be considered; for example, molecular weight, which is known to affect the self-assembly of diblock copolymers.²² Previously it has been seen that the PMAA block in both G1 and G2 is too small to significantly influence the particle size (Figures 5.9). Additionally, the K values calculated for G1 and G2 are comparable to respective statistical (or mainly-statistical) copolymers investigated in previous chapters. Therefore, it is expected that these copolymers will behave in a similar way to statistical copolymers. Conversely, G3 seems to behave in a similar way to the statistical copolymers, despite all other results (high K and a large corona) suggesting otherwise. Therefore, it should be considered that this observation could be coincidental and resulted from a combination of multiple factors, such as charge density, composition and molecular weight. To quantify where the behaviour of the copolymers deviates from the statistical model, multiple molecular weights of each copolymer must be synthesised and assessed. Since the self-assembly of statistical copolymers is molecular-weight independent, no molecular-weight effect should be observed if the copolymer self-assembly follows the statistical model.

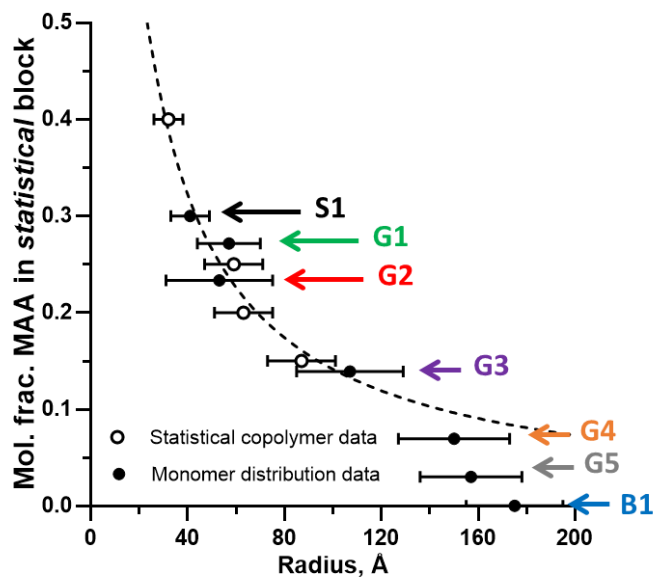


Figure 5.11. A comparison between the behaviour of statistical copolymers of BMA and MAA with different monomer compositions and BMA-MAA copolymers with different molecular architectures with respect to the composition of the statistical component and the radius of the particle formed. Here the open symbols show statistical copolymer data collected in Chapter 3 and the closed symbols show the monomer distribution data collected in this chapter.

This work demonstrates how a range of copolymer dispersions with varying particle size and structure can easily be formulated using copolymers of similar monomer composition and molecular weight. By simply altering the molecular architecture of the copolymer, the particle size can be tuned. However, this work also demonstrates that complex copolymer distributions, such as diblock copolymers, are not always required to create particles of a certain size, and similar particles can be easily and cheaply be formulated by tuning the composition of statistical copolymers.

5.4 Conclusions

A range of BMA-MAA copolymers with similar molecular weights (30 kDa) and compositions (70:30, BMA:MAA) were synthesised using RAFT solution copolymerisation in ethanol. Different reaction procedures were used to create copolymers with different monomer

distributions. A statistical copolymer, S1, was synthesised by simultaneous addition of BMA and MAA to the reaction mixture and was left to react until high monomer conversions were achieved. In order to synthesise a distinct block copolymer, B1, a PMAA₇₀ macro-CTA was first synthesised and isolated. This macro-CTA was then extended with BMA to create a well-defined block copolymer. Pseudo-gradient copolymers, G1-5, were synthesised by initially homopolymerising MAA and introducing BMA to the reaction mixture at a time point in the reaction. This allowed the MAA to reach a certain conversion creating a pure PMAA block at the start of the copolymer. By varying the time when BMA was added created different lengths of the PMAA block, where the DP of the initial PMAA block increased for G1, G2, G3, G4, and G5, respectively. Once purified, these copolymers were dispersed in aqueous conditions using a “solvent-switch” method and the resulting dispersions were analysed by both SAXS and TEM and it was found that all the copolymers self-assembled into spherical particles. However, it was clear that the monomer distribution had a large effect on the copolymer particle size. Both SAXS and TEM demonstrated that generally a more statistical distribution of monomer along the copolymer backbone induced a smaller particle size. It is concluded that the increase of particle size is caused by a reduction in the efficiency by which the MAA units can stabilise the particle as a result of the monomer distribution. The utilisation of MAA was quantified by calculating the ratio between the total surface area that MAA could potentially cover in a specific copolymer particle ($tSA_{MAA,p}$) and the total surface area of the particle (SA_p) to give a value for the reciprocal efficiency coefficient, K . A minimum K value was observed for the S1 copolymer dispersion with a value of 0.50. This suggests that stabilisation can be achieved if 50% of the particle surface is covered with MAA, assuming that all the MAA is able to locate on the surface of the particle. G1 and G2 have K values slightly larger than 0.50 suggesting that there is a slight reduction in the utilisation of MAA. G3, G4, G5 and B1 all have very high K values indicating lower utilisation of MAA. This was

thought to be caused by the formation of a large corona, whereby MAA units close to the particle core have little effect on the stabilisation. This results in the aggregation of copolymer chains and an increase in particle size to reduce the surface area to volume ratio. Finally, comparison with data collected for statistical BMA-MAA copolymers (Chapter 4) showed that the initial PMAA block had to reach a large DP (57) before the copolymer particles began to deviate from the behaviour observed for statistical copolymers. However, in order to accurately assess the point at which the copolymer becomes “too blocky” to be dominated by a critical surface charge density and independent of molecular weight, more copolymers need to be analysed where the molecular weight is systematically varied.

5.5 References

- 1 M. Huo, J. Yuan, L. Tao and Y. Wei, *Polym. Chem.*, 2014, **5**, 1519–1528.
- 2 A. Rösler, G. W. Vandermeulen and H. A. Klok, *Adv. Drug Deliv. Rev.*, 2001, **53**, 95–108.
- 3 M. A. C. Stuart, W. T. S. Huck, J. Genzer, M. Müller, C. Ober, M. Stamm, G. B. Sukhorukov, I. Szleifer, V. V. Tsukruk, M. Urban, F. Winnik, S. Zauscher, I. Luzinov and S. Minko, *Nat. Mater.*, 2010, **9**, 101–113.
- 4 X. Wu, Y. Qiao, H. Yang and J. Wang, *J. Colloid Interface Sci.*, 2010, **349**, 560–564.
- 5 K. S. Kim, N. Gunari, D. Macneil, J. Finlay, M. Callow, J. Callow and G. C. Walker, *ACS Appl. Mater. Interfaces*, 2016, **8**, 20342–20351.
- 6 R. Albigès, P. Klein, S. Roi, F. Stoffelbach, C. Creton, L. Bouteiller and J. Rieger, *Polym. Chem.*, 2017, **8**, 4992–4995.

- 7 I. Martín-Fabiani, J. Lesage De La Haye, M. Schulz, Y. Liu, M. Lee, B. Duffy, F. D'Agosto, M. Lansalot and J. L. Keddie, *ACS Appl. Mater. Interfaces*, 2018, **10**, 11221–11232.
- 8 Y. Chang and C. L. McCormick, *Macromolecules*, 1993, **26**, 6121–6126.
- 9 Y. Hu, G. L. Smith, M. F. Richardson and C. L. McCormick, *Macromolecules*, 1997, **30**, 3526–3537.
- 10 Y. Morishima, S. Nomura, T. Ikeda, M. Seki and M. Kamachi, *Macromolecules*, 1995, **28**, 2874–2881.
- 11 A. Hashidzume, A. Kawaguchi, A. Tagawa, K. Hyoda and T. Sato, *Macromolecules*, 2006, **39**, 1135–1143.
- 12 T. Kawata, A. Hashidzume and T. Sato, *Macromolecules*, 2007, **40**, 1174–1180.
- 13 Y. Hirai, T. Terashima, M. Takenaka and M. Sawamoto, *Macromolecules*, 2016, **49**, 5084–5091.
- 14 G. Hattori, M. Takenaka, M. Sawamoto and T. Terashima, *J. Am. Chem. Soc.*, 2018, **140**, 8376–8379.
- 15 M. Matsumoto, T. Terashima, K. Matsumoto, M. Takenaka and M. Sawamoto, *J. Am. Chem. Soc.*, 2017, **139**, 7164–7167.
- 16 S. Imai, Y. Hirai, C. Nagao, M. Sawamoto and T. Terashima, *Macromolecules*, 2018, **51**, 398–409.
- 17 M. Matsumoto, M. Sawamoto and T. Terashima, *ACS Macro Lett.*, 2019, **8**, 320–325.
- 18 T. J. Neal, D. L. Beattie, S. J. Byard, G. N. Smith, M. W. Murray, N. S. J. Williams, S.

- N. Emmett, S. P. Armes, S. G. Spain and O. O. Mykhaylyk, *Macromolecules*, 2018, **51**, 1474–1487.
- 19 A. Blanazs, A. J. Ryan and S. P. Armes, *Macromolecules*, 2012, **45**, 5099–5107.
- 20 A. A. Cockram, T. J. Neal, M. J. Derry, O. O. Mykhaylyk, N. S. J. Williams, M. W. Murray, S. N. Emmett and S. P. Armes, *Macromolecules*, 2017, **50**, 796–802.
- 21 S. L. Canning, T. J. Neal and S. P. Armes, *Macromolecules*, 2017, **50**, 6108–6116.
- 22 Y. Mai and A. Eisenberg, *Chem. Soc. Rev.*, 2012, **41**, 5969.
- 23 A. A. Cockram, R. D. Bradley, S. A. Lynch, P. C. D. Fleming, N. S. J. Williams, M. W. Murray, S. N. Emmett and S. P. Armes, *React. Chem. Eng.*, 2018, **3**, 645–657.
- 24 V. J. Cunningham, L. P. D. Ratcliffe, A. Blanazs, N. J. Warren, A. J. Smith, O. O. Mykhaylyk and S. P. Armes, *Polym. Chem.*, 2014, **5**, 6307–6317.
- 25 L. A. Fielding, M. J. Derry, V. Ladmiraal, J. Rosselgong, A. M. Rodrigues, L. P. D. Ratcliffe, S. Sugihara and S. P. Armes, *Chem. Sci.*, 2013, **4**, 2081–2087.
- 26 D. E. Discher and A. Eisenberg, *J. Coll. Interface Sci*, 2000, **290**, 525.
- 27 C. J. Mable, R. R. Gibson, S. Prevost, B. E. McKenzie, O. O. Mykhaylyk and S. P. Armes, *J. Am. Chem. Soc.*, 2015, **137**, 16098–16108.
- 28 M. J. Derry, O. O. Mykhaylyk and S. P. Armes, *Angew. Chemie - Int. Ed.*, 2017, **56**, 1746–1750.
- 29 M. Rabyk, A. Destephen, A. Lapp, S. King, L. Noirez, L. Billon, M. Hruby, O. Borisov, P. Stepanek and E. Deniau, *Macromolecules*, 2018, **51**, 5219–5233.
- 30 J. P. Schneider, D. J. Pochan, B. Ozbas, K. Rajagopal, L. Pakstis and J. Kretsinger, *J.*

- Am. Chem. Soc.*, 2002, **124**, 15030–15037.
- 31 Y. Hong, R. L. Legge, S. Zhang and P. Chen, *Biomacromolecules*, 2003, **4**, 1433–1442.
- 32 C. J. Bowerman, W. Liyanage, A. J. Federation and B. L. Nilsson, *Biomacromolecules*, 2011, **12**, 2735–2745.
- 33 N. R. Lee, C. J. Bowerman and B. L. Nilsson, *Biomacromolecules*, 2013, **14**, 3267–3277.
- 34 K. Wang, J. D. Keasling and S. J. Muller, *Int. J. Biol. Macromol.*, 2005, **36**, 232–240.
- 35 T. R. Paxton, *J. Polym. Sci. Part B Polym. Lett.*, 1963, **1**, 73–76.
- 36 J. Noolandi and K. M. Hong, *Macromolecules*, 1983, **16**, 1443–1448.

*Chapter 6. Solution and film behaviour of
amphiphilic triblock acrylate copolymers*

Chapter 6.

Solution and film behaviour of amphiphilic triblock acrylate copolymers

6.1 Introduction

Over the past 50 years there has been a large focus on reducing the amount of volatile organic compounds within the paint and coatings industry, and creating systems that are water-based.¹⁻

⁴ This push to reduce volatile organic compounds (VOCs) is largely due to the concerning issue of greenhouse gas emissions causing climate change.⁵ However, this task has proven to be challenging and complete water-borne replacements for many current solvent-borne paint products have not yet been found. A particular class of paint that is proving difficult to replicate as a water-borne system is gloss paint. Gloss paints are largely applied to doors, skirting boards, and other wooden surfaces to provide a protective barrier to prevent external damage. These coatings need to be mechanically robust (strong and flexible) and must be water-resistant. These inherent properties make these paints hard to formulate for a water-based system. Specifically, formulating a coating that is water-soluble/compatible in solution but becomes water-resistant upon drying is challenging since these two properties are contradictory.

Although the overall task of achieving comparable properties from water-based systems has proved to be difficult, a vast number of important findings around this subject have been established. Martín-Fabiani *et al.* has recently explained why films formed from copolymer latexes, synthesised by emulsion copolymerisation with additional surfactant, are prone to

severe water-whitening.⁶ This research suggests that the added surfactant (which is needed to stabilise the latex during polymerisation) promotes the formation of large water pockets that scatter a large amount of light and cause opacity.⁶ When the surfactant is removed, such as in secondary dispersion copolymers, the uptake of water in the films remains high. However, water is only present at the phase boundary with relatively small length scales. Therefore, these systems are less prone to water-whitening. Furthermore, Lesage De La Haye *et al.* investigated what effect crosslinking copolymer latexes at different points in their film formation procedure had on the mechanical film properties.⁷ They found that if the crosslinking occurred during particle formation then the interdiffusion of chains during the drying process was inhibited, which resulted in a brittle film. However, if the crosslinking occurred during the drying process then coalescence of the copolymer particles occurred before the chain mobility was restricted by the crosslinking. This method of crosslinking was found to produce films with a high modulus and strength along with a high strain at failure.⁷

Over the past few years, a large amount of research has focussed on investigating the use of block copolymers as binders in water-based paint formulations to form copolymer films with improved mechanical properties.⁸⁻¹² By using block copolymers composed of a component with a low glass transition temperature (T_g), and a component with a high T_g , nanoscale phase separation can be induced. A two-phase system allows properties of both polymer blocks to be utilised. The soft block (low T_g) aids film formation of the copolymer whilst the hard block (high T_g) increases the stiffness and toughness of the coating. Bouteiller *et al.* recently demonstrated how poly(butyl acrylate-*b*-acrylic acid) copolymer particles synthesised by reversible addition-fragmentation chain transfer (RAFT) aqueous emulsion polymerisation can be used to form tough transparent films.¹³ As the latex dries, the core-shell structure of the particle is maintained because the hard acrylic acid shell prevents interdiffusion of the soft butyl acrylate cores. This results in a honeycomb-like network of cores separated by a

percolating network of acrylic acid, providing a tough film.¹³ Hydrogen bonding between the acrylic acid groups in the outer continuous phase provides resistance against a variety of organic solvents. Furthermore, no water-whitening was observed when the film was immersed in water for 72 hours, since the copolymers were synthesised *via* surfactant free emulsion polymerisation.⁶ However, despite the added benefits of a percolating network of acrylic acid with regards to the mechanical properties, resistance to organic solvents and lack of water-whitening, this continuous network of copolymers offers a direct path for the transport of water through the copolymer coating reducing its water-resistance. When this film was annealed above the T_g of acrylic acid ($T > 100$ °C), the increased mobility of the hard block allowed inversion of the phase separated structure to the most thermodynamically stable conformation resulting in butyl acrylate becoming the continuous phase.¹³

Herein, we hypothesise that by designing ABA triblock copolymers, where the A block is composed of a statistical copolymer of hydrophile and hydrophobe of similar hardness, the water resistance of the copolymer film can be increased, whilst still maintaining a stable dispersion as particles in water. By statistically distributing a hydrophobe amongst the hydrophilic stabiliser block the size of the hydrophilic regions within the triblock film are reduced, increasing its water-resistance. Furthermore, using an ABA triblock copolymer with alternating hard and soft segments induces covalently crosslinked phase separation within the bulk structure. This crosslinking should have a positive impact on the mechanical properties of the final copolymer film. Therefore, this chapter demonstrates the synthesis of a library of poly(acrylic acid-*stat*-styrene)-*b*-poly(butyl acrylate)-*b*-poly(acrylic acid-*stat*-styrene) (P[(AA-*st*-St)_x-*b*-BA_y-*b*-(AA-*st*-St)_x]) ABA triblock copolymers in a controlled, but high-throughput, manner so that a large range of mechanical properties can be achieved. Additionally, this research demonstrates the importance of block copolymer design and

structure on the film properties by studying the differences between films cast from both solvent and water.

6.2 Triblock copolymer synthesis

6.2.1 Synthesis of P(AA-*st*-St) macro-CTA *via* RAFT solution polymerisation

Three P(AA-*st*-St) macro-CTAs varying in chain length were synthesised. The protocol describes the quantities used to synthesise AA₅₆.

AA (33.9 g, 0.471 mol), St (49.1 g, 0.471 mol) AIBN (0.186 g, 0.00114 mol), and DBzTTC (1.65 g, 0.00568 mol) were mixed in MEK (105 mL) (Figure 6.1a). The mixture was degassed with N₂ for 60 minutes and then heated to 80 °C to initiate polymerisation. This polymerisation was quenched in air after 7 hours at a monomer conversion of 68%. The initial P(AA-*st*-St) macro-CTA was purified by multiple precipitations into hexane and the product was collected as a solid yellow powder.

6.2.2 High-throughput syntheses of triblock copolymers *via* RAFT solution polymerisation

Specific quantities (Appendix 14) of the purified P(AA-*st*-St) macro-CTA were added to 8 reaction vessels of the ChemSpeed high-throughput robot. The macro-CTA was then dissolved in MEK at 50 °C. Once the all the macro-CTA was fully dissolved, the solution was cooled to ambient temperature and BA (5.00 g, 35.2 mmol) was added. Quantities of an AIBN solution in MEK were added to the 8 reaction vessels and then a stream of nitrogen was blown through all the reaction vessels for 30 minutes in order to expel any oxygen from the reaction vessel. The mixtures were then heated to 80 °C and stirred with an overhead anchor stirrer for 8 hours.

The reaction mixtures were left to cool to ambient temperature overnight and decanted into 100 mL sample pots (Figure 6.1b).

6.3 Results and discussion

6.3.1 Synthesis and characterisation of copolymers

A library of P[(AA-*st*-St)_x-*b*-BA_y-*b*-(AA-*st*-St)_x] ABA triblock copolymers was synthesised using RAFT copolymerisation. A symmetrical, bifunctional RAFT agent was used in order to achieve a symmetrical triblock copolymer.¹⁴ The first step towards forming these triblock copolymers was to synthesise a large batch of macro-CTA that would form the “A” blocks of the triblock copolymer. This macro-CTA was synthesised *via* RAFT copolymerisation of styrene (St) and acrylic acid (AA) in MEK to form a statistical copolymer (Figure 6.1a). Both PSt and PAA are reported to have high glass transition temperatures ($T_g \sim 100$ °C) and will form a “hard” phase within the triblock copolymer. All the synthesis in this chapter was performed in an industrial polymer laboratory, thus there were additional protocols in place to maintain high levels of health and safety. One limitation was that no reactions were to be left on overnight, therefore restricting the reaction time of any polymerisations to 8 hours (one working day). Initially, it was found that RAFT copolymerisation of styrene and acrylic acid was not able to reach high monomer conversion after 8 hours at a concentration of 30% w/w. The concentration was increased to 50% w/w so that a suitable conversion (68%) was achieved within the 8-hour timescale. The resulting copolymers were isolated by precipitation into hexane; this process was repeated multiple times in order to remove any residual monomer.

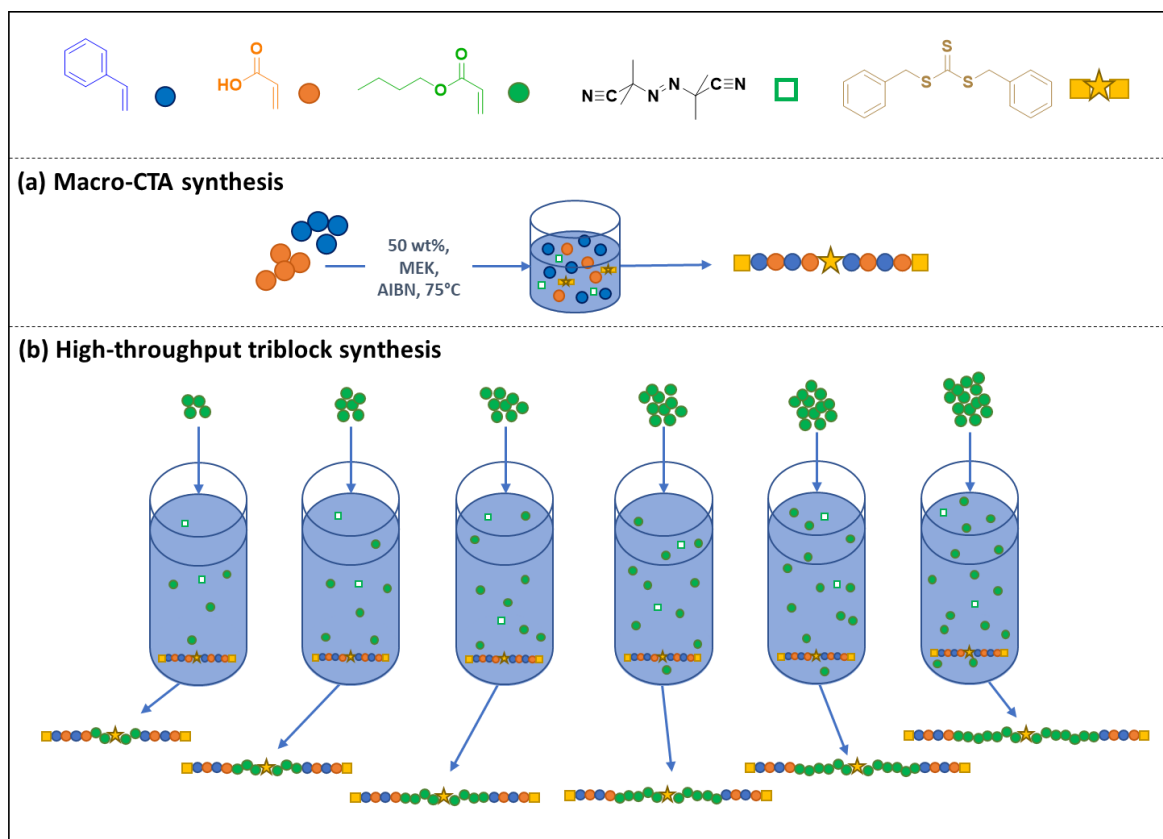


Figure 6.1. The RAFT polymerisation used to produce the library of different P[(AA-*st*-St)-*b*-BA-*b*-(AA-*st*-St)] triblock copolymers, where (a) is the P(AA-*st*-St) macro-CTA synthesis used to prepare A₅₆, A₁₀₈, and A₁₄₀ (Table 6.1), and (b) is the high throughput synthesis of the triblock copolymers, A₅₆B₁₀₀₋₇₅₀A₅₆, A₁₁₂B₁₀₀₋₇₅₀A₁₁₂, and A₁₄₀B₁₀₀₋₇₅₀A₁₄₀ (Table 6.2), using ChemSpeed High-Throughput Robot.

Three P(AA-*st*-St) macro-CTAs were synthesised with similar compositions (50:50) but different degrees of polymerisation (DP). By varying the DPs of the macro-CTAs the effect of the hard segment length within the triblock copolymer could be assessed. Once the macro-CTAs were synthesised and purified, the DP and compositions were calculated by ¹H NMR spectroscopy and molecular weight analysis was performed using APC (Section 2.2.4, Table 6.1). It was found that the composition of all three of the macro-CTAs were 42:58 (AA:St), which slightly deviates from the original monomer feed ratio suggesting deviations in the reaction rates of the two monomers. The reactivity ratios of the St-AA pair in a range of

solvents are known to be much less than 1 (e.g., $r_{St} = 0.15$, and $r_{AA} = 0.25$).¹⁵ Therefore, at a 50:50 (AA:St) composition the copolymer can be considered to be fairly alternating. However, since there is a lower mole fraction of AA in the final copolymer composition, the copolymer composition is likely to deviate along the copolymer chain. The initial composition will be 50:50 but as the copolymer chain grows the composition will become more styrene-rich. The DPs of the three macro-CTAs were determined to be 112, 216 and 280, respectively (Table 6.1). However, it is important to bear in mind that these macro-CTAs were synthesised with a symmetrical, bifunctional RAFT agent (Figure 6.1a) meaning that the trithiocarbonate functional group of the RAFT agent is located approximately in the middle of the macro-CTA.¹⁶ Therefore, the copolymer will grow from the middle if reacted with a third monomer to create an ABA triblock structure, where the A blocks will be half the DP of the respective macro-CTA (i.e., 56, 108, and 140). Thus, the three macro-CTAs are denoted throughout this chapter as A_{56} , A_{112} , and A_{140} where the subscript indicates the length of the hard blocks in the final triblock copolymer. Furthermore, it should be noted again that the macro-CTAs (A_x) are statistical copolymers of AA and St with respective compositions of 42:58. Molecular weight analysis showed that the molecular weight of the macro-CTAs increased with the DP and all the copolymers had an $M_w/M_n < 1.3$ (Table 6.1). The T_g s of A_{56} , A_{112} , and A_{140} were measured using DSC (Section 2. 2.10) and were found to be 108, 120, and 115 °C, respectively. Both PSt and PAA are reported to have high T_g s of 100 and 105 °C, respectively. Overall, the T_g s measured here are higher than those of the individual homopolymers, which could be caused by the formation of an anhydride with a higher T_g due to dehydration of AA at temperatures above 100 °C.^{17,18}

Table 6.1. Composition, molecular weight, and thermal data collected for macro-CTAs A₅₆, A₁₀₈, and A₁₄₀ used for the P(AA-*st*-St) synthesis.

Copolymer	NMR		GPC			DSC
	DP of copolymer*	Mol. Frac. of AA	M_n (kDa)	M_w (kDa)	M_w/M_n	T_g (°C)
A ₅₆	112 (56 + 56)	0.42	9.1	11.4	1.26	108
A ₁₀₈	216 (108 + 108)	0.42	15.9	19.8	1.24	119
A ₁₄₀	280 (140 + 140)	0.42	19.2	24.5	1.28	105

*- corresponds to the total DP of both A blocks used for synthesising ABA triblock, where the A blocks will be half the DP of the respective macro-CTA.

A high throughput synthesis was utilised in order to create a large library of triblock copolymers where the copolymer properties were varied across the series (Figure 6.1b). Using a high throughput synthesis method allows a large number of copolymers to be synthesised in a very short amount of time (18 copolymers in 1 day). All the copolymerisations were performed at 40% w/w and reached reasonable monomer conversion (> 70%) within 8 h. (Table 6.2). However, the conversions were lower when a longer macro-CTA (A₁₄₀) was used resulting in these triblocks having an average conversion of 74%. Each macro-CTA was extended to target 6 different butyl acrylate (BA) chain lengths creating 18 ABA triblock copolymers in total, where the DP of both the hard (A) and soft (B) blocks were varied along with the total DP of the triblock copolymer (Figure 6.2). Molecular weight analysis of the triblock copolymers demonstrated high blocking efficiency of the BA, where M_w increased as the targeted DP of the soft block increased (Figure 6.3). Additionally, all the triblocks had an $M_w/M_n < 1.45$ (Table 6.2). An increase in M_w/M_n is expected if there is some residual unreacted macro-CTA present as well as diblock copolymers formed through cleavage of the trithiocarbonate group located in the middle of the triblock chain; both these phenomenon lead

to a low molecular weight tail as can be observed in the APC trace (Figure 6.3). The T_g s of the triblocks were investigated using DSC to assess the influence of the soft BA block. Generally, the addition of BA induced an additional T_g at low temperatures (-27.0 °C to -44.2 °C) and this T_g decreased as the length of the BA block increased. However, when the composition of the triblock copolymer was largely weighted to either the soft or hard component only one T_g was observed from the dominating component.

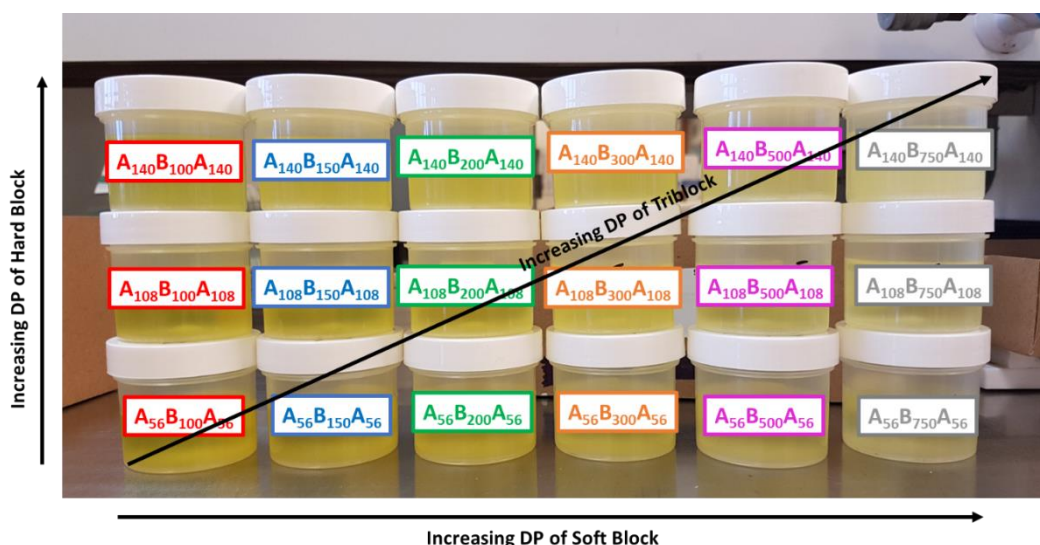


Figure 6.2. A photograph of the triblock solutions synthesised on the ChemSpeed High-Throughput Robot depicting how the copolymer is varied across the triblock copolymer series.

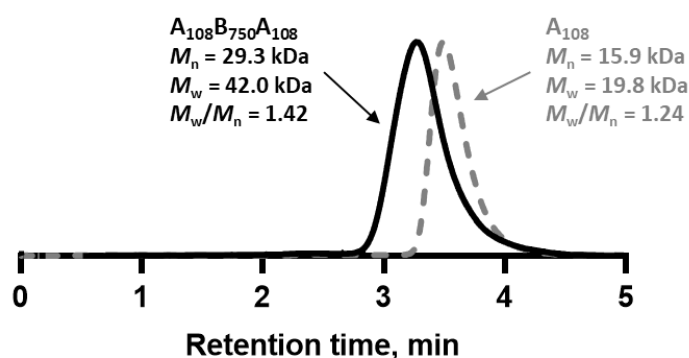


Figure 6.3. An example APC trace of $A_{108}B_{750}A_{108}$ (black solid line) and A_{108} (grey dashed line) demonstrating the blocking efficiency.

Table 6.2. Composition, molecular weight, and thermal data of the P[(AA-*st*-St)-*b*-BA-*b*-(AA-*st*-St)] triblock copolymers.

Macro-CTA	Triblock	NMR		APC			DSC	
		DP (BA)	Conv. (%)	M_n (kDa)	M_w (kDa)	M_w/M_n	T_g (Soft)	T_g (Hard)
A ₅₆	A ₅₆ B ₁₀₀ A ₅₆	100	89	11.4	15.4	1.34	-31	-
	A ₅₆ B ₁₅₀ A ₅₆	150	93	13.4	18.1	1.35	-38	-
	A ₅₆ B ₂₀₀ A ₅₆	200	92	14.5	19.7	1.25	-40	-
	A ₅₆ B ₃₀₀ A ₅₆	300	92	18.5	25.0	1.35	-42	-
	A ₅₆ B ₅₀₀ A ₅₆	500	92	24.8	33.1	1.34	-44	-
	A ₅₆ B ₇₅₀ A ₅₆	750	88	32.2	41.5	1.29	-44	-
A ₁₀₈	A ₁₀₈ B ₁₀₀ A ₁₀₈	100	78	17.3	21.6	1.25	-	100
	A ₁₀₈ B ₁₅₀ A ₁₀₈	150	82	18.0	23.0	1.28	-33	125
	A ₁₀₈ B ₂₀₀ A ₁₀₈	200	86	21.3	26.2	1.23	-38	125
	A ₁₀₈ B ₃₀₀ A ₁₀₈	300	85	19.9	26.3	1.32	-40	-
	A ₁₀₈ B ₅₀₀ A ₁₀₈	500	88	25.3	35.0	1.38	-42	-
	A ₁₀₈ B ₇₅₀ A ₁₀₈	750	86	29.3	42.0	1.43	-43	-
A ₁₄₀	A ₁₄₀ B ₁₀₀ A ₁₄₀	100	74	20.5	25.8	1.26	-	100
	A ₁₄₀ B ₁₅₀ A ₁₄₀	150	72	22.5	27.9	1.24	-	105
	A ₁₄₀ B ₂₀₀ A ₁₄₀	200	71	22.9	29.1	1.27	-27	125
	A ₁₄₀ B ₃₀₀ A ₁₄₀	300	76	24.9	32.3	1.30	-34	-
	A ₁₄₀ B ₅₀₀ A ₁₄₀	500	72	25.3	32.2	1.28	-39	-
	A ₁₄₀ B ₇₅₀ A ₁₄₀	750	75	34.6	47.2	1.37	-41	-

6.3.2 Solution behaviour of the macro-CTAs and triblock copolymers in an organic solvent

The macro-CTAs were dissolved in MEK to form 1% w/w solutions and analysed using SAXS (Figure 6.4). The SAXS patterns show a clear plateau in intensity in the low q region ($q \approx 0.04 \text{ \AA}^{-1}$) and a slope with a gradient that is close to -2. This scattering is indicative of a Gaussian coil.¹⁹ Consequently, these scattering patterns were all modelled using the Debye function for a Gaussian coil described in section 2.5.1. Using this model, the radius of gyration (R_g) of the copolymer chain can be calculated. It was found that the R_g systematically increased as the length of the copolymer chain increased, where A_{56} , A_{108} , and A_{140} , have an R_g of 27 Å, 37 Å, and 42 Å, respectively.

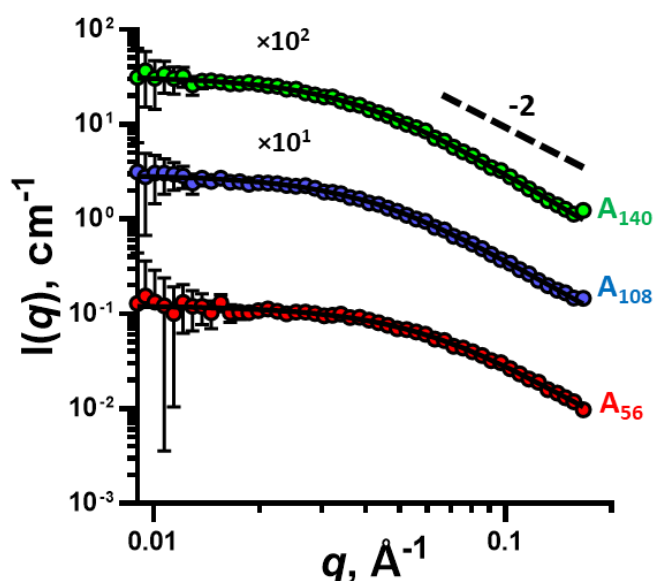


Figure 6.4. SAXS patterns of 1% w/w macro-CTA solutions in MEK (symbols) modelled with a Gaussian chain model (black line), demonstrating that the copolymers are fully dissolved. Some patterns are shifted upward by arbitrary factors (as indicated on the plots) to avoid overlap. Scattering patterns were collected using a Bruker AXS Nanostar instrument.

Additionally, the triblock copolymers were dissolved in MEK to form 1% w/w solutions. These copolymer solutions were consequently analysed using SAXS to investigate how the triblock copolymers behave in solution. It was found that MEK was a reasonable solvent for the triblock

copolymers as they all dissolved readily and demonstrated the slope of -2 at high q of the scattering patterns without an indication of a particle morphology formation (Figure 6.5). Despite this, it is clear from the scattering patterns that extending the macro-CTA with BA had an effect on copolymer solubility in MEK. The solubility of the copolymers in MEK varies as the copolymer composition changes as indicated by the varying gradients at low q . A non-zero gradient at low q -values suggests that some of the chains are interacting with each other and are possibly forming larger objects such as loose fractals. As a result, the radius of gyration of a single copolymer chain cannot be obtained. However, it must be stressed that these interactions are weak and that the triblocks are in an unconstrained structure.

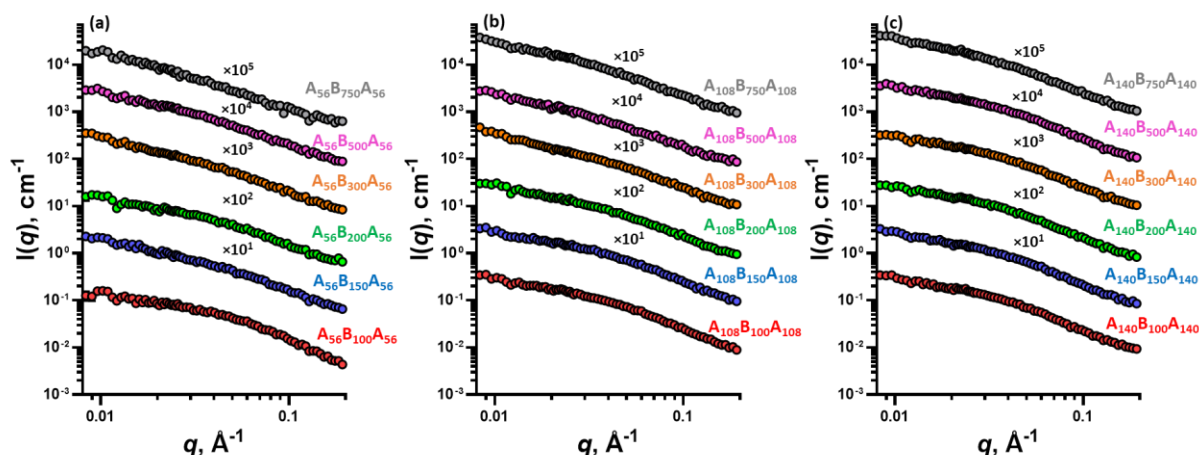


Figure 6.5. SAXS patterns of 1% w/w triblock copolymer solutions in MEK (symbols) that demonstrate that the copolymers within the solution are dissolved and do not assemble into particles, where (a) $A_{56}B_{100-750}A_{56}$, (b) $A_{108}B_{100-750}A_{108}$ and (c) $A_{140}B_{100-750}A_{140}$ triblock solutions. Some patterns are shifted upward by arbitrary factors (as indicated on the plots) to avoid overlap. Scattering patterns were collected using a Bruker AXS Nanostar instrument.

3.3 Solution behaviour of the macro-CTAs and triblock copolymers in an aqueous solution

The behaviour of the macro-CTA (A_{56} , A_{108} , and A_{140}) in aqueous conditions was analysed by SAXS. Dispersions of the macro-CTAs were formulated using a solvent switch method where the copolymers were initially dissolved at 75% w/w in IPA and diluted with ammonia and water to produce stable dispersions. The macro-CTA dispersions were diluted to both 5% w/w and 1% w/w for SAXS analysis (Figure 6.6).

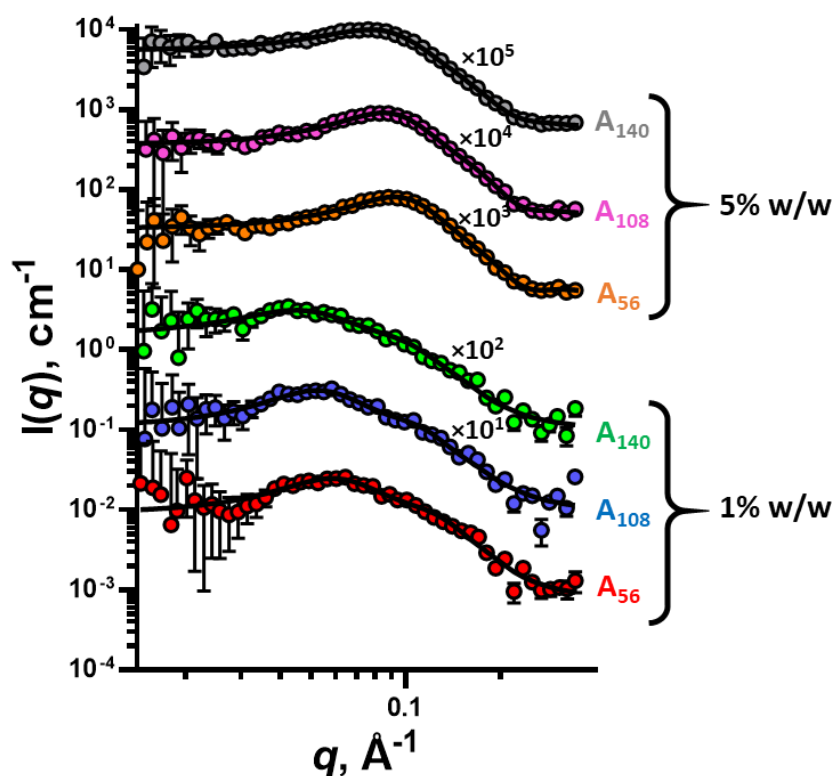


Figure 6.6. SAXS patterns of macro-CTA (A_{56} , A_{108} , and A_{140}) aqueous dispersions (symbols) at 1% w/w and 5% w/w concentration that are modelled with the sphere model (solid line). Some patterns are shifted upward by arbitrary factors (as indicated on the plots) to avoid overlap. Scattering patterns were collected using a Bruker AXS Nanostar instrument.

The SAXS patterns of the macro-CTA dispersions clearly show that these copolymers self-assemble into particulate structures and can be fit with a simple sphere structural model (Section 2.5.2). However, a hard sphere structure factor was also incorporated based on the

Percus-Yevick approximation (Section 2.4.1) to account for the long-range charge interactions of the particles (Figure 6.6) as was done in chapter 3.²⁰ The formation of spherical particles from amphiphilic copolymers is concordant with previous work in this thesis and by Sawamoto and co-workers and further clarifies this behaviour.^{20,21} As with the P(BMA-*stat*-MAA) copolymers described in chapters 3 and 4, despite the differing DPs of A₅₆, A₁₀₈ and A₁₄₀, they all form spherical particles of a similar size ($R = 17 \text{ \AA}$). This observation is concordant with previous research as it has been found that the size of statistical copolymer particles is independent of molecular weight but heavily dependent on copolymer composition and the ratio of hydrophile and hydrophobe. Since the particle size remains constant whilst the molecular weight of the copolymer increases, the aggregation number of the particle must decrease, respectively, where A₅₆ particles will have a larger aggregation number than both A₁₀₈ and A₁₄₀.

Additionally, aqueous dispersions of the triblock copolymers were also formulated using a similar solvent-switch method to the macro-CTAs and diluted in water to 1% w/w for SAXS analysis. From the SAXS patterns collected for the 1% w/w copolymer dispersions (Figure 6.7) it is clear that the copolymers self-assemble to form particles through the hydrophobic interactions of BA that induce aggregation to reduce any unfavourable interactions between BA and water. Again, a peak in intensity caused by the electrostatic particle-particle interactions is observed in the Guinier region for the majority of the patterns collected; this feature can be fit with the hard sphere structure factor as has been done in the case of the macro-CTA dispersions. Furthermore, the position of the form factor intensity minima, that is indicative of particle size, moves to lower q -values as the length of the BA block increases, suggesting that the particle size increases with respect to BA DP.

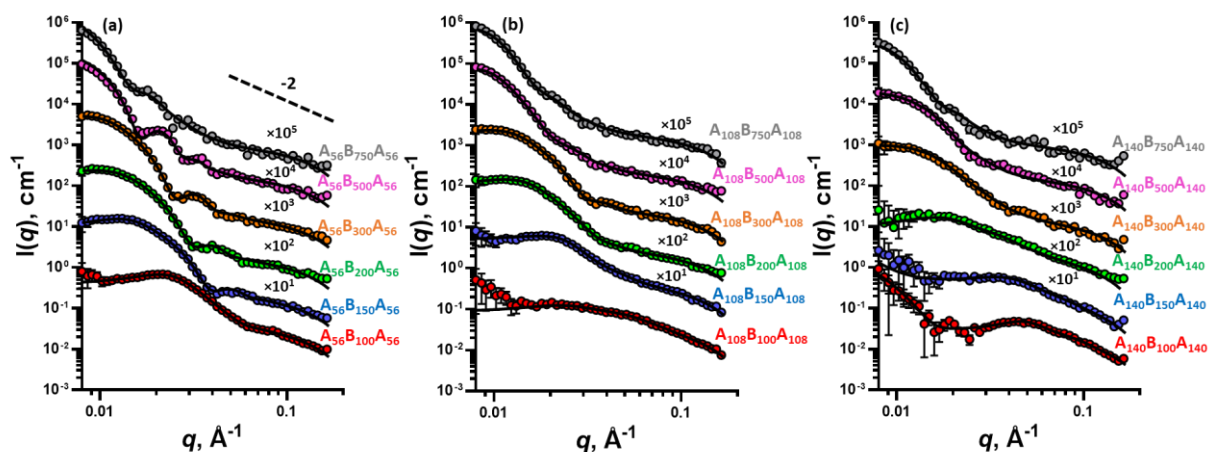


Figure 6.7. SAXS patterns of 1% w/w triblock copolymer aqueous dispersions (symbols) that are modelled with the two-population model (solid line), where (a) $A_{56}B_{100-750}A_{56}$, (b) $A_{108}B_{100-750}A_{108}$ and (c) $A_{140}B_{100-750}A_{140}$ triblock dispersions. Some patterns are shifted upward by arbitrary factors (as indicated on the plots) to avoid overlap. Scattering patterns were collected using a Bruker AXS Nanostar instrument.

Spherical block copolymer particles in a dispersion, where the soluble stabiliser block behaves as a Gaussian chain, typically produce scattering patterns with a -2 gradient in the high- q region. However, a slope that is shallower than -2 is observed in the high- q region ($q > 0.08 \text{ \AA}^{-1}$) of the majority of aqueous dispersion scattering patterns (Figure 6.7). This suggests that there is an additional structural feature that produces scattering within the high- q region. This high- q feature is more prominent in the copolymers where the P(AA-*st*-St) stabiliser blocks are a larger fraction of the overall composition (*e.g.*, $A_{140}B_{100}A_{140}$) (Figure 6.7) and can clearly be seen when the concentration of the dispersion is increased since the number of particles that are scattering X-rays has increased with regard to the solvent background (indicated by arrows in Figure 6.8). This suggests that the high- q feature is related to an additional structural feature within the stabiliser block.

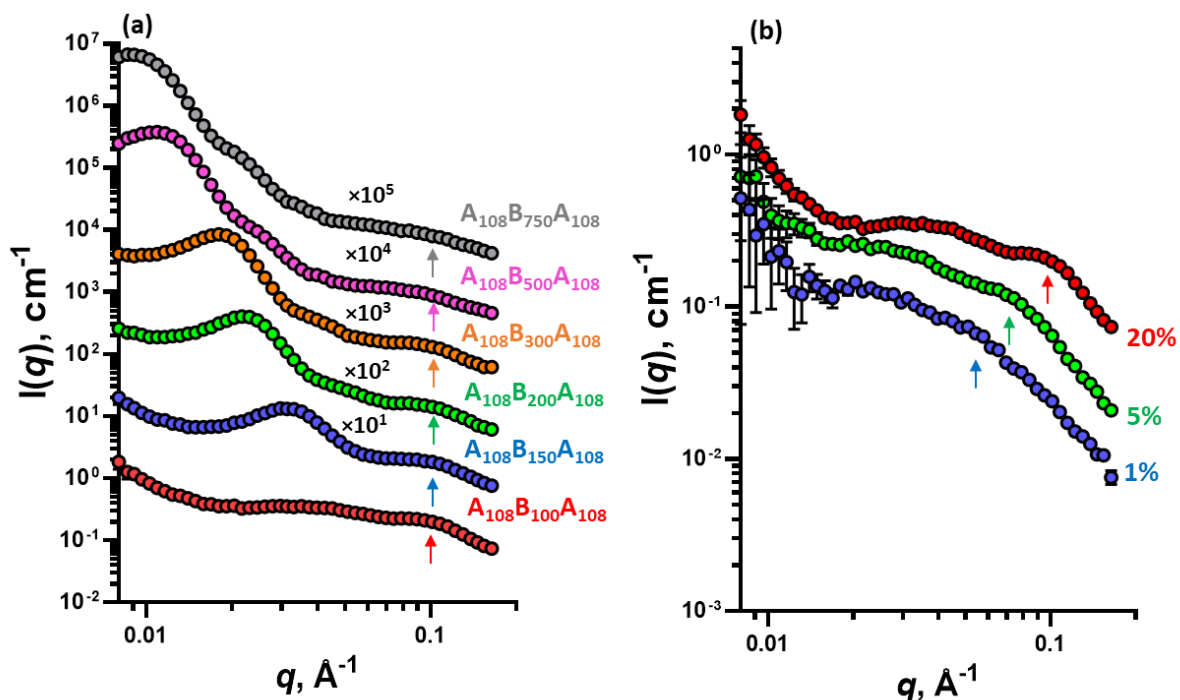


Figure 6.8. SAXS patterns of triblock copolymer aqueous dispersions (symbols), where (a) $A_{108}B_{100-750}A_{108}$ triblock dispersions at 20 %w/w concentration and (b) $A_{108}B_{100}A_{108}$ triblock dispersion at 1, 5, and 20% w/w concentrations; the arrows are used to highlight the presence of the structural peak referred to in the text. Some patterns are shifted upward by arbitrary factors (as indicated on the plots) to avoid overlap. Scattering patterns were collected using a Bruker AXS Nanostar instrument.

The structural feature that is observed in both Figures 6.7 and Figure 6.8 is present in a higher- q region ($q \sim 0.1 \text{ \AA}^{-1}$) and, therefore, has a relatively small length scale in comparison to the size of the primary copolymer particle. The small length-scale and the increased presence of scattering at high q in the copolymer dispersions with a larger fraction of stabiliser block further indicates that the scattering is caused by an additional structural feature within the P(AA-*st*-St) block located within the particle surface. Since this is the case, two potential explanations were explored: (1) that there are SLD fluctuations within the corona block of the particle caused by the statistical distribution of styrene and acrylic acid; and (2) that the hydrophobic nature of styrene causes the statistical block to undergo single chain folding on the particle surface through hydrophobic interactions - this phenomenon is often observed for amphiphilic statistical copolymers.²²⁻²⁷ Both cases appear to be valid explanations for this phenomenon,

however, the observation that the macro-CTAs will undergo spontaneous self-assembly to form spherical particles (Figure 6.6) indicates that the amphiphilic nature of the stabiliser block is enough to initiate self-folding of the chain (Figure 6.9). Furthermore, the former case, where the scattering at high q is a result of SLD fluctuations, is more likely if both monomers within the stabiliser block are water-soluble.

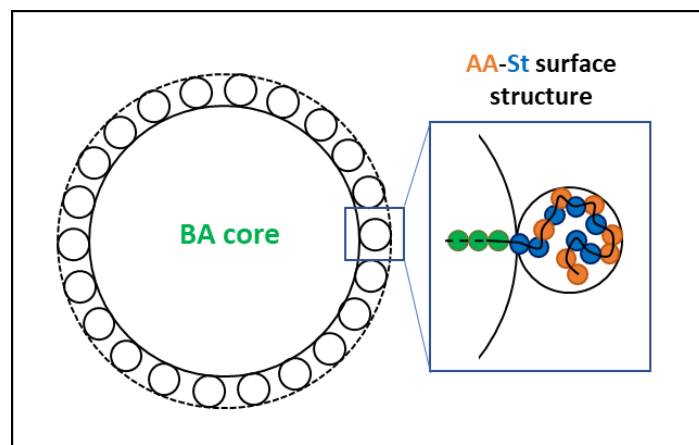


Figure 6.9. A diagram describing the predicted structure of the triblock copolymer aqueous dispersions where the P(AA-*st*-St) stabiliser block is confined by the copolymer particle surface and “self-folds” through hydrophobic interactions.

Since the stabiliser block of the copolymer particle provides additional structure that is assumed to be spherical based upon the behaviour of the macro-CTAs in water (Figure 6.6), and therefore does not behave as a Gaussian chain, the standard copolymer micelle structural model cannot be used to model the SAXS patterns of the triblock dispersions. Instead, a two-population structural model that has been previously used to model core-particulate shell polymer-silica colloidal particles that accounts for spherical structures on the surface of the copolymer particle was used and is described in section 2.5.8.²⁸

For simplicity, the radius of the surface structure (r_2) was not fit during modelling of the SAXS

patterns but is assumed to be equal to $r_2 = \sqrt[3]{\frac{3V_{AA-St}}{4\pi}}$, since the structure is unimolecular, where

V_{AA-St} is the volume of the copolymer chain block and is directly related to the DP of the respective macro-CTA. The V_{AA-St} for A_{56} , A_{108} , and A_{140} , were calculated to be 6988 \AA^3 , 13477 \AA^3 , and 17470 \AA^3 , respectively. Therefore, r_2 for $A_{56}B_{100-750}A_{56}$, $A_{108}B_{100-750}A_{108}$, and $A_{140}B_{100-750}A_{140}$ particles were fixed at 12 \AA , 15 \AA , and 16 \AA , respectively, while the core radius, R_{core} , was unfixed during SAXS model fitting. The results from this fitting can be seen in Table 6.3.

Table 6.3. Structural analysis results for P(AA-*st*-St) and P[(AA-*st*-St)-*b*-BA-*b*-(AA-*st*-St)] copolymer dispersions where, R_{core} is the mean particle core radius, σ_{core} is the standard deviation of the mean particle core radius, r_2 is the radius of the self-folded P(AA-*st*-St) chain on the surface of the particle (this value is fixed throughout the fitting at a value based upon the volume of the hard block), R_{PY} is the effective interparticle distance in the dispersion and the f_{PY} is the effective volume fraction corresponding to the hard sphere structure factor based on Percus-Yevick (PY) approximation.

Copolymer	R_{core} (Å)	σ_{core} (Å)	r_2 (Å)	R_{PY}	f_{PY}
A ₅₆	16	5	-	47	0.15
A ₁₀₈	16	7	-	53	0.16
A ₁₄₀	17	7	-	59	0.11
A ₅₆ B ₁₀₀ A ₅₆	53	14	12	117	0.15
A ₅₆ B ₁₅₀ A ₅₆	90	13	12	193	0.12
A ₅₆ B ₂₀₀ A ₅₆	119	18	12	224	0.10
A ₅₆ B ₃₀₀ A ₅₆	156	20	12	271	0.10
A ₅₆ B ₅₀₀ A ₅₆	247	28	12	<i>a</i>	<i>a</i>
A ₅₆ B ₇₅₀ A ₅₆	281	52	12	<i>a</i>	<i>a</i>
A ₁₀₈ B ₁₀₀ A ₁₀₈	18	9	15	115	0.08
A ₁₀₈ B ₁₅₀ A ₁₀₈	55	34	15	120	0.15
A ₁₀₈ B ₂₀₀ A ₁₀₈	99	24	15	196	0.12
A ₁₀₈ B ₃₀₀ A ₁₀₈	120	22	15	232	0.11
A ₁₀₈ B ₅₀₀ A ₁₀₈	191	39	15	306	0.15
A ₁₀₈ B ₇₅₀ A ₁₀₈	219	52	15	317	0.17
A ₁₄₀ B ₁₀₀ A ₁₄₀	15	5	16	60	0.21
A ₁₄₀ B ₁₅₀ A ₁₄₀	26	10	16	70	0.12
A ₁₄₀ B ₂₀₀ A ₁₄₀	32	23	16	148	0.12
A ₁₄₀ B ₃₀₀ A ₁₄₀	101	41	16	200	0.08
A ₁₄₀ B ₅₀₀ A ₁₄₀	150	41	16	200	0.08
A ₁₄₀ B ₇₅₀ A ₁₄₀	219	50	16	308	0.18

^a These parameters were not modelled as the scattering features were outside of the q -range investigated

The modelling results indicate that there is a clear trend in particle size, where the core radius increases as the length of the hydrophobic core-forming BA block increases. Additionally, the core radius increases as the stabiliser block length is reduced. These two influencing factors are commonly seen for block copolymer nano-particle assemblies.²⁹ Furthermore, when the triblock copolymers possess a very large stabiliser block (*e.g.*, the A₁₄₀B₁₀₀₋₇₅₀A₁₄₀ copolymers) their aggregation into larger particles appears to be significantly hindered until the BA DP reaches 300 and the core radii for A₁₄₀B₁₀₀A₁₄₀, A₁₄₀B₁₅₀A₁₄₀ and A₁₄₀B₂₀₀A₁₄₀ remain between 30 to 40 Å.

6.3.4 Structural characterisation of triblock copolymer films cast from an organic solvent

The analysis of the triblocks in both MEK and aqueous media demonstrate how differently the copolymers behave in different solvent environments. In MEK, the copolymers were generally found to be dissolved chains with some weak association into loose fractals, whereas, in water the copolymers readily aggregate together to form well-defined spherical particles with a particulate shell. Since the solution behaviour in each case is so different, it is important to see how these behaviours transfer into the bulk behaviour when films are cast of the triblocks. Therefore, triblock copolymer films were prepared from both the organic solutions and the aqueous dispersions. The structural phase separation within these films was assessed by SAXS and AFM. Firstly, films were drop-cast from a 40% w/w solution in MEK and formed transparent yellow films, where the yellowness of the film decreased as the triblock copolymer increased in molecular weight. This reduction in yellow colour is expected as the colour is caused by the trithiocarbonate group of the RAFT CTA present in the films, which decreases as the molecular weight of the triblock copolymer increases. These films were cast onto dry-release film and left to dry in ambient conditions for 1 week. If possible, the triblock film

was removed from the dry-released film and transmission mode SAXS was performed on the free-standing film. Some triblock films were too soft and tacky to be removed from the dry-release film without damaging the triblock film and destroying the morphology formed, in this case SAXS was performed on the triblock film whilst still attached to the dry-release film and a background scattering pattern of the dry-release film was subtracted from the combined scattering pattern.

It was expected that the hard and soft blocks within the triblock copolymer would undergo phase separation within the film and, since these two blocks have distinct scattering length densities, SAXS can be used to investigate the length-scale of separation (Figure 6.10). A peak in intensity was observed in the majority of the SAXS patterns of the triblock films cast from solvent. Firstly, the presence of this peak indicates that there is a structural order, which is likely to be associated with phase-separation occurring within the film.³⁰ Secondly, the position of the peak indicates the length-scale of the phase-separation.³⁰ The absence of a peak in the SAXS patterns of $A_{140}B_{100}A_{140}$ suggests that the DP of the soft block (PBA, DP = 100) is not large enough to induce phase-separation from the large hard block [P(AA-*st*-St), DP = 140]. Similarly, there are only very small and ill-defined peaks observed in the scattering patterns of $A_{108}B_{100}A_{108}$ and $A_{140}B_{150}A_{140}$, which suggests that although some phase-separation has been induced, it is minimal and unordered.

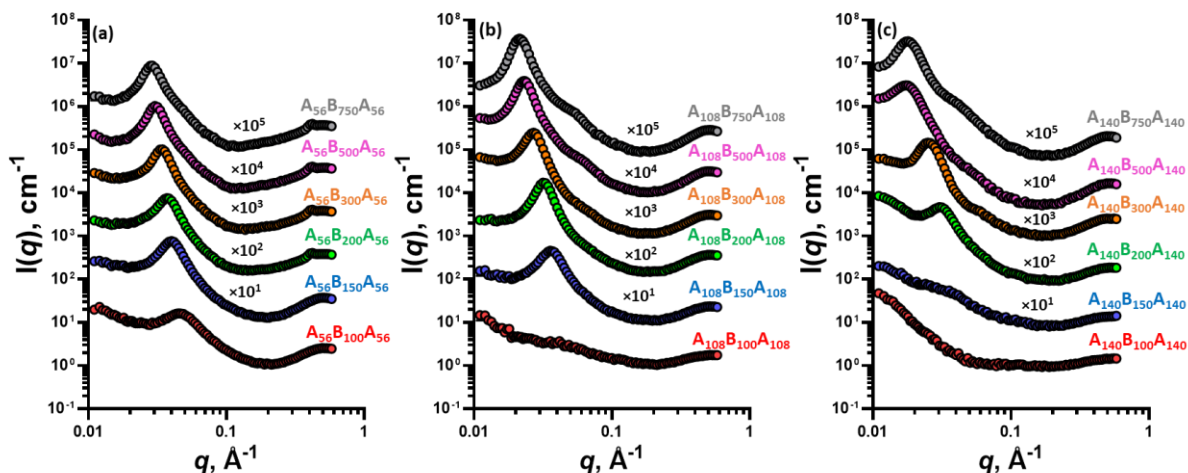


Figure 6.10. SAXS patterns of triblock copolymer films cast from a 40% w/w solution in MEK (symbols) for (a) $A_{56}B_{100-750}A_{56}$, (b) $A_{108}B_{100-750}A_{108}$ and (c) $A_{140}B_{100-750}A_{140}$ samples. Some patterns are shifted upwards by arbitrary factors (as indicated on the plots) to avoid overlap. Scattering patterns were collected using a Xenocs Xeuss instrument.

Aside from $A_{108}B_{100}A_{108}$, $A_{140}B_{100}A_{140}$, and $A_{140}B_{150}A_{140}$, the SAXS patterns of the solvent cast triblock copolymer films show a sharp peak in intensity suggesting that there is prominent phase separation within the film. The position of the primary peak (q^*) indicates the length scale of the phase separation and the d -spacing can be calculated using the equation $d = \frac{2\pi}{q}$.

The SAXS patterns for the individual triblock series (*e.g.*, $A_{108}B_{100-750}A_{108}$) shows that the primary peak position shifts to a lower q -value as the DP of the soft BA block is increased (Figure 6.10 and Table 6.3) demonstrating that the size of the phase-separation is increasing, respectively. Additionally, if the peaks are compared between copolymers with the same length of soft-block but synthesised with different length macro-CTAs then the effect of the hard-block can be resolved (Figure 6.11). This analysis indicates that increasing the length of the hard block has a similar effect to increasing the length of the soft-block and the overall size of the phase separation increases (Table 6.4). Furthermore, increasing the overall triblock DP whilst maintaining a constant ratio of soft and hard units further increases the size of the phase separation (Table 6.4).

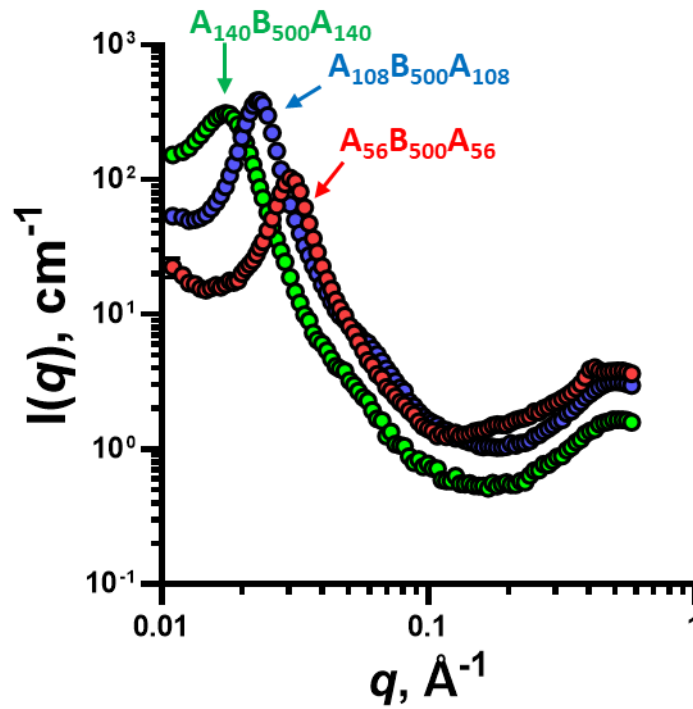


Figure 6.11. SAXS patterns of $A_{56}B_{500}A_{56}$, $A_{108}B_{500}A_{108}$, $A_{140}B_{500}A_{140}$ triblock copolymer films cast from a 40% w/w solution in MEK (symbols), demonstrating how the length-scale of the phase separation increases as the length of the hard block (A) increases. Scattering patterns were collected using a Xenocs Xeuss instrument.

Table 6.4. Structural analysis by SAXS and AFM investigating the bulk and surface phase separation of the solvent-cast copolymer films, respectively, where q^* is position of the primary structural peak in the SAXS pattern, d_{SAXS} is the real space distance corresponding to q^* ($d_{\text{SAXS}} = 2\pi/q^*$), and d_{AFM} is the length scale of the phase separation measured by AFM (Appendix 15).

Triblock	q^* (\AA^{-1})	d_{SAXS} (\AA)	d_{AFM} (\AA)
A ₅₆ B ₁₀₀ A ₅₆	0.046	137	-
A ₅₆ B ₁₅₀ A ₅₆	0.043	146	-
A ₅₆ B ₂₀₀ A ₅₆	0.037	170	193
A ₅₆ B ₃₀₀ A ₅₆	0.036	175	216
A ₅₆ B ₅₀₀ A ₅₆	0.030	209	279
A ₅₆ B ₇₅₀ A ₅₆	0.029	217	306
A ₁₀₈ B ₁₀₀ A ₁₀₈	-	-	-
A ₁₀₈ B ₁₅₀ A ₁₀₈	0.037	170	-
A ₁₀₈ B ₂₀₀ A ₁₀₈	0.030	209	-
A ₁₀₈ B ₃₀₀ A ₁₀₈	0.028	224	308
A ₁₀₈ B ₅₀₀ A ₁₀₈	0.023	273	335
A ₁₀₈ B ₇₅₀ A ₁₀₈	0.023	273	355
A ₁₄₀ B ₁₀₀ A ₁₄₀	-	-	-
A ₁₄₀ B ₁₅₀ A ₁₄₀	0.038	165	-
A ₁₄₀ B ₂₀₀ A ₁₄₀	0.029	217	-
A ₁₄₀ B ₃₀₀ A ₁₄₀	0.027	233	-
A ₁₄₀ B ₅₀₀ A ₁₄₀	0.019	331	427
A ₁₄₀ B ₇₅₀ A ₁₄₀	0.019	331	450

An additional peak is present in all of the triblock copolymer films at $q = 0.513 \text{ \AA}^{-1}$, this peak equates to a distance of about 12 \AA . This peak remains in the same position despite the variations in copolymer composition and is likely to be caused by the packing of the copolymer chains within the phase separated blocks. In order to test this hypothesis, SAXS patterns were collected for both PBA and P(AA-*st*-St) in their solid states (Figure 6.12).

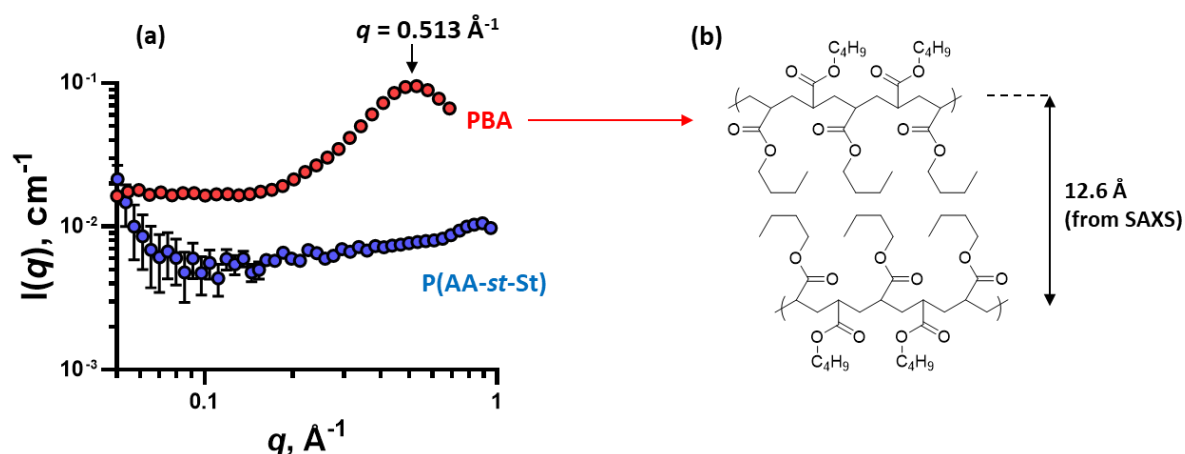


Figure 6.12. (a) SAXS patterns of solid-state PBA and P(AA-*st*-St) samples (symbols). (b) Diagram indicating the structural packing of BA units that induces a peak at $q = 0.513 \text{ \AA}^{-1}$ in the X-ray scattering pattern of PBA. Scattering patterns were collected using a Bruker AXS Nanostar instrument.

The SAXS pattern of PBA (Figure 6.12a) clearly shows a peak in a similar region to the one observed in the triblock copolymer films (Figure 6.10), whereas the pattern of P(AA-*st*-St) shows no such peak. This suggests that the peak observed in the triblock films is a result of structural packing of BA within the soft phase of the copolymer film (Figure 6.12b). Butyl acrylate has relatively long pendent groups that prevents the copolymer backbones from packing tightly together and instead the copolymer chains remain at a fixed distance from each other. The distance at which these chains are spaced is calculated to be 12.6 \AA (Figure 6.12b). A maximum packing distance, where the pendent groups are positioned without overlap, can be calculated as the product of the average C-C-C bond length (2.3 \AA) and the number of bonds

within the pendent group. The maximum packing distance was calculated to be 13.8 Å, which is larger than the measured separation. This means the pendent chains are not in a fully stretched position. A similar phenomenon has been observed in poly(behenyl methacrylate-*b*-benzyl methacrylate) [P(BeMA-*b*-BzMA)] nano-particles in mineral oil at 20 °C, where crystalline packing of the PBeMA within the particle corona was observed in the SAXS patterns.³¹ The crystalline packing of PBeMA chains was found to be 34.9 Å in length. The chain-chain packing of PBeMA is larger than that of PBA observed here since the alkyl chain of BeMA is 22 carbons long compared to BA, which has an alkyl chain length of just 4 carbons. PBeMA is a crystalline polymer and therefore the copolymer chains will undergo spontaneous packing at temperatures below its crystallisation temperature to form a well-ordered crystalline structure, which is observable by SAXS. However, PBA is an amorphous polymer and therefore does not form a crystal structure. Since PBA is amorphous, the ordered chain-chain packing observed is highly unexpected.

SAXS analysis has clearly confirmed the presence of phase separation in the majority of the triblock copolymer films and has allowed elucidation of how varying the copolymer properties affects the size of the phase separation. However, only one well-defined peak relating to the phase separated structure is observed in the SAXS patterns suggesting that the bulk structure of most of the compositions studied is not uniform enough to produce secondary and tertiary peaks. Attempts were made to obtain a more pronounced secondary peak by annealing the film overnight at 150 °C, which is above the T_g of the hard block. However, this was not successful and led only to a slight sharpening of the primary peak. This means that the structural morphology of the copolymer film cannot be assessed purely through peak positioning analysis of the SAXS patterns and a second structural characterisation technique is required.

Atomic force microscopy (AFM) was used to further investigate the phase separation of the triblock copolymer films cast from MEK (Figure 6.13). Unlike transmission mode SAXS, that

investigates the entire bulk of the film, AFM is only able to assess the surface structure. For this reason, it is important that the film is as flat as possible to allow a high-quality image to be collected. This was a problem for the films that had a high hard to soft block ratio, since the fundamental properties of the copolymers would distort the film upon drying resulting in a brittle, uneven film. Therefore, AFM images were not collected for $A_{56}B_{100}A_{56}$, $A_{108}B_{100}A_{108}$, $A_{108}B_{200}A_{108}$, $A_{140}B_{100}A_{140}$, $A_{140}B_{200}A_{140}$ and $A_{140}B_{300}A_{140}$. These brittle films demonstrated minimal/no phase separation in the SAXS patterns collected (Figure 6.10).

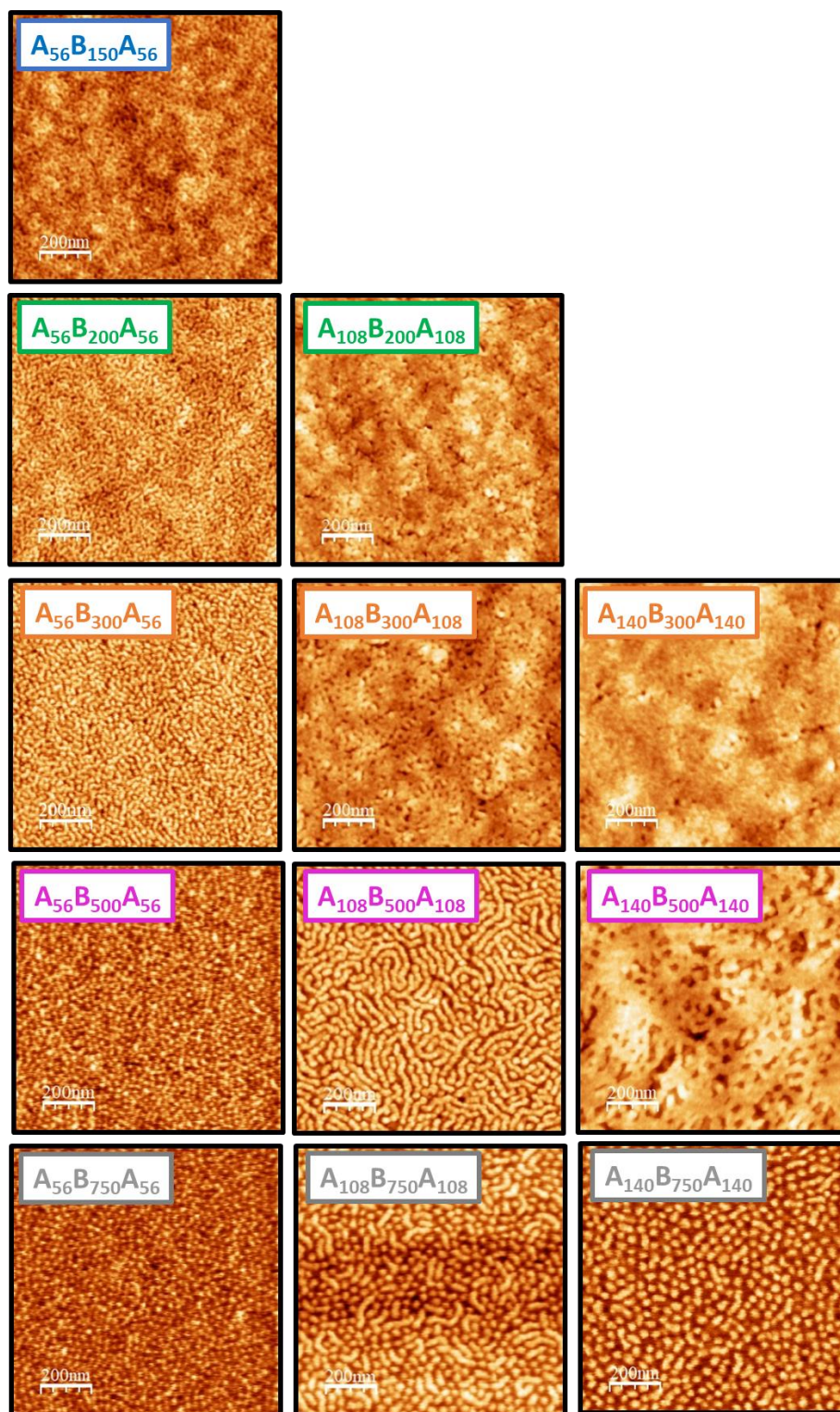


Figure 6.13. AFM height images of triblock copolymer films cast from a 40% w/w solution in MEK measured using ScanAsyst® PeakForce® tapping mode (lighter colour = higher structure relating to the hard phase, and *vice versa*), where the copolymer labels are shown on the respective images.

The AFM height images of the triblock films cast from MEK (Figure 6.13) firstly indicate that there is phase separation visible on the surface of the film, and secondly, that the structure and size of the phase separation varies as the copolymer composition is altered. From the AFM images it is clear that the size of the phase separation (Appendix 15) increases as the length of the hard block and the soft block increases, which is concordant with the conclusion established using SAXS. Furthermore, copolymers with the same hard-to-soft block ratio but with different total triblock lengths (*e.g.*, $A_{56}B_{200}A_{56}$, $A_{108}B_{300}A_{108}$, and $A_{140}B_{500}A_{140}$) demonstrate an increase in the size of the phase separation, which is again concordant with the SAXS results.

Unlike SAXS, the surface structure of the phase separation can be observed in the AFM images and from this it is clear that the relative ratios of the hard and soft components within the triblock copolymer have a large effect on the phase-separated structural morphology. Using A_{108} triblock series as an example, $A_{108}B_{200}A_{108}$ has a hard-block volume fraction (f_{HB}) of ~ 0.45 and shows no clear surface structure (Figure 6.13). However, as f_{HB} is reduced to ~ 0.36 for $A_{108}B_{300}A_{108}$ a clear structure can be observed. The soft phases (dark regions) emerge from the hard phase (light region) creating an ill-defined bicontinuous structure. When f_{HB} is further reduced to ~ 0.25 , and the total amount of soft phase is increased in $A_{108}B_{500}A_{108}$, the regions of soft phase combine to create a defined cylindrical structure where the rods are parallel with the surface. The final sample in this series, $A_{108}B_{750}A_{108}$, has an f_{HB} of ~ 0.18 and the AFM image shows that the soft phase is becoming dominant and forms a matrix around the hard phase. Self-consistent mean-field theory (SCMF) is often used to create a theoretical phase diagram of diblock-copolymer morphologies in bulk as a factor of f .³² It should be noted that this theory has been developed for diblock copolymers, whereas the copolymers being studied in this chapter are triblock copolymers. Nonetheless, based on this theory a copolymer with a minor component volume fraction of ~ 0.45 ($A_{108}B_{200}A_{108}$) is predicted to have a lamellae morphology. If the structure of $A_{108}B_{200}A_{108}$ is lamellae, then the surface phase separation may

not be observed if the lamellae sheets lie parallel with the film surface. SCMF suggests that as f decreases (*i.e.* $0.45 > 0.36 > 0.25 > 0.18$) the morphology will transition from lamellae, to gyroidal, to hexagonal cylinders and finally to a body-centred cubic structure. This theory generally agrees with the AFM observations made experimentally, for example the A₁₀₈ series shows clear transitions from a gyroid to cylinders to spheres as the BA block increases in size. However, the experimental morphologies observed are not very well ordered and appear to have some mixed phases (*e.g.* A₁₀₈B₇₅₀A₁₀₈ – small cylinders and spheres). The lack of order could be caused by a relatively large dispersity in chain lengths (Table 6.2); if the block length is polydisperse then the volume fractions of each block will vary and therefore an ill-defined structure will be observed.³³

By using two powerful structural characterisation techniques, such as SAXS and AFM, to analyse triblock films, the results can be both compared and used in unison. Firstly, the distance of the phase separation calculated using SAXS is systematically smaller than the distance measured using AFM (Table 6.4). This is because the distance observed *via* SAXS are d -spacings corresponding to crystallographic planes formed by structurally ordered objects, which tends to be smaller than the distance between the objects, defined by the period length of phase separation, measured by AFM.³⁰ Secondly, since the bulk triblock copolymer morphology can be assigned using AFM, the theoretical diffraction peaks that these structures would produce can be compared with the experimental SAXS data. Figure 6.14 demonstrates how the theoretical diffraction peak positions for a BCC structure, and hexagonally packed cylinders, compare with the scattering patterns of A₁₀₈B₇₅₀A₁₀₈, and A₁₀₈B₅₀₀A₁₀₈, respectively.

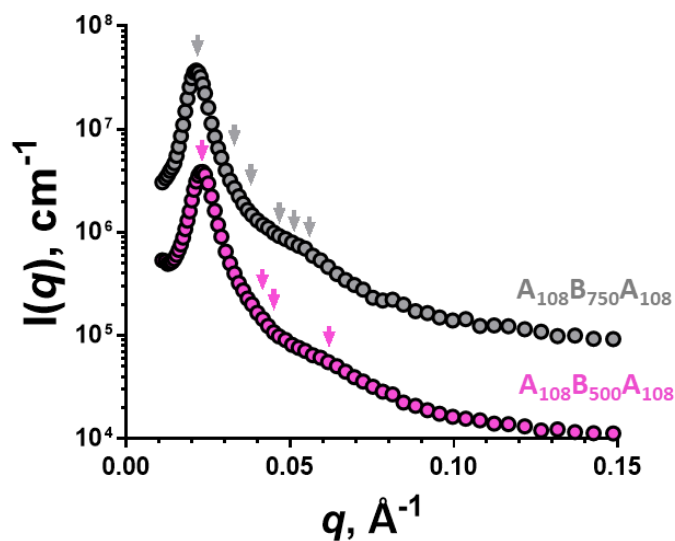


Figure 6.14. SAXS patterns of $A_{108}B_{750}A_{108}$ and $A_{108}B_{500}A_{108}$ triblock copolymer films cast from a 40% w/w solution in MEK (symbols), where the arrows indicate the theoretical positions of the diffraction peaks for a BCC structure (grey arrows) and a hexagonal structure (pink arrows). Some patterns are shifted upwards by arbitrary factors (as indicated on the plots) to avoid overlap. Scattering patterns were collected using a Xenocs Xeuss instrument.

A BCC structure has Miller indices, hkl , of 011, 002, 112, 013, 222, and 123, which relate to q -ratios (q/q^*) of $\sqrt{1}$, $\sqrt{2}$, $\sqrt{3}$, $\sqrt{5}$, $\sqrt{6}$ and $\sqrt{7}$, respectively. Whereas the Miller indices, hkl , of a hexagonal structure are 010, 110, 020 and 120, which relate to q -ratios (q/q^*) of $\sqrt{1}$, $\sqrt{3}$, $\sqrt{4}$, and $\sqrt{7}$, respectively. Figure 6.13 demonstrates that although the phase separated structure within the triblock films is not ordered enough to display sharp diffraction peaks relating to the expected crystal structure reflections, there are broad diffuse peaks in the regions corresponding to the location of the expected diffraction peaks. The distance, d_{011} , between the crystallographic planes, in a BCC structure, measured by SAXS can be used to calculate the particle-particle distance, a (Appendix 16);³⁰ this can then be compared with the size measured by AFM. The general equation used to relate d to a for a BCC structure is:

$$\frac{1}{d^2} = \frac{h^2 + k^2 + l^2}{a^2} \quad (6.1)$$

$A_{108}B_{750}A_{108}$ has a BCC structure where d_{011} is 273 Å (Table 6.4) that converts to a particle-particle distance of 334 Å. This calculated value is similar to the value measured by AFM ($d_{AFM} = 353$ Å, Table 6.4) and demonstrates the consistency between the two structural characterisation methods used within this chapter. A similar calculation can be performed on copolymers that have a hexagonal phase separation in the bulk (*e.g.*, $A_{108}B_{500}A_{108}$). The hexagonal structure of $A_{108}B_{500}A_{108}$ has an inter-plane distance, d_{010} , of 273 Å, which converts to a particle-particle distance of 315 Å; again, this is similar to the measured distance (Table 6.4).

6.3.5 Structural characterisation of triblock copolymer films cast from aqueous dispersion

Films were also cast from aqueous dispersions of the copolymers in order to assess how the solvent environment affects the phase separated structure in the film. SAXS and AFM were again used in combination to investigate the bulk and surface phase separation of the hard and soft phases within the triblock copolymers. The films were prepared by drop-casting the 20% w/w triblock copolymer dispersions onto dry release film in a similar way to the previous films cast from MEK. Transmission mode SAXS was used to investigate the size and structure of the phase separation within the bulk of the film and SAXS patterns were collected for all the triblock copolymer films (Figure 6.15).

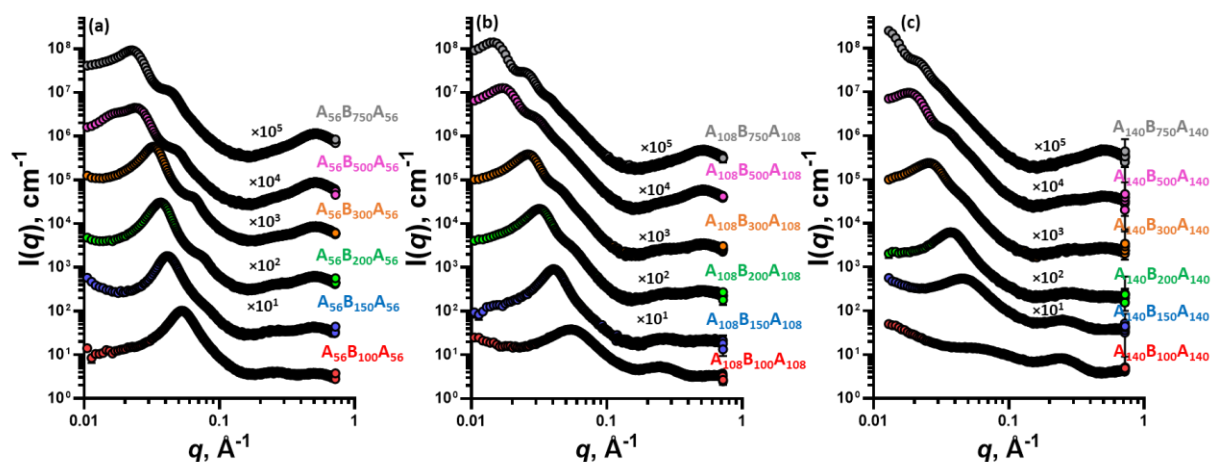


Figure 6.15. SAXS patterns of triblock copolymer films cast from a 20% w/w aqueous dispersion (symbols), for (a) $A_{56}B_{100-750}A_{56}$, (b) $A_{108}B_{100-750}A_{108}$ and (c) $A_{140}B_{100-750}A_{140}$ samples. Some patterns are shifted upwards by arbitrary factors (as indicated on the plots) to avoid overlap. Scattering patterns were collected using a Xenocs Xeuss instrument.

A primary intensity peak is observed in the SAXS patterns for all of the triblock films cast from water demonstrating that there is a phase separation present in all the films. This was not the case for the films cast from MEK, and $A_{108}B_{100}A_{108}$, $A_{140}B_{100}A_{140}$, and $A_{140}B_{150}A_{140}$ had either minimal or no phase separation - this suggests that an aqueous environment favours/facilitates phase separation. The hydrophobic interactions of BA induce the formation of particles when the triblock copolymer is in an aqueous environment (Figure 6.7) and the formation of these particles induces microscopic phase separation within the dispersion. Therefore, when the aqueous film is cast, there are already large regions of hard and soft blocks aggregated together making it easy for large-scale phase separation to occur within the film. Conversely, in MEK the triblock copolymers are dissolved and therefore do not phase separate in the solution phase making it more difficult to induce phase separation within the film. Furthermore, the evaporation of solvent during the drying process will cause both the dissolved chains and the dispersed particles to lose mobility. However, due to the size and rigidity of the particles, these systems will have substantially less mobility than the dissolved chains.

As mentioned previously, the SAXS patterns of all the triblock copolymer films cast from water demonstrate phase separation by the presence of a primary peak in intensity (q^*), where the position of this peak indicates the length scale of phase separation. A similar trend is observed in the films cast from water (Table 6.5, Figure 6.15) as was seen in the films cast from MEK (Table 6.4, Figure 6.13), where the size of the phase separation increases as the length of the soft block or hard blocks, or the total triblock, is increased. Despite these similarities between the water cast films and the solvent cast films, the general structure of the phase separation is different is demonstrated by the difference in the shape of the scattering patterns (Figure 6.16). Firstly, the primary peak for each of the triblock copolymers appears at a lower q -value when cast from water rather than MEK. Therefore, the triblock copolymers generally phase separate on a larger length-scale when cast from water. Furthermore, secondary and tertiary intensity peaks are observed in a selection of the scattering patterns of the water-cast films. The presence of these additional peaks suggests that the phase separation in the bulk of the film is more uniform and better defined than the solvent-cast films.

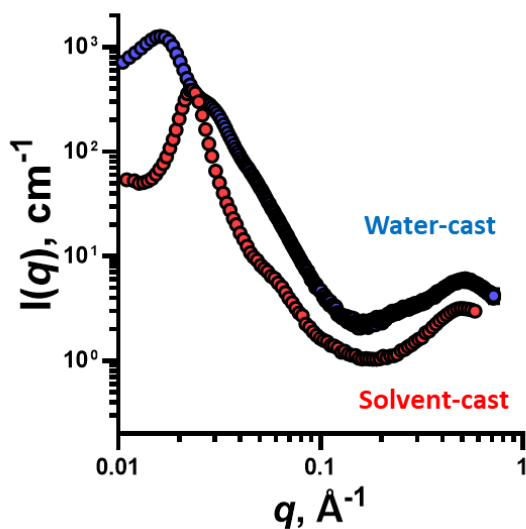


Figure 6.16. SAXS patterns of $A_{108}B_{500}A_{108}$ copolymer films cast from either a 20% w/w aqueous dispersion (blue symbols), or a 40% w/w solution in MEK (red symbols). Scattering patterns were collected using a Xenocs Xeuss instrument.

In addition to the high intensity peaks present at low q -values, there are a number of peaks present in the high q region that are a result of smaller, well-ordered structures within the film. The solvent cast films had a peak present at $q = 0.513 \text{ \AA}^{-1}$ that was a result of the packing of PBA within the soft phases. However, the aqueous films possess two peaks in the high q region that vary in intensity as the copolymer composition changes. Firstly, there is a peak at $q = 0.513 \text{ \AA}^{-1}$ similar to the solvent-cast films, which can therefore be attributed to the packing of PBA within the soft phase. However, there is an additional peak at $q = 0.276 \text{ \AA}^{-1}$, which corresponds to a length of 22 \AA and may be the result of the particulate shell structure formed by the statistical A block proposed for the triblock copolymer particles (Figure 6.9). The relative intensities of the two peaks vary with the copolymer composition, with the peak at $q = 0.513 \text{ \AA}^{-1}$ increasing in intensity as the length of the soft block increases while the peak at $q = 0.276 \text{ \AA}^{-1}$ becomes more prominent when there is a large hard block component, such as in

$A_{140}B_{100}A_{140}$ (Figure 6.15). These relative intensities further justify the cause of these structural peaks.

Previous studies investigating the structure of similar diblock copolymer spherical micelle films suggest that the spherical cores keep their shape as the film dries, whereas the corona blocks coalesce to form a continuous matrix.¹³ This phenomenon will produce different scattering patterns depending on how the particles stack upon drying. A well-ordered cubic structure, such as body centred cubic and face centred cubic, would produce sharp diffraction peaks relating to the crystallographic planes of the crystal structure. However, in this case the peaks are broad and appear to be similar in shape to the scattering intensities produced by the hard sphere structure factor describing interactions of close packed particles. Based upon this, attempts were made to fit the SAXS models with a sphere form factor (Section 2.5.2) with an integrated hard-sphere structure factor (Section 2.4.1). These attempts were successful for the majority of the triblock films ($A_{56}B_{100-300}A_{56}$, $A_{108}B_{100-300}A_{108}$, and $A_{140}B_{100-300}A_{140}$) and support the observations made in other studies on similar systems throughout the literature (Figure 6.17).^{6,7,11-13} However, the additional features at low q -values are not accounted for within this structural model and therefore are not included during the modelling process. The results from this modelling indicate that the spherical domain size increases as the length of the hydrophobic BA block increases; this observation is similar to the observation for the triblock copolymer dispersions (Table 6.5).

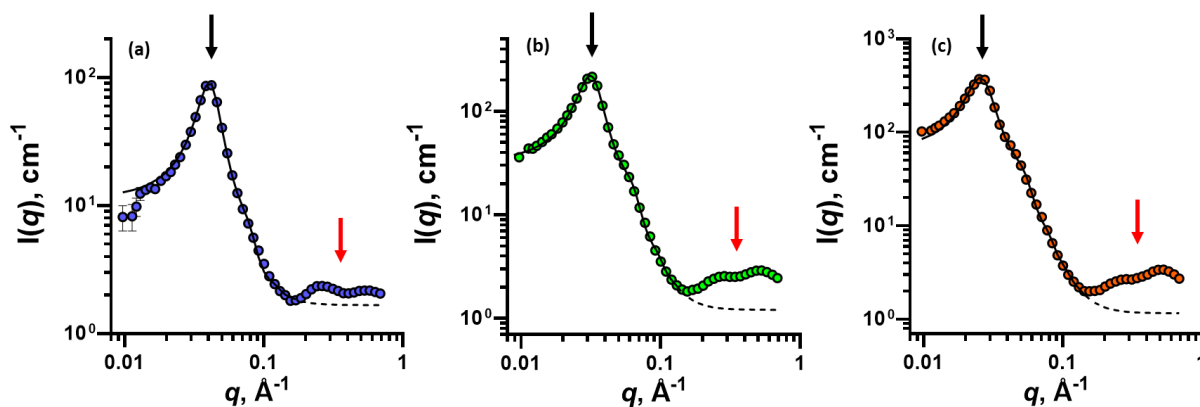


Figure 6.17. SAXS patterns of triblock copolymer films cast from a 20% w/w aqueous dispersion (symbols) fit with a sphere form factor with an integrated hard sphere structure factor (black line), where (a) is $A_{108}B_{150}A_{108}$, (b) is $A_{108}B_{200}A_{108}$, and (c) is $A_{108}B_{300}A_{108}$. The black arrow indicated where there is a good correlation between the experimental scattering pattern and the structural model and the red arrow indicates the region where there is deviation from the model due to additional structures that have not been accounted for (e.g. the packing of the BA chains). The scattering patterns were collected using a Xenocs XeuSS instrument.

Comparison between the modelled spherical domain radius within the triblock film and the core radius of the particle in the aqueous dispersion showed that generally the domain size is significantly smaller than the respective particle size (Table 6.5). Furthermore, the core domain size appears to be dominated largely by the size of the BA block and is fairly independent of the length of the hard block. For example, $A_{56}B_{300}A_{56}$, $A_{108}B_{300}A_{108}$, and $A_{108}B_{300}A_{108}$, have a hydrophobic domain size of 54 Å, 53 Å and 58 Å, respectively. This indicates the BA chains within the core compress and the size of the domain reduces, as the water evaporates, to a size that is related to the length of the BA block (Figure 6.18a). However, this reduction in domain size is not observed for the triblock copolymers with the largest hard block length and a relatively small BA block (i.e., $A_{140}B_{100-200}A_{140}$). This suggests the BA chains within these copolymers are already fairly compressed in the particulate state due to the large stabilising block. Furthermore, it is only when the BA block becomes larger than the stabiliser block

(A₁₄₀B₃₀₀A₁₄₀) that a reduction in the domain size upon drying is observed. Similar reductions have been observed previously in polymer latex films.⁶

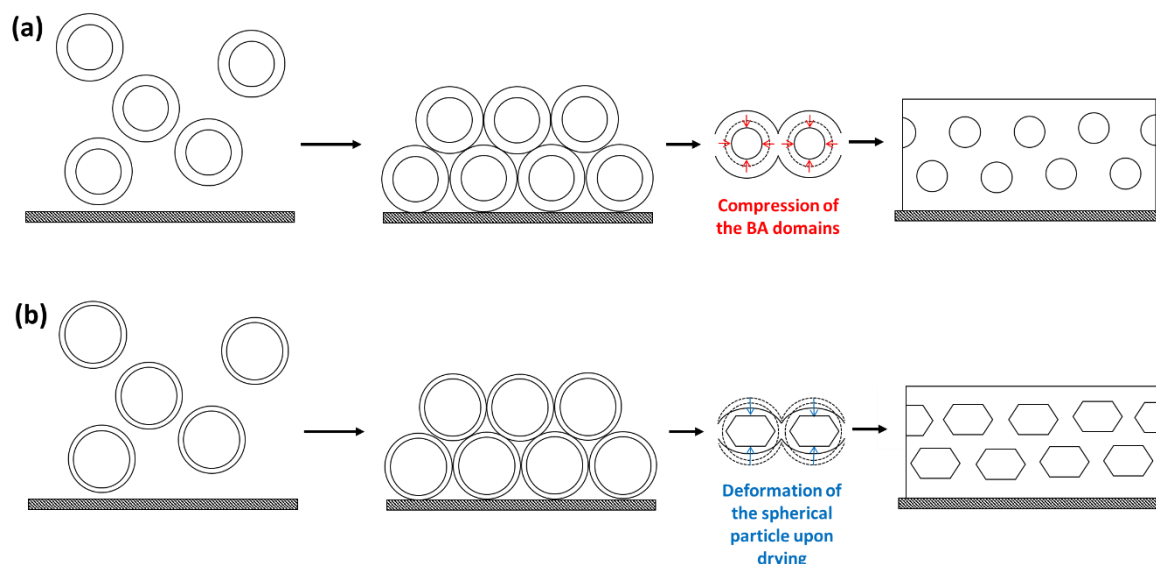


Figure 6.18. Schematic that describes the formation of the kinetically trapped structure within the water-cast films that occurs during the drying process, where, (a) describes the formation of the packed soft sphere structure within a matrix of the hard phase where the BA domains shrink during the drying process, and (b) describes the formation of an orientated elongated structure that is formed by copolymers with a large soft block.

The triblock films that do not fit to this model are the copolymers that have a large BA component *i.e.*, A₅₆B₅₀₀A₅₆, A₅₆B₇₅₀A₅₆, A₁₀₈B₅₀₀A₁₀₈, A₁₀₈B₇₅₀A₁₀₈, A₁₄₀B₅₀₀A₁₄₀, and A₁₄₀B₇₅₀A₁₄₀. This suggests that the particles within the copolymer films arrange in a different structure to the previously examined films. In a packed sphere system, there is a maximum volume fraction (0.71) that can be filled by the spheres creating a residual volume not filled by the spheres. In this case, the spheres are the soft particle cores and the residual volume is filled by the hard matrix of AA and St. The copolymers that do not fit the close packed hard sphere model all have a soft block volume fraction that is greater than 0.71. This means that the spherical cores will distort during the drying process in order to reduce the residual volume and therefore cannot be fit with the hard sphere model (Figure 6.18b).^{34,35}

Table 6.5. Structural analysis by SAXS investigating the bulk phase separation within the water-cast copolymer films, where q^* is the position of the primary structural peak in the SAXS pattern, d is the length scale of the phase separation, R_s is the mean radius of the spherical BA domain within the film, σ_s is the standard deviation of the mean spherical domain radius, R_{PY} is the interdomain distance in the film matrix and the f_{PY} is the effective volume fraction corresponding to the hard sphere structure factor based on Percus-Yevick (PY) approximation.

Triblock	q^* (\AA^{-1})	d (\AA)	R_s (\AA)	σ_s (\AA)	R_{PY} (\AA)	f_{PY}
A ₅₆ B ₁₀₀ A ₅₆	0.053	119	34	6	58	0.34
A ₅₆ B ₁₅₀ A ₅₆	0.041	153	44	10	76	0.36
A ₅₆ B ₂₀₀ A ₅₆	0.04	157	52	18	86	0.37
A ₅₆ B ₃₀₀ A ₅₆	0.031	203	54	33	96	0.37
A ₅₆ B ₅₀₀ A ₅₆	0.024	262	-	-	-	-
A ₅₆ B ₇₅₀ A ₅₆	0.023	273	-	-	-	-
A ₁₀₈ B ₁₀₀ A ₁₀₈	0.053	119	30	4	51	0.22
A ₁₀₈ B ₁₅₀ A ₁₀₈	0.041	153	45	11	76	0.34
A ₁₀₈ B ₂₀₀ A ₁₀₈	0.030	209	50	19	96	0.31
A ₁₀₈ B ₃₀₀ A ₁₀₈	0.029	217	53	27	116	0.29
A ₁₀₈ B ₅₀₀ A ₁₀₈	0.019	331	-	-	-	-
A ₁₀₈ B ₇₅₀ A ₁₀₈	0.015	419	-	-	-	-
A ₁₄₀ B ₁₀₀ A ₁₄₀	0.067	94	22	1	43	0.11
A ₁₄₀ B ₁₅₀ A ₁₄₀	0.045	140	32	10	58	0.19
A ₁₄₀ B ₂₀₀ A ₁₄₀	0.036	175	45	13	78	0.27
A ₁₄₀ B ₃₀₀ A ₁₄₀	0.028	224	58	22	113	0.25
A ₁₄₀ B ₅₀₀ A ₁₄₀	0.019	331	-	-	-	-
A ₁₄₀ B ₇₅₀ A ₁₄₀	-	-	-	-	-	-

AFM images were recorded of the aqueous-cast films to assess the surface structure (Figure 6.19). However, unlike the AFM images of the solvent-cast films there was little surface phase separation observed in the images of the aqueous-cast films. The absence of a surface phase separation is likely to be a result of the lack of freedom for the phases to rearrange themselves upon drying and the soft hydrophobic block remains buried amongst the hard phase (Figure 6.18). These restrictions result in a single phase being present on the film surface and therefore no surface phase separation can be observed using AFM (Figure 6.19). However, surface structure is observed for some films and is thought to be caused by drying defects that create an uneven film ($A_{56}B_{500}A_{56}$). Other more well-defined structures are observed in the images of $A_{108}B_{200}A_{108}$ and $A_{108}B_{300}A_{108}$, where spherical soft regions (dark regions, Figure 6.19) are seen in a matrix of the hard phase (light regions, Figure 6.19).

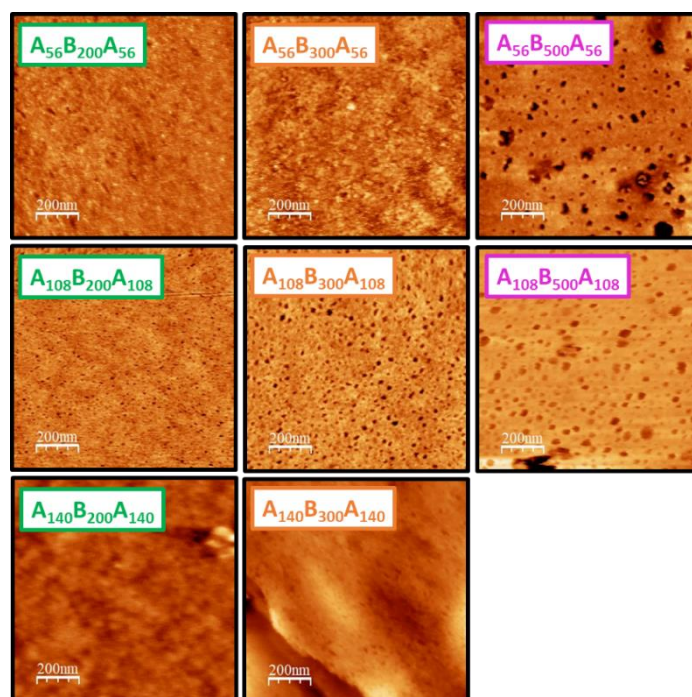


Figure 6.18. AFM height images of triblock copolymer films cast from a 20% w/w aqueous solution measured using ScanAsyst® PeakForce® tapping mode, where the copolymer labels are shown on the respective images.

The results gathered through SAXS and AFM demonstrate that the solvent environment from which the copolymer film is cast plays a major role in the resultant structure within the film. It is also clear that the film structure is strongly linked to how the copolymer behaves within the solution phase. If the copolymer is fully dissolved within the solvent phase then the copolymer will have the freedom to arrange into the most favourable and lowest energy structure. Whereas, if the copolymers assemble in solution through solvophobic interactions then the mobility of the copolymer chains is restricted and they are unable to rearrange into a favourable conformation upon drying due to the high T_g of the stabiliser block and remain in a kinetically trapped state.

3.6 Structural characterisation of annealed triblock copolymer films cast from aqueous dispersion

The aqueous-cast films were thought to be in a kinetically trapped state due to the high T_g of the stabiliser block preventing coalescence of the soft particle cores. Therefore, if the temperature was raised above the T_g of the hard block (~ 120 °C) then the copolymer mobility should increase, allowing rearrangement into a more thermodynamically stable conformation. To test this hypothesis, *in situ* grazing incident SAXS (GISAXS, Section 2.2.5) was performed on an aqueous-cast $A_{108}B_{500}A_{108}$ film while the film was annealed (Figure 6.20). In this experiment an initial scattering pattern was acquired at ambient temperature (22 °C), following this the triblock film was heated above the T_g of the hard block to 150 °C where frames were collected every 60 seconds in order to monitor the change in structure during the annealing process. The SAXS analysis shows that the structure present in the water-cast film at 22 °C begins to rearrange when heated to 150 °C. A gradual change is observed and an equilibrated structure is eventually reached after 30 minutes and the film is cooled back to ambient temperature.

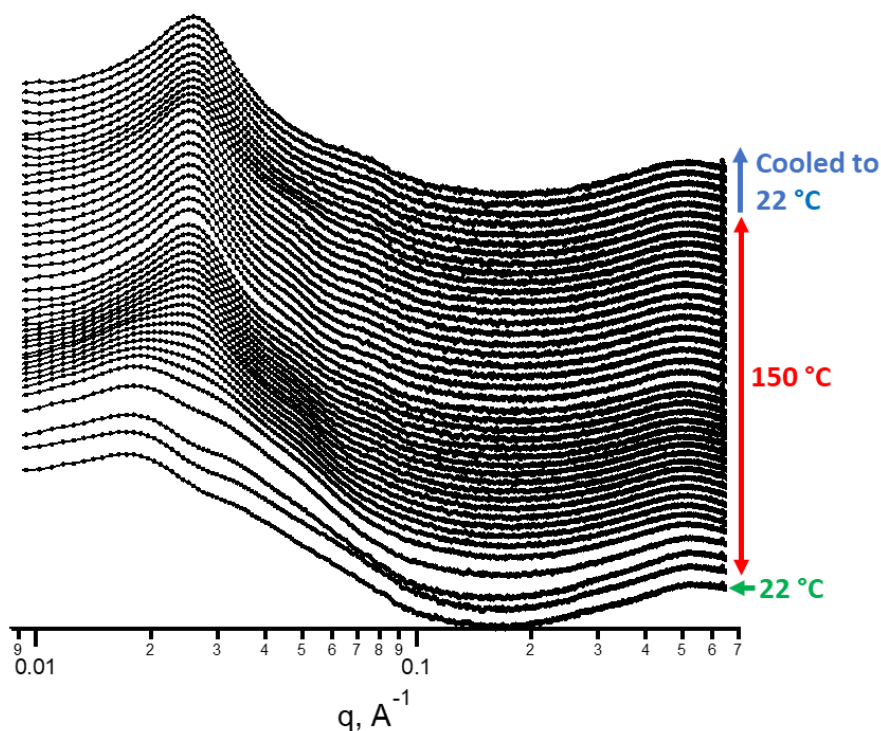


Figure 6.20. Time-resolved GISAXS patterns collected for the $A_{108}B_{500}A_{108}$ water-cast film during the annealing process at 150 °C. Scattering patterns were collected using a Xenocs Xeuss instrument.

Since a change is observed in the structure of the water-cast film once the temperature is raised above the T_g of both blocks, it is evident that the original structure was in a kinetically trapped state and a more thermodynamically stable structure can only be achieved by annealing. Additionally, the final SAXS pattern taken after the annealing process is almost identical to the SAXS pattern collected for the solvent-cast film of the same triblock copolymer. This indicates that the solvent cast film has achieved a more thermodynamically stable structure in ambient conditions. This rearrangement of bulk structure has previously been reported by Chenal *et al.* where they reported that the kinetically-trapped hard matrix structure undergoes inversion when the film is annealed to form a structure where the hard domains are surrounded by a continuous matrix of the soft component.¹³ AFM images were taken from both the film before

annealing (Figures 6.21a and 6.21b) and the annealed film (Figures 6.21c and 6.21d) and these were compared with the images taken of the films cast from solvent in ambient conditions (Figures 6.21e and 6.21f). These images demonstrate a clear change in the phase separated structure once the water-cast film is annealed. The AFM images also demonstrate that the structure of the annealed film is similar to the film cast from solvent in ambient conditions - this is in agreement with the conclusions drawn from the SAXS investigation.

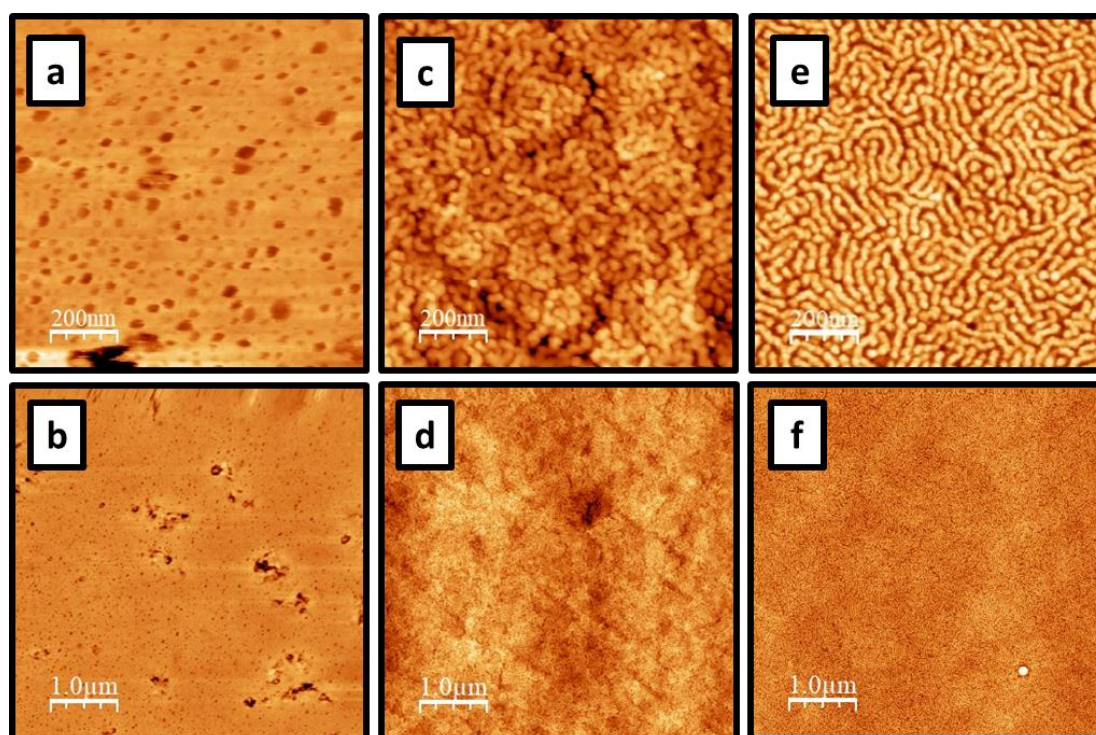


Figure 6.21. AFM height images of triblock copolymer films measured using ScanAsyst® PeakForce® tapping mode: (a) and (b) are images of $A_{108}B_{500}A_{108}$ cast from a 20% w/w aqueous solution recorded for $1\mu\text{m} \times 1\mu\text{m}$ and $5\mu\text{m} \times 5\mu\text{m}$ area respectively; (c) and (d) are images of $A_{108}B_{500}A_{108}$ cast from a 20% w/w aqueous solution and annealed for 30 minutes at $150\text{ }^\circ\text{C}$ recorded for $1\mu\text{m} \times 1\mu\text{m}$ and $5\mu\text{m} \times 5\mu\text{m}$ area, respectively; and (e) and (f) are images of $A_{108}B_{500}A_{108}$ cast from a 40% w/w solution in MEK recorded for $1\mu\text{m} \times 1\mu\text{m}$ and $5\mu\text{m} \times 5\mu\text{m}$ area, respectively.

Both SAXS and AFM are in good agreement with each other, and have demonstrated the structural differences in the films cast from different solvent environments and how the

copolymer properties affect the phase separation within the films. When the triblock copolymer is fully dissolved in the solution phase the triblock copolymer has a large amount of mobility that is not restricted by unfavourable interactions with the solvent. This mobility allows the copolymer to arrange into a lower energy structure as the solvent evaporates and a film is formed. However, when the selected solvent is not compatible with one of the copolymer blocks then the triblock copolymers aggregate together to form particles to avoid any unfavourable solvent interactions. As a result, the copolymers have a restricted mobility and cannot rearrange into a thermodynamically stable structure as the solvent evaporates and so remains kinetically trapped. Annealing the aqueous film above the T_g of the hard block, provides mobility to the copolymer chains allowing them to rearrange into a lower energy structure. However, annealing the film does not provide as much mobility as solvation by MEK, hence why the annealed film appears less well defined by AFM (Figure 6.21).

6.3.7 Mechanical characterisation of the triblock copolymer films

As film structure is likely to have a significant impact on the mechanical properties of films, the mechanical properties of water-cast films and solvent-cast films were investigated. Triblock films were cast in plastic moulds and left to dry under ambient conditions for one week. The films were then removed from the moulds and cut into strips with a width of 7 mm and the thicknesses of these films were individually measured using a micrometer. All of the films cast from the triblock in MEK were very uniform and showed no signs of de-wetting from the substrate or bubbles within the film. However, the aqueous films showed large amounts of de-wetting from the plastic mould and bubbles would form during the drying process; these two factors made it hard to achieve uniform films in all cases. The de-wetting observed is likely to be due to incompatibilities between the water and the substrate,^{36,37} whereas, the formation

and stabilisation of bubbles within the aqueous dispersions is a result of the amphiphilic nature of the copolymers and their ability to behave like surfactants.³⁷

Since the length of the soft and hard blocks were varied across all 18 triblock copolymers (Figure 6.2), a range of film properties were achieved. However, some films were either too brittle or too soft to be analysed. For the solvent cast films, the mechanical tests clearly indicate that increasing the length of the soft block systematically increases the flexibility of the film (higher extension-to-break and lower modulus, Table 6.6 and Figure 6.22a) and increasing the length of the hard block increases the film strength (higher modulus, lower extension-to-break, Table 6.6 and Figure 6.22a). This behaviour is intuitive since it is well known that, at a fixed temperature, polymers become more pliable by lowering their T_{gs} .³⁸ Therefore, by introducing a larger soft component to the copolymer, the triblock copolymer film is becoming more amorphous. Furthermore, the hard segments within the triblock copolymer film will aggregate together to form glassy regions (as shown by SAXS and AFM) that act as cross-linking points across the film. Therefore, increasing the length of the hard block increases the size of the glassy regions and consequently increases the strength of the crosslinking and the toughness of the triblock film.

Table 6.6. Tensile extension results where ▲ indicates that the triblock film was too brittle to test and ● indicates that the film was too soft to test.

Triblock	Solvent		Aqueous	
	Modulus (MPa)	Extension-to-break (%)	Modulus (MPa)	Extension-to-break (%)
A ₅₆ B ₁₀₀ A ₅₆	▲	▲	▲	▲
A ₅₆ B ₁₅₀ A ₅₆	83.7 ± 16.6	85.2 ± 34.9	▲	▲
A ₅₆ B ₂₀₀ A ₅₆	35.6 ± 9.2	99.5 ± 39.4	89.8 ± 31.4	17.3 ± 6.9
A ₅₆ B ₃₀₀ A ₅₆	0.45 ± 0.13	206.1 ± 40.2	63.3 ± 9.0	26.5 ± 4.1
A ₅₆ B ₅₀₀ A ₅₆	●	●	116.9 ± 20.1	17.1 ± 4.6
A ₅₆ B ₇₅₀ A ₅₆	●	●	●	●
A ₁₀₈ B ₁₀₀ A ₁₀₈	▲	▲	▲	▲
A ₁₀₈ B ₁₅₀ A ₁₀₈	▲	▲	▲	▲
A ₁₀₈ B ₂₀₀ A ₁₀₈	▲	▲	▲	▲
A ₁₀₈ B ₃₀₀ A ₁₀₈	171.7 ± 34.6	13.3 ± 3.7	238.3 ± 45.9	10.5 ± 5.4
A ₁₀₈ B ₅₀₀ A ₁₀₈	1.19 ± 0.21	176.8 ± 20.9	123.2 ± 11.1	9.4 ± 1.0
A ₁₀₈ B ₇₅₀ A ₁₀₈	●	●	●	●
A ₁₄₀ B ₁₀₀ A ₁₄₀	▲	▲	▲	▲
A ₁₄₀ B ₁₅₀ A ₁₄₀	▲	▲	▲	▲
A ₁₄₀ B ₂₀₀ A ₁₄₀	▲	▲	▲	▲
A ₁₄₀ B ₃₀₀ A ₁₄₀	259.4 ± 102.8	10.4 ± 4.6	▲	▲
A ₁₄₀ B ₅₀₀ A ₁₄₀	89.8 ± 23.3	27.8 ± 10.9	254.5 ± 180.5	11.2 ± 9.6
A ₁₄₀ B ₇₅₀ A ₁₄₀	●	●	188.1 ± 50.5	14.5 ± 6.1

Although the film properties are largely dictated by the copolymer composition and design, the solvent environment also has a significant effect on the film behaviour. The mechanical tests indicate that a triblock copolymer film cast from water produces a harder film (higher modulus)

than the same copolymer cast from MEK (Table 6.6 and Figure 6.22b). This is likely to be a result of the phase separated structure within the film and the respective location of the hard and soft blocks. Casting the copolymer from water produces a kinetically trapped phase-separated structure where the hard-block forms a continuous matrix. Whereas, when the copolymers are allowed to reach thermodynamic phase-separation the continuous phase is often the soft block. The variations between the structure results in the difference in mechanical properties clearly demonstrating the importance of solvent environment.

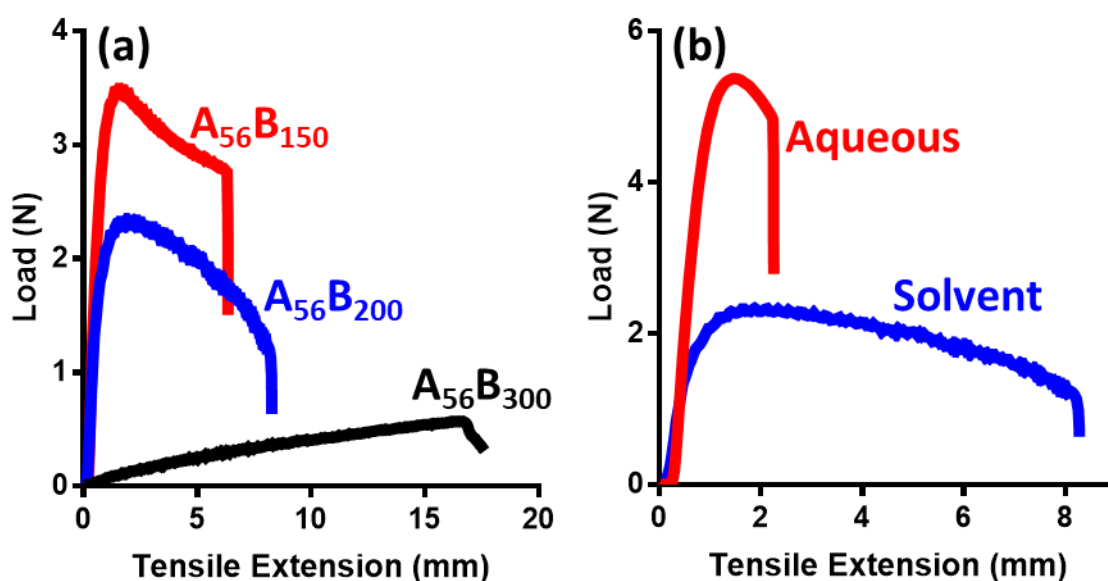


Figure 6.22. The tensile extension traces for triblock copolymer films, where (a) demonstrates the effect increasing the length of the soft block, and (b) demonstrates the effect of changing the solvent environment from which the A₅₆B₂₀₀A₅₆ copolymer film is cast.

6.4 Conclusions

Three poly(acrylic acid-*stat*-styrene), P(AA-*st*-St), macro-CTAs, of different DPs (112, 216, and 280) but similar monomer ratios (42:58, AA:St), were synthesised by RAFT solution polymerisation in MEK using a bifunctional, symmetrical RAFT agent. These were then extended with butyl acrylate, BA, to form a soft middle block resulting in ABA triblock copolymers. 18 triblock copolymers were synthesised in total where the DP of the soft block was varied (100, 150, 200, 300, 500 and 750). Molecular weight analysis demonstrated that the macro-CTAs were extended with high blocking efficiency and all had $M_w/M_n < 1.5$.

The solution structures of the copolymers were determined in both MEK and water using SAXS. SAXS analysis showed that the solubility of the amphiphilic copolymers varied in MEK as the copolymer composition varied. However, all the copolymers were dissolved in MEK and did not assemble into particles. In water, the copolymers self-assembled into spherical particles. Additionally, the amphiphilic nature of the P(AA-*st*-St) stabiliser blocks resulted in small, folded structures on the particle surface to reduce any unfavourable interactions. The size of these particles was modelled using SAXS and it was found that the particle size increased as the length of the hydrophobic soft block increased, as is expected for self-assembled block copolymers.

Triblock copolymer films were cast from solvent and water and investigated using AFM and SAXS in order to observe the effects of block length and solvent environment on the film structure. SAXS analysis of the solvent cast films demonstrated that the length scale of the phase separation increased as the length of the soft block increased. Additionally, the length scale of the phase separation increased as both the hard block length and the overall triblock length is increased. Unfortunately, the bulk film structure was not well-defined enough that any further information about the phase-separation could be gained from SAXS. However, an

additional peak at $q = 0.513 \text{ \AA}^{-1}$ was observed and was found to be a result of elongated chain-chain packing of BA within the soft phase. AFM found that the surface structure of the solvent cast films was highly dependent on the ratio of the hard and soft components. When there were significantly higher amounts of the soft block in the copolymer the soft component would form the continuous phase and *vice versa*. Furthermore, the morphological transitions observed by AFM agreed with the well-known behaviour of diblock copolymers, where the morphology changes from gyroid, to cylinders, to spheres as the volume fraction of the soft phase increases. SAXS analysis of the water cast films again demonstrated that the length scale of the phase separation increased when the lengths of the individual blocks were increased. However, the structure of the phase separation within copolymer films was dominated by the particulate structure in the aqueous solution phase forming a close packed sphere-like structure. It was hypothesised that these structures were kinetically trapped due to the restricted movement of the blocks in the particulate structure. This hypothesis was tested by annealing a film above the T_g of the hard block and monitoring the change in structure by time-resolved GISAXS. This experiment found that once the aqueous cast film was annealed at 150 °C for 30 minutes the film structure became similar to the solvent cast film, indicating firstly that the structure observed in the aqueous film was kinetically trapped, and secondly, that the structure observed in the solvent cast films is the thermodynamically stable structure.

Finally, the mechanical properties of the films were assessed and it was found that in the solvent cast films the ratio of soft block to hard block was very important in terms of the film properties. If there was a high level of hard block the films would have a high modulus and a low extension-to-break, whereas, when the level of soft block was increased the modulus was reduced and the extension-to-break would increase. However, the films cast from water didn't show such an obvious trend and the tested triblock films showed similar behaviours. These similarities between the aqueous films is likely due to the films having a similar structural

morphology formed by copolymer block phase separation upon drying. Additionally, the aqueous cast copolymers produced films with a higher modulus and a lower extension-to-break than the solvent cast films. This is caused by the differences in structure between the two systems, where the continuous phase in the case of the aqueous cast films is always the hard-block and therefore produces a harder film. This work has demonstrated that the solution behaviour of block copolymers has a direct effect on the film structure and the resulting mechanical properties.

6.5 References

- 1 J. C. S. Chang, *Indoor Air*, 1999, **9**, 253–258.
- 2 M. De Meijer, *Prog. Org. Coatings*, 2001, **43**, 217–225.
- 3 K. D. Weiss, *Prog. Polym. Sci.*, 1997, **22**, 203–245.
- 4 J. Ho, B. Mudraboyina, C. Spence-Elder, R. Resendes, M. F. Cunningham and P. G. Jessop, *Green Chem.*, 2018, **20**, 1899–1905.
- 5 D. Luo, R. Corey, R. Propper, J. Collins, A. Komorniczak, M. Davis, N. Berger and S. Lum, *Environ. Sci. Policy*, 2011, **14**, 585–593.
- 6 I. Martín-Fabiani, J. Lesage De La Haye, M. Schulz, Y. Liu, M. Lee, B. Duffy, F. D’Agosto, M. Lansalot and J. L. Keddie, *ACS Appl. Mater. Interfaces*, 2018, **10**, 11221–11232.
- 7 J. Lesage De La Haye, I. Martin-Fabiani, M. Schulz, J. L. Keddie, F. D’Agosto and M. Lansalot, *Macromolecules*, 2017, **50**, 9315–9328.
- 8 Y. Huang, R. Chang, L. Han, G. Shan, Y. Bao and P. Pan, *ACS Sustain. Chem. Eng.*,

- 2016, **4**, 121–128.
- 9 K. S. Kim, N. Gunari, D. Macneil, J. Finlay, M. Callow, J. Callow and G. C. Walker, *ACS Appl. Mater. Interfaces*, 2016, **8**, 20342–20351.
- 10 W. Wang, J. Zhang, F. Jiang, X. Wang and Z. Wang, *ACS Appl. Polym. Mater.*, 2019, **1**, 571–583.
- 11 Z. Qiao, T. Qiu, W. Liu, L. Zhang, J. Tu, L. Guo and X. Li, *Polym. Chem.*, 2017, **8**, 3013–3021.
- 12 R. Albigès, P. Klein, S. Roi, F. Stoffelbach, C. Creton, L. Bouteiller and J. Rieger, *Polym. Chem.*, 2017, **8**, 4992–4995.
- 13 M. Chenal, J. Rieger, C. Vechambre, J.-M. Chenal, L. Chazeau, C. Creton and L. Bouteiller, *Macromol. Rapid Commun.*, 2013, 1524–1529.
- 14 A. M. Bivigou-Koumba, J. Kristen, A. Laschewsky, P. Müller-Buschbaum and C. M. Papadakis, *Macromol. Chem. Phys.*, 2009, **210**, 565–578.
- 15 C. B. Chapman and L. Valentine, *J. Polym. Sci.*, 1959, **34**, 319–335.
- 16 R. T. A. Mayadunne, E. Rizzardo, J. Chiefari, J. Krstina, G. Moad, A. Postma and S. H. Thang, *Macromolecules*, 2000, **33**, 243–245.
- 17 M. C. McGaugh and S. Kottle, *Polym. Lett.*, 1967, **5**, 817–820.
- 18 A. Eisenberg, T. Yokoyama and E. Sambalido, *J. Polym. Sci. Part A-1 Polym. Chem.*, 1969, **7**, 1717–1728.
- 19 V. J. Cunningham, L. P. D. Ratcliffe, A. Blanazs, N. J. Warren, A. J. Smith, O. O. Mykhaylyk and S. P. Armes, *Polym. Chem.*, 2014, **5**, 6307–6317.

- 20 T. J. Neal, D. L. Beattie, S. J. Byard, G. N. Smith, M. W. Murray, N. S. J. Williams, S. N. Emmett, S. P. Armes, S. G. Spain and O. O. Mykhaylyk, *Macromolecules*, 2018, **51**, 1474–1487.
- 21 S. Imai, Y. Hirai, C. Nagao, M. Sawamoto and T. Terashima, *Macromolecules*, 2018, **51**, 398–409.
- 22 M. Ouchi, N. Badi, J.-F. Lutz and M. Sawamoto, *Nat. Chem.*, 2011, **3**, 917–924.
- 23 O. Altintas and C. Barner-Kowollik, *Macromol. Rapid Commun.*, 2016, **37**, 29–46.
- 24 M. Artar, E. Huerta, E. W. Meijer and A. R. A. Palmans, 2014, pp. 313–325.
- 25 M. Matsumoto, M. Sawamoto and T. Terashima, *ACS Macro Lett.*, 2019, **8**, 320–325.
- 26 S. Imai, Y. Hirai, C. Nagao, M. Sawamoto and T. Terashima, *Macromolecules*, 2018, **51**, 398–409.
- 27 M. Matsumoto, T. Terashima, K. Matsumoto, M. Takenaka and M. Sawamoto, *J. Am. Chem. Soc.*, 2017, **139**, 7164–7167.
- 28 J. A. Balmer, O. O. Mykhaylyk, A. Schmid, S. P. Armes, J. P. A. Fairclough and A. J. Ryan, *Langmuir*, 2011, **27**, 8075–8089.
- 29 Y. Mai and A. Eisenberg, *Chem. Soc. Rev.*, 2012, **41**, 5969–5985.
- 30 T. A. Mykhaylyk, O. O. Mykhaylyk, S. Collins and I. W. Hamley, *Macromolecules*, 2004, **37**, 3369–3377.
- 31 M. J. Derry, O. O. Mykhaylyk, A. J. Ryan and S. P. Armes, *Chem. Sci.*, 2018, **9**, 4071–4082.
- 32 Y. Mai and A. Eisenberg, *Chem. Soc. Rev.*, 2012, **41**, 5969.

- 33 N. A. Lynd, A. J. Meuler and M. A. Hillmyer, *Prog. Polym. Sci.*, 2008, **33**, 875–893.
- 34 K. B. Singh and M. S. Tirumkudulu, *Phys. Rev. Lett.*, 2007, **98**, 1–4.
- 35 C. C. Roberts and L. F. Francis, *J. Coatings Technol. Res.*, 2013, **10**, 441–451.
- 36 S. Khesghi and L. E. Scriven, *Chem. Eng. Sci.*, 1991, **46**, 519–526.
- 37 L. Xue and Y. Han, *Prog. Mater. Sci.*, 2012, **57**, 947–979.
- 38 J. M. G. Cowie and V. Arrighi, *Polymers: Chemistry and physics of modern materials*, CRC Press, Boca Raton, 2008.

Chapter 7. Conclusions and future work

Chapter 7.

Conclusions and future work

In this thesis a range of amphiphilic copolymers have been synthesised by RAFT solution polymerisation and their self-assembly behaviour in aqueous media has been investigated using SAXS. In addition, a study of triblock copolymer self-assembly in bulk, as the most interesting case for industrial application, has been performed. Self-assembly in a solution has been induced in all cases using a “solvent switch” method, which involves first dissolving the copolymer in a suitably good solvent (IPA) and diluting the solution slowly with water. The addition of water creates an unfavourable environment for the hydrophobic component of the copolymers, which causes them to aggregate into nano-scale morphologies. At this step a base (TEA or NH_3) was also added to the dispersions during the “solvent-switch” in order to provide additional colloidal stabilisation for the acidic polymers.

Firstly, the effect of copolymer composition, molecular weight, and molecular weight distribution on the self-assembly of P(BMA-*stat*-MAA) copolymers was assessed. Copolymers were synthesised in a range of molar compositions (between 77:23 and 93:7 BMA/MAA) and with a variety of copolymer molecular weights (6 – 22 kDa). Two different synthesis methods were employed in order to vary the molecular weight distribution; RAFT solution copolymerisation and conventional free radical polymerisation. The statistical copolymers synthesised by RAFT had low dispersity ($M_w/M_n \sim 1.2$) but were found to have a short BMA-rich block towards the end of each copolymer chain due to a reduction in the rate of conversion of MAA towards the end of the polymerisation. Conversely, the copolymers synthesised using conventional FRP had higher dispersities ($M_w/M_n \sim 1.9$) and a fully statistical distribution of

the two different monomers along the copolymer backbone. The sizes of the statistical copolymer self-assemblies were assessed using SAXS and TEM. It was found that all the copolymers self-assembled to form well-defined spherical particles at 1% w/w in aqueous media. Importantly, copolymer particle size was found to be independent of both molecular weight and the molecular weight distribution of the copolymer and instead was found to be highly dependent on the copolymer composition with copolymers containing larger mole fractions of MAA aggregated to form smaller particles, whereas larger particles were formed by copolymers with smaller mole fractions of MAA. This behaviour was rationalised in terms of particle surface charge density, where the copolymers aggregate together in order to induce a critical surface charge density that allows colloidal stability to be achieved. The critical surface charge density was quantified as the fraction of the particle surface covered by the charged monomer (MAA), known as $SA_{\text{frac.MAA}}$. A particle structural model has been developed where it was assumed that (i) the copolymer particles were perfectly spherical and (ii) that all the charged groups were located on the particle surface. This model fits reasonably well for the RAFT synthesised copolymers between a narrow range of $SA_{\text{frac.MAA}}$ (0.2 – 0.4), justifying the assumptions that were made.

The versatility of the particle structural model was examined further by investigating the self-assembly of statistical copolymers as a function of hydrophobicity, in addition to copolymer composition. This involved synthesising a range of P(AMA-*stat*-MAA) copolymers, where the hydrophobic component (AMA) was systematically varied by increasing the alkyl chain length of the methacrylate monomer (MMA, EMA, BMA, HMA, EHMA). As the alkyl chain length increased, the hydrophobicity of the repeat units increased, creating a systematic hydrophobicity variation. The same compositional dependence on copolymer particle size was observed, where the copolymers with larger mole fractions of MAA aggregated together to form smaller particles and *vice versa*. However, this study revealed that the hydrophobicity of

the hydrophobic component had a large effect on particle size, where copolymers with more hydrophobic moieties formed larger particles. These copolymer systems were fit with particle structural model. It was found that all the copolymer series fitted well to the structural model enabling a $SA_{\text{frac.MAA}}$ to be calculated for each copolymer series. $SA_{\text{frac.MAA}}$ was found to increase as the hydrophobicity of the hydrophobic component increased. Additionally, a linear trend between the logP (a quantity often used to quantify hydrophobicity/hydrophilicity) of the hydrophobic component and the $SA_{\text{frac.MAA}}$ required to induce stabilisation of the particle dispersion was observed. This relationship can be used to predict the statistical copolymer particle size on the basis of hydrophobicity and copolymer composition, making it a practical tool for particle design.

Although this work has demonstrated that the charge density model is robust to changes in the hydrophobic monomer, further studies are required to determine the universality of this model. Firstly, a copolymer system containing only acrylic monomers should be investigated to allow the effect of lowering the overall T_g of the copolymer to be examined. Additionally, monomers with inherent crystallinity, such as behenyl methacrylate, could be introduced and studied to see whether crystallisation within the particle core influences the copolymer self-assembly and particle size. Furthermore, to fully understand the self-assembly of statistical copolymers, the effect of varying the hydrophilic component must be investigated. Therefore, the effect of using a cationic, zwitterionic, or neutral hydrophilic monomer in place of methacrylic acid should be assessed. Examination of this predictive self-assembly behaviour using different monomers to synthesise the copolymer nanoparticles increases the potential application for this technology.

As demonstrated, particle size is principally independent of molecular weight for statistical copolymer assemblies. In contrast, the sizes of block copolymer particles in water are largely determined by the respective DPs of the hydrophobic and hydrophilic blocks. Therefore, the effect of hydrophile/hydrophobe distribution on particle size and copolymer self-assembly was

examined. A series of “pseudo-gradient” P[MAA-*b*-(MAA-*stat*-BMA)] copolymers were synthesised, where the respective block lengths and the copolymer composition of the statistical block were varied. An overall copolymer molar composition of BMA:MAA 70:30 was maintained. These copolymer aqueous dispersions were studied using SAXS and TEM. It was found that all the copolymers aggregated to form spherical particles where the particle size was largely dependent on the distribution of hydrophile/hydrophobe along the copolymer backbone. Blockier copolymer structures produced larger particles than those with a more statistical distribution of the two different monomers. Interestingly, these “pseudo-gradient” copolymers appear to follow a similar self-assembly behaviour as the previously examined statistical copolymers (chapters 3 and 4) up to a DP of 43 for the stabiliser PMAA block. This suggests that that, despite the large stabiliser block, the particle size is largely determined by the copolymer composition of the statistical block. However, it is currently unknown how molecular weight affects the self-assembly behaviour of these intermediate pseudo-gradient copolymer structures. Therefore, this work should be further expanded to fully understand the how molecular weight effects the particle size of pseudo-gradient copolymer dispersions. This will allow the specific monomer distribution needed to induce a switch from a statistically-dominated regime, where particle size is molecular weight independent, to a block copolymer regime, where the particle size is dependent on molecular weight. This work would involve expanding the current range of copolymers investigated by varying the copolymer molecular weight. This would allow the monomer distributions where the particle size is independent of molecular weight (*i.e.*, statistical behaviour) to be determined, and *vice versa*.

As mentioned previously, amphiphilic copolymers are used in a variety of industrial applications; one of these is in paints and coatings. There is a large drive within the paints and coatings industry to replace VOCs used within paint formulations for more environmentally friendly alternatives such as water.¹⁻⁴ However, maintaining the high-performance properties

possessed by solvent-borne paints, *i.e.*, water-resistance, film toughness, viscosity and long open times has proven to be a challenge. Therefore, it is important to formulate potential copolymer systems in both aqueous and solvent-borne environments and investigate properties of the films they form. Here, a large library of P[(AA-*stat*-St)-*b*-BA-*b*-(AA-*stat*-St)] ABA triblock copolymers were synthesised, where the DPs of the individual hard and soft blocks were varied. These copolymers were designed to utilise important properties from both statistical and block copolymers. Firstly, a statistical block that incorporates a hydrophobic monomer (St) as well as a hydrophilic monomer (AA) improves the water resistance of the coating when the copolymer film is formed. Secondly, using copolymer blocks with varying T_g s induces phase separation within the copolymer film. This phase separation is known to have positive effects on the mechanical properties of the films.^{5,6} Additionally, using a triblock architecture introduces more covalent links between the phase separated domains, consequently increasing the strength of the copolymer film. The solution behaviour of the copolymers in MEK and water was assessed using SAXS. It was found that the triblock copolymers aggregated through hydrophobic interactions to form spherical particles in water. However, in MEK the copolymers did not aggregate and coexisted as dissolved chains. Films of the triblock copolymers were cast from both solvent environments, and the structural phase separation in the films was studied using a combination of SAXS and AFM. It was found that the copolymer films cast from MEK were able to phase separate into well-defined structures. The size and morphology of the phase separation was dependent on the block length and hard-to-soft block ratio, respectively. Furthermore, these morphological transformations were consistent with theoretical predictions made for the self-assembly of diblock copolymers in the bulk state. Conversely, the water-cast films partially retained the particulate structure present in solution, producing kinetically-trapped phase separated structures. The films cast from MEK and water had vastly different mechanical properties owing to the differences in internal

structure. These findings demonstrate the importance of solvent choice in the film forming process and how the copolymer solution behaviour can directly affect the film structure. Finally, *in situ* GISAXS was utilised to observe the structural changes which occurred during the annealing of a water-cast film at 150 °C. It was found that the kinetically trapped structure of the water-cast films were able to rearrange into the thermodynamic structure observed in the MEK-cast films since the film was heated above the T_g of the hard segment. Although the clear effects of copolymer design and solvent environment have been demonstrated, these systems need to be adapted further in order to produce a high performing functional copolymer film cast from water.

The work in this thesis has demonstrated that amphiphilic statistical copolymers readily self-assemble into well-defined spherical particles, where the particle size can easily be controlled by the copolymer composition and hydrophobicity. Therefore, these systems can offer a cheaper and more industrially viable alternative to block copolymer particles in many industrial applications. Furthermore, the work presented here could be used to investigate how simple statistical copolymers can be used as biomolecule mimics by controlling the copolymer molecular weight, composition, and chemical properties. The charge density model mentioned previously can be utilised effectively to predict the copolymer molecular weight needed to achieve single chain nanoparticles (SCNP). The effect of copolymer molecular weight, composition, and chemical properties on the tertiary and internal structures formed by single-chain folding of statistical copolymers should be investigated. By mapping out these effects on a simple copolymer system, a greater understanding of the factors involved in the assembly of both synthetic and biological single-chain nanoparticles could be gained. This would allow bespoke single-chain nanoparticles targeting a particular functional properties to be synthesised. These simple and industrially relevant single-chain nanoparticles could be utilised

for functional processes such as catalysis, energy storage, biomedical applications and water purification.^{7–10}

7.1 References

- 1 J. C. S. Chang, *Indoor Air*, 1999, **9**, 253–258.
- 2 M. De Meijer, *Prog. Org. Coatings*, 2001, **43**, 217–225.
- 3 J. Ho, B. Mudraboyina, C. Spence-Elder, R. Resendes, M. F. Cunningham and P. G. Jessop, *Green Chem.*, 2018, **20**, 1899–1905.
- 4 D. Luo, R. Corey, R. Propper, J. Collins, A. Komorniczak, M. Davis, N. Berger and S. Lum, *Environ. Sci. Policy*, 2011, **14**, 585–593.
- 5 Y. Huang, R. Chang, L. Han, G. Shan, Y. Bao and P. Pan, *ACS Sustain. Chem. Eng.*, 2016, **4**, 121–128.
- 6 D. Chen, S. Yi, W. Wu, Y. Zhong, J. Liao, C. Huang and W. Shi, *Polymer (Guildf.)*, 2010, **51**, 3867–3878.
- 7 C. K. Lyon, A. Prasher, A. M. Hanlon, B. T. Tuten, C. A. Tooley, P. G. Frank and E. B. Berda, *Polym. Chem.*, 2015, **6**, 181–197.
- 8 M. Ouchi, N. Badi, J.-F. Lutz and M. Sawamoto, *Nat. Chem.*, 2011, **3**, 917–924.
- 9 A. M. Hanlon, C. K. Lyon and E. B. Berda, *Macromolecules*, 2016, **49**, 2–14.
- 10 O. Altintas and C. Barner-Kowollik, *Macromol. Rapid Commun.*, 2016, **37**, 29–46.

Chapter 8. Appendices

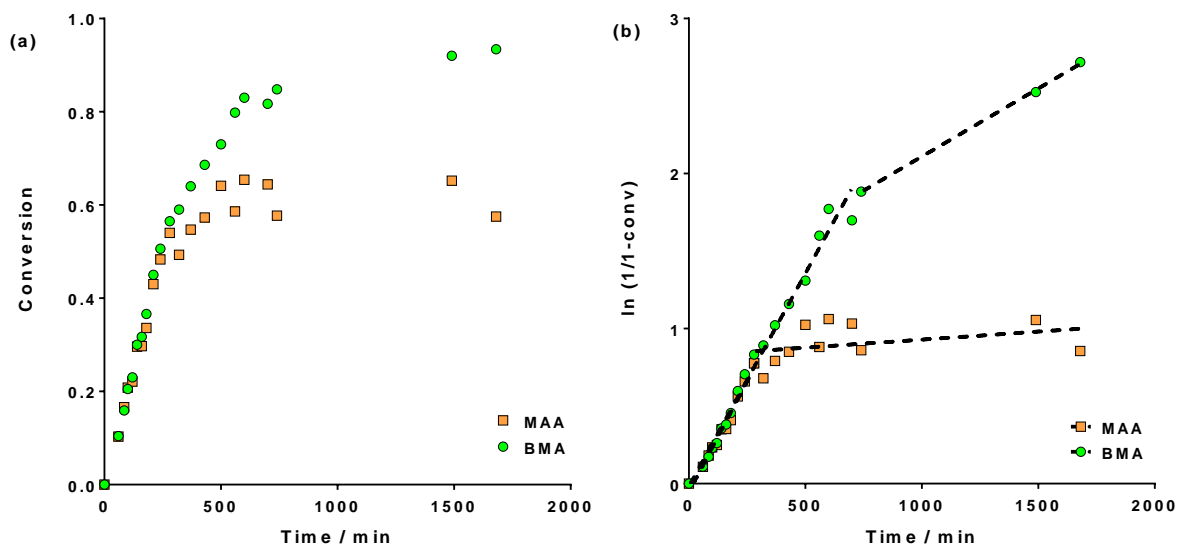
Chapter 8.

Appendices

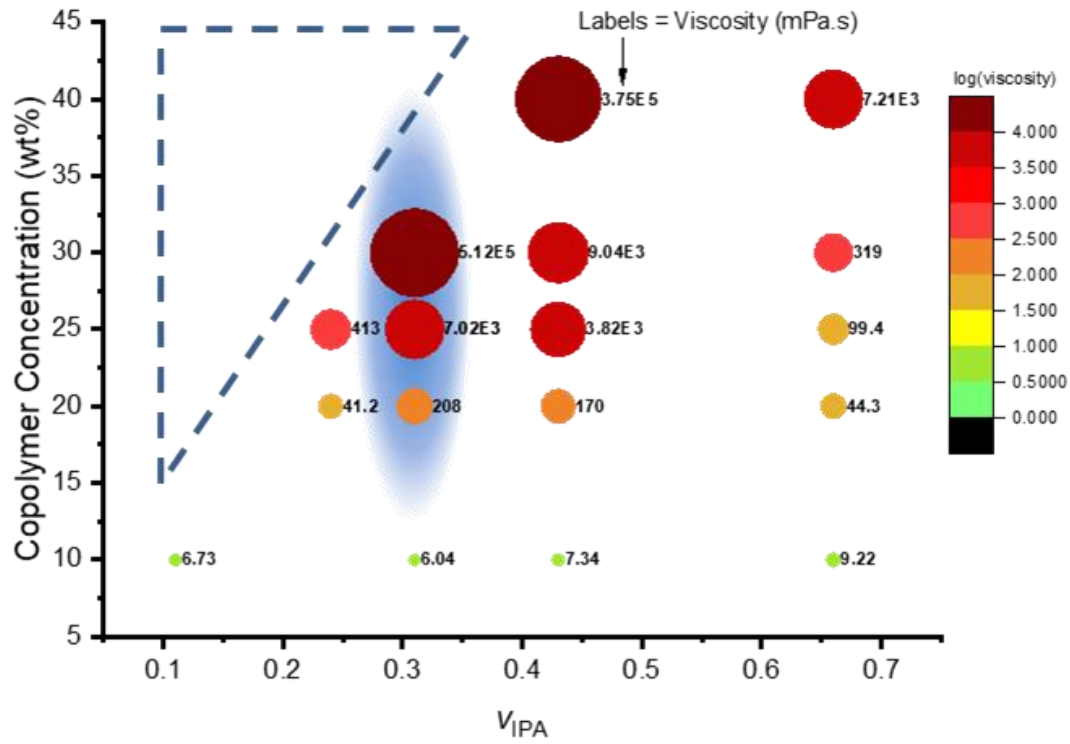
Appendix 1. Summary of reagent quantities required in the synthesis of the statistical copolymers in chapter 3.

	MAA / g	BMA/ g	PETTC / g	ACVA / g	IPA / g
BM _{77:23} (22k)	2.4728	9.5272	0.1356	0.0224	48.6
BM _{77:23} (15k)	2.4728	9.5272	0.2712	0.0448	49.3
BM _{77:23} (10k)	2.4728	9.5272	0.4067	0.0672	49.9
BM _{77:23} (5k)	2.4728	9.5272	0.8135	0.1343	51.8
BM _{85:15} (22k)	1.5780	10.4220	0.1354	0.224	48.6
BM _{85:15} (15k)	1.5780	10.4220	0.2708	0.0447	49.3
BM _{85:15} (10k)	1.5780	10.4220	0.4098	0.0677	49.9
BM _{85:15} (5k)	1.5780	10.4220	0.8197	0.1353	51.8
BM _{93:7} (22k)	0.7566	11.2434	0.1358	0.0224	48.6
BM _{93:7} (15k)	0.7566	11.2434	0.2715	0.0448	49.3
BM _{93:7} (10k)	0.7566	11.2434	0.4092	0.0676	49.9
BM _{93:7} (5k)	0.7566	11.2434	0.8297	0.1370	51.8

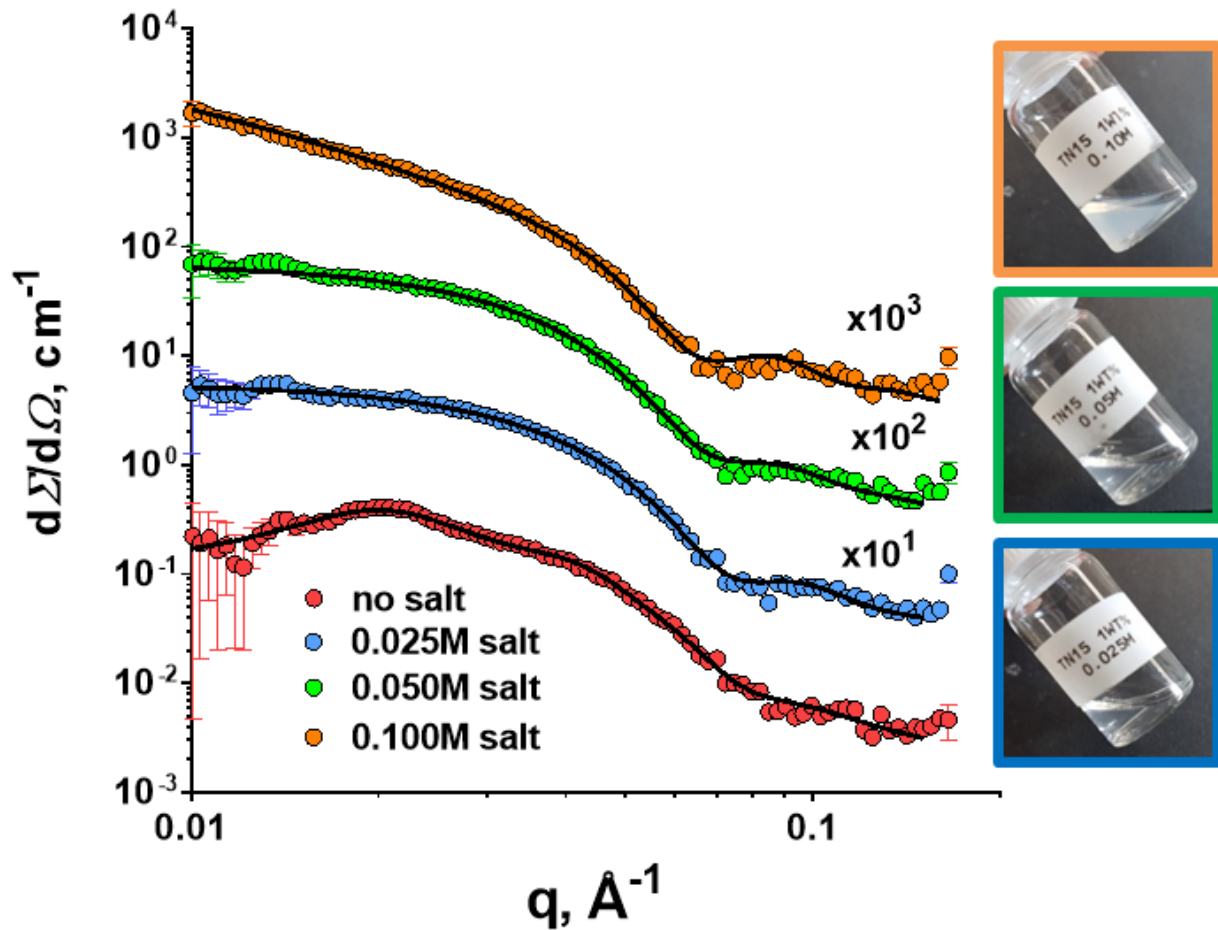
Appendix 2. Kinetics of polymerisation of BMA and MAA monomers. (a) monomer conversion as determined by ^1H NMR spectroscopy and (b) pseudo-first order kinetic plots. The conversion rate of monomer to polymer at the beginning of the polymerization is similar for both BMA and MAA; however, the total conversion is 93 mol% and 65 mol%, respectively.



Appendix 3. Bubble graph of zero shear viscosity against copolymer concentration and the volume fraction of IPA in the solvent (V_{IPA}) measured for BM_{85:15(22k)} copolymer samples. A viscosity peak observed in the graph is indicated by the blue-colored region, and the region of unachievable sample formulations is marked with the dashed triangle.



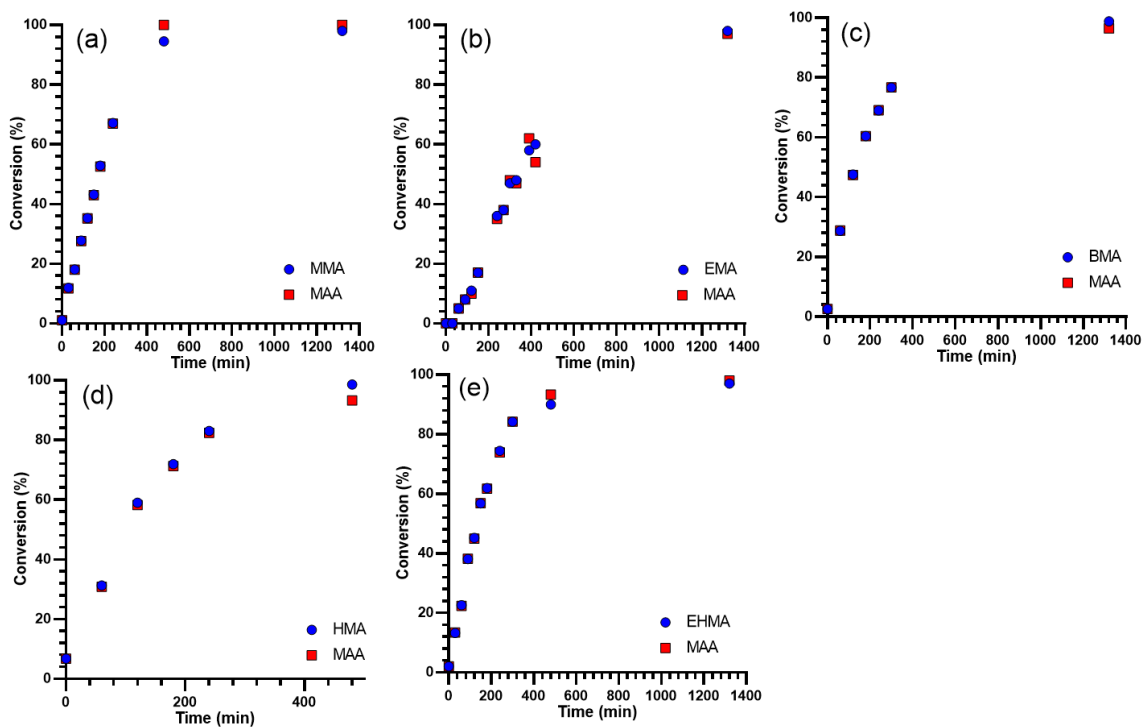
Appendix 4. SAXS patterns of 1 wt% aqueous solutions of BM_{85:15(22k)} (symbols) with different concentrations of background electrolyte (NaCl). The Bruker AXS Nanostar instrument was used for the measurements. Some patterns are shifted upward by a factor indicated on the plots to avoid overlap. The SAXS data are fitted with a simple sphere model.



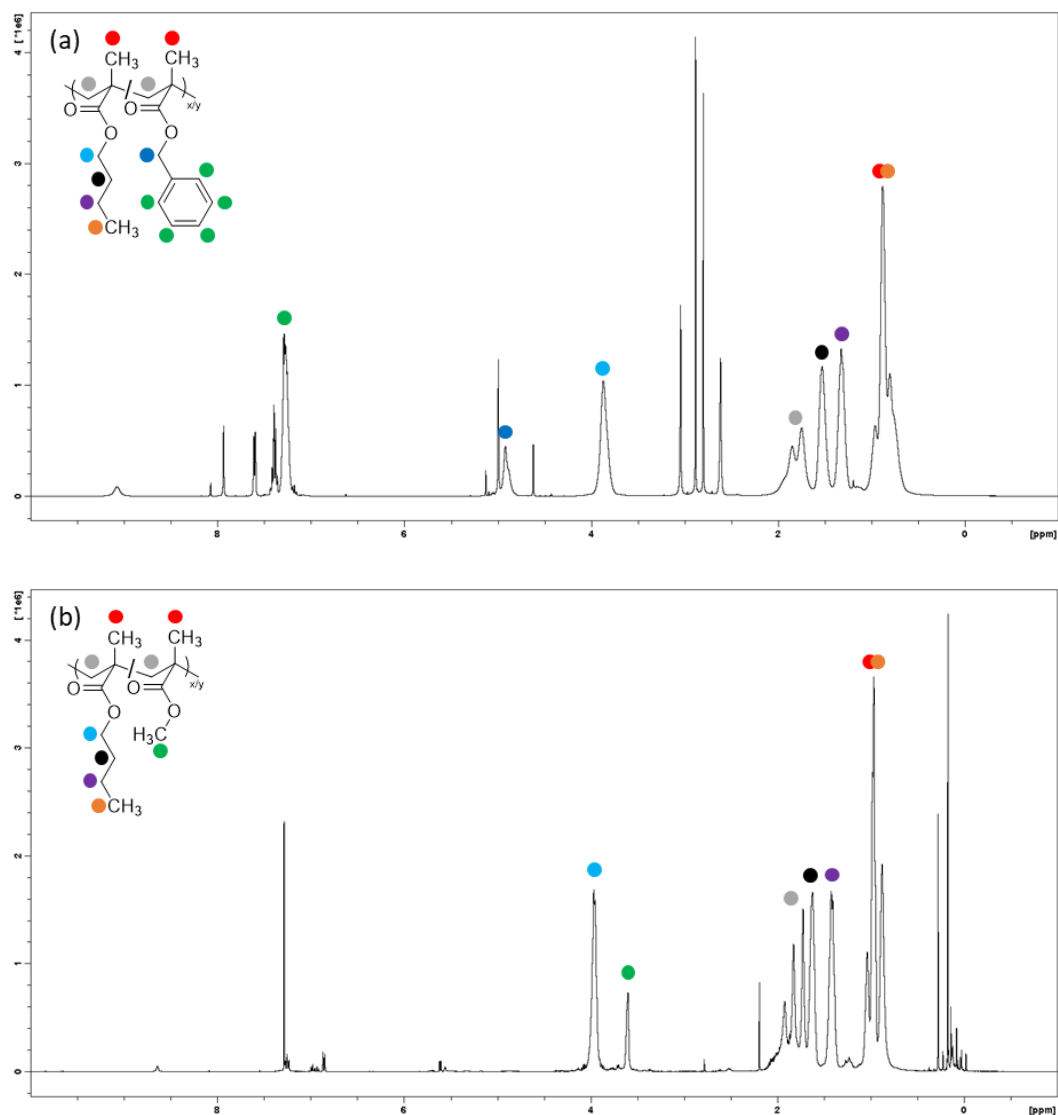
Appendix 5. Electrophoretic data of 0.25 wt% copolymer aqueous dispersions with a background electrolyte (KCl, 0.75 mol/m³) collected using a Malvern Zetasizer Nano ZS instrument.

Label	Polymer Conc (wt%)	Radius (nm)	Mobility ($\mu\text{mcm/Vs}$)	Zeta potential [Henry] (mV)	Apparent charge (Q)
BM77:23(22k)	0.25	4.2	-2.999	-62.75	-20
BM85:15(22k)	0.25	5.2	-2.520	-52.52	-22
BM85:15(10k)	0.25	5.3	-3.639	-77.73	-34
BM85:15(5k)	0.25	5.5	-3.730	-75.77	-35
BM93:7(22k)	0.25	8.5	-3.767	-77.56	-65
BM93:7(15k)	0.25	8.3	-4.144	-85.40	-69

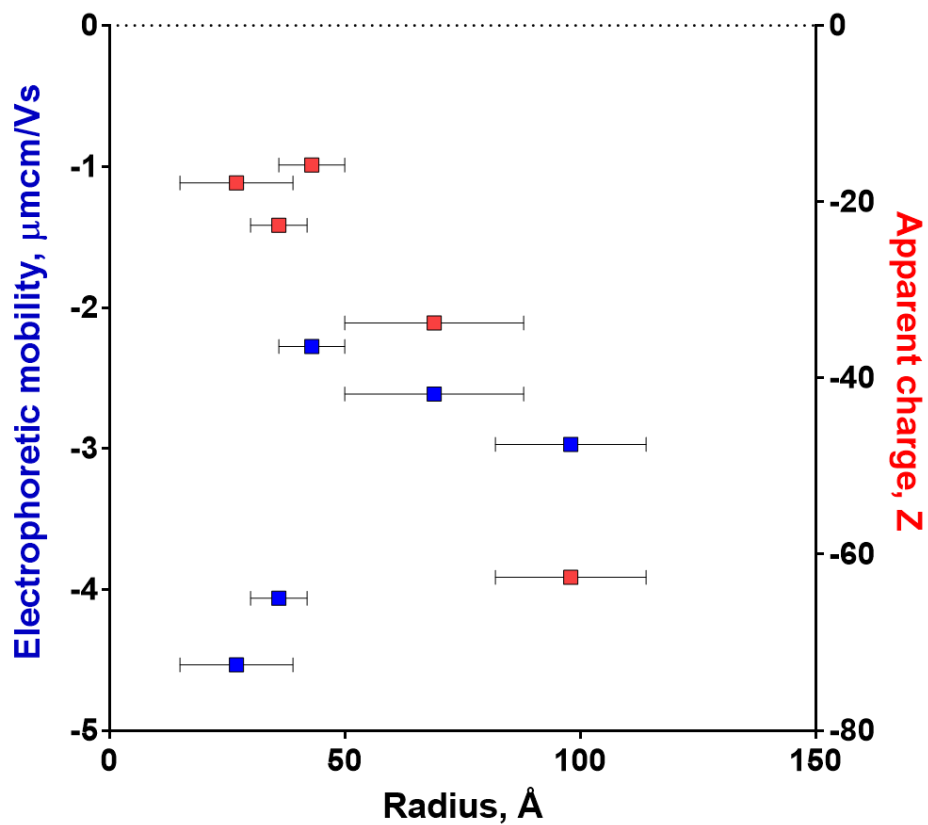
Appendix 6. Monomer conversion versus time for the polymerization of MAA with alkyl methacrylates: (a) MMA, (b) EMA, (c) BMA, (d) HMA and (e) EHMA. All polymerizations were performed at 50 wt% monomer in IPA except the BMA/MAA copolymerisations which were performed in dioxane. The monomer conversions were determined by ^1H NMR spectroscopy.



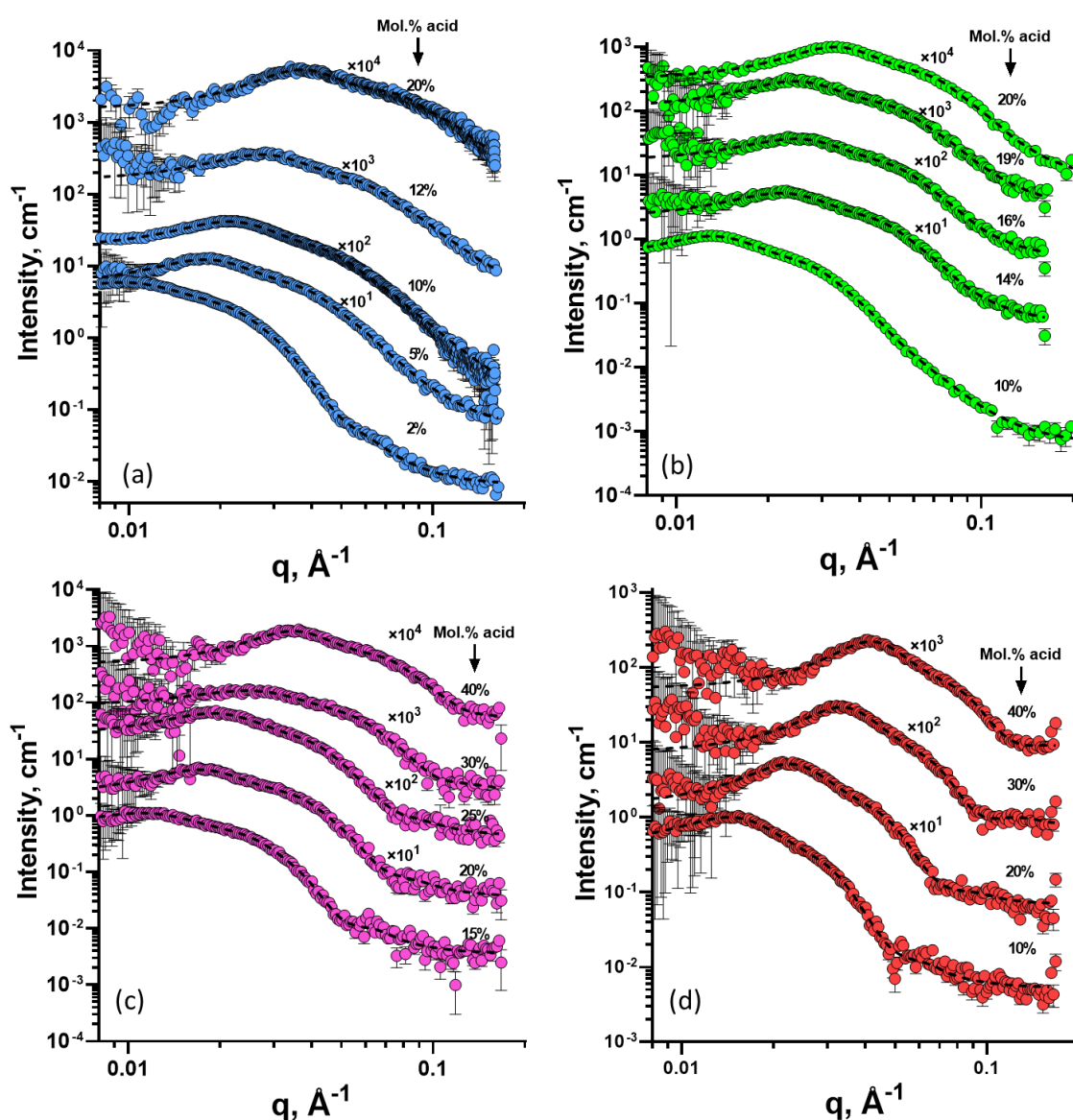
Appendix 7. ^1H NMR spectra of the product of two different alkylation techniques performed on BM_{8515} where (a) is the product of benzylation (P[butyl methacrylate-*stat*-benzyl methacrylate]) and (b) is the product of methylation (P[butyl methacrylate-*stat*-methyl methacrylate]).



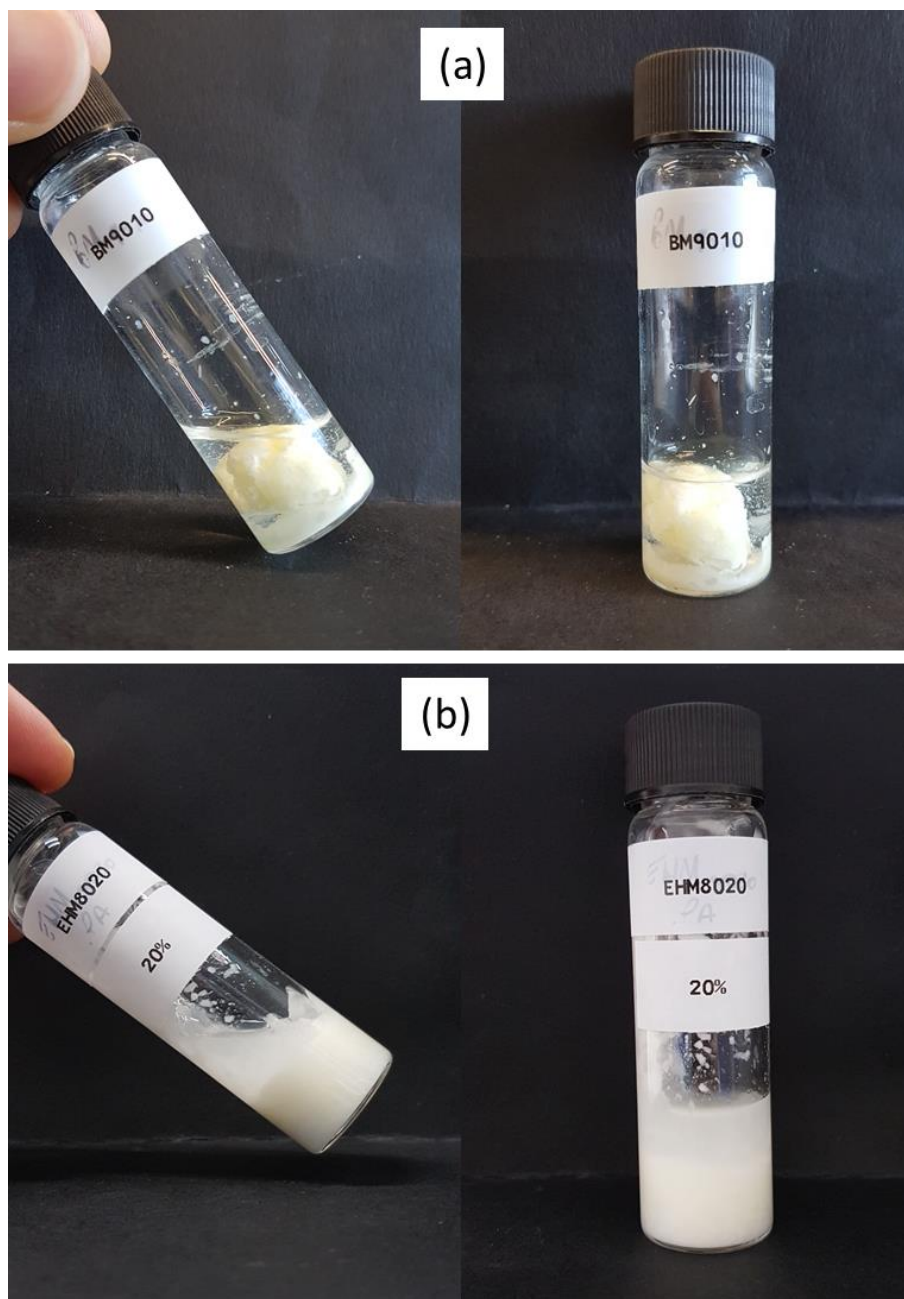
Appendix 8. Electrophoretic data of 0.1 wt% EHM copolymer aqueous dispersions with a background electrolyte (KCl, 0.9 mol/m³) collected using a Malvern Zetasizer Nano ZS instrument demonstrating that the particles formed by these copolymers are anionic.



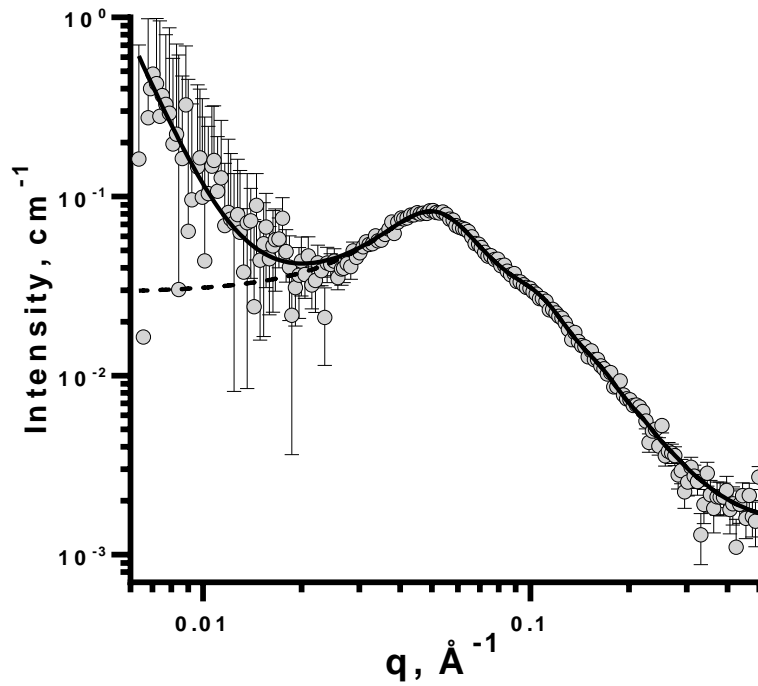
Appendix 9. SAXS patterns recorded for 1.0 wt% aqueous dispersions of the statistical copolymer particles (symbols) fitted using a refined spherical particle model (dashed lines) comparing the size of the particles formed by copolymers with different molar composition of MAA, where (a) is the MM series (excluding the patterns fit with the spheroid model), (b) is the EM series (excluding the patterns fit with the spheroid model), (c) is the BM series, and (d) is the HM series. Some patterns are shifted upwards by arbitrary factors, indicated on the plots, to avoid overlap. Either a Bruker AXS Nanostar instrument or a Xenocs Xeuss instrument were used to perform these SAXS measurements.



Appendix 10. Images of the unstable copolymer compositions that have precipitated during the solvent switch process to form particles in water, where (a) is BM9010 and (b) is EHM8020.



Appendix 11. SAXS pattern recorded for a 1.0 wt% aqueous dispersion of MM₆₀₄₀ copolymer particles (symbols) fitted using the spheroid model with an incorporated aspect ratio (dotted line) to extract a particle size. Additionally, a unified parametrization was incorporated in the fitting model (solid line) to account for the upturn at low q -values caused by particle aggregation. A Bruker AXS Nanostar instrument was used for these measurements.

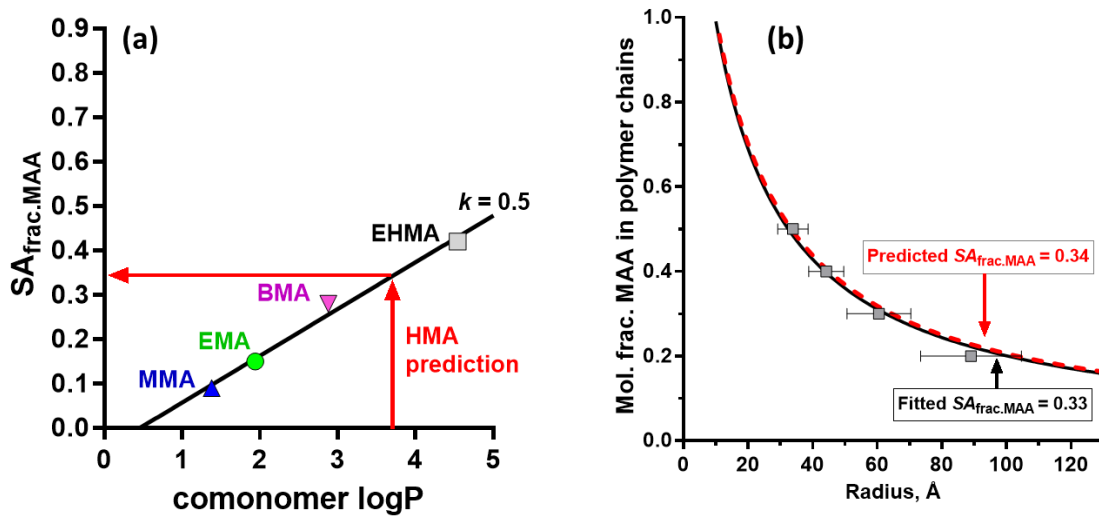


Appendix 12. Structural characteristics of 2.0 wt% dispersions of BM₈₀₂₀ obtained from simultaneous fitting of SANS patterns using the core-shell model: mean particle core radius (R_{core}), standard deviation of the mean particle core radius ($\sigma_{R_{\text{core}}}$), the shell thickness (Δr), the scattering length density of the H₂O:D₂O mixture (ζ_{sol}), the scattering length density of the particle core (ζ_{core}), and the scattering length density of the particle shell (ζ_{shell}).

H ₂ O:D ₂ O (v:v)	R_{core} (Å)	$\sigma_{R_{\text{core}}}$ (Å)	Δr (Å) ^a	ζ_{sol} ^b ($\times 10^{10} \text{ cm}^{-2}$)	ζ_{core} ($\times 10^{10} \text{ cm}^{-2}$)	ζ_{shell} ($\times 10^{10} \text{ cm}^{-2}$)
100:0	35	10	4.95	-0.56	0.625	0.685
83.5:16.5	35	10	4.95	0.58	0.625	0.685
40:60	35	10	4.95	3.58	0.625	0.685
0:100	35	10	4.95	6.33	0.625	0.685

^a the shell is fixed at the thickness or 1 MAA unit, ^b the SLD of the solvent is known and is therefore fixed during the fitting

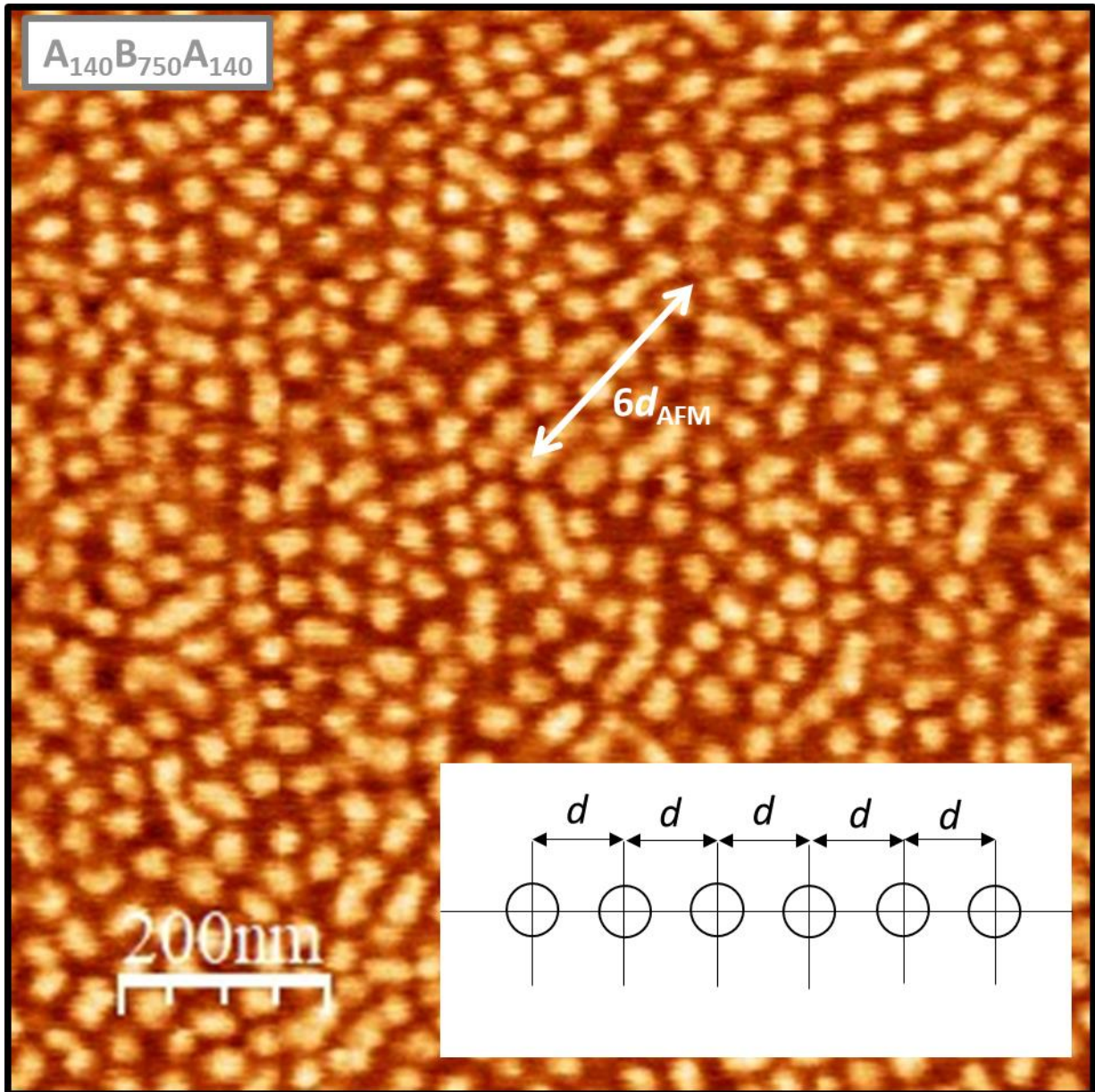
Appendix 13. A graphical depiction of how the linear relationship between $SA_{\text{frac.MAA}}$ and $\log P$ and the PSC model was used as a predictive tool to formulate a structural trend for the HM series, where (a) shows the linear relationship between $\log P$ and the $SA_{\text{frac.MAA}}$, and (b) shows the predicted size against copolymer composition (red dashed line), the experimental size data against the measured copolymer composition (symbols), and the structural model fit to the experimental data (black solid line) which outputs a value for $SA_{\text{frac.MAA}}$.



Appendix 14. Summary of reagent quantities required in the synthesis of the triblock copolymers in chapter 6.

Triblock	Macro-CTA (g)	BA (g)	AIBN (g)	MEK (g)
A ₅₆ B ₁₀₀ A ₅₆	4.36	5.50	0.0141	18.3
A ₅₆ B ₁₅₀ A ₅₆	3.43	6.50	0.0110	18.5
A ₅₆ B ₂₀₀ A ₅₆	2.97	7.50	0.0096	19.5
A ₅₆ B ₃₀₀ A ₅₆	2.25	8.50	0.0070	20.0
A ₅₆ B ₅₀₀ A ₅₆	1.43	9.00	0.0046	19.4
A ₅₆ B ₇₅₀ A ₅₆	1.00	9.50	0.0033	19.5
A ₁₀₈ B ₁₀₀ A ₁₀₈	7.54	5.00	0.0130	23.3
A ₁₀₈ B ₁₅₀ A ₁₀₈	6.03	6.00	0.0100	22.4
A ₁₀₈ B ₂₀₀ A ₁₀₈	5.28	7.00	0.0090	22.8
A ₁₀₈ B ₃₀₀ A ₁₀₈	4.02	8.00	0.0070	22.3
A ₁₀₈ B ₅₀₀ A ₁₀₈	2.71	9.00	0.0050	21.8
A ₁₀₈ B ₇₅₀ A ₁₀₈	2.01	10.00	0.0030	22.3
A ₁₄₀ B ₁₀₀ A ₁₄₀	8.76	4.50	0.0120	24.7
A ₁₄₀ B ₁₅₀ A ₁₄₀	7.14	5.50	0.0090	23.5
A ₁₄₀ B ₂₀₀ A ₁₄₀	6.33	6.50	0.0080	23.8
A ₁₄₀ B ₃₀₀ A ₁₄₀	4.87	7.50	0.0060	23.0
A ₁₄₀ B ₅₀₀ A ₁₄₀	3.51	9.00	0.0050	23.2
A ₁₄₀ B ₇₅₀ A ₁₄₀	2.60	10.00	0.0030	23.4

Appendix 15. AFM height image of an example triblock copolymer film ($A_{140}B_{750}A_{140}$) cast from a 40% w/w solution in MEK measured using ScanAsyst® PeakForce® tapping mode (lighter colour = higher structure relating to the hard phase, and *vice versa*), where the arrow demonstrates the measured distance and the cartoon below demonstrates how d_{AFM} is calculated.



Appendix 16. A cartoon depiction of a BCC crystal structure, firstly showing the distances between the crystallographic planes, d_{011} , and secondly the distance between particles, a .

